DISSERTATIONES
CHIMICAE
UNIVERSITATIS
TARTUENSIS
**201**

SANDER RATSO

# Electrocatalysis of oxygen reduction on non-precious metal catalysts

DISSERTATIONES CHIMICAE UNIVERSITATIS TARTUENSIS
**201**

DISSERTATIONES CHIMICAE UNIVERSITATIS TARTUENSIS
**201**

**SANDER RATSO**

# Electrocatalysis of oxygen reduction on non-precious metal catalysts

UNIVERSITY OF TARTU
Press

Institute of Chemistry, Faculty of Science and Technology, University of Tartu, Estonia

The dissertation is accepted for the commencement of the degree of *Doctor Philosophiae* in Chemistry on November 26th, 2020 by the Council of Institute of Chemistry, Faculty of Science and Technology, University of Tartu.

Supervisors: Assoc. Prof. Kaido Tammeveski
Institute of Chemistry, University of Tartu, Estonia

PhD Ivar Kruusenberg
National Institute of Chemical Physics and Biophysics, Estonia

Opponent: PhD Juan Herranz
Paul Scherrer Institute, Switzerland

Commencement: January 14th, 2021 at 14.15, Ravila 14A–1020, Tartu (Chemicum) and Microsoft Teams (*online*)

This work has been partially supported by ASTRA project PER ASPERA Graduate School of Functional Materials and Technologies receiving funding from the European Regional Development Fund under project in University of Tartu, Estonia


ISSN 1406-0299
ISBN 978-9949-03-524-3 (print)
ISBN 978-9949-03-525-0 (pdf)



University of Tartu Press
www.tyk.ee

# TABLE OF CONTENTS

# 1. LIST OF ORIGINAL PUBLICATIONS

This thesis consists of fourteen original articles listed below. The articles are referred in the text by Roman numerals I–XIV.

I **S. Ratso**, I. Kruusenberg, M. Vikkisk, U. Joost, E. Shulga, I. Kink, T. Kallio, K. Tammeveski, Highly active nitrogen-doped few-layer graphene/ carbon nanotube composite electrocatalyst for oxygen reduction reaction in alkaline media, Carbon 73 (2014) 361–370.

II I. Kruusenberg, **S. Ratso**, M. Vikkisk, P. Kanninen, T. Kallio, A.M. Kannan, K. Tammeveski, Highly active nitrogen-doped nanocarbon electrocatalysts for alkaline direct methanol fuel cell, Journal of Power Sources 281 (2015) 94–102.

III **S. Ratso**, I. Kruusenberg, U. Joost, R. Saar, K. Tammeveski, Enhanced oxygen reduction reaction activity of nitrogen-doped graphene/multi-walled carbon nanotube catalysts in alkaline media, International Journal of Hydrogen Energy 41 (2016) 22510–22519.

IV I. Kruusenberg, D. Ramani, **S. Ratso**, U. Joost, R. Saar, P. Rauwel, A.M. Kannan, K. Tammeveski, Cobalt-nitrogen co-doped carbon nanotube cathode catalyst for alkaline membrane fuel cells, ChemElectroChem 3 (2016) 1455–1465.

V **S. Ratso**, I. Kruusenberg, A. Sarapuu, P. Rauwel, R. Saar, U. Joost, J. Aruväli, P. Kanninen, T. Kallio, K. Tammeveski, Enhanced oxygen reduction reaction activity of iron-containing nitrogen-doped carbon nanotubes for alkaline direct methanol fuel cell application, Journal of Power Sources 332 (2016) 129–138.

VI **S. Ratso**, I. Kruusenberg, A. Sarapuu, M. Kook, P. Rauwel, R. Saar, J. Aruväli, K. Tammeveski, Electrocatalysis of oxygen reduction on iron- and cobalt-containing nitrogen-doped carbon nanotubes in acid media, Electrochimica Acta 218 (2016) 303–310.

VII **S. Ratso**, I. Kruusenberg, M. Käärik, M. Kook, R. Saar, M. Pärs, J. Leis, K. Tammeveski, Highly efficient nitrogen-doped carbide-derived carbon materials for oxygen reduction reaction in alkaline media, Carbon 113 (2017) 159–169.

VIII **S. Ratso**, I. Kruusenberg, M. Käärik, M. Kook, R. Saar, P. Kanninen, T. Kallio, J. Leis, K. Tammeveski, Transition metal-nitrogen co-doped carbide-derived carbon catalysts for oxygen reduction reaction in alkaline direct methanol fuel cell, Applied Catalysis B: Environmental 219 (2017) 276–286.

IX **S. Ratso**, I. Kruusenberg, M. Käärik, M. Kook, L. Puust, R. Saar, J. Leis, K. Tammeveski, Highly efficient transition metal and nitrogen co-doped carbide-derived carbon electrocatalysts for anion exchange membrane fuel cells, Journal of Power Sources 375 (2018) 233–243.

X **S. Ratso**, M. Käärik, M. Kook, P. Paiste, V. Kisand, S. Vlassov, J. Leis, K. Tammeveski, Iron and nitrogen co-doped carbide-derived carbon and carbon nanotube composite catalysts for oxygen reduction reaction, ChemElectroChem 5 (2018) 1827–1836.

XI **S. Ratso**, N. Ranjbar Sahraie, M.T. Sougrati, M. Käärik, M. Kook, R. Saar, P. Paiste, Q. Jia, J. Leis, S. Mukerjee, F. Jaouen, K. Tammeveski, Synthesis of highly-active Fe-N-C catalysts for PEMFC with carbide-derived carbons, Journal of Materials Chemistry A 6 (2018) 14663–14674.

XII **S. Ratso**, M. Käärik, M. Kook, P. Paiste, J. Aruväli, S. Vlassov, V. Kisand, J. Leis, A.M. Kannan, K. Tammeveski, High performance catalysts based on Fe/N co-doped carbide-derived carbon and carbon nanotube composites for oxygen reduction reaction in acid media, International Journal Hydrogen Energy 44 (2019) 12636–12648.

XIII **S. Ratso**, M.T. Sougrati, M. Käärik, M. Merisalu, M. Rähn, V. Kisand, A. Kikas, P. Paiste, J. Leis, V. Sammelselg, F. Jaouen, K. Tammeveski, Effect of ball-milling on the oxygen reduction reaction activity of iron and nitrogen co-doped carbide-derived carbon catalysts in acid media, ACS Applied Energy Materials 2 (2019) 7952–7962.

XIV **S. Ratso**, A. Zitolo, M. Käärik, M. Merisalu, M. Rähn, A. Kikas, V. Kisand, P. Paiste, J. Leis, V. Sammelselg, S. Holdcroft, F. Jaouen, K. Tammeveski, Non-precious metal cathodes for anion exchange membrane fuel cells from ball-milled iron and nitrogen doped carbide-derived carbons (Renewable Energy, accepted).

**Author's contribution**

Paper I The author was responsible for the synthesis of catalysts, performed all electrochemical measurements and data analysis. The author is responsible for the interpretations of electrochemical testing results.

Paper II The author was responsible for the synthesis of graphene-carbon nanotube composites, performed all electrochemical measurements with that catalyst and data analysis. The author participated in the writing of the manuscript.

Paper III The author was responsible for the synthesis of catalysts, performed all electrochemical measurements and data analysis. The author is responsible for the interpretation of electrochemical testing results and primarily responsible for writing the manuscript.

Paper IV The author was responsible for the synthesis of catalysts, performed all electrochemical measurements excluding fuel cell testing and analysed the data. The author is responsible for the interpretation of electrochemical testing results and participated in writing the manuscript.

Paper V The author was responsible for the synthesis of catalysts, performed all electrochemical measurements except fuel cell testing and data analysis. The author is responsible for the interpretations of electrochemical testing results and participated in writing the manuscript.

Paper VI The author was responsible for the synthesis of catalysts, performed all electrochemical measurements and data analysis. The author is responsible for the interpretation of electrochemical testing results and participated in writing the manuscript.

Paper VII The author was responsible for the synthesis of catalysts, performed all electrochemical measurements and data analysis. The author is responsible for the interpretation of all testing results and primarily responsible for writing the manuscript.

Paper VIII The author was responsible for the synthesis of catalysts, performed all electrochemical measurements and data analysis. The author is responsible for the interpretation of all testing results and primarily responsible for writing the manuscript.

Paper IX The author was responsible for the synthesis of catalysts, performed all electrochemical measurements and data analysis. The author is responsible for the interpretation of all testing results and primarily responsible for writing the manuscript.

Paper X The author was responsible for the synthesis of catalysts, performed all electrochemical measurements and data analysis. The author is responsible for the interpretation of all testing results and primarily responsible for writing the manuscript.

Paper XI The author was responsible for the synthesis of catalysts, performed all electrochemical measurements, X-ray diffraction measurements and data analysis. The author is responsible for the interpretation of all testing results excluding Mössbauer spectroscopy and X-ray absorption spectroscopy and is primarily responsible for writing the manuscript.

Paper XII The author was responsible for the synthesis of catalysts, performed all electrochemical measurements and data analysis. The author is responsible for the interpretation of all testing results and primarily responsible for writing the manuscript.

Paper XIII The author was responsible for the synthesis of catalysts, performed all electrochemical measurements, X-ray diffraction measurements, $N_2$ adsorption measurements and data analysis. The author is responsible for the interpretation of all testing results excluding Mössbauer spectroscopy and is primarily responsible for writing the manuscript.

Paper XIV The author was responsible for the synthesis of catalysts, performed all electrochemical measurements and data analysis. The author is responsible for the interpretation of all testing results excluding X-ray absorption spectroscopy and is primarily responsible for writing the manuscript.

# 2. ABBREVIATIONS AND SYMBOLS

| | |
|---|---|
| $A$ | geometric surface area of an electrode |
| AEI | anion exchange ionomer |
| AEM | anion exchange membrane |
| AEMFC | anion-exchange membrane fuel cell |
| BE | binding energy |
| BET | Brunauer-Emmett-Teller |
| BR | biuret |
| CDC | carbide-derived carbon |
| CH | carbohydrazide |
| CNTs | carbon nanotubes |
| CoPc | cobalt(II)phthalocyanine |
| CVD | chemical vapour deposition |
| $c_{O2}^{b}$ | concentration of oxygen in the bulk solution |
| CV | cyclic voltammetry |
| $D_{O2}$ | diffusion coefficient of oxygen |
| $d_p$ | diameter of pores |
| DCDA | dicyandiamide |
| DFT | density functional theory |
| DMFC | direct methanol fuel cell |
| $E$ | electrode potential |
| $E^0$ | standard potential |
| $E_{1/2}$ | half-wave potential |
| $E_{onset}$ | onset potential |
| EDX | energy dispersive X-ray spectroscopy |
| $F$ | Faraday constant |
| FCEV | fuel cell electyric vehicle |
| FePc | iron(II)phthalocyanine |
| GC | glassy carbon |
| GDL | gas diffusion layer |
| GO | graphene oxide |
| HOR | hydrogen oxidation reaction |
| $I$ | current |
| $I_d$ | diffusion-limited current |
| $I_k$ | kinetic current |
| ICP-MS | inductively coupled plasma mass spectrometry |
| $j$ | current density |
| $j_d$ | diffusion-limited current density |
| $j_k$ | kinetic current density |
| K-L | Koutecky-Levich |
| MA | mass activity |
| MEA | membrane-electrode assembly |
| M-N-C | metal-nitrogen-carbon |

| | |
|---|---|
| MOF | metal-organic framework |
| MWCNTs | multi-walled carbon nanotubes |
| $n$ | number of electrons transferred per $O_2$ molecule |
| NPMC | non-precious metal catalyst |
| OCV | open circuit voltage |
| ORR | oxygen reduction reaction |
| PEFC | polymer electrolyte fuel cell |
| PEMFC | proton-exchange membrane fuel cell |
| PGM | platinum group metal |
| Phen | 1,10-phenanthroline |
| $P_{max}$ | maximum power density |
| PSD | pore size distribution |
| Pt/C | carbon-supported Pt catalyst |
| QSDFT | quenched solid density functional theory |
| RDE | rotating disk electrode |
| RHE | reversible hydrogen electrode |
| RRDE | rotating ring-disk electrode |
| SC | semicarbazide |
| SCE | saturated calomel electrode |
| SD | site density |
| SEM | scanning electron microscopy |
| SHE | standard hydrogen electrode |
| SSA | specific surface area |
| SWCNTs | single-walled carbon nanotubes |
| TEM | transmission electron microscopy |
| TOF | turnover frequency |
| $V_p$ | total volume of pores |
| $V_\mu$ | volume of micropores |
| $v$ | potential scan rate |
| XAS | X-ray absorption spectroscopy |
| XPS | X-ray photoelectron spectroscopy |
| XRD | X-ray powder diffraction |
| $\nu$ | kinematic viscosity of the solution |
| $\omega$ | electrode rotation rate |

# 3. INTRODUCTION

Moving on from the carbon energy cycle that is destroying our environment and deteriorating living conditions worldwide is one of the priorities for humanity in the 21st century. According to the International Energy Agency, the energy consumption in the world is increasing by 1% every year with transportation quickly becoming the largest energy sector [1–3]. However, nearly all the energy used for transportation is still being produced by burning fossil fuels. Polymer electrolyte membrane fuel cells have emerged as one of the pathways towards reducing the $CO_2$ emissions from automotive applications and have already seen wide-scale use in fuel cell electric vehicles [4]. In such a fuel cell, the energy from a hydrogen molecule is converted cleanly into electrical energy with water being the only product [5]. The main remaining problems towards replacement of internal combustion engines by polymer electrolyte fuel cells are cost and durability [6]. These issues stem from the sluggish oxygen reduction reaction (ORR), which takes place at the fuel cell cathode. Due to the strong oxygen-oxygen double bond, the $O_2$ molecule requires a good electrocatalyst to be split at an appreciable rate and a low overpotential. So far, nearly all commercially available fuel cell systems have used platinum-based catalysts on the cathode to achieve this, but it has become apparent that the long-term activity and stability targets cannot be met by Pt-based materials while keeping costs low enough [7]. Since 1964, when Jasinski first published his study on a non-platinum fuel cell catalyst, the search for a replacement for the platinum catalyst has constantly gathered momentum [8]. This has been fuelled by the discovery of new carbon nanomaterials such as carbon nanotubes (CNTs) [9] and graphene [10], as carbon has been the support material of choice for both platinum-based and non-platinum catalysts. Design of the carbon material at close to atomic levels has allowed for the rational design of non-precious metal catalysts for oxygen electroreduction with ever-increasing activity and stability.

The aim of this PhD thesis was thus to explore the electrocatalytic activity of undoped and doped carbon nanotubes [I–VI, X, XII], graphene [I–III], carbide-derived carbon [VII–XIII] and composites thereof [I–III, X, XII] towards the ORR, design new and better catalysts from these supports and to establish structure-property relationships, which would allow for new enhancements to be made in the field of fuel cell electrocatalysis.

# 4. LITERATURE OVERVIEW

## 4.1 Polymer electrolyte fuel cells

A fuel cell, at a very basic level, is a device for converting a fuel (for example, hydrogen) and an oxidant (air) directly into electricity, heat and a product (water). There are five types of fuel cells that have seen commercial use so far: 1) the polymer electrolyte fuel cell (PEFC), 2) the alkaline fuel cell, 3) the solid oxide fuel cell, 4) the molten carbonate fuel cell and 5) the phosphoric acid fuel cell. Polymer electrolyte fuel cells, in turn, are divided into proton exchange membrane fuel cells (PEMFC), anion exchange membrane fuel cells (AEMFC) and direct methanol fuel cells (DMFC). For transportation purposes, PEFCs make the most sense as they operate at low temperatures (under 100 °C) and require no liquid or corrosive components (such as molten carbonates, liquid hydroxides or phosphoric acid) [11]. This makes them perfect for use in automobiles not only from a safety standpoint, but also an efficiency one since they can be easily stopped and started again without the need to heat the system back up to high temperatures. A PEFC, taking the example of a PEMFC operates using the simple reaction:

$$2H_2 + O_2 \rightarrow 2H_2O \quad (1)$$

Hydrogen, which is used as the fuel, is oxidised on the anode, while oxygen is reduced on the cathode to water using the protons released from the oxidised hydrogen. The protons are conducted to the cathode through a proton exchange membrane (PEM). Since the membrane is an electrical insulator, the electrons move through an external circuit, where they can be used to do useful work as shown in Figure 1. Taking a single-cell membrane electrode assembly (MEA) as an example, the fuel cell typically consists of catalysts either deposited on or integrated into a carbon material which make up the anode and the cathode. The electrodes, in turn, are deposited onto the polymeric membrane (almost always Nafion™) and sandwiched between gas diffusion layers (GDLs). The GDLs are commonly made of carbon fibres or carbon paper and have the purpose of efficiently transporting gases to and water from the electrodes.

The MEA is in turn sandwiched between bipolar flow field plates, which serve as further channels for gas and water vapour transport and are made of graphite or metal coated with corrosion-resistant layers (due to the acidic conditions inside a PEMFC) [12]. They also support the MEA and give the structural strength to the fuel cell stack.

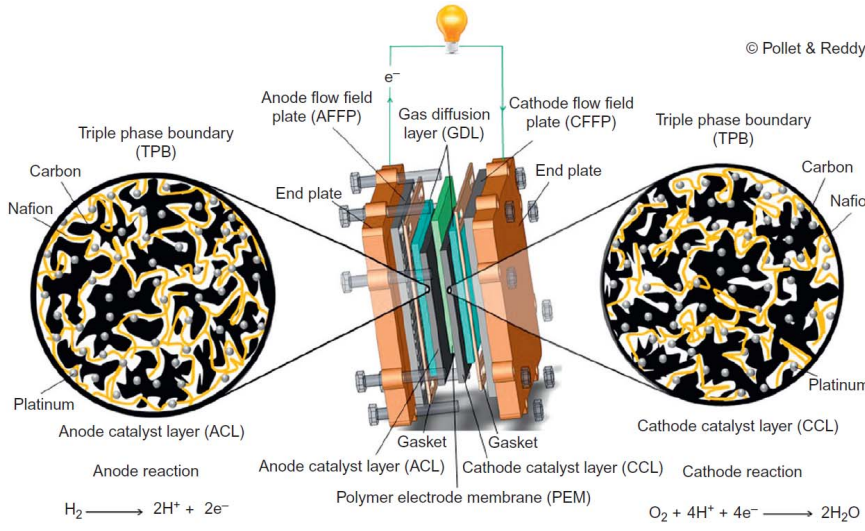


**Figure 1.** Schematic of a PEMFC [11].

The maximum theoretical efficiency of such a fuel cell is 83%, however, the practical efficiency is closer to 40% (still more than double of the engines used in today's cars) [13]. This is largely due to the activation, ohmic and mass-transport losses in the fuel cell which all take place when current is drawn from the cell. The actual cell voltage is always lower than the equilibrium potential of the cell (1.23 V) due to these losses. Ohmic losses arise from the transfer of protons in the proton exchange membrane and are normally minimised by using a very thin membrane (the common Nafion 211 membrane has a thickness of 25.4 µm [14]). Mass-transport losses are alleviated by efficient transport of reactants to and products from the catalyst layers via GDLs and an efficient pore structure as well as thin electrodes (in commercial solutions, the cathode, which is the thicker electrode, is normally 5–30 µm thick, but with non-precious metal electrodes the thickness can be >100 µm [15]). The largest loss by far comes from the activation overpotential of the oxygen reduction reaction (ORR) taking place on the cathode [15]. While the hydrogen oxidation reaction (HOR) is quite a fast reaction, which proceeds either according to the Volmer-Tafel or Volmer-Heyrovsky mechanism, the ORR requires four electrons to be transferred to the $O_2$ molecule and the cleavage of a double oxygen-oxygen bond, making the kinetics much more complex and the reaction sluggish. Most of the work done on PEFCs so far has been on PEMFCs due to the availability of the Nafion proton exchange membrane. In alkaline membrane fuel cells, where the membrane conducts $OH^-$ instead, the progress has long been inhibited by low-performing anion exchange membranes (AEM), but with membranes exhibiting ion conductivities over 0.1 mS $cm^{-1}$ now available [16], there is a huge potential for AEMFC technology to catch up to that of PEMFC. Recent studies on non-

precious metal catalysts (NPMC) switching from a commercial AEM to a highly conductive one have demonstrated performance gains higher than an order of magnitude [17]. In addition to using hydrogen as the fuel, methanol has also been proposed as an alternative (in DMFCs). Methanol has some important advantages over hydrogen: it is in liquid rather than gaseous form at standard conditions and therefore easier to store and transport, does not embrittle common metals such as steel and aluminium and has a higher energy density (at standard conditions) [18]. The main problem with DMFCs is the diffusion of methanol through the membrane onto the cathode side, where the platinum-based catalysts start to oxidise it, leading to a mixed potential and poisoning of the cathode by CO [19–21].

## 4.2 Oxygen reduction reaction

The electroreduction of oxygen is one of the most important electrochemical reactions. In addition to providing energy via fuel cells, it forms the basis of life in biological respiration. In acidic aqueous solutions the ORR can follow either a 4-electron pathway [22,23]:

$$O_2 + 4H^+ + 4e^- \rightarrow 2H_2O \qquad E_0 = 1.229\ \text{V}, \tag{2}$$

or 2-electron pathway:

$$O_2 + 2H^+ + 2e^- \rightarrow H_2O_2 \qquad E_0 = 0.67\ \text{V}, \tag{3}$$

followed by further reduction of hydrogen peroxide

$$H_2O_2 + 2H^+ + 2e^- \rightarrow 2H_2O \qquad E_0 = 1.77\ \text{V} \tag{4}$$

or disproportionation

$$2H_2O_2 \rightarrow 2H_2O + O_2 \tag{5}.$$

In alkaline conditions the ORR can also proceed via two pathways. The 4-electron pathway:

$$O_2 + 2H_2O + 4e^- \rightarrow 4OH^- \qquad E_0 = 0.401\ \text{V}, \tag{6}$$

or 2-electron pathway:

$$O_2 + H_2O + 2e^- \rightarrow HO_2^- + OH^- \qquad E_0 = -0.065\ \text{V}, \tag{7}$$

followed by further reduction

$$HO_2^- + H_2O + 2e^- \rightarrow 3OH^- \qquad E_0 = 0.867\ \text{V}, \tag{8}$$

or disproportionation

$$2HO_2^- \rightarrow 2OH^- + O_2 \quad (9)$$

with all the standard potential ($E_0$) values given versus the standard hydrogen electrode (SHE) at 25 °C. The general scheme of the ORR is given in Figure 2, in alkaline (a) and acidic (b) conditions.

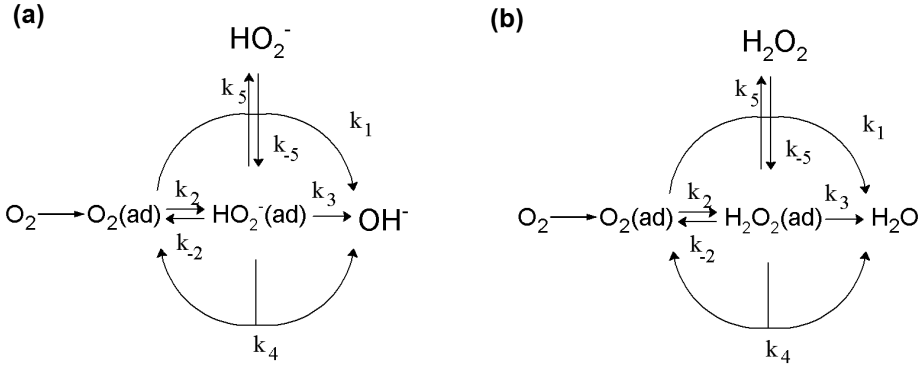


**Figure 2.** General scheme of the ORR in alkaline (a) and acidic (b) media. $k_i$ denotes the heterogeneous rate constants of various steps and (ad) denotes adsorbed species.

In fuel cell conditions, the 4e⁻ pathway is always preferred as hydrogen peroxide or the hydroperoxide anions can act to corrode the components of the fuel cell if not further reduced. Also, the formation of $H_2O_2$ (or $HO_2^-$) decreases the fuel cell efficiency. On noble metal surfaces such as Pt, the ORR undergoes a direct four-electron pathway without any desorption of $H_2O_2$ or $HO_2^-$, but on surfaces or electrocatalytic sites that bind these intermediates weaker they can desorb and thus react with other components. In acidic conditions Pt is well-known to be the most active electrocatalyst towards the ORR and selectively reduces $O_2$ via the four-electron pathway [24]. However, in alkaline conditions the chemisorption of $O_2$ is hindered by specifically adsorbed $OH^-$ species and thus the first step of the ORR can also be an outer-sphere reaction, where it is reduced to superoxide anion ($O_2^{\bullet-}$, shown in Figure 3) [25]. This creates a certain degree of nonspecificity to the surface on which this reduction reaction takes place and allows for the use of a much wider range of NPMCs in alkaline media compared to acidic [25]. Still, even some non-precious metal catalytic sites, like the M-$N_4$ coordination centre, are known to catalyse a direct 4e⁻ reduction of oxygen in both acidic and alkaline conditions [25–27].

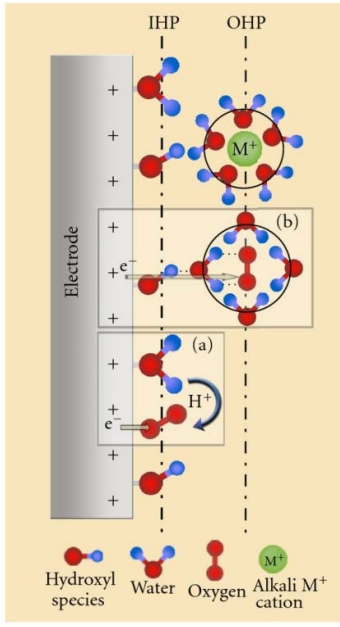


**Figure 3.** Outer-sphere ORR process in alkaline conditions [25].

## 4.3 Oxygen reduction on non-precious metal catalysts

PEFCs were invented in the early 1960s by Willard Thomas Grubb and Leonard Niedrach of General Electric (GE) for the Gemini missions [28]. Since the early days, the large amount of Pt needed to produce the GE fuel cells was noted to be a significant problem towards commercialisation [28]. Recently, PEFCs have seen a lot of success: major automotive companies such as Toyota, Hyundai, Honda, Ford, Chevrolet and Mercedes-Benz have all come out with their own PEM fuel cell vehicles and Plug Power, a company producing hydrogen-powered forklifts, posted more than $230M of revenue in 2019 [29]. However, all of these commercial solutions are still powered by Pt-based catalysts. So, what is wrong with using platinum? The global platinum supply is estimated at 69,000 tons and 192.5 tons were produced in 2019 [30,31]. A Toyota Mirai (the most produced fuel cell electric vehicle, FCEV) needs 35 grams of Pt for its fuel cell, meaning that if all the Pt currently produced was used for FCEVs, 5.5 million of such vehicles could be produced per year. The global car fleet was estimated to be over 1 billion in 2010 [32], so to replace the entire car fleet with Toyota Mirais (or vehicles using the same amount of Pt in the PEFC) would take over 18 years at the current pace. This requires that 35,000 tons (before taking into account the losses of making catalysts from the mined Pt) of the 69,000 tons available would need to be dedicated to FCEVs, which means that the recycling rate for Pt would need to be near 100% in the long term. Another thing to consider is that currently, the price for a Toyota Mirai is $58550 compared to $24525 for a Toyota Prius (an identical vehicle with a hybrid drivetrain). Clearly this is not a competitive

price. The main problem stems from the fact that an average Pt ore contains only 4 g of Pt per ton of ore and that most of the mining is done in deep mines in South Africa, driving up the price even more. Because the mining is mostly concentrated in only one area, there are also concerns about the stability and elasticity of the supply should the demand increase notably [5]. Pt-based catalysts have seen a tremendous increase in both specific activity and mass activity (by mass of Pt) in the recent decade as well [33–35], however incorporating these advancements made on the catalyst level to full-size fuel cell stacks has proven a challenge [36]. Even the most optimistic forecasts set the ultimate Pt loading at 0.1 g $kW^{-1}$ [34], which would mean that $1/7^{th}$ of the whole Pt on Earth would need to be dedicated to PEFC technology (not taking into account recycling and catalyst synthesis losses).

Clearly, in the long term, Pt-based catalysts are not the solution for PEFCs in FCEVs and even the US Department of Energy has included moving on to NPMC materials in their PEMFC roadmaps in the last few years [6,7]. The search for Pt replacements for oxygen reduction also has a long history, even predating PEFCs. As mentioned, the ORR also takes place in the respiratory system of mammals. Due to the low electrical conductivity of biological systems, the reaction rate is much lower than what is needed for a fuel cell, however. In 1964, Jasinski published the first study using a bio-inspired cobalt phthalocyanine (CoPc) catalyst deposited on Ni (as a highly conductive substrate) [8]. The next year he improved on his results considerably by using a carbon black instead of Ni as the substrate [37]. The carbon black had the advantage of having a much larger surface area, allowing for more of the CoPc to be adsorbed and therefore, more electrocatalytically active sites to be exposed. Nowadays, this strategy of using a carbon support to increase the utilisation is key in both precious and non-precious metal catalysts [33,38,39]. This was improved upon by introducing a high-temperature treatment which improved the contact between the $MN_4$ macrocycles and the substrate (but also changed the nature of the active site, which will be discussed further on)[40]. The next important enhancement was done in 1989 by Yeager and co-workers, who replaced the expensive $MN_4$ macrocycles with a mixture of simple nitrogen source (polyacrylonitrile, PAN) and simple metal salts (Co or Fe acetate). These mixtures were pyrolysed at high temperatures (300–950 °C) to create some of the best NPMCs at that time [41]. However, unlike the physically adsorbed macrocycle-based catalysts, which had a well-defined structure, these new heat-treated materials proposed the important question about the exact nature of the active sites for ORR after pyrolysis, which has only begun to be answered in the recent years [26,42–45].

### 4.3.1 Oxygen reduction on metal-nitrogen-carbon (M-N-C) catalysts

Metal-nitrogen-carbon or M-N-C catalysts thus contain a transition metal, nitrogen and carbon. Carbon makes up most of the material (by at.%) and provides the chemical stability, electrical conductivity, porous structure and mechanical

strength of the material. Traditionally, carbon materials with a high surface area such as Vulcan carbon XC72 and Black Pearls BP2000 have been widely used as a support material for heterogeneous catalysts, notably as carriers for Pt nanoparticles [33,46]. However, carbon by itself is not very active towards the ORR. To create active sites for the ORR without using platinum, doping it with transition metals and/or nitrogen has been the most successful strategy so far [33,47–49]. In the case of unpyrolysed transition metal phthalocyanines, the activity of metals decreases in the following order: Fe > Co > Ni > Cu > Mn [50], but most catalysts today are pyrolysed, therefore the nature of the active site is very different from a pure metal phthalocyanine [51,52] and the activity trends also different. Before going into discussion about the exact nature of the active site, it is important to understand how these materials are made.

The most common methods for creating M-N-C catalysts are:

1) The doping method, where a synthesis mixture, comprising of a carbon carrier, nitrogen dopant (either a polymer or smaller molecule with a high density of N atoms) and a metal source (commonly a cheap salt) is pyrolysed to dope the carbon material. The nitrogen and metal source can be combined (for example, a macrocycle containing the desired metal). The precursors are commonly mixed either in liquid (sonication, stirring in a solvent) [I–IX] or solid phase [VII–XIII] (grinding, mixing, milling) after which the mixture is pyrolysed at high temperatures to fuse them together, which changes the chemical nature of the dopants and the substrate, creating active sites for ORR [53–57]. The advantage of this method is the use of a pre-existing carbon, which defines the structure, porosity and degree of graphitisation of the final catalyst.
2) The *in situ* doping method, which is similar to method 1, but the doped carbon network is created during the pyrolysis from carbon, nitrogen and metal sources (these can either be the same source, such as a Fe-doped ZIF-8, for example, or from different sources such as a carbon-based polymer, nitrogen-containing molecule and an iron salt). This method can facilitate (in most cases) a higher concentration of nitrogen and metals compared to method 1, but it is more difficult to control the structure and porosity of the final catalyst. This is commonly alleviated by using a precursor (or precursors) which has a well-defined structure, such as metal-organic frameworks (MOFs) [44,45,58–61], metal macrocycles [62,63], macrocyclic aerogels [64] or polymers [65,66].
3) The hard-template method (also called the sacrificial support method, SSM), which incorporates the same strategy as 1) but in addition, a hard template (commonly made of silica) is used to confine the precursors during the pyrolysis. This allows to define the final structure of the catalyst by using a template which is stable during the pyrolysis (such as silica) [67–69]. Therefore this method combines two of the positive sides from methods 1 and 2, but has the disadvantage of having to remove the template after pyrolysis, a process which can also modify the resulting catalyst by etching some of the metal (not always a negative side as the final catalyst can therefore be more stable [67]).

In many cases, these methods are combined, i.e. the catalyst produced by the soft-template method is also doped afterwards by either adding more nitrogen-containing compounds and pyrolysing the mixture [70] or pyrolysis in ammonia [44,45,61]. Acid washing is also common addition to all of the methods to remove inactive metal species, which could contaminate the fuel cell during operation, but carries the disadvantage of having to undertake a secondary heat-treatment to deprotonate the N-groups on the surface (which can bind anions and therefore decrease the activity of the catalyst) [71].

The most important questions in any research done on catalytic reactions are:
1) What is the chemical nature and structure of the catalytic centre?
2) How is the reaction proceeding on that centre?

These two questions have been the centrepiece of research done on M-N-C electrocatalysts for ORR ever since pyrolysed macrocycles were used for ORR electrocatalysis in 1976 [40]. Two main types of active sites towards ORR have been identified in M-N-C catalysts: M-$N_x$ single metal-atom sites, where the iron atom is coordinated to multiple (usually 4) nitrogen atoms [43,44,72–74], or metallic iron and/or iron carbide particles covered by nitrogen-doped graphitic carbon layers, labelled NC@M [25,45,75–79] (Figure 4). In addition to the metal-based catalytic centres, M-N-C catalysts also contain $N_xC_y$ active sites, which will be further discussed in the next chapter. M-$N_x$ sites are generally considered to reduce oxygen via a 4-electron pathway, while on NC@M sites the ORR is thought to proceed either via the 2+2 or 2×2-electron pathway, with the underlying metal stabilising the intermediates [43,45,61].

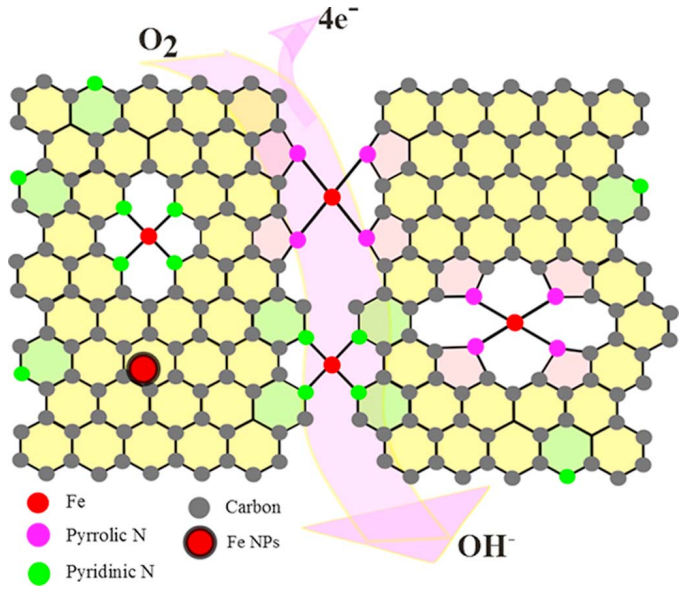


**Figure 4.** Different types of active sites in M-N-C catalysts [43].

The exact nature of the M-$N_x$ sites most active towards the ORR is extremely difficult to determine due to the plurality of even this one type of active site in a given catalyst. Due to the imprecise method of synthesis (high-temperature pyrolysis), all catalysts thus far have had multiple types of active sites present. Commonly these active species are identified in a catalyst by X-ray photoelectron spectroscopy (XPS), Mössbauer spectroscopy or X-ray absorption spectroscopy (XAS). However, with all of these methods, the signal from different M-$N_x$ sites (and in the case of XPS, also other nitrogen moieties) is overlapping and thus a large part of the identification is the deconvolution and fitting of peaks [27]. In perfect systems such as graphene direct atomic-level imaging has also been achieved [74], but most of the catalysts are an amorphous mess compared to graphene and determining how many and what atoms are bound to the metal centre is rather speculative with current imaging capabilities.

Due to the difficulties in synthesising a catalyst with a single type of active site, the exact reaction mechanism on this type of catalysts has also been difficult to determine. Figure 5 shows a general scheme of the ORR taking place on a M-N-C (in this case, Fe-N-C) catalyst with a multitude of active sites in acidic conditions [27].

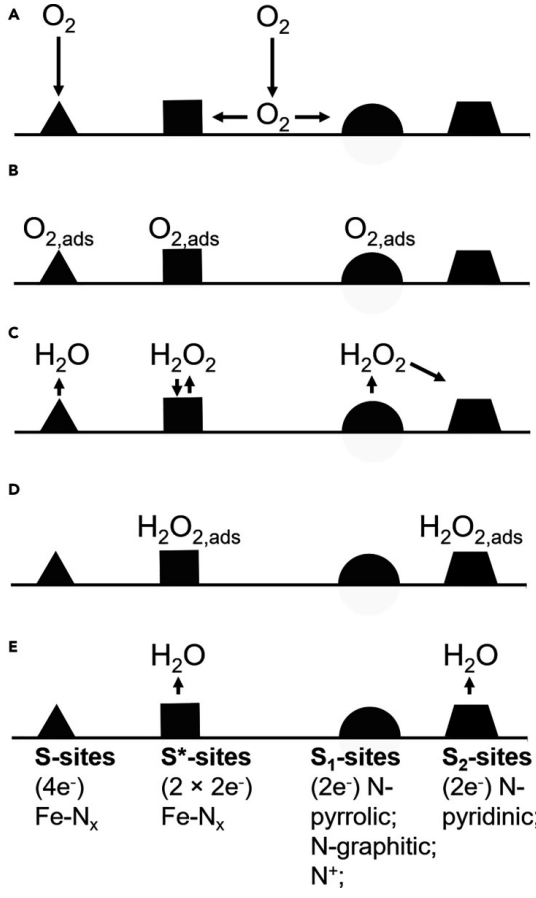


**Figure 5.** ORR on a M-N-C catalyst with different active sites: S, S*, $S_1$ and $S_2$ [27].

As shown, Fe-$N_x$ sites catalyse a direct 4-electron reduction of oxygen to water or the 2x2$e^-$ reduction, where both of the steps take place on either the same active site or another S* site. On nitrogen moieties without any coordinated iron, the ORR undertakes the 2+2$e^-$ reduction with the first steps of oxygen adsorption and reduction to $H_2O_2$ taking place on pyrrolic or graphitic nitrogen and the second step on pyridinic nitrogen (more discussion on this will follow in subsection 4.3.2) In alkaline conditions, as discussed, the reaction preferably takes place in the outer Helmholtz plane (OHP) and is thus tilted towards the 2-electron mechanisms [25,27,80]. However, it must be noted that the surrounding carbon also has an influence on the active sites and can thus change the selectivity. Similar moieties have also been characterised in the case of Co and Mn [70,81].

Nevertheless, the main goal of the research into M-N-C catalysts has always been to replace Pt on the cathode of PEMFCs. Looking at a comparison of a state-of-the-art M-N-C catalyst and a state-of-the-art Pt/C catalyst [82] (Table 1, updated for 2019) reveals that while by electrode area the activity is similar, the mass activity is two orders of magnitude lower. This also means that the electrode mass, and more importantly, volume required to reach the same power as the Pt/C catalyst will be much larger. In a confined space such as an automobile, making the electrode 100 times thicker is obviously not possible. Thickening the electrode also creates considerable issues with $O_2$ transport in the catalyst layer.

**Table 1.** Comparison of state-of-the-art Pt/C and M-N-C catalysts in PEMFCs at 0.9 V [39].

| Catalyst | Loading | Mass activity | Catalyst activity |
|---|---|---|---|
| Pt/C | 0.1 $mg_{Pt}$ $cm^{-2}$ | 443 $A/g_{Pt}$ | 44.3 mA $cm^{-2}$ |
| (CM-PANI)-Fe-C | 6.8 mg $cm^{-2}$ | 5.2 A/g | 36 mA $cm^{-2}$ |

There are two main reasons the mass activity of M-N-C catalysts is so much lower: site density (SD) and turnover frequency (TOF). In a recent cross-laboratory study on some of the best Fe-N-C catalysts for the ORR, the catalyst with the highest site density had a SD of $0.6\times10^{19}$ (accessible) sites $cm^{-3}$ [83] compared to $3.2\times10^{20}$ sites $cm^{-3}$ for Pt/C [24]. Looking at TOF, the TOFs reached in the same study [83] were 0.5–7$e^-$ $site^{-1}$ $s^{-1}$, while commercial Pt/C is known to have a TOF value of ≥25$e^-$ $site^{-1}$ $s^{-1}$ at 0.8 V [24]. Another study reported a TOF of 0.17 $e^-$ $site^{-1}$ $s^{-1}$ for a Fe-N-C catalyst [84].

Reaching a site density comparable to Pt/C with an atomically dispersed M-N-C catalyst is extremely difficult. By definition, the M-N-C sites have to be separated from each other, but also coordinated to (in the ideal case, four) nitrogen atoms, which are in turn, separated by a carbon lattice. For these sites to be electrochemically accessible and reduce $O_2$ in an MEA, they have to be located near to or on the surface of the catalyst particles, not deep inside the pores. Simply increasing the metal content in the catalyst precursor does not lead to a higher concentration of active sites, because during high-temperature pyrolysis the metal

atoms tend to agglomerate into particles, creating NC@M sites, which are less active. Therefore, the recent strategies for increasing site density have focused on separating the metal atoms prior to and during the pyrolysis step, which is accomplished either by dispersing them in a MOF, in complexes with large ligands or anchoring using $SiO_2$ [60,64,67,85]. The second issue, TOF, is somewhat more difficult to improve without knowing the exact nature of the active sites. Still, a lot of progress has been made in the case of Fe-N-C catalysts by tuning the $d_{z2}$ orbital electron density of the central Fe atom [27,86]. By increasing the defectiveness of the carbon material surrounding the Fe-$N_4$ centre, it is possible to increase its electron withdrawing nature, which in turn lowers the electron density on the $d_{z2}$ orbital so that it can be tuned to bind intermediates just strong enough. However, by introducing too many defects into the carbon material can make the Fe-$N_4$ site bind oxygen too strongly and has another very important downside: it decreases the catalysts' stability.

Stability is the second key property that NPMCs still lack compared to Pt/C. The 2020 target for fuel cells set by the DOE is 5000 h, but in a recent study it was shown that most of the NPMCs lose over 50% of their current in the first 100 h, especially the ones that perform the best at beginning-of-life [39]. The main reasons for activity loss are micropore flooding [87], active site protonation and anion adsorption [71], demetallation [88,89] and oxidation of the carbon material [90]. Since some types of M-$N_x$ sites are known to be situated in micropores [91], creating M-$N_x$ active sites requires nitrogen (which is the main site for protonation) and as said, defects in the carbon plane (which can be oxidised), none of these mechanisms can be avoided completely with the current methods. While these effects are known to be more detrimental in acidic (and thus more corrosive) conditions, they also deteriorate the catalysts in alkaline media [92,93].

### 4.3.2 Oxygen reduction on metal-free catalysts

The second type of replacement catalysts developed forgoes metals entirely and the focus has been on maximising the activity of nitrogen-doped carbon nanomaterials [49,94]. Metal-free catalysts offer a couple of important advantages over metal-based catalysts, as the first mechanism of activity loss (demetalation of the active site) is not present here (thus these catalysts are intrinsically more stable) and also circumvent the use of metals in the synthesis, of which the production of some is actually quite bad for the environment (for example, Mn and Co-based catalysts) [81,95–97].

By introducing electron-rich nitrogen atoms into the carbon support, the π electrons in carbon are conjugated to the lone-pair electrons of nitrogen atom [98]. The effect of nitrogen doping depends highly on the placement of the dopant atoms in the lattice [99–101]. Reportedly there are four different types of nitrogen species in N-doped carbon-based materials, pyridinic-N, pyrrolic-N, quaternary-N (graphitic-N), and pyridinic $N^+$–$O^-$. Although metal-free N-doped carbon catalysts

have become an increasingly researched topic in the last 10 years, the origin of the ORR activity in N-doped carbon materials remains a controversial topic. There have been a number of debates about this, such as the spatial location (basal or edge sites) or chemical nature (which nitrogen moiety or combination is responsible for the ORR activity). The lone pair of electrons on a pyridinic N atom (a nitrogen atom in a six-member carbon ring bound to two carbon atoms) has long been thought to be the site responsible for most of the ORR activity due to the π-conjugation it forms [102,103]. Studies made with catalysts containing almost exclusively pyridinic N or comparisons with a large number catalysts with different moieties have confirmed the positive effect of pyridinic N on the ORR kinetics [53,102,104–106]. Theoretical calculations as well as studies with real catalysts have proven that graphitic N (a nitrogen atom in a six-member carbon ring bound to three carbon atoms) also contributes to the ORR activity of a N-doped carbon material [107,108]. However, real life catalysts do not comprise of perfect $sp^2$ graphitic sheets, the material is often rather amorphous and defective. Indeed, a high number of defects and edge sites is also a known descriptor for highly active N-doped carbon catalysts for ORR [109]. In addition to this, a large surface area is obviously needed for a high number of active sites on the catalyst surface. Another important factor for ORR activity in N-doped carbons is the amount of nitrogen both on the surface and in the bulk of the material. Surface concentration of nitrogen of up to 8.4% were shown by Rao et al. to increase the ORR electrocatalytic activity in acidic solutions [110]. In alkaline conditions, similar results have been found [111,112], suggesting that the number of active sites for both alkaline and acidic $O_2$ cleavage rises as the surface nitrogen content increases. The increase of bulk N content has been shown to have an effect on the valence and conductive bands near the Fermi level, resulting in metallic conductivity [113,114], which in turn increases the catalytic activity as the speed of electron transport rises. Unfortunately, even the best metal-free catalysts have not yet reached the level of electrocatalytic activity seen in M-N-C materials, especially in acidic conditions.

## 4.4 Oxygen reduction on carbon nanomaterials

Since Jasinski substituted Ni powder for carbon black as a support for CoPc, carbon has been the support of choice for both non-precious metal and metal-free catalysts. A variety of carbon materials have been used as a starting material to produce electrocatalysts for ORR, such as mesoporous carbon [115–117], carbon aerogels [118,119] and xerogels [120], carbon nanotubes [121–123], graphene [124–126] or composite materials [127–133]. All these carbon nanomaterials have some common properties that make them good catalyst supports, such as high specific surface area, electrical conductivity and chemical stability and porosity. The porous structure helps with the mass transfer, large surface area is favourable for the creation of a higher number of active sites, electrical conductivity helps to transport electrons needed for $O_2$ reduction on these active sites and since the

materials are also chemically stable, the carbon itself is quite resilient (although can be oxidised in fuel cell working conditions, as discussed in subsection 4.3.1).

Graphene is a carbon nanomaterial made of a single layer of graphite. Its two-dimensional honeycomb $sp^2$ structure gives it exceptional properties such as a high specific surface area of 2630 $m^2\ g^{-1}$, electron mobility of 250,000 $cm^2\ V^{-1}\ s^{-1}$ (100 times that of silicon), thermal conductivity (5000 W $mK^{-1}$ – 2x more than diamond) and strength (terminal strength of 130 GPa – 200x more than steel) [10,134]. In reality, single-layer graphene is extremely hard to synthesise, especially in large quantities (such as would be needed for making electrocatalysts for fuel cells) and the common type of graphene used for applications is few-layer graphene [49,135,136]. The most important synthesis methods of graphene are chemical vapour deposition (CVD) and chemical exfoliation of graphite [137–139], which are both rather expensive (especially CVD) and have a relatively large environmental footprint [140], although new methods for faster and less polluting chemical exfoliation [140] and synthesis directly from $CO_2$ have been proposed [141].

Carbon nanotubes (CNTs) are a form of carbon made of sheets of graphene rolled up into tubes [9]. They are made of six-member rings of carbon with a hybridisation between $sp^2$ and $sp^3$ due to pyramidalisation [142], with the tips of nanotubes also having some five-member rings. Due to this they are easier to modify and dope with heteroatoms. Depending on the number of graphene sheets rolled up the CNTs are divided into single-walled, double-walled and multi-walled CNTs [134,142]. Because CNTs are synthesised using metal catalysts, removal of traces of these metals is a common issue and can lead to impurities, which have a significant effect on the electrocatalytic activity of catalysts derived from CNTs [143]. For this purpose, leaching in pure acids, acid mixtures or strong oxidisers is commonly used [143–146]. In addition, it has been shown that oxidising CNTs prior to doping increases the effectiveness of doping due to the formation of oxygen-containing groups, which increase their solubility (and therefore dispersion in a precursor mixture) and which are easily substituted for heteroatoms [147,148].

Carbide-derived carbons (CDCs) are a carbon material made by removing the metal/semi-metal atoms from the lattice of a carbide, which leaves behind a porous carbon network. CDCs can offer a control on the porosity of the carbon material, from narrow to wide pore size distributions in both the micro- and mesoporous domains. They are produced by removing metal atoms from a carbide lattice via chlorination and are already applied in commercial supercapacitors, due to their high specific surface area (SSA) over 2000 $m^2\ g^{-1}$ and porosity [149]. The surface area, degree of disorder and pore size distribution are easily tunable by selection of starting carbide and chlorination temperatures [150,151] ranging from α-SiC-based carbon with a median pore diameter of ~0.7 nm and virtually only microporosity to $Mo_2C$-derived carbon, which can have a median pore diameter of ~4.0 nm and no micropores at all [152] with reproducible large-scale results [153]. The most common synthesis method for CDCs is a thermo-chemical treatment of carbide powder in chlorine gas flow at high temperature. Depending

on the chemical composition of the carbide, but also of the desired porosity and nanostructure of the target CDC, the synthesis temperature can be varied in between 300–1100 °C [154,155]. Chlorination temperatures above 1200 °C tend to yield turbostratic low-surface area carbon materials, which usually offer less interest for the energy storage related applications. CDCs are thus promising as a microporous host for metal-based sites and for doping with nitrogen or other heteroatoms.

## 4.5 PEMFCs using non-precious metal cathode catalysts

PEMFC technology is, as discussed in chapter 4.3, the oldest among the different types of PEFCs. As such, they also have the longest history of having NPMCs utilised as the cathode catalyst. On the anode side, where the HOR requires very little Pt loading as discussed in chapter 4.1, there has been little interest in replacing the common Pt/C. On the cathode side however, there has been significant research activity invested into finding a suitable NPMC (as discussed in chapter 4.3). The main activity benchmarks are current density at 0.8 V (or more recently, 0.9 V) and the maximum power density ($P_{max}$). At times, current density values at 0.6 V have also been reported as this is near the bottom of the useful voltage window for most purposes [33,39]. Commonly, most PEMFCs operate at 100% RH due to the need to humidify the membrane and ionomer for decreasing ionic resistance. An enormous amount of progress has been made in the last 10 years: a recent review showed that in this time, the $j_{0.8V}$ has gone from 20 mA cm$^{-2}$ to 380 mA cm$^{-2}$, while the $P_{max}$ has increased from 334 to 1512 mW cm$^{-2}$ [39]. These advancements have largely been made due to breakthroughs in synthesis and better understanding of the NPMCs and their active sites. At the first half of the decade, most catalysts were produced by the doping method, where a carbon substrate is doped via pyrolysis with either a nitrogen-containing gas ($NH_3$) or mixing the carbon with a nitrogen-rich small organic molecule or polymer [56,156]. In 2011, Dodelet's working group reported a new method of creating a Fe-N-C catalyst with improved performance using ball-milling of a carbon support, 1,10-phenanthroline (Phen) and iron(II) acetate ($Fe(OAc)_2$) [55]. This had some important advantages over the previous methods: ball-milling instead of solution-based impregnation ensures that most of the dopants are located near the surface of the carbon material and most of the resulting active sites will be accessible during electrocatalysis. In addition, the use of Phen, which creates a $Fe(Phen)_3^{2+}$ complex, avoids the agglomeration of iron into particles during the pyrolysis step. Using these advantages, the $j_{0.8V}$ increased to 50 mA cm$^{-2}$. This was improved on by the same group by replacing the carbon support with a MOF, which led to a significant increase of the $j_{0.8V}$ to 273 mA cm$^{-2}$ and the power density to 750 mW cm$^{-2}$ [58]. The MOF-derived method has the important advantage of being able to incorporate a very high amount of nitrogen into the catalyst by using a nitrogen-rich linker in the MOF (such as imidazolate) and a sacrificial central metal atom (such as zinc). The MOF method has been later improved on by

further separating the Fe [60] (or other metal such as Co [157] or Mn [70]) atoms either by dispersing them directly as the central atom of the MOF or multi-step synthesis, leading to a $P_{max}$ of up to 1369 mW $cm^{-2}$ [158]. Unfortunately, the MOF method is known to create mainly active surface sites [26,83], which are very accessible and have a high TOF at beginning-of-life, but are quickly demetalated or otherwise unstable [88,90,159]. The SSM method employed by University of New Mexico and commercialised by Pajarito Powder, LLC made an important impact of NPMCs for PEMFCs by demonstrating large-scale synthesis and commercial viability [67]. Here, as discussed in subsection 4.3.1, the precursors are pyrolysed inside of a confined template, which is afterwards removed, leaving a catalyst with a structure defined by the voids in the template. This allows for the creation of defined meso/macroporosity, which is especially important at higher current densities. The catalysts produced by Pajarito Powder are also known to be among the most stable in the literature due to a large amount of active sites throughout the whole material and not only on the surface [83]. The doping method has also seen many advancements, with the supports being changed from common carbon blacks such as Vulcan carbon XC72 and Black Pearls BP2000 to nanomaterials such as graphene [160], carbon nanotubes [161], carbon aerogels [118,162] and carbide-derived carbons [VII–XIV] leading to large increases in activity. On the stability side, unfortunately, these materials are also problematic as doping is difficult to achieve uniformly in the whole material. The progress made in the last decade in NPMCs for PEMFCs has led to the technology already being commercialised in smaller devices [163], however, it is clear that for NPMCs to be viable in automotive PEMFCs, more advances need to be made in both activity and stability [34,38,39,164].

## 4.6 AEMFCs using non-precious metal cathode catalysts

AEMFC technology is somewhat younger and underdeveloped compared to the mature PEMFC technology, largely due to the difficulty in achieving similar ionic conductivities for $OH^-$ as for $H^+$ and the low chemical (and mechanical) stabilities of membranes and ionomers at high pH as well as their susceptibility to carbonation [165]. However, in the last 10 years, significant enhancements have been made in solving all of these problems, leading to AEMFCs with performances comparable to and even exceeding those of PEMFCs, albeit with $CO_2$-free air [166,167]. Even less data has been published with NPMCs as the cathode or anode, albeit in recent years the field of AEMFCs has seen significant growth [16,168–170]. As discussed in section 4.2, the ORR in alkaline conditions is somewhat more complex than in acidic due to the competing inner- and outer-sphere reactions. However, this also means that a variety of NPMCs can catalyse the ORR efficiently [171,172]. Recently, Sarapuu et al. have reviewed the application of M-N-C type catalysts and heteroatom-doped nanocarbon catalysts as cathode materials in AEMFCs [173]. Oxides, such as $MnO_2$ and $Co_3O_4$ [174–176] as well as spinels [177], cobalt ferrite [178] and silver [179], have shown significant performances

in AEMFCs or alkaline conditions in addition to carbon-based catalysts. Due to the lack of an available AEM and anion exhcange ionomer (AEI), such as the Nafion™ standard in PEMFCs, it is difficult to compare the performances of different NPMCs achieved with different AEMs and AEIs. Usually the activity is compared to a Pt/C standard catalyst, but some types of ionomers are known to have an enhanced effect on the ORR activity of Pt/C [180]. As such, rotating disk electrode (RDE) results are commonly reported instead. The ORR activity of carbon-based catalysts has steadily increased during the decade, with M-N-C catalysts going from a kinetic current density ($j_k$) at 0.8 V vs RHE of 1.5 mA $cm^{-2}$ [181] to up to 32 mA $cm^{-2}$ at 0.8 V [XIV] in RDE studies. In real MEAs, the increase has also been significant, with maximum power densities rising from <100 mW $cm^{-2}$ [16] to over 1 W $cm^{-2}$ [182], albeit as discussed, it is difficult to ascertain how much of it has been due to system-level enhancements and how much from the advances done in catalysts. In the case of M-N-C materials, a common problem in AEM MEAs is known to be the active site density of such materials. Due to the need for such a small concentration of active sites to efficiently transform $O_2$ into $OH^-$, local mass transfer losses in the ionomer layer can be very high [183]. As such, an addition of secondary catalytic centres (such as the already described $MnO_2$ [182]) or higher amount nitrogen moieties such as pyridinic or quaternary (graphitic) N [IV–VI,IX,X,XIV] can lead to massive enhancements in fuel cell performance. Some studies have completely forgoed metals and opted to rely on nitrogen moieties completely, as described in subsection 4.3.2, but fuel cell studies on such materials are few and far between and commonly have lower activities than those incorporating metals [184] [II].

# 5. AIMS OF THE STUDY

The aim of this PhD project was to create novel electrocatalysts, study the activity of non-precious metal catalysts based on advanced carbon supports towards the ORR and as cathodes in polymer electrolyte fuel cells and derive synthesis-structure-activity correlations from this study. The work was divided into three parts, with the following aims:

1. To develop nitrogen-doped graphene/MWCNT composite materials and nitrogen-doped CDC catalysts, characterise their physico-chemical properties and activity towards the ORR and as a DMFC cathode [I–III,VII].
2. To develop iron-/cobalt- and nitrogen-doped MWCNT catalysts, characterise their physico-chemical properties and electrocatalytic activity towards the ORR and in DMFC/AEMFC [IV–VI].
3. To develop iron-/cobalt- and nitrogen-doped CDCs or CDC/MWCNT composite catalysts, characterise their physico-chemical properties and activity towards the ORR and in DMFC/AEMFC/PEMFC [VIII–XIV].

# 6. EXPERIMENTAL

## 6.1 Purification of carbon nanotubes

For the purification of MWCNTs from traces of metal catalysts used in their production, they were leached in a mixture of concentrated $H_2SO_4$ and $HNO_3$ using a procedure developed in our laboratory [143]. Shortly, 500 mg of MWCNTs (purity >95%, diameter 30±10 nm, length 5–20 μm from Nano-Lab, USA [I–VI] or NC7000, Nanocyl SA, Belgium [X,XII]) were weighed into a 500 ml three-necked reactor. After that 25 ml of concentrated $H_2SO_4$ and 25 ml of concentrated $HNO_3$ was added to the MWCNTs. The mixture was then heated on a magnetic stirrer for 2 h at 50 °C and for 2 h at 80 °C. After cooling the MWCNTs were washed with Milli-Q water on a vacuum filter and dried at 60 °C.

## 6.2 Synthesis of graphene oxide

Graphene oxide (GO) is a graphene-based material with oxygen-containing functionalities (carbonyl, carboxylic, epoxy and hydroxyl groups) on the surface [127]. It is commonly prepared by chemical exfoliation of graphite and reduction of GO back to graphene is a common method for graphene production. The high concentration of oxygen-containing groups also makes it easy to dope with heteroatoms [127]. To prepare GO, graphite powder (Graphite Trading Company) was oxidised by a modified Hummers' method [185,186]. Firstly, 50 ml of concentrated sulphuric acid and 2.0 g of graphite powder were mixed in a 250 ml beaker at room temperature. Then, the mixture was sonicated for 1 h. Next, sodium nitrate (2.0 g) and potassium permanganate (6.0 g) divided to smaller portions were slowly added into the beaker in a sequence. At the same time the mixture was stirred on a magnetic stirrer. Afterwards, the mixture was heated at 35 °C for 18 h. When the heating was completed, the beaker was put into an ice bath and 80 ml of deionised water was added into the solution. After few minutes, 20 ml of $H_2O_2$ (30%, Merck) was added. The mixture was then washed few times with 10% HCl solution and with water on a vacuum filter. Finally, the obtained brown solid was dried in vacuum at 75 °C [I,II].

## 6.3 Synthesis of carbide-derived carbons

All of the CDC materials used in the work were purchased from Skeleton Technologies OÜ (Estonia). Micro/mesoporous CDC samples were made from titanium carbide [VII–XII], titanium carbonitride [VII], silicon carbide [XIII,XIV], boron carbide [XI,XII] or molybdenum carbide [XII] by using a chlorination procedure described elsewhere [187]. Generally, carbide powder was placed into a horizontal quartz-tube reactor and was treated with chlorine gas (2.8, AGA) at a flow rate of 1.5 L $min^{-1}$ at 900 ºC. After that, the reactor was heated up to 1000 ºC and flushed

with argon (4.0, AGA, 1 L $min^{-1}$) to remove the excess of chlorine and other gaseous by-products from carbon. The deep dechlorination of CDC powder was done using hydrogen (4.0, AGA, 1 L $min^{-1}$) flow at 800 ºC. For the titanium carbide-derived carbon (TiCDC) used in [X,XI], a post-activation process was undertaken. CDC powder (5 g) was placed in a quartz reaction vessel and loaded into tubular horizontal quartz reactor. Thereupon the reactor was flushed with argon to remove air and the furnace was heated up to 800 °C. Then the CDC was treated with hydrogen gas (4.0, AGA, 1 L $min^{-1}$) for 0.5 h, after that the temperature was raised to 900 °C. The argon flow was then passed at a flow rate of 1.5 L $min^{-1}$ through distilled water heated up to 75–80 °C and the resultant argon/water vapour mixture was let to interact with a carbon at 900 °C for the predetermined time (30 or 45 min). After that, the reactor was flushed with argon for 30 more minutes at 900 °C to complete the activation of a carbon surface and then slowly cooled to room temperature in argon atmosphere [188].

## 6.4 Synthesis of nitrogen-doped MWCNT/graphene composite material

Following purification described in section 6.1, the nanotubes were sonicated in ethanol until a homogeneous dispersion was achieved. GO was weighed and added so that the amount of GO would correspond to the weight of the nanotubes. Then either dicyandiamide (DCDA), urea [I,II] or biuret (BR), carbohydrazide (CH) or semicarbazide hydrochloride (SC) [III] as nitrogen precursors and polyvinylpyrrolidone (PVP) as a dispersing agent were added. In what follows, these catalyst materials are designated as 1-NC (doped with urea), 2-NC (doped with DCDA), NG/NCNT-BR (doped with biuret), NG/NCNT-CH (doped with carbohydrazide) and NG/NCNT-SC (doped with semicarbazide) accordingly. The amount of nitrogen precursor was 20 times that of carbon nanomaterial. The final mixture was further sonicated for 2 h and then dried at 75 °C in vacuum. The material was gathered into a quartz boat and pyrolysed in flowing argon atmosphere at 800 °C for 2 h. After that the furnace was slowly cooled to room temperature and the product was collected and weighed.

## 6.5 Synthesis of Fe-,Co- and nitrogen-doped carbon nanotubes

MWCNTs purified according to the procedure in section 6.1 were suspended in ethanol by sonication for 30 min. $FeCl_3$ (anhydrous, Sigma-Aldrich) or $CoCl_2$ (anhydrous, Sigma-Aldrich) was added to homogeneous suspension, the amount of Fe corresponded to 2.5% and the amount of Co to 5% of the weight of the MWCNTs. After that DCDA (Sigma-Aldrich) as the nitrogen precursor was added; the mass ratio of DCDA to MWCNTs was 20:1. PVP was added as a dispersing agent. The suspension was sonicated for 2 h and dried in vacuum at

70 °C. The material was pyrolysed in a quartz tube furnace in flowing $N_2$ atmosphere by raising the temperature at a rate of 10 °C $min^{-1}$ to 800 °C and keeping at this temperature for 2 h. After that the quartz tube was removed from the heating zone to speed up the cooling process and the product was collected. These as-prepared materials are designated as Co/N/MWCNT [IV], Fe-NCNT-1 [V] Fe-NCNT1 and Co-NCNT1 [VI]. An acid leaching treatment was applied to remove soluble metal species from the catalysts. The materials were kept in a mixture of 0.5 M $HNO_3$ and 0.5 M $H_2SO_4$ at 50 °C for 8 h and washed repeatedly with Milli-Q water. The catalysts were then dried overnight in vacuum at 60 °C and subjected to a second pyrolysis, which was conducted in the same conditions as the first one (800 °C for 2 h). The resulting materials are designated as Fe-NCNT-2 [V], Fe-NCNT2 and Co-NCNT2 [VI].

## 6.6 Synthesis of doped carbide-derived carbon catalysts

To enhance their electrocatalytic activity towards the ORR, the CDC materials synthesised by the procedures described in section 6.3 were doped with Fe or Co and/or nitrogen. For doping with only nitrogen, TiC-derived CDCs (nominated **1094** and **130614-2,** both made from TiC using different procedures known only to Skeleton Technologies) were first ball-milled in a Fritsch Pulverisette 7 mill using 5 mm $ZrO_2$ balls. The material was weighed over 50 $ZrO_2$ balls into a ball-milling container and ethanol was added to achieve a motor-oil like viscosity. PVP was also added in an amount according to 1/10 of the carbon material to enhance the ball-milling process. The catalysts were ball-milled for 1 h, after which the material was washed, dried and weighed. To the milled CDC material, 20 times the weight of the carbon material of DCDA was added in ethanol. The mixture was sonicated for 2 h to achieve a homogenous dispersion and dried in vacuum at 75 °C. The material was collected into a quartz boat and pyrolyzed in a flowing nitrogen atmosphere at 800 °C for 2 h. After that the furnace was slowly cooled to room temperature and the products were collected and weighed. These materials are nominated **1094-N** and **13-N**, respectively [VII].

For synthesising an N-doped carbon from TiCN, titanium carbonitride ($TiC_{0.5}N_{0.5}$, H.C. Starck, Lot. 75624, 150 g) powder was treated with chlorine gas (2.8, AGA) in the horizontal tubular quartz furnace for 4 h at 800 °C. A flow-rate of chlorine was 2.5 l/min. Gaseous titanium tetrachloride, produced during the chlorination process, was neutralised in alkali solution. During heat-up and cooling the reactor was purged with argon. The reaction product (carbon powder) was additionally purified in hydrogen flow at 800 °C during 2.5 h to remove all the chlorine residues left in the carbon. The overall yield of the process was 5.1 g of the N-doped porous carbon powder. This catalyst is nominated **040-N**. [VII]

For doping with cobalt and nitrogen, the same procedure as for **1094-N** and **13-N** was followed (the precursor carbon here was **1094**), but $CoCl_2$ (anhydrous, Sigma-Aldrich) with the Co corresponding to 5 wt.% of the CDC was added in the dispersion and sonication step. After the first pyrolysis, an acid leaching

treatment was applied to remove soluble metal species from the catalyst. The material was kept in a mixture of 0.5 M $HNO_3$ and 0.5 M $H_2SO_4$ at 50 °C for 8 h and washed repeatedly with Milli-Q water. The catalyst was then dried overnight in vacuum at 60 °C and subjected to a second pyrolysis, which was conducted in the same conditions as the first one (800 °C for 2 h). The resulting material is designated as Co/N/CDC [IX] or Co-N-CDC [VIII].

Fe- and N-doped CDC-based materials were synthesised with a variety of methods and precursors:

1) Fe/N/CDC [IX] and Fe-N-CDC [VIII] were synthesised with the same method as Co/N/CDC and Co-N-CDC, except that 2.5 wt.% of $FeCl_3$ (anhydrous, Sigma-Aldrich) was added to the precursor mixture instead of $CoCl_2$.
2) For the synthesis of $Fe_1$-N/CDC-1 and $Fe_x$-N/CDC-2 [XI], the following procedure was followed: CDC powders produced from titanium carbide and boron carbide were received from Skeleton Technologies OÜ (Estonia). In a typical synthesis, 200 mg of CDC along with 50 mg of 1,10-phenanthroline and the appropriate mass of iron(II) acetate to reach either 0.5, 1 or 2 wt.% Fe in the overall catalyst precursor before pyrolysis (e.g. 8 mg iron(II) acetate for 1 wt.% Fe in catalyst precursor) were weighed and placed into a $ZrO_2$ planetary ball-mill with 100 $ZrO_2$ balls of 5 mm diameter and ball-milled for 4 segments of 30 min with 5 min cool down periods between each segment at a rotation rate of 400 rpm. The resulting powder was then pyrolysed in a quartz tube oven at 800 °C under Ar flow for 1 h. The pyrolysis duration at 800 °C was controlled by quickly inserting the quartz boat into the heating zone using a magnet, and removing the tube from the oven after 1 h had passed. The catalysts are named in the following text by their iron content before pyrolysis and precursor type. For example, the boron carbide-derived catalysts with 1.0 wt.% of iron in the catalyst precursor before pyrolysis has the designation of $Fe_1$-N/CDC-1.
3) For the synthesis of Fe-N-C catalysts from SiCDC [XIII], the following procedure was followed: CDCs made from silicon carbide were purchased from Skeleton Technologies OÜ (Estonia). The CDCs were weighed (typically 200 mg) along with 1,10-phenanthroline (Sigma-Aldrich, 100, 50 or 25 mg) and iron(II) acetate (Sigma-Aldrich, 4 mg) and poured into a $ZrO_2$ grinding jar along with 100 $ZrO_2$ balls of 5 mm in diameter. To certain mixtures, $ZnCl_2$ was also added as a pore-forming agent. This powder mixture was then ball-milled at a given rotation rate of the ball-miller (either 100, 200, 400 or 800 rpm) with 4 consecutive cycles of 30 min segments and 5 min cool-down periods. The catalysts are labelled $Fe_a$-$Phen_b$-SiCDC-Znc d rpm, where a is the amount of Fe in the starting catalyst mixture, in wt.%, and b is the amount of Phen in wt.% with respect to the mass of both CDC and Phen, c is the mass ratio of $ZnCl_2$ to CDC in the mixture (where applicable) and d is the rotation rate of the ball-miller. The milled powder was then pyrolysed in a tubular furnace under Ar atmosphere for 1 h and the tube was then removed from the heating zone to quickly cool down the sample. For comparison, a catalyst was also synthesised by dispersing the CDC in an ethanol solution of Phen (50 mg) and

iron(II) acetate, which was then dried and pyrolysed at the same conditions as the ball-milled catalysts. This catalyst is labelled $Fe_{0.5}$-$Phen_{20}$-SiCDC-wet. Catalysts without any Phen in the starting mixture and without both Phen and ball-milling were also prepared.

4) For comparing the effect of different ball-milling conditions [XIV], a synthesis protocol was followed: the SiCDC material (200 mg) was weighed and poured into a $ZrO_2$ grinding jar, which contained also either 50 $ZrO_2$ balls of 5 mm in diameter or 20 g of $ZrO_2$ beads of 0.5 mm in diameter. After that, 50 mg of Phen (Acros Organics) and 4 mg of iron(II) acetate (Sigma-Aldrich) was added. After this, the grinding jar was sealed and rotated in a planetary ball-mill at either 100, 200, 400 or 800 rpm with 4 consecutive cycles of 30 min segments and 5 min cool-down periods between each cycle. The catalysts are labelled FeN-SiCDC-x-y, where x is the diameter (in mm) of the $ZrO_2$ beads and y is the rotation rate of the ball-miller (in rpm). Some materials were ball-milled in the presence of ethanol and these have the suffix (-wet) added to the catalyst name. The steps were as described above, except that 4 ml of ethanol was added before sealing the grinding jar. For one selected catalyst (FeN-SiCDC-0.5-400-wet-PVP), 20 mg of PVP and 4 ml ethanol were added in order to further enhance the ball-milling process. After the ball-milling, all catalyst precursors were sieved to remove the balls, dried and flash pyrolyzed (quickly entered into the heating zone when the furnace was already hot and quickly removed afterwards) at 800 °C for 1 h in inert atmosphere and quickly removed from the heating zone afterwards.

## 6.7 Synthesis of doped carbide-derived carbon and MWCNT composites

Fe- and N-doped composite catalysts were also prepared from CDCs and MWCNTs. For doping the **1094** CDC material with iron and nitrogen [X], 20 mg of CDC along with 5 mg of Phen and 0.8 mg iron(II)acetate (for 1 wt.% Fe in catalyst precursor before pyrolysis) were placed into a planetary $ZrO_2$ ball-mill along with 50 $ZrO_2$ balls with a diameter of 5 mm. The mixture was ball-milled for 4 segments of 30 min using a rotation rate of 400 rpm with 5 min stationary periods in between to cool down the mixture and the mill. The mixture of Phen, CDC and iron(II) acetate was then pyrolysed in a quartz tube oven under $N_2$ flow at 800 °C using flash pyrolysis. The resulting catalyst is named Fe−N/CDC-1. 20 mg of Fe−N/CDC-1 was then mixed together with 20, 10 or 40 mg of MWCNTs (Nanocyl SA, Belgium), 20 times the amount (in mass) of DCDA to carbon nanotubes and 0.8, 0.4 or 1.6 mg of iron(II) acetate (to keep the iron to carbon ratio the same) and a small amount of PVP, then ball-milled and pyrolysed again using the same procedure. According to the relative contents of Fe−N/CDC and MWCNT, these catalysts are designated as Fe−N/comp-0.5 (that is 0.5 parts of Fe−N/CDC to 1-part of MWCNT), Fe−N/comp-1 and Fe−N/comp-2.

For the synthesis of Fe-N-CDC catalyst from $B_4C$ (CDC-1), $Mo_2C$ (CDC-2) and TiC (CDC-3) [XII], the following procedure was followed: The as-purchased CDC material (100 mg) was mixed with $Fe(OAc)_2$ (2 mg) and Phen (25 mg) for a total mass of iron of 0.5 wt.% in the catalyst precursor mixture. The mixture was ball-milled with 50 $ZrO_2$ balls of 5 mm diameter in a $ZrO_2$ grinding jar. This mixture was then transferred into a ceramic boat and pyrolysed at 800 ºC for 1 h with the boat inserted and removed from the heating zone quickly. After this, 100 mg of MWCNTs (Nanocyl, Belgium), 2000 mg of DCDA and 10 mg of PVP along with another 2 mg of $Fe(OAc)_2$ were added to the pyrolysed material and milled and pyrolysed again with the same protocol. An acid etching step in a mixture of 0.5 M $H_2SO_4$ and 0.5 M $HNO_3$ to remove inactive metal species was then undertaken and after that the materials were again pyrolysed at 800 ºC for 30 min. The samples are named Fe-Phen-comp-1 (derived from $B_4C$), Fe-Phen-comp-2 (derived from $Mo_2C$) and Fe-Phen-comp-3 (derived from TiC). Catalysts with no CNT addition step were also synthesised and studied, these are named Fe-Phen-CDC-1, Fe-Phen-CDC-2 and Fe-Phen-CDC-3.

## 6.8 Electrode preparation and electrochemical measurements

Oxygen reduction polarisation curves were measured using the rotating disk electrode (RDE) method. The experiments were undertaken using six different rotation rates ($\omega$), from 4600 to 360 rpm. The speed of the electrode was controlled using a CTV101 speed control unit connected to an EDI101 rotator (Radiometer). A three-electrode electrochemical cell filled with 0.1 M KOH solution (p.a. quality, Merck) or 0.5 M $H_2SO_4$ solution (p.a. quality, Merck), which was saturated with $O_2$ (99.999%, AGA) or Ar (99.999%, AGA), was used to carry out the experiments at room temperature (23 ± 1 °C). A gas flow was maintained over the solution during the experiments. All the potentials are referred to saturated calomel electrode (SCE), which was the reference electrode for these experiments. A platinum coil or carbon rod separated from the cell by a glass frit served as the counter electrode. The experiments were controlled using an Autolab potentiostat/galvanostat PGSTAT30 (Eco Chemie B.V., The Netherlands) via General Purpose Electrochemical System (GPES) or NOVA 2.0 software. For the substrate material, GC disks (GC-20SS, Tokai Carbon, Japan) with geometric area ($A$) of 0.2 $cm^2$ were pressed into a Teflon holder and the electrodes were polished to a mirror finish with 1 and 0.3 μm alumina slurries (Buehler). To clean the electrodes from polishing debris, sonication in both 2-propanol and Milli-Q water for 5 min was undertaken. The catalyst material suspensions in water [I,II] or ethanol [III–X] (1 mg $ml^{-1}$) containing either Tokuyama $OH^-$ ionomer AS-4 (Tokuyama Corporation, Japan), FAA3 ionomer (Fumatech, Germany) or Nafion were pipetted onto the GC disk electrodes. The concentrations of ionomer in the suspensions were varied and are given in the results section under the relevant results. The suspensions were then homogenised via sonication for 1 h prior to

modifying the electrodes. After that the suspension was pipetted onto the GC surface in fractions to cover the surface of GC uniformly and allowed to dry in air. The final loadings of the catalysts are given in the results section next to the relevant Figures.

In [XI–XIII], a different setup was used for electrochemical testing using the RDE method. The GC electrodes (Pine Research, Grove City, PA, USA) were used as a substrate for the catalyst. The geometric area of the GC disks was 0.196 $cm^2$ and all currents are normalised to this area (current density). To modify the GC disk electrodes with the catalysts, inks were prepared with 10 mg of catalyst, 300 µl of ethanol, 108 µl of Nafion and 37 µl of $H_2O$. The ink was then sonicated for 1 h and pipetted onto a GC electrode in a single 7 µl aliquot, giving a catalyst loading of 0.8 mg $cm^{-2}$. The working electrode was then inserted into an electrochemical cell filled with 0.5 M $H_2SO_4$ (made from 95–97% $H_2SO_4$, Sigma-Aldrich), which was saturated with $O_2$. The reference electrode was a reversible hydrogen electrode (RHE) and a carbon rod was used as the counter electrode.

The specific polarisation programs were varied during the study and are given in the results part to simplify reading.

## 6.9 MEA preparation and fuel cell tests

The activity of the catalysts prepared in this study was investigated in DMFCs [II,V,VIII], PEMFCs [X,XIII] and AEMFCs [IV,IX,X,XIV].

For testing the activity of 2-NC in a DMFC [II], a FAA3 membrane (Fumatech) was ion-exchanged in 0.5 M NaOH with stirring for 1 h and washed in deionised water. Before assembling the fuel cell, the membrane was soaked in 1 M MeOH. The cathode catalyst inks were prepared by mixing with isopropanol and 12 wt.% solution of FAA3 ionomer in N-Methyl-2-pyrrolidone. The components were first mixed by a magnetic stirrer for 45 min, then subjected to 10 min of sonication and finally mixed by a magnetic stirrer overnight. The resulting slurry was painted on a pre-weighed GDL with a microporous layer (FuelCellEtc GDL-CT) by an air brush and dried in a vacuum oven at 40 °C for 1 h. The GDL was then weighed to determine the weight of the dry catalyst layer. The catalyst loadings on the cathodes were $2.2 \pm 0.3$ mg $cm^{-2}$. The same procedure was used to fabricate a reference MEA with Pt supported on a high-surface-area carbon (Alfa Aesar, 60 wt.% Pt). The FAA3 content in this case was 30 wt.% according to the optimised value reported by Carmo et al. [189] and the Pt loading was 0.5 mg $cm^{-2}$. The anode electrodes for the MEAs were fabricated from PtRu supported on high-area carbon (Alfa Aesar, 40 wt.% Pt, 20 wt.% Ru) with similar method as the cathodes. The FAA3 ionomer content in this case was 30 wt.% and the PtRu loading was $3.0 \pm 0.2$ mg $cm^{-2}$. The MEAs were not hot-pressed due to the sensitivity of the FAA3 membrane to pressure and temperature. The fuel cell was assembled with a FAA3 membrane, painted electrodes and Teflon® gaskets. The cell was then clamped together with eight screws and tightened to a torque of 10 Nm. The active area of the fuel cell was 5.29 $cm^2$ and the temperature 40 °C.

Cell voltage and current were controlled by a Metrohm Autolab PGSTAT20 potentiostat with a BSTR10A booster. The flow rate of 1 M MeOH was 2.0 ml $min^{-1}$ and for $O_2$ the flow rate was 200 ml $min^{-1}$. Once the open circuit voltage (OCV) stabilised, polarisation curves were measured with a voltage sweep from the OCV to 0.05 V at a scan rate of 2 mV $s^{-1}$. After measurements, the samples for scanning electron microscopy (SEM, JEOL JSM-7500FA) were cut from the MEA.

For the DMFC activity tests of Fe-NCNT-2 [V], the conditions were the same, but the catalyst loading on the Fe-NCNT-2 cathode was 1.50 mg $cm^{-2}$ and on the Pt/C cathode 1.35 mg $cm^{-2}$. The ionomer content for the Pt/C catalyst layer was 30 wt.% of its dry mass and for Fe-NCNT-2 40 wt.%. A higher content in the latter case was used to improve the dispersion of the catalyst to the ink. The anode electrodes for the MEAs were fabricated from PtRu supported on high-area carbon (Alfa Aesar, 40 wt.% Pt, 20 wt.% Ru) with similar method as the cathodes. The FAA3 ionomer content in this case was 30 wt.% and the PtRu loading was 3.5 mg $cm^{-2}$. The flow rate of 1 M methanol at the anode was 0.5 ml $min^{-1}$ and 200 ml $min^{-1}$ for dry $O_2$ at the cathode.

For testing the activity of Fe-N-CDC and Co-N-CDC in a DMFC [VIII], the preparation and testing conditions were the same, but the catalyst loadings were 1.73 mg $cm^{-2}$ on the Fe-N-CDC cathode, 1.83 mg $cm^{-2}$ on the Co-N-CDC cathode and 1.27 $mg_{Pt}$ $cm^{-2}$ on the Pt/C cathode. The PtRu loading on the anode was $4.25 \pm 0.10$ $mg_{PtRu}$ $cm^{-2}$. The ionomer content in the catalyst layers was 30 wt.% of the total electrode mass. The fuel solution at the anode was first 1 M methanol at 0.2 ml $min^{-1}$. The cell was let to stabilise until the OCV did not change and then polarisation curves from OCV to 0.05 V ($\nu = 3$ mV $s^{-1}$) were measured until reproducible performance was achieved. Then the fuel solution was changed to 1 M methanol in 0.1 M KOH and the measurement procedure repeated.

For PEMFC testing in [X], the ink formulation for MEA preparation was the following: 20 mg of Fe–N–C cathode catalyst material mixed in 652 µL of 5 wt.% Nafion solution containing 15–20% water, 326 µL of pure ethanol and 272 µL of water. Then the inks were deposited on a clean gas-diffusion layer (Sigracet S10-BC) in 400 µL aliquots. The cathodes were dried at 80 °C for at least 2 h. The anode used for all PEFC tests was a commercial Pt/C catalyst with a loading of 0.5 $mg_{Pt}$ $cm^{-2}$ on Sigracet S10-BC. The MEAs were prepared by hot-pressing the anode and cathode (both 4.84 $cm^2$) on a Nafion NRE-211 membrane at 135 °C for 2 min using a force of 500 lb. The MEAs were then sandwiched in a single-cell (Fuel Cell Technologies, USA) using a torque of 10 Nm. A Bio-Logic potentiostat with 50 A load in an in-house fuel cell testing station and EC-Lab software were used to evaluate MEA performance of the catalysts, while the temperature of a fuel cell was kept at 80 °C. Pure $O_2$ was used on the cathode and pure $H_2$ on the anode side of PEMFC. The gases were pre-humidified to 100% RH. The cell temperature was 80 °C during the measurements and the humidifiers were kept at 90 °C to ensure 100% RH. A reference measurement using the same conditions, but a 5 wt.% Pt/C cathode catalyst with a loading of 80 $\mu g_{Pt}$ $cm^{-2}$, was also conducted.

For PEMFC testing in [XIII], first 32 mg of the catalyst was dispersed in 1043 µL of 5 wt.% Nafion solution, 522 µL of pure ethanol, and 435 µL of water. Then the inks were spread evenly on gas-diffusion layers (Sigracet S10-BC) in 250 µL aliquots and dried at 800 °C for at least 2 h. The anode used for all PEMFC tests was a commercial Pt/C catalyst with a loading of 0.5 $mg_{Pt}$ $cm^{-2}$ on Sigracet S10-BC (Baltic Fuel Cells). The MEAs were prepared by hot-pressing the anode and cathode (both 8 $cm^2$) on a Nafion NRE-211 membrane at 135 °C for 2 min using a force of 500 lb. The MEAs were then sandwiched in a homemade single cell with serpentine flow fields using 3 bar of compression. A bipotentiostat (BioLogic) with EC-Lab software was used to evaluate MEA performance of the catalysts. Pure $O_2$ was used on the cathode and pure $H_2$ on the anode side of PEMFC, with 2 bar total gas pressure. The gases were pre-humidified to 100% RH. The cell temperature was 80 °C during the measurements, and the humidifiers were kept at 82 °C to ensure 100% RH in the cell.

For AEMFC tests with Co/N/MWCNT-1 [IV], MEAs were fabricated with commercial carbon-supported Pt catalyst (Pt/C) as anode catalyst and Co/N/MWCNT-1 on cathode sides of the Tokuyama anion exchange membrane (A201, Tokuyama Corporation, Japan). MEAs were also fabricated with commercial Pt/C catalyst both as anode and cathode for comparison purposes. The catalyst ink was prepared by adding Milli-Q water to catalyst material (2 mL for 100 mg of catalyst). To extend the reaction zone of the catalyst layer, 5 wt.% ionomer (AS-4 ionomer, Tokuyama Corporation, Japan) dispersion (0.8 mL for 100 mg of catalyst) was added to the catalyst slurry. The catalyst layer was coated on the A201 AEM with 5 $cm^2$ geometrically active area by spraying method on both sides of the membrane and vacuum-dried at 70 °C for 15 min. The catalyst loadings were about 0.4 and 0.6 mg $cm^{-2}$ on the anode and cathode sides, respectively. The MEA was assembled by sandwiching the catalyst coated membrane inside the test cell (Fuel Cell Technologies, Inc., Albuquerque, NM, USA) with gas diffusion layers (fabricated by a wire rod coating method) on both sides. Gas sealing was achieved by using silicone coated fabric gasket (Product # CF1007, Saint-Gobain Performance Plastics, USA) and with a uniform torque of 0.45 kg m. The single-cell fuel cell performance was evaluated with humidified (100% RH) $H_2$ and $O_2$ gases from 35 to 50 °C using Greenlight Test Station (G50 Fuel Cell System, Hydrogenics, Vancouver, Canada). The gas flow rates were fixed at 100 and 200 SCCM for $H_2$ and $O_2$, respectively.

In AEMFC tests in [IX], the M/N/CDC catalysts were also used as the cathode catalysts for $H_2/O_2$ fuel cells using a commercial Pt/C anode catalyst and Tokuyama A201 series AEM as the polymer electrolyte. The catalyst materials were dispersed in a mixture of deionised water and 5 wt.% Tokuyama AS-4 ionomer (0.8 ml per 100 mg of catalyst) by sonication followed by mixing on a magnetic stirrer for at least 24 h. The catalysts were then coated on a Tokuyama A201 AEM and dried in vacuum at 40 °C. The geometric area of the catalyst layers was 5 or 4.84 $cm^2$ and the catalyst loading for anode and cathode 1 and 1.5 mg $cm^{-2}$, respectively. After drying, the catalyst-covered membrane was soaked in 0.1 M KOH overnight to convert the membrane into $OH^-$ form, washed

with deionised water and then hot-pressed between Sigracet 29-BC gas diffusion layers at 80 °C using a force of 500 lb. For comparison, a MEA with a cathode of 46.1 wt.% Pt/C catalyst (TKK) was also fabricated using the same method. For fuel cell testing, the MEA was sandwiched in a test cell (Fuel Cell Technologies Inc., Albuquerque, USA) with Teflon gasketing using a torque of 8 Nm. The single-cell fuel cell performance was evaluated with humidified (100% RH) $H_2$ and $O_2$ gases at 50 °C using Greenlight Fuel Cell Test Station (G50 Fuel Cell System, Hydrogenics, Vancouver, Canada). The flow rates for $O_2$ and $H_2$ were 0.8 and 0.4 nlpm, respectively.

To compare the ORR activity of Fe-N-comp catalysts in [X] determined from the RDE tests to Pt/C in a real fuel cell environment, single-cell $H_2/O_2$ AEMFC testing was undertaken. First, 50 mg of the catalyst (Fe−N-comp or Pt/C) was suspended in 1 ml of water and 375 µl of Tokuyama AS-4 ionomer solution and sonicated for 2 h. The suspension was then stirred on a magnetic stirrer for at least 24 h and sonicated for another hour before painting it on Tokuyama A201 AEM. The geometric area for the catalyst layer was 6.25 $cm^2$ for the MEA tests, the anode loading was 1.1±0.1 mg $cm^{-2}$ (0.46±0.05 $mg_{Pt}$ $cm^{-2}$) and the cathode loading was 2.6±0.2 mg $cm^{-2}$. For comparison, a MEA with a cathode of 46.1 wt.% Pt/C catalyst (TKK) was also fabricated using the same method with a geometric area of 4.84 $cm^2$, for which the loadings on the anode and cathode were 1 and 2.3 mg $cm^{-2}$, respectively. The corresponding Pt loadings were thus 0.46 and 1.06 $mg_{Pt}$ $cm^{-2}$. For fuel cell testing, the MEA was sandwiched in a test cell (Fuel Cell Technologies Inc., Albuquerque, USA) with Teflon gaskets using a torque of 8 Nm. The gas-diffusion layers used were AvCarb P50 on the anode and Sigracet 29-BC on the cathode side. The single-cell fuel cell performance was evaluated with $H_2$ and $O_2$ gases at 50 °C using Greenlight Fuel Cell Test Station (G50 Fuel Cell System, Hydrogenics, Vancouver, Canada). The anode was kept at 80% RH and the cathode at 100% RH. The flow rates for $O_2$ and $H_2$ were 1 nlpm and the backpressure was 20 kPa.

MEAs for AEMFC measurements in [XIV] were prepared by first dispersing the catalyst in a 3:1 mixture (by volume) of methanol:Milli-Q water. The mixture contained 1 wt.% total of solids, which in turn was comprised of 85% catalyst and 15% of hexamethyl-*p*-terphenyl poly(benzimidazolium) (HMT-PMBI) ionomer [190]. The dispersion was sonicated for 1 h, after which it was pipetted onto a Freudenberg H23C4 GDL of geometric area of 5 $cm^2$ in 200 µl aliquots (multiple droplets of the solution were deposited). The loading of FeN-SiCDC catalyst on the cathode was 2 mg $cm^{-2}$. PtRu/C catalyst (Alfa Aesar HiSPEC™ 12100 50 wt.% Pt, 25 wt.% Ru) with a loading of 0.8 $mg_{PtRu}$ $cm^{-2}$ on Freudenberg H23C4 GDL was used as the anode. The ink formulation and electrode preparation procedure for the anode was the same as for the cathode. The electrodes and the HMT-PMBI membrane were soaked in 1 M KOH solution for 1 day prior to testing and then installed into a 5 $cm^2$ single cell (Fuel Cell Technologies, USA) and the cell assembled with a torque of 7 N m. The single cell fuel cell performance was evaluated at the cell temperature of 60 °C with Greenlight Fuel Cell Test Station (G50 Fuel cell system, Hydrogenics, Vancouver, Canada). Fully

humidified oxygen (0.2 NLPM) and 82% RH hydrogen (0.4 NLPM) were fed into the cell with a backpressure of 200 kPa.

## 6.10 Physical characterisation methods

Scanning electron microscopy (SEM) images were taken of the carbon materials and catalysts by first coating a GC disk substrate similar to the RDE electrode or a Si wafer plate with the material. Images were then taken using a Helios™ NanoLab 600 (FEI) scanning electron microscope.

Transmission electron microscopy (TEM) was performed by pipetting an aliquot of the studied material in isopropanol on a TEM grid, which was then studied under a high-resolution (scanning) transmission electron microscope (HR-(S)TEM) Titan 200, equipped with an energy dispersive X-ray (EDX) Super X detector system (FEI).

Raman spectra were recorded using a Renishaw inVia micro-Raman spectrometer (spectral resolution 2 $cm^{-1}$) employing the 514 nm line of an argon-ion laser for excitation.

$N_2$ adsorption/desorption isotherms of the catalyst samples were recorded at the boiling temperature of nitrogen (77 K) using a NovaTouch LX2 Analyser (Quantachrome) or a Micrometrics TRISTAR analyzer. The samples were degassed under vacuum at 200 °C for at least 24 h and backfilled with $N_2$ gas before the measurement. The specific surface area ($S_{BET}$) was calculated according to either the Brunauer-Emmett-Teller (BET) theory or the quenched solid density functional theory (QSDFT) up to a nitrogen relative pressure of $P/P_0 = 0.2$. The total volume of pores ($V_{tot}$) was measured near to saturation pressure of $N_2$ ($P/P_0 = 0.97$). The microporosity ($V_{\mu}$) was calculated from t-plot method using deBoer statistical thickness. The average diameter of pores ($d_p$) was calculated for a slit-type pore geometry using the following equation: $d_p = 2V_{tot}/S_{BET}$. The calculations of pore size distribution (PSD) from $N_2$ sorption isotherms were done using a QSDFT equilibria model for slit type pore.

The powder X-ray diffraction (XRD) patterns were collected with a Bruker D8 Advance diffractometer with Ni filtered Cu Kα radiation and LynxEye line detector. Scanning steps of 0.013°2θ from 5 to 90°2θ and a total counting time of 173 s per step were used. Alternatively, XRD analysis was conducted using a PANanalytical X'Pert powder X-ray diffractometer and with Cu Kα radiation from 10 to 90° 2θ using a step size of 0.033° 2θ.

XPS measurements were conducted using a SCIENTA SES 100 spectrometer. For excitation the Mg Kα radiation (1253.6 eV) from the nonmonochromatic twin anode X-ray tube (Thermo XR3E2) was used. All of the XPS spectra were acquired under ultrahigh-vacuum conditions. The survey scan was collected using the following parameters: energy range, 0–1000 eV; pass energy, 200 eV; step size, 0.5 eV; step duration, 1 s. To measure core-level XPS spectra, the following parameters were used: energy range, 390–410 eV; pass energy, 200 eV; step size, 0.2

or 0.1 eV; step duration, 1 s; number of scans, at least 20. The raw data were processed using the Casa XPS software. Data processing involved removal of Kα and Kβ satellites, correction with electron spectrometer transmission function, and peak fitting using the Gauss–Lorentz hybrid function GL 70 (Gauss 30%, Lorentz 70%) and Shirley-type backgrounds. The semi-quantitative analysis was done using methods described by Seah et al. for quantitative XPS measurements [191]. The C-C component (at 284.6 eV) of the C1s peak is used for reference. For semi-quantitative analysis Scofield cross-sections and inelastic mean free paths given by the TPP-2M formula were used.

$^{57}$Fe Mössbauer spectra were measured at room temperature with a source of $^{57}$Co in Rh [XI, XIII]. The spectrometer was operated with a triangular velocity waveform and a NaI scintillation detector was used for γ-ray detection. Velocity calibration was performed with an α-Fe foil.

*Ex situ* X-ray absorption spectroscopy (XAS) [XI] measurements on the sample with the sample loading reaching a ~0.05 edge height at the Fe K edge were collected in the fluorescence mode at the beamline 8-ID at the NSLS-II, Brookhaven National Laboratory. Multiple scans were collected to increase the signal-to-noise ratio, and to ensure the repeatability of the data. Scans were calibrated, aligned, merged and normalised with background removed using the IFEFFIT suite [192]. XAS [XIV] data were collected at the Fe K-edge in fluorescence geometry at the SAMBA beamline of the synchrotron SOLEIL (France) using a sagittally bent double crystal Si(220) monochromator and a Canberra 35-elements germanium detector. Data treatment and linear combination fitting were performed with the Athena software [193].

In order to determine the bulk concentration of elements in the catalysts, inductively coupled plasma mass spectrometry (ICP-MS) was used. Sample digestion, prior to analysis with ICP-MS was performed with Anton Par Multiwave PRO microwave digestion system using NXF100 digestion vessels (PTFE-TFM liner) in 8 N rotor. 10 mg of sample was weighed into PTFE vessels and 3 mL of $HNO_3$ (Carl Roth ROTIPURAN Supra) along with 3 mL of $H_2O_2$ (Fluka TraceSELECT Ultra) were slowly added to the vessel. After the initial vigorous reaction had subsided 1 mL of HF (Carl Roth ROTIPURAN Supra) was added, the vessels were capped and digested in the microwave unit. A stepwise power-controlled digestion procedure for 8 vessels was employed: ramp to 600 W in 10 min, ramp to 1000 W in 8 min, ramp to 1500 W in 8 min, hold at 1500 W for 30 min. It was observed during the method development that temperatures in excess of 200 °C were needed for complete digestion. After digestion the samples were diluted using 2% $HNO_3$ solution (prepared from 69% $HNO_3$, Carl Roth ROTIPURAN Supra) to a final dilution factor of 70 000 and analysed using Agilent 8800 ICP-MS/MS. $^{11}$B, $^{90}$Zr and $^{47}$Ti were measured using NoGas mode in MS/MS "on mass" configuration and $^{56}$Fe, $^{57}$Fe were measured using MS/MS "on mass" configuration with He (6 mL min$^{-1}$) as collision gas in the CRC (collision-reaction cell). For the samples synthesized with natural iron, $^{56}$Fe was used to quantify the iron content assuming natural distribution of iron isotopes, otherwise $^{57}$Fe was used, assuming 95% abundance of $^{57}$Fe.

# 7. RESULTS AND DISCUSSION

## 7.1 Electrocatalysis of oxygen reduction on nitrogen-doped nanocarbons

The first part of the thesis deals with the electrocatalytic activity of nitrogen-doped carbon nanomaterials towards the ORR. The first chapter deals with the ORR activity of nitrogen-doped MWCNT/graphene composite materials in alkaline media [I, II, III] and in a direct methanol fuel cell [II], while the second chapter is dedicated to the ORR activity of nitrogen-doped CDCs [VII].

### 7.1.1 Nitrogen-doped MWCNT/graphene composite materials

Owing to the extraordinary properties of both graphene and MWCNT described in section 4.4, they were selected as precursors for nitrogen-doped ORR catalysts. This work was inspired by a previous study done in our working group on graphene [126], where it was noted that graphene sheets have the tendency to stack up again during the high-temperature pyrolysis procedure. To avoid this, MWCNTs (which were also already confirmed to have significant activity towards the ORR on their own in our working group [121]) were selected as the spacer material between the graphene sheets. To synthesise N-doped catalysts from these two carbon materials, graphite was first oxidised into GO (section 6.2) and commercial MWCNTs were purified (section 6.1). After this, they were mixed with a nitrogen precursor and PVP in liquid phase, sonicated and pyrolysed (section 6.4). During the pyrolysis procedure, the fast decomposition of the nitrogen precursors into gaseous components acts to separate the GO sheets even further and to reduce them into graphene. The precursors used in this work are given in Figure 6.

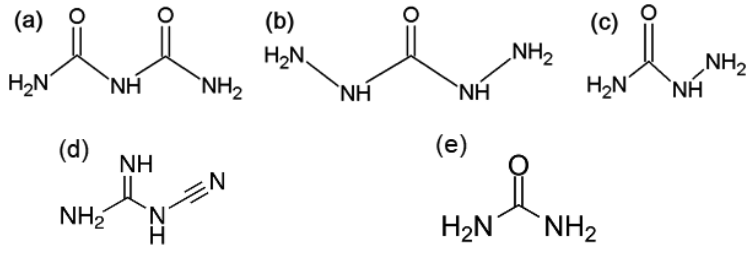


**Figure 6.** Chemical structures of the nitrogen precursors: (a) biuret (BR), (b) carbohydrazide (CH), (c) semicarbazide (SC), (d) dicyandiamide (DCDA) and (e) urea.

All of them have a few things in common: they are very nitrogen-rich and decompose at less than 800 °C. In general, during the pyrolysis process all of these nitrogen sources first form graphitic carbon nitride (g-$C_3N_4$), which in turn decomposes at >700 °C to give $NH_3$ and carbon nitride gases ($C_2N_2^+$, $C_3N_2^+$, $C_3N_3^+$) [194–197]. Depending on the specific precursor, by-products such as HNCO, cyanuric acid, triuret, ammelide, ammeline, melamine, melam, melem and melon can also be formed. Using the „flash“ type of pyrolysis, where the sample is quickly entered into the heating zone of the furnace, it is likely that all of these components are present at the same time and react with both the carbon and each other as well. This means that doping with each of the nitrogen sources will give very different results.

SEM images of the 2-NC and NG/NCNT-BR material are shown in Figure 7. The crumpled sheet morphology characteristic to graphene is clearly visible, with MWCNTs deposited on top of and between the sheets, as intended. The MWCNTs act as spacers to prevent restacking of graphene nanosheets and therefore increase the availability of the active sites on those sheets. In addition, the MWCNTs themselves are catalytically active. TEM (Figure 7b) confirmed these finding as no larger graphite stacks were visible.

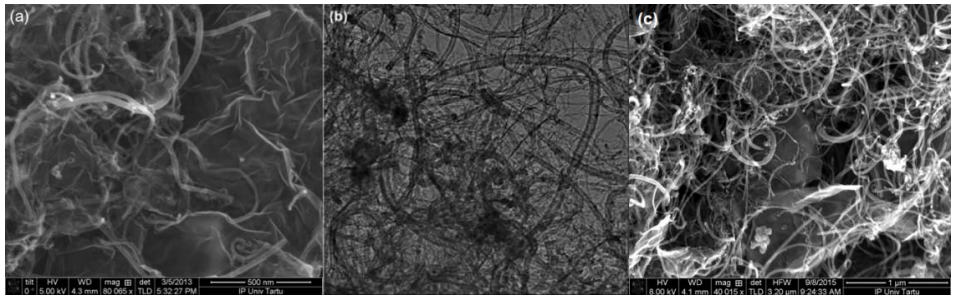


**Figure 7.** SEM images of 2-NC (a) and NG/NCNT-BR (c) materials and a TEM image of the 2-NC material (b).

To determine elemental composition on the surface of the catalyst materials, as well as the type of nitrogen moieties each of the nitrogen precursors created on the surface, XPS analysis of each of the catalysts was undertaken. The XPS survey spectra and the core-level N1s spectra for the catalysts derived from biuret, carbohydrazide and semicarbazide are given in Figure 8.

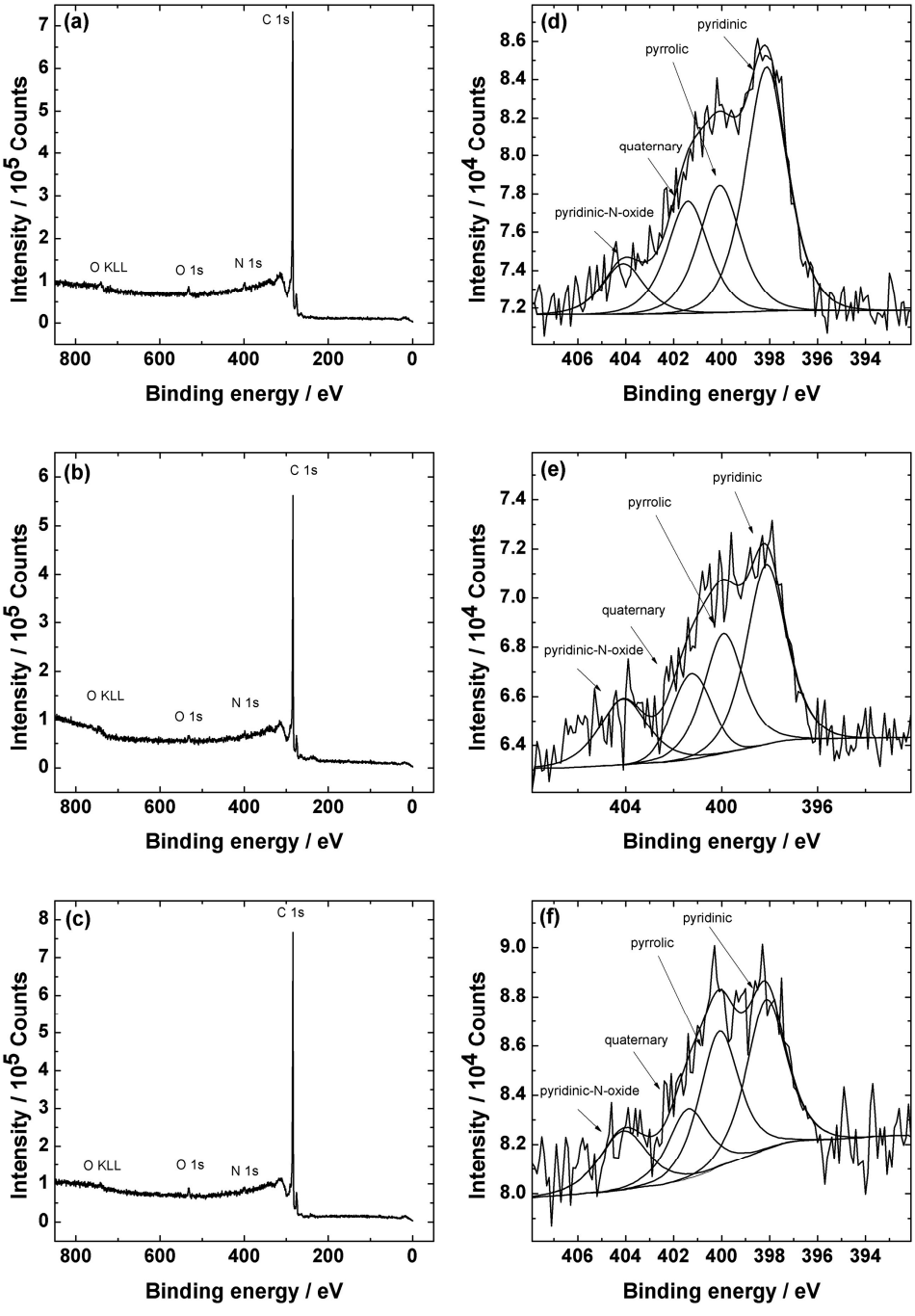


**Figure 8.** XPS survey spectra (a–c) and N1s spectra (d–f) for NG/NCNT-BR, NG/NCNT-CH and NG/NCNT-SC samples, respectively.

The XPS peaks at 284.8, 532.1 and 400.0 eV denote the binding energies of C1s, O1s and N1s, respectively. As can be seen, most of the oxygen-containing groups of GO and purified MWCNTs have been either reduced or replaced by nitrogen moieties at the end of the pyrolysis. The presence of an N1s peak around 400 eV indicates the successful incorporation of nitrogen atoms into graphene/MWCNT material. The types of nitrogen species were identified by deconvolution of the core-level N1s spectra. The peaks in the high-resolution N1s spectra in Figure 2d–f can be deconvoluted into four components: pyridine-N-oxide (404.1 eV) [198], quaternary (graphitic) N (401.1 eV), pyrrolic N (400.1 eV) and pyridinic N (398.1 eV). The total nitrogen content in NG/NCNT-BR, NG/NCNT-CH and NG/NCNT-SC was 2.8, 2.5 and 1.7 at.%, respectively. The relative contents of nitrogen moieties are given in Table 2. Interestingly, while the absolute concentration of species changed, the relative contents of nitrogen moieties stayed more or less the same. The XPS spectra corresponding to 1-NC and 2-NC materials are presented in Figure 9.

**Table 2.** Surface nitrogen contents and speciation of nitrogen for NG/NCNT-BR, NG/NCNT-CH, NG/NCNT-SC, 1-NC and 2-NC.

| Catalyst | Total N (at.%) | Pyridinic N % | Pyrrolic N % | Quaternary (graphitic) N % | Pyridine-N-oxide % |
|---|---|---|---|---|---|
| NG/NCNT-BR | 2.8 | 46 | 24 | 21 | 10 |
| NG/NCNT-CH | 2.5 | 39 | 26 | 17 | 17 |
| NG/NCNT-SC | 1.7 | 35 | 32 | 16 | 17 |
| 1-NC | 6.0 | 56 | 24 | 12 | 8 |
| 2-NC | 4.0 | 50 | 26 | 15 | 9 |

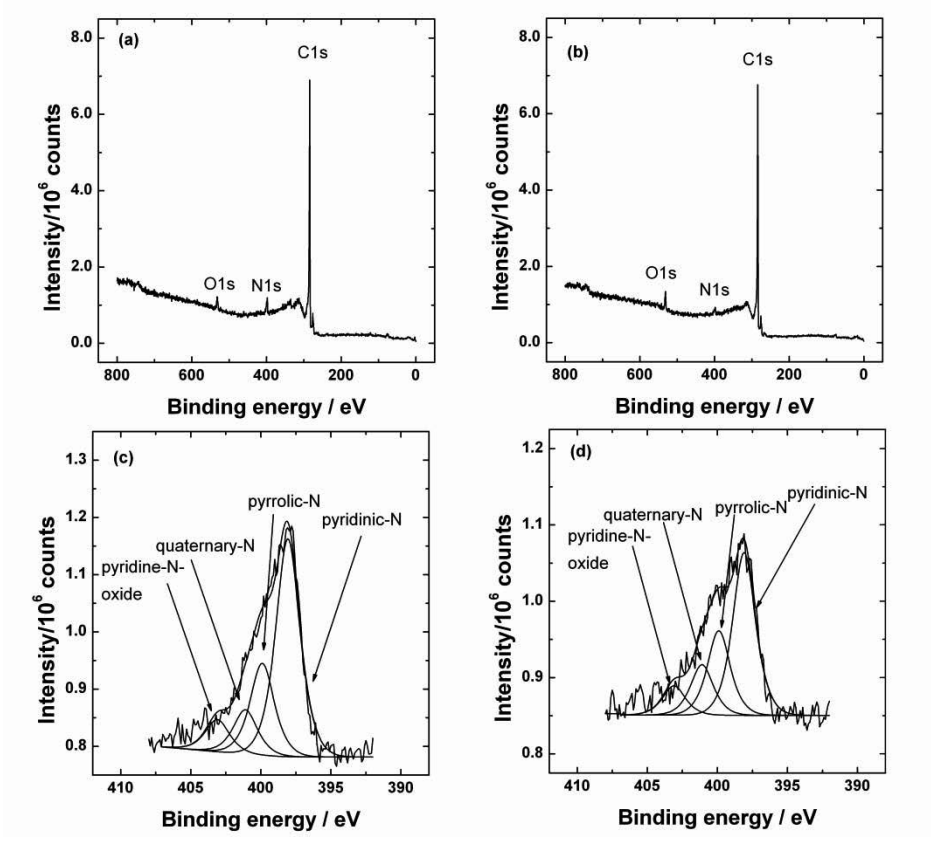


**Figure 9.** XPS survey spectra (a,b) and N1s spectra (c,d) for 1-NC and 2-NC samples, respectively.

In the case of 1-NC and 2-NC, the overall N content of 1-NC was higher (as was thus the content of pyridinic and quaternary nitrogen, which are considered the most important components). The relative quaternary N content was lower than in the case of all of the samples from the first set along with the content of oxidised pyridine N-oxide.

To describe the structure of carbon in the 1-NC and 2-NC samples, Raman spectroscopy of these materials was done in the Institute of Physics, University of Tartu. The resulting Raman spectra are given in Figure 10.

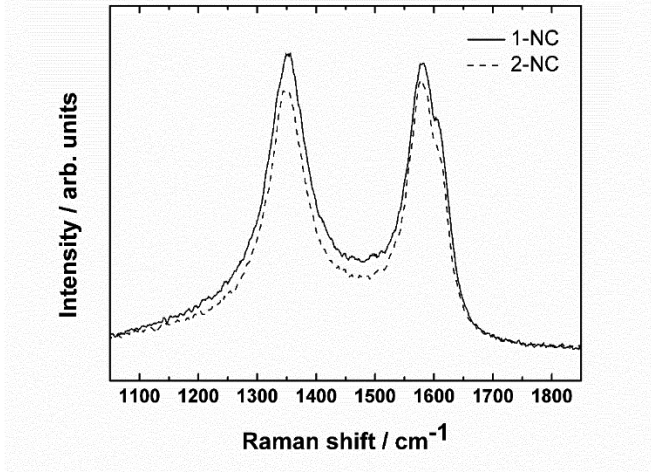


**Figure 10.** Raman spectra of 1-NC and 2-NC materials.

The most important signals in the Raman spectra of carbon materials are the D-band situated at ~1350 $cm^{-1}$ and the G-band situated at 1550–1600 $cm^{-1}$. The D-band arises from a breathing mode vibration of six-member carbon rings [199] and notes the presence of disordered carbon planes. The G-band arises from the tangential vibrations of carbon atoms in graphite and is characteristic of $sp^2$-hybridised carbons [200]. 1-NC and 2-NC both showed peaks at 1350 and 1580 $cm^{-1}$. The $I_D/I_G$ ratio was found to be 0.96 and 1.03 for 1-NC and 2-NC samples, respectively. Slightly larger intensity of the D peak of the sample prepared by pyrolysis of carbon and urea is in accordance with the XPS measurements and refers to a higher content of $sp^3$ carbon in this material. There is also a visible shoulder on the G-peak at ~1604 $cm^{-1}$ which is associated with defective graphitic structures [201]. Overall, the Raman spectra showed that the 1-NC material was somewhat more disordered than 2-NC.

The RDE method was used as the primary method for testing the ORR activity of the N-doped MWCNT/graphene catalysts. The ORR was studied on GC electrodes modified with 0.1 mg $cm^{-2}$ of the selected catalyst, which was deposited from a 1 mg $ml^{-1}$ dispersion also containing 0.25% of Tokuyama AS-4 ionomer. The ionomer served as both a dispersing agent and a binder. Figure 11 shows the results on the undoped GO/MWCNT composite and all of the doped materials. The undoped material showed a rather low activity towards the ORR, with an onset potential ($E_{onset,}$ defined as the potential at –0.05 mA) of –200 mV vs SCE. There is a clear second reduction wave at –0.8 V, which is can be ascribed to quinone-type groups [202] reducing some of the $H_2O_2$ further to water. This is supported by the K-L data shown in Figure 12, where the number of electrons transferred per $O_2$ molecule ($n$) increases from 2 ($O_2$ reduction to $H_2O_2$) to 3 (both two- and four-electron electroreduction processes taking place). The K-L plots (Figure 12) were derived from the ORR polarisation data with the number of electrons transferred per $O_2$ molecule ($n$) shown in the inset. The $n$ value was calculated from the K-L equation [203]:

$$\frac{1}{I} = \frac{1}{I_k} + \frac{1}{I_d} = -\frac{1}{nFAkc_{O_2}^b} - \frac{1}{0.62nFAD_{O_2}^{2/3}\nu^{-1/6}\omega^{1/2}c_{O_2}^b}, \quad (10)$$

where $I$ is the measured current, $I_k$ and $I_d$ are the kinetic and diffusion-limited currents, respectively, $k$ is the rate constant for $O_2$ reduction (cm $s^{-1}$), $A$ is the geometric electrode area ($cm^2$), $F$ is the Faraday constant (96485 C $mol^{-1}$), $\omega$ is the rotation rate (rad $s^{-1}$), $D_{O2}$ is the diffusion coefficient of oxygen ($1.9\times10^{-5}$ $cm^2$ $s^{-1}$) [204], $C_{O2}$ is the concentration of oxygen in the bulk ($1.2\times10^{-6}$ mol $cm^{-3}$) [204] and $v$ is the kinematic viscosity of the solution (0.01 $cm^2$ $s^{-1}$) [205]. The values of $D_{O2}$ and $C_{O2}$ are given for 0.1 M KOH solution.

Using SC as the dopant shifted the onset potential to –175 mV vs SCE and increased the reduction current values notably. Switching the nitrogen precursor to CH shifted the $E_{onset}$ potential a further 30 mV to the positive side and increased the reduction current values at a given rotation rate of the electrode, with the ORR becoming diffusion-limited at more negative potentials. Doping with BR had a much more profound effect on the ORR activity than either SC or CH: the onset shifted to –130 mV vs SCE and $n$ was near 4 in the whole potential window studied. The peak at around –0.2 V vs SCE shown at lower rotation speeds is due to the reduction of oxygen trapped in the inner structures of the catalyst layer, indicating that this catalyst has a complex structure with a high specific surface area. Doping with urea yielded a catalyst with moderate activity (1-NC), with onset potential of –132 mV vs SCE, but no clear reduction current plateaux on the RDE polarisation curves and the $n$ value of around 3.5–3.7. DCDA doping (2-NC) was much more successful with an activity similar to NG/NCNT-BR ($E_{onset}$ of –121 mV), albeit lower reduction currents.

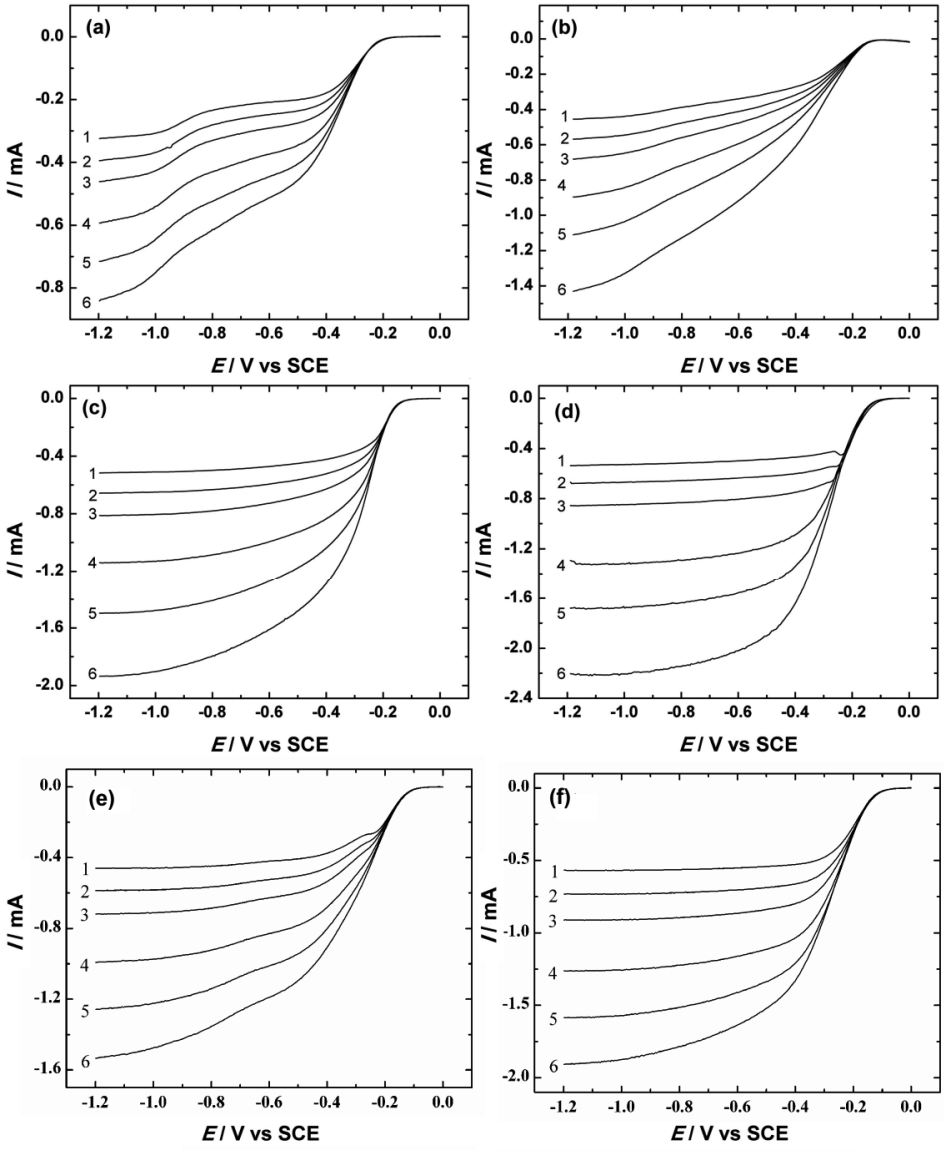


**Figure 11.** RDE voltammetry curves for oxygen reduction on (a) undoped GO/MWCNT, (b) NG/NCNT-SC, (c) NG/NCNT-CH, (d) NG/NCNT-BR, (e) 1-NC and (f) 2-NC modified GC electrodes in $O_2$-saturated 0.1 M KOH. $\nu = 10$ mV $s^{-1}$, $\omega =$ (1) 360, (2) 610, (3) 960, (4) 1900, (5) 3100 and (6) 4600 rpm. $A = 0.2$ $cm^2$.

Since there is no way to quantitatively measure the number of electrochemically accessible active sites on this type of materials, it is inconclusive exactly what causes the increase in activity. It has been shown, however, both experimentally [102,206] and with DFT (density functional theory) calculations [107,108] that pyridinic and quaternary (graphitic) N increase the ORR activity of carbon materials [207]. It has been proposed that nitrogen atoms can create a high positive charge density on the neighbouring carbon atoms and thus change the adsorption mode of the $O_2$ molecule from end-on adsorption to side-on adsorption [208] in addition to weakening of the O=O bond. Pyridinic nitrogen has been shown to donate a *p*-electron into the aromatic π-system of the carbon ring, thereby destabilizing the carbon atoms next to it and providing local charge [208,209], has been shown to enhance the second step of the oxygen reduction reaction in acidic media [72] and enable the adsorption of $O_2$ on the carbon atoms next to it in alkaline media. Graphitic nitrogen, which also destabilises the carbon ring it is doped into since it has a higher electronegativity than carbon [210], has been shown to facilitate the chemisorption of oxygen onto the adjacent carbon atom in the first step of the ORR and pyrrolic nitrogen has been correlated with the two-electron reduction of oxygen into hydrogen peroxide as well [72]. Other activity descriptors such as a high surface area (not measured here, but likely quite high due to the high SSA of the starting materials) and defectiveness (visible from Raman spectra) also likely contributed to the high ORR activity of these materials. Compared to results on N-doped graphene [126], which was doped using the same procedure, the separation of graphene layers by addition of MWCNTs was very successful as a means of increasing the ORR activity.

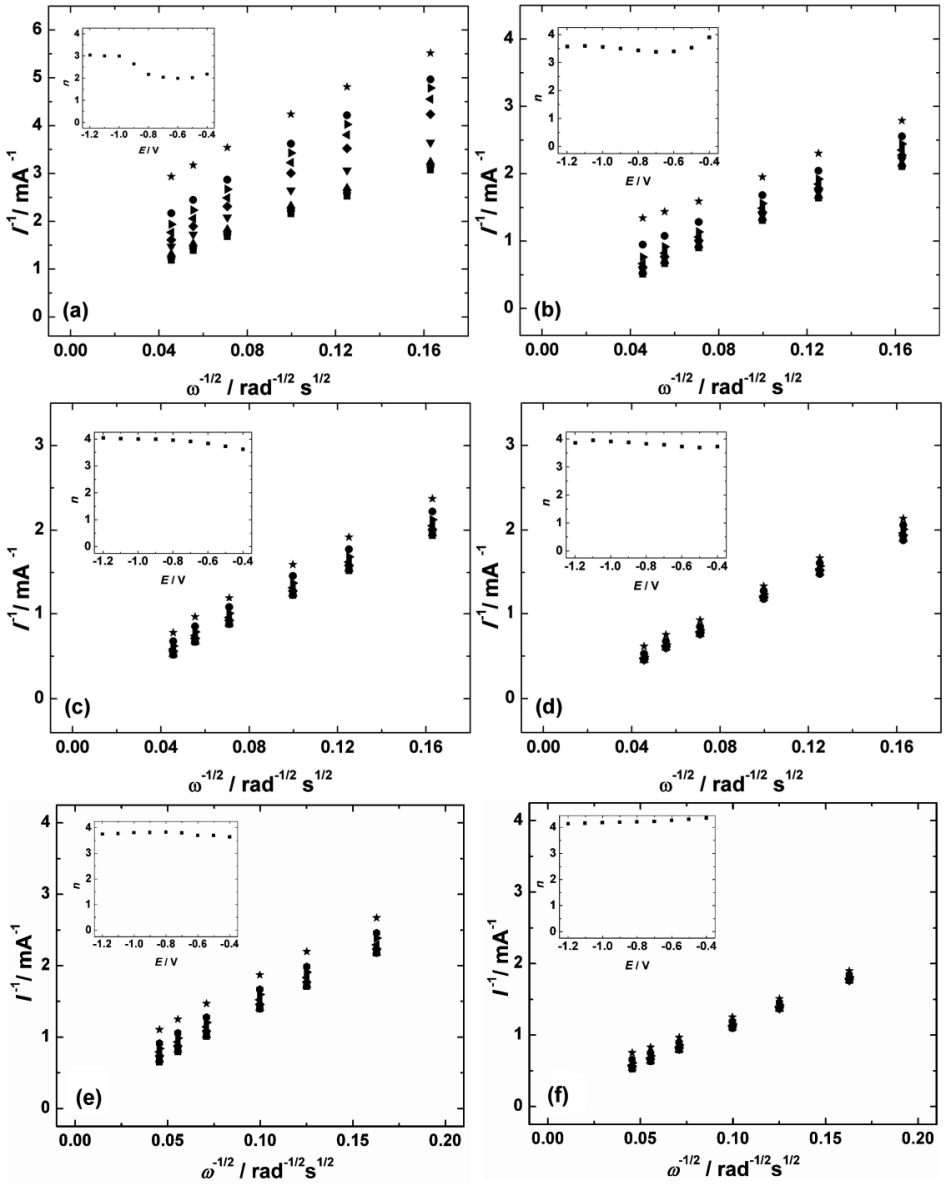


**Figure 12.** Koutecky–Levich plots for oxygen reduction on (a) undoped GO/MWCNT, (b) NG/NCNT-SC, (c) NG/NCNT-CH, (d) NG/NCNT-BR, (e) 1-NC and (f) 2-NC modified GC electrodes in 0.1 M KOH. $E$ = (★) −0.4, (●), −0.5, (▶) −0.6, (◀) −0.7, (♦) −0.8, (▾) −0.9, (▴) −1.0, (●) −1.1 and (■) −1.2 V. Inset shows the potential dependence of $n$. Data derived from Fig. 11.

The stability of both NG/NCNT-BR and 2-NC were tested during 1000 potential cycles from –1.2 V to 0 V vs SCE (Figure 13). After every 100 cycles an LSV curve and RDE polarisation curve were recorded. The LSV peak current values were nearly identical during the whole test and the ORR polarisation curves showed minimal activity loss (with no shift in the onset potential), indicating that these materials have excellent stability in alkaline media.

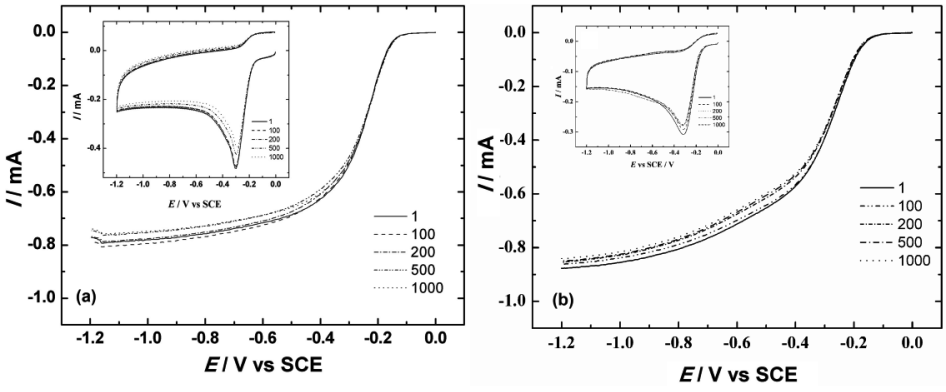


**Figure 13.** Stability of NG/NCNT-BR and 2-NC modified GC electrodes in $O_2$-saturated 0.1 M KOH during 1000 potential cycles with the inset showing LSV results. $\nu = 10$ mV $s^{-1}$, $\omega = 960$ rpm, inset $\nu = 100$ mV $s^{-1}$. $A = 0.2$ $cm^2$.

Comparison of the N-doped composite catalysts with a commercial Pt/C catalyst are visible in Figure 14. Both the 2-NC and the NG/NCNT-BR catalyst performed near to the activity of the 20 wt.% Pt/C catalyst from E-TEK, with similar half-wave potentials ($E_{1/2}$), albeit more negative onset potentials.

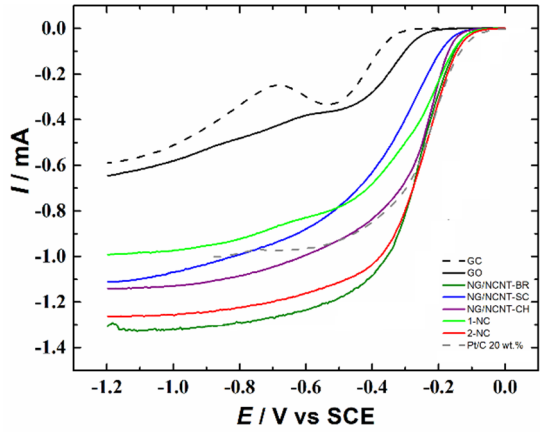


**Figure 14.** Comparison of GC, GO and N-doped composite catalysts with 20 wt.% Pt/C in $O_2$-saturated 0.1 M KOH. $\nu = 10$ mV $s^{-1}$, $\omega = 1900$ rpm. $A = 0.2$ $cm^2$.

For comparison purposes with other catalysts in the literature as well as the materials presented later in this work, the $j_k$ values at 0.8 V vs RHE were also calculated. The formula for converting potentials from SCE to RHE used is $E_{RHE} = E_{SCE} + 1.008$ V, which was determined by calibrating the SCE used. The current values were divided by the electrode area to obtain the ORR current densities. The results are given in Table 3. The 2-NC material obviously has an edge over the other N-doped catalyst, which is why it was chosen for testing in a DMFC.

**Table 3.** ORR parameters of N-doped MWCNT/graphene composite catalyst materials and Pt/C in 0.1 M KOH.

| Catalyst | $E_{onset}$ (mV vs SCE) | $E_{1/2}$ (mV vs SCE) | $j_k$ at 0.8 V vs RHE (mA cm$^{-2}$) |
|---|---|---|---|
| NG/NCNT-BR | –130 | –270 | 2.2 |
| NG/NCNT-SC | –170 | –364 | 0.8 |
| NG/NCNT-CH | –145 | –267 | 1.9 |
| 1-NC | –132 | –300 | 1.8 |
| 2-NC | –121 | –260 | 2.6 |
| 20 wt.% Pt/C | –105 | –236 | 1.7 |

After pre-selecting the 2-NC catalyst from the preliminary RDE tests, a full scale DMFC experiment was conducted with this material [II]. Prior to DMFC testing, the methanol tolerance of the 2-NC material was also studied, due to the possibility of methanol crossover from the anode side to the cathode side. This is a common issue when using Pt/C catalysts, because Pt is also highly active towards methanol electro-oxidation, leading to a mixed potential and adsorption of side products such as CO, which poison the electrode [21]. The activity of the 2-NC catalyst was first tested in $O_2$-saturated 0.1 M KOH, after which a 0.1 M KOH methanol solution was added, so that the end concentration of methanol in the electrochemical cell would be 3 M without changing the KOH concentration. The cell was then re-saturated with oxygen and another RDE voltammetry curve was recorded. As seen in Figure 15, the ORR performance of 2-NC does not change significantly (most importantly, there is no methanol oxidation peak) when going from a methanol-free environment to 3 M MeOH solution, so the catalyst is quite resistant to methanol poisoning.

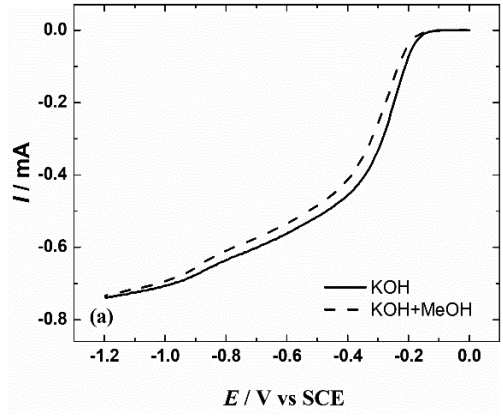


**Figure 15.** RDE voltammetry curves for oxygen reduction on a 2-NC modified GC electrode in $O_2$-saturated 0.1 M KOH solution with and without 3 M MeOH. $\nu = 10$ mV $s^{-1}$, $\omega = 960$ rpm.

The 2-NC material was spray-painted as the cathode of an alkaline anion-exchange membrane fuel cell with a FAA3 membrane from Fumatech (more details of the MEA preparation are given in section 6.9) with the results given in Figure 16. The FAA3 membrane was selected due to its better resistance to methanol cross-over compared to the Tokuyama membranes. The activity was compared with a 60 wt.% Pt/C material. The 2-NC material outperformed even the high-loading Pt/C in the DMFC test, with a maximum power density of 0.72 mW $cm^{-2}$ (same as the Pt/C) and an OCV of 0.64 V (compared to 0.44 V for the Pt/C). It is to be noted, however, that the 2-NC material reaches its maximum power density at much higher potentials. The results were also highly competitive with other alkaline DMFCs at the time, including N-doped CNTs [211] and other studies using Pt/C as the cathode [212,213].

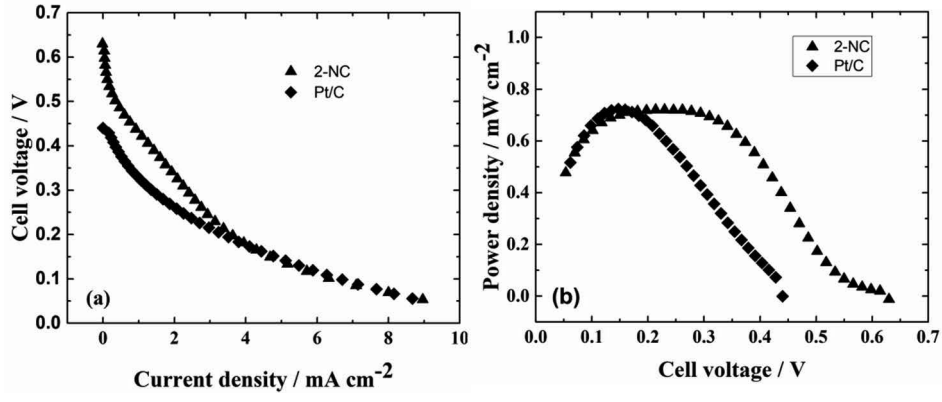


**Figure 16.** Fuel cell performance of the catalysts in 1 M MeOH at 40 °C showing (a) polarisation curves and (b) power density curves.

This work on nitrogen-doped MWCNT/graphene composites was among the first to demonstrate the activity of metal-free catalysts for alkaline DMFCs. It also showed the success of this doping method (wet mixing of small N-containing molecules with carbon nanomaterials followed by pyrolysis in inert atmosphere) in creating a high relative concentration of pyridinic N on the surface of the material, on which the later improvements made in this work are based. It also showed that DCDA is the most successful of the dopants.

### 7.1.2 Nitrogen-doped CDCs

Carbide-derived carbons are a spectacular carbon material for ORR catalysis, as discussed in chapter 4.4. After developing and optimising the nitrogen doping method on MWCNT/graphene composites, this was also used to dope different CDC materials [VII]. TiC was selected as the starting carbide, because TiC yields some of the highest surface areas when chlorinated into a CDC [214]. A TiCN material was also chlorinated for comparison.

SEM micrographs of the doped CDCs (**1094-N** and **13-N**) and the TiCN-derived carbon material (**040-N**) are displayed in Figure 17, showing amorphous particles of varying sizes. The variety in particle sizes fills the space efficiently with catalytically active material. The doped materials have a more etched surface due to the processes taking place during the pyrolysis (which includes doping with $NH_3$, that etches some of the carbon). The TiCN-derived carbon (Figure 17c) has a smooth surface, with notably larger particles.

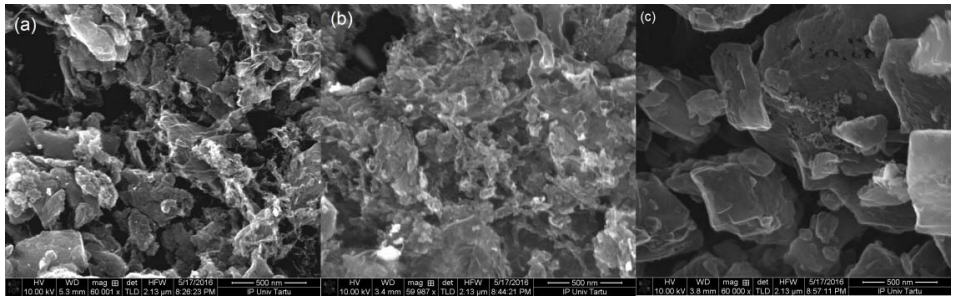


**Figure 17.** SEM images of **1094-N** (a), **13-N** (b) and **040-N** (c) materials.

XPS analysis of the three catalysts was undertaken to determine the surface elemental composition and the N speciation (Figure 18 and Table 4). The bulk N concentration was determined via SEM-EDX. Notably, **13-N** had a very high surface N concentration (3.6 at.%) compared to its bulk N concentration of only 0.7 at.%, as well as a very high surface oxygen content of 8.7 at.%. Compared to the other materials, it also had a higher concentration of pyridinic N. In the case of both **1094-N** and **040-N**, the bulk N concentration (5.3 and 6.3 at.%, respectively) was much higher than the surface N concentration.

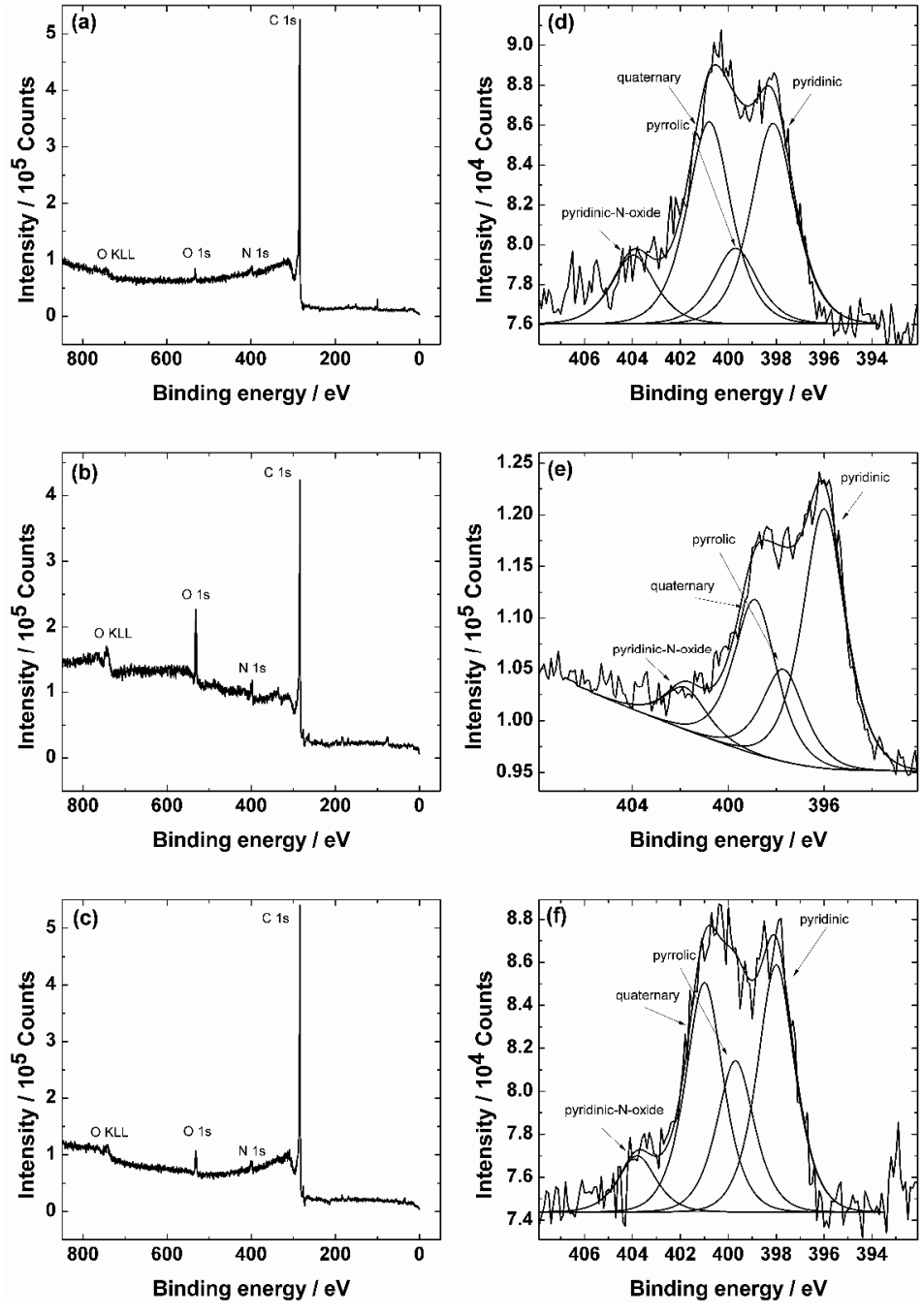


**Figure 18.** XPS survey spectra (a–c) and N1s spectra (d–f) for **040-N**, **13-N** and **1094-N** samples, respectively.

**Table 4.** Bulk and surface nitrogen contents and speciation of nitrogen for **040-N**, **13-N** and **1094-N**.

| Catalyst | Bulk N (at.%) | Surface N (at.%) | Pyridinic N % | Pyrrolic N % | Quaternary (graphitic) N % | Pyridine-N-oxide % |
|---|---|---|---|---|---|---|
| 040-N | 6.3 | 1.8 | 36 | 14 | 37 | 13 |
| 13-N | 0.7 | 3.6 | 47 | 26 | 28 | 8 |
| 1094-N | 5.3 | 1.7 | 36 | 32 | 29 | 8 |

Raman spectra for the three studied materials are shown in Figure 19 and reveal the same two bands as for the MWCNT/graphene composites: a D-band at ~1350 $cm^{-1}$ and a G-band at around 1580 $cm^{-1}$. The inset in Figure 19 represents the intensity ratios $I_D/I_G$ and reveals that the ratio is 1.07 and 1.1 for **040-N** and **13-N** samples and 0.93 for **1094-N**, respectively. Relatively smaller $I_D/I_G$ for the sample **1094-N** refers to a higher content of graphitic $sp^2$ carbon in this material [215]. The shoulder at ~1604 $cm^{-1}$ associated with defective graphitic structures [201] is also seen on the G-band.

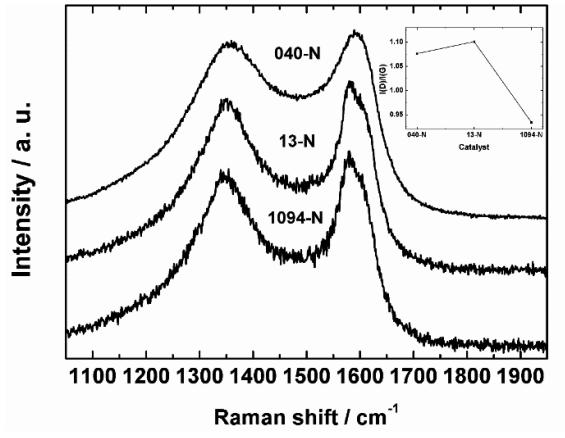


**Figure 19.** Raman spectra of **040-N**, **13-N** and **1094-N** materials with the inset showing the intensity ratio of $I_D/I_G$ for D and G bands. The intensity for $I_D$ and $I_G$ were extracted by fitting spectra with two Lorentzians.

$N_2$ physisorption was used to study the porosity of the catalysts. The specific surface area ($S_{BET}$) of the CDC-N materials was calculated according to BET theory up to a nitrogen relative pressure of $P/P_0 = 0.2$. The total volume of pores ($V_p$) was measured at near to a saturation pressure ($P/P_0 = 0.99$). The volume of micropores ($V_\mu$) was calculated from t-plot method by using deBoer statistical thickness. An average pore size ($d_p$) was calculated for slit-type pore geometry by using the formula: $d_p = 2V_p/S_{BET}$. Calculated BET specific surface areas, pore

volumes, micropore volumes and average pore sizes are given in Table 5. The **1094-N** material had the highest surface area of all the materials and the smallest average pore size. The **13-N** material had the largest pore volume of all of the catalysts, while **040-N** had a somewhat lower SSA and pore volume than the other catalysts, being largely mesoporous compared to the microporous **1094-N** and **13-N**. This is due to the structural differences between TiC and TiCN which lead to a different pore structure after chlorination. **1094-N** and **13-N** both had a TiC precursor with some differences in the chlorination process (known only to Skeleton Technologies), leading to two catalysts with rather similar porosities (although **13-N** was notably more mesoporous).

**Table 5.** Textural properties of the CDC-N materials: BET surface areas ($S_{BET}$), pore volume ($V_p$), micropore volume ($V_\mu$) and average pore size ($d_p$).

| Catalyst | $S_{BET}$, $m^2g^{-1}$ | $V_p$, $cm^3g^{-1}$ | $V_\mu$, $cm^3g^{-1}$ | $d_p$, nm |
|---|---|---|---|---|
| 1094-N | 2024 | 1.20 | 0.91 | 1.18 |
| 13-N | 1988 | 1.67 | 1.42 | 1.68 |
| 040-N | 779 | 1.20 | 0.20 | 3.08 |

As a first test, the ORR activity of undoped CDCs was measured to have a starting point and to confirm the effect of nitrogen doping towards the electrocatalytic properties. RDE voltammetry curves and K-L plots of the undoped CDC materials are shown in Figure 20. The onset potential for the undoped **130614-2** (precursor for **13-N**) material was –272 mV vs SCE, which is rather negative, and the reduction current values were also rather low. The ORR activity that the material had can be attributed to the quinone-type groups on the surface reducing oxygen into hydrogen peroxide and at more negative potentials (with the start of the second reduction wave at –0.6 V) to water accompanied by an increase in *n* [202]. Similar results can be seen for **1094**, which was the precursor for **1094-N**, albeit this material had a much higher activity towards the ORR than **130614-2**. Oxygen groups on the surface of the catalyst precursor have a positive effect on the N doping as the carbon atoms bonded to oxygen are more easily substituted than those in a compact carbon lattice [216].

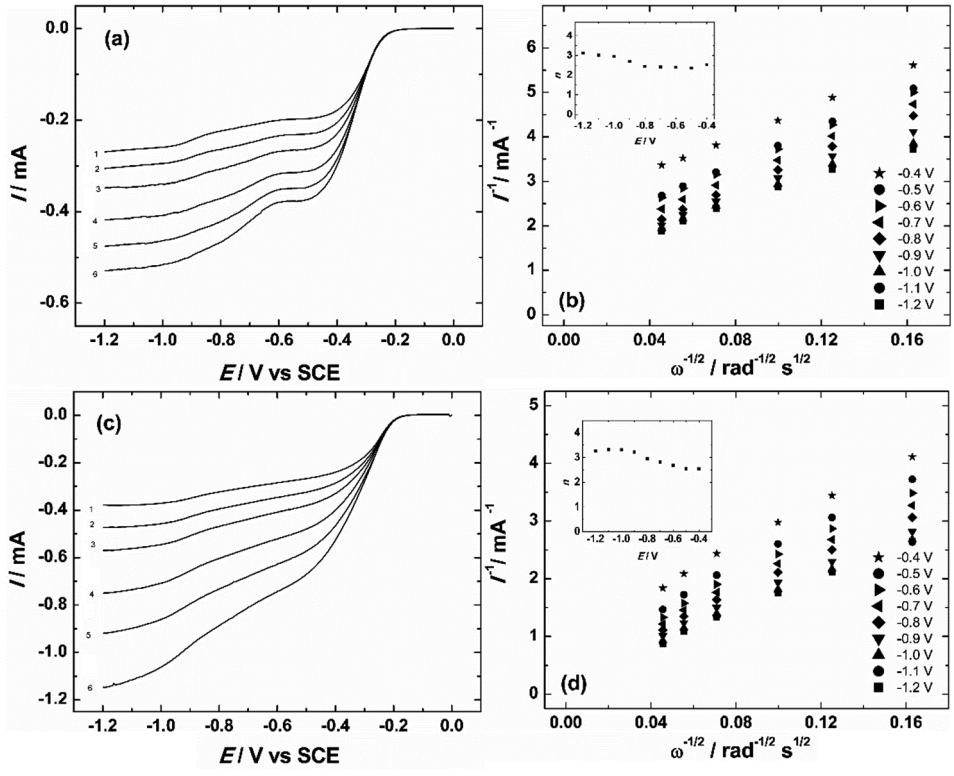


**Figure 20.** RDE voltammetry curves for oxygen reduction on (a) undoped **130614-2** and (c) undoped **1094** modified GC electrodes in $O_2$-saturated 0.1 M KOH. $\nu$ = 10 mV $s^{-1}$, $\omega$ = (1) 360, (2) 610, (3) 960, (4) 1900, (5) 3100 and (6) 4600 rpm. Koutecky-Levich plots for oxygen reduction on (b) **130614-2** and (d) **1094** modified GC electrodes in 0.1 M KOH. Inset shows the potential dependence of *n*.

Figure 21a shows the RDE results obtained for material **130614-2** doped using DCDA. The onset potential has shifted to –110 mV vs SCE, showing a marked increase in activity towards ORR and the presence of a new type of active site on the material. The nitrogen-doped active sites are known to weaken to O=O bond and create a large positive charge on the neighbouring carbon atoms and change the adsorption mode of $O_2$ molecules on the carbon material from end-on to side-on adsorption [208], both of which increase the ORR activity. The doped catalyst also shows much increased reduction current densities along with a plateau forming on negative potentials, indicating a diffusion-limited process and much higher electrocatalytic activity towards the ORR than the undoped CDC. Extra-polating the K-L plots (Figure 21b) gives an intercept near zero, thus the reaction is almost diffusion-limited with a small kinetic component. The value of *n* is close to 4 on the whole plateau, so oxygen reduction undertakes the 4-electron pathway on this material. The ORR polarisation curves for **1094-N** are shown on Figure 21c. The overall activity of this catalyst was very similar to the material synthesised

from **130614-2**, which is interesting as the base materials had very different activities and as extent of the nitrogen doping is very different (5.25 at.% vs 0.7 at.%) in the bulk of the material. The K-L plots (Figure 21d) show a diffusion limited process and the value of *n* was near 4 in the whole studied potential range, so the $O_2$ is believed to reduce via the 4-electron pathway on this catalyst with little to no $H_2O_2$ formed. The values of *n* exceeding 4 are due to the highly porous and uneven surface of the modified electrode. This shows that the nitrogen amount in the lattice of these materials in the bulk has very little effect on the ORR activity, as there was a large difference in the bulk nitrogen contents. The surface total nitrogen content also seemingly has a small effect, as **13-N** has over twice as much nitrogen species on the surface of the material than **1094-N** (3.6 at.% vs 1.7 at.%) according to the XPS analysis, yet the activity is very similar. The small difference in the activities of the doped catalysts when compared to the undoped ones also reveals that activity of an undoped CDC material is not a large factor in determining its suitability for nitrogen doping to achieve active ORR catalysts. These conclusions can be used in further works when choosing a CDC material to modify. For both catalysts the high activity is associated to high pyridinic-N and quaternary-N contents along with a very high specific surface area, facilitating a 4-electron oxygen reduction. However, as there is not yet a consensus in the scientific community, which nitrogen species is the most important in ORR, we can make no definite conclusions about the origin of this activity. The material synthesized via chlorination of titanium carbonitride (**040-N**) showed somewhat lower electrocatalytic activity towards the ORR (Figure 21e) than the materials doped with the pyrolysis method. The onset potential was at –140 mV vs SCE but the reduction currents were decreased and the K-L plots show a kinetically limited process. The *n* value did rise to nearly 4 on more negative potentials, but there were amounts of $H_2O_2$ produced at more positive potentials as the *n* value was 3.5. This is surprising as the **040-N** material had a larger average pore diameter, which should be more available to $O_2$ molecules than the micropores of **13-N** and **1094-N**. One reason for the higher activity of the materials doped using DCDA is likely their higher availability of edge sites (as seen from the etched morphology in SEM), which are known to facilitate oxygen adsorption [217] and also accountable for the lower activity can be the smaller specific surface area and the smaller pyridinic nitrogen content.

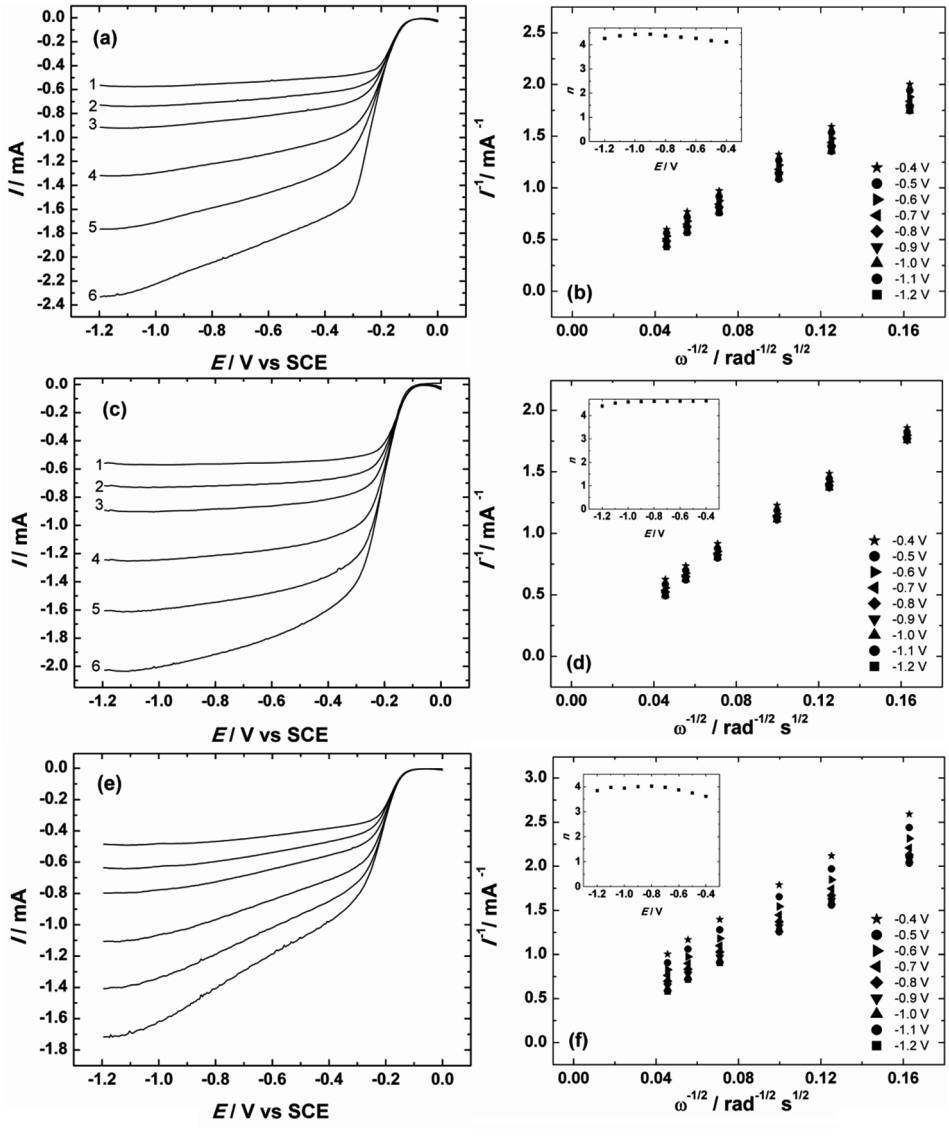


**Figure 21.** RDE voltammetry curves for oxygen reduction on (a) **13-N**, (c) **1094-N** and (e) **040-N** modified GC electrodes in $O_2$-saturated 0.1 M KOH. $\nu = 10$ mV $s^{-1}$, $\omega$ = (1) 360, (2) 610, (3) 960, (4) 1900, (5) 3100 and (6) 4600 rpm. Koutecky-Levich plots for oxygen reduction on (b) **13-N**, (d) **1094-N** and (f) **040-N** modified GC electrodes in 0.1 M KOH. Inset shows the potential dependence of $n$. $A = 0.2$ $cm^2$.

Figure 22 and Table 6 show a comparison of the activity of N-doped CDCs with a commercial Pt/C catalyst (with Tokuyama AS-4 as the binder). Compared to the 20 wt.% Pt/C, the N-doped CDCs have activity near to the commercial Pt catalyst and are thus excellent candidates for alkaline membrane fuel cell applications. As the material obtained via chlorination of titanium carbonitride, **040-N**, was much less active than the materials synthesised from CDC and DCDA, the latter process is recommended to achieve a nitrogen-doped CDC catalyst highly active towards ORR. Compared to the MWCNT/graphene composites presented in the last chapter, the progress is obvious as well, as the $j_k$ value at 0.8 V vs RHE for **1094-N** is almost triple that of 2-NC, which was the best catalyst in that study.

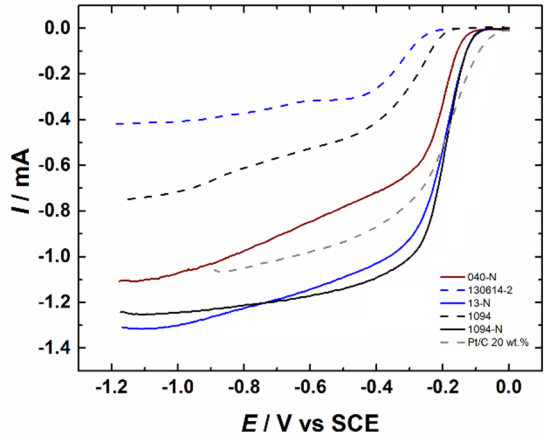


**Figure 22.** A comparison of RDE results of $O_2$ reduction on **040-N**, as-received **130614-2** and **1094**, N-doped **13-N** and **1094-N** and Pt/C modified GC electrodes in $O_2$-saturated 0.1 M KOH. $\nu = 10$ mV s$^{-1}$, $\omega = 1900$ rpm. $A = 0.2$ cm$^2$.

**Table 6.** ORR parameters of the N-doped carbide-derived carbon catalysts and Pt/C in 0.1 M KOH.

| Catalyst | $E_{onset}$ (mV vs SCE) | $E_{1/2}$ (mV vs SCE) | $j_k$ at 0.8 V vs RHE (mA cm$^{-2}$) |
|---|---|---|---|
| 1094 | –213 | –270 | – |
| 130614-2 | –272 | –364 | – |
| 040-N | –140 | –267 | 2.9 |
| 1094-N | –110 | –300 | 7.2 |
| 13-N | –110 | –260 | 5.4 |
| 20 wt.% Pt/C | –105 | –236 | 1.7 |

As discussed in the literature overview, one of the key issues with modern fuel cells is their stability. Platinum-based catalysts mostly have trouble remaining as active during the lifetime of a fuel cell as they were at the start. Figure 23 shows the results of doing 1000 cycles of $O_2$ reduction on a **1094-N** modified GC electrode. The material was cycled in CV mode and after every 100 cycles an RDE experiment was carried out. After 1000 cycles the activity of the catalyst is nearly the same than that of a pristine sample. There is little to no effect on the onset potential, while the limiting diffusion current values are somewhat smaller.

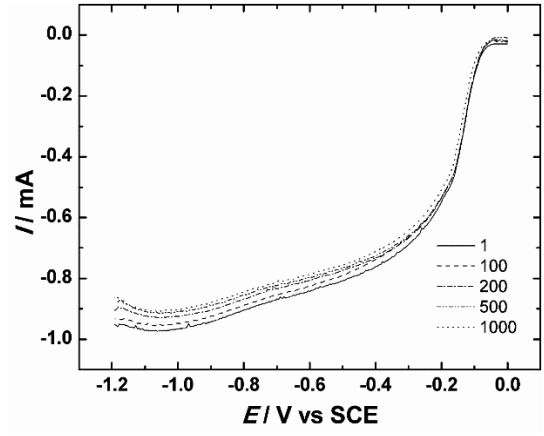


**Figure 23.** Stability of **1094-N** modified GC electrode in $O_2$-saturated 0.1 M KOH during 1000 potential cycles. $\nu$= 10 mV $s^{-1}$, $\omega$ = 960 rpm.

This study was the first done on the ORR electrocatalytic activity of N-doped carbide-derived carbon catalysts. It demonstrated the viability of CDC supports towards creating NPMCs with this simple synthesis method.

## 7.2 Electrocatalysis of oxygen reduction on transition metal and nitrogen-doped MWCNTs

The second part of the thesis deals with the electrocatalysis of ORR on Fe/Co and nitrogen-doped MWCNTs in alkaline conditions [IV,V] for either the alkaline DMFC [V] or $H_2/O_2$ AEMFC [IV] and in acidic conditions [VI].

### 7.2.1 Fe-,Co- and nitrogen-doped MWCNTs as a catalyst for alkaline membrane fuel cells

Looking at the DMFC results in chapter 7.1, while the 2-NC material bested the commercial Pt/C, it is clear that the power densities on an absolute scale are still very low (compared to, for instance, AEMFCs using $H_2$ as a fuel at the time, which

reached >100 mW $cm^{-2}$ of power density). As discussed in chapter 4.3.2, while metal-free catalysts are quite active towards the ORR in alkaline conditions, the catalyst materials incorporating both nitrogen and metals can exceed that. Inspired by the previous work on MWCNTs and composites [I, II, III] which showed a lot of promise in DMFCs [II], a strategy for incorporating Fe or Co into the catalyst material was developed [IV, V]. To introduce metal-based active sites, $FeCl_3$ or $CoCl_2$ were simply added to the synthesis mixture prior to sonication (details in section 6.5). Different amounts of salts (and different salts such as $Co(NO_3)_2$ and $Fe(OAc)_2$ in addition to the metal chlorides) were tested, with 2.5 wt.% of $FeCl_3$ (this catalyst is called Fe-NCNT-1 in what follows) or 5 wt.% of $CoCl_2$ (this catalyst is called Co/N/MWCNT-1 in what follows) in the precursor mixture showing the best results. The catalysts were then further purified to remove any unstable metal species using acid leaching and another pyrolysis step was undertaken to remove any adsorbed anions (the resulting materials are called Fe-NCNT-2 and Co/N/MWCNT-2 in what follows, respectively).

The microstructure and morphology of the Fe-NCNT-1 and Fe-NCNT-2 catalysts were studied using scanning/transmission electron microscopy (S/TEM) and SEM. Figures 24a-e display S/TEM micrographs and Figure 24f shows a SEM image of the bulk Fe-NCNT-2 catalyst. In the Fe-NCNT-1 catalyst, a lot of Fe nanoparticles were visible in the TEM image (Figure 24a). To further examine the crystallographic structure of these nanoparticles, the samples were analysed with XRD. The XRD patterns show a number of diffraction peaks attributed to Fe, $Fe_3C$ and small amounts of $Fe_2O_3$ (Figure 25) [218]. The broad XRD peak at about 26.5º is indexed to the (002) planes of the graphitic carbon. Acid leaching successfully removed a lot of the Fe and $Fe_3C$ nanoparticles as visible from Figure 24b, however, on the basis of both XRD and TEM results it is evident that leaching in hot acid does not completely remove the Fe and $Fe_3C$ particles. This is a result of the encasement of Fe/$Fe_3C$ nanoparticles into graphitic carbon shells (visible in Figure 24c, where a 20 nm particle is encapsulated in a 5–10 layered graphitic type shell). The formation of graphitised carbon structures around iron or iron carbide nanoparticles during the pyrolysis has been observed in several earlier studies [219–222], in some cases these particles catalyse the growth of CNTs [161, 223–225]. This cannot be confirmed solely on the basis of TEM images, but is a possible reason for the stability of such Fe species even during the acid treatment. The HAADF-STEM image in Figure 24d provides a different contrast, which clearly differentiates between the CNTs, Fe-containing nanoparticles and flakes of amorphous carbon. EDX mapping performed on the area indicated in Figure 24d is represented in Figure 24e. Here the uniform Fe element distribution in the sample clearly indicates that the nanoparticles are of various sizes ranging from 10 to 200 nm; these nanoparticles also tend to agglomerate. Figure 24f is a SEM image of the larger morphology of the catalyst, showing bundles of MWCNTs with some metal nanoparticles and amorphous carbon also visible.

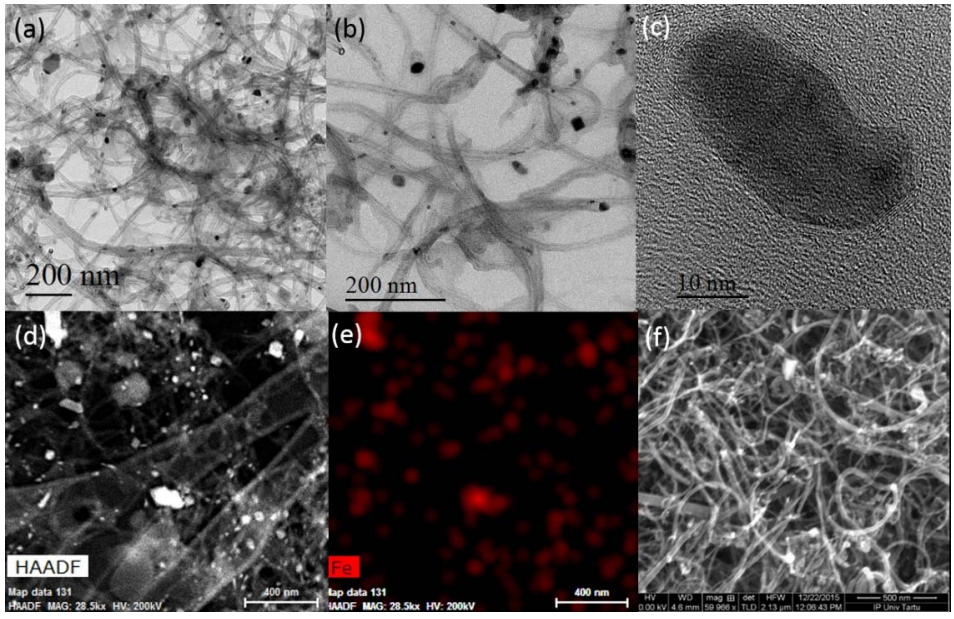


**Figure 24.** TEM images of Fe-NCNT-1 (a) and Fe-NCNT-2 (b) catalysts; High magnification TEM image of a Fe nanoparticle in Fe-NCNT-2 encapsulated by graphitic layers (c); HAADF-STEM image of the Fe-NCNT-2 catalyst (d) on which EDX mapping was performed (e); SEM image of Fe-NCNT-2 (f).

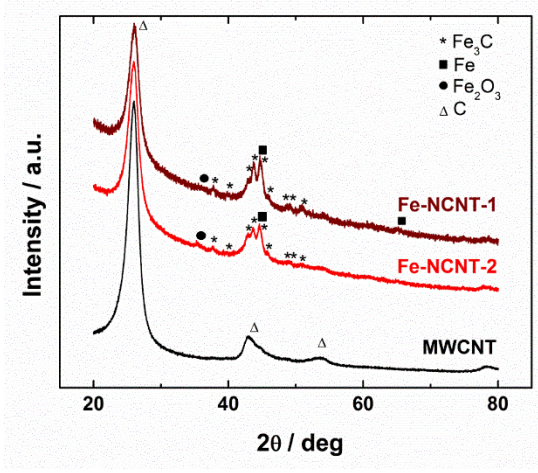


**Figure 25.** XRD patterns for Fe-NCNT catalysts and MWCNTs.

Figure 26a shows an SEM image of Co/N/MWCNT-1 and Figure 26b an image of the Co/N/MWCNT-2 material. Bright dots (Co nanoparticles) and bundles on carbon nanotubes can be seen in both Figures. After the acid leaching, the amount of metal particles in the catalyst has obviously reduced and there is practically no amorphous carbon visible in Figure 26b. According to SEM-EDX, the Co/N/MWCNT-1 catalyst contained 3.7 at.% of Co and the acid-leached material only 3.3 at.%.

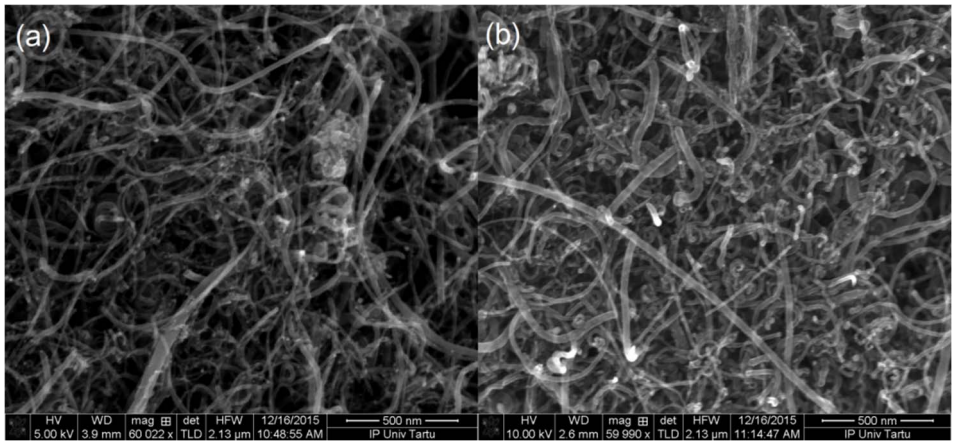


**Figure 26.** SEM images of (a) Co/N/MWCNT-1 and (b) Co/N/MWCNT-2 samples.

Figures 27 and 28 show the TEM and high-angle annular dark field scanning transmission electron microscopy (HAADF-STEM) images of the Co/N/MWCNT-1 material. Figure 27a shows bamboo-type MWCNTs along with Co nanoparticles more clearly visible on the HAADF-STEM image in Figure 27b. The size of the nanoparticles is mostly <10 nm, with some larger agglomerates also visible in Figure 27c. The inset shows the EDX spectrum used for mapping C, Co and N on the catalyst material. The element maps are shown in Figures 27d-f and reveal a uniform distribution of Co and N along with a correlation of their placement in the catalyst material, indicating an existence of Co-N sites or Co particles covered in N-doped carbon layers (active sites for ORR).

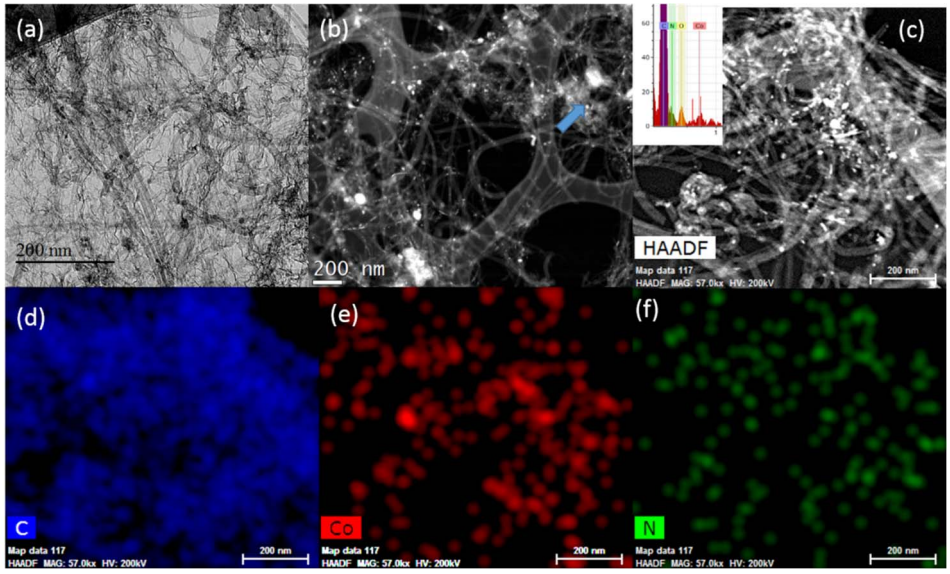


**Figure 27. (**a) TEM overview of Co/N/MWCNT-1 catalyst, (b) overview HAADF-STEM image, (c) higher magnification HAADF-STEM used for elemental EDX mapping. The inset is a part of the EDX spectra used for the mapping. (d–f) EDX elemental distribution of C, Co, and N, respectively.

Figure 28a shows a TEM overview image of the Co/N/MWCNT-2 catalyst. It is clear that the acid leaching is not successful in removing all of the metal species in the case of Co either, for which the reason can be seen from Figure 28b. Much like the Fe-based material, the Co particles are coated in a layer of graphitic carbon 5–10 nm thick. The HAADF-STEM image in Figure 28c better shows the 20–30 nm Co nanoparticles and the EDX mapping in Figure 28d also shows that the well-dispersed Co particles are covered in carbon. In addition to the particles, a uniform distribution of Co in the carbon material can also be seen, likely noting to atomically dispersed Co-N sites. The size of Co particles has increased due to the secondary pyrolysis, which gives the metal more time to agglomerate at high temperatures.

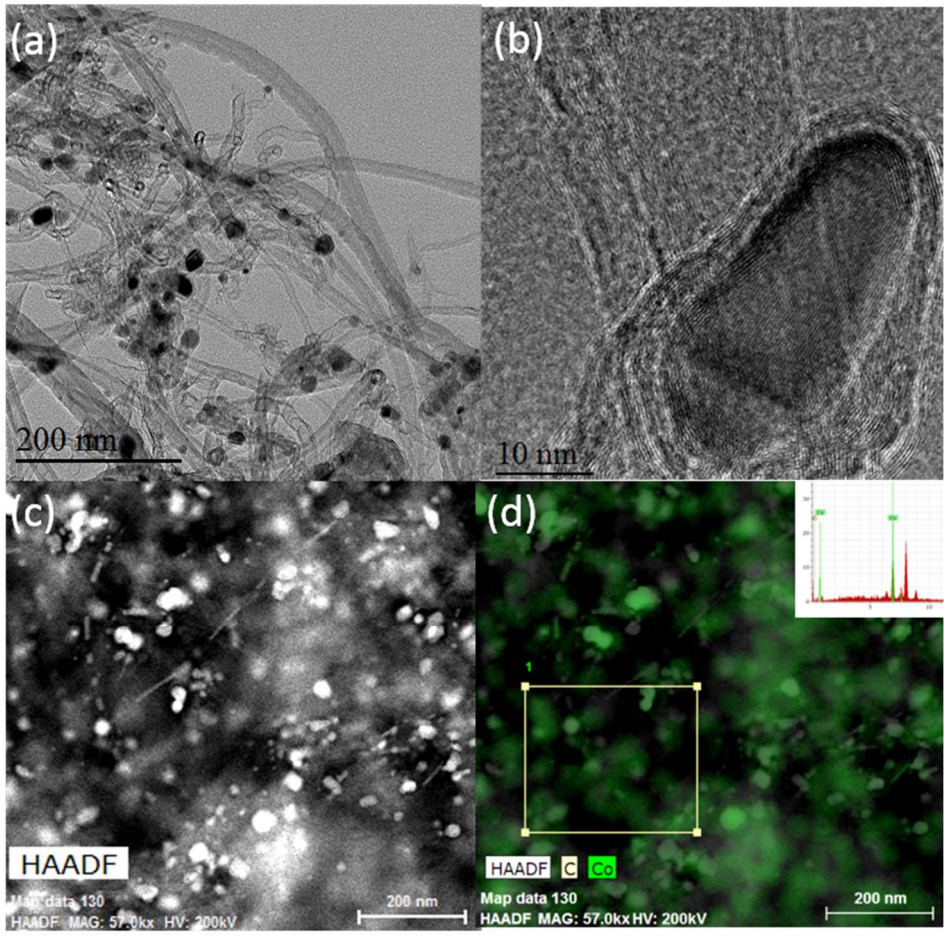


**Figure 28.** (a) TEM overview of Co/N/MWCNT-2 catalyst material, (b) HR-TEM image of Co nanoparticle after acid leaching and secondary pyrolysis, (c) higher magnification HAADF-STEM, and d) EDX elemental distribution of C and Co. The inset is a part of the EDX spectra used for the mapping.

Figure 29 shows the XRD analysis results for the Co-, N-doped materials and pristine MWCNTs. In addition to the graphitic peak at 26.5º the catalysts exhibit peaks according to the (111), (200) and (220) facets of metallic cobalt. The peak at 44º contains contribution from metallic cobalt, cobalt oxide, cobalt nitride and cobalt carbide. Clearly, there are small amounts of particulate cobalt species in different forms present even after the acid treatment.

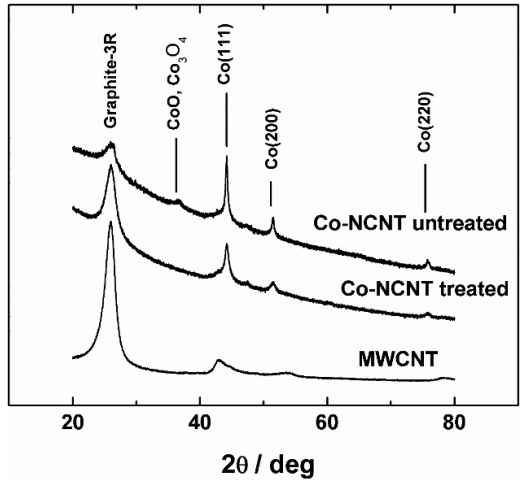


**Figure 29.** XRD patterns for Co/N/MWCNT-1 and Co/N/MWCNT-2 catalysts and MWCNT material.

The surface composition of Fe-NCNT catalysts was analysed using XPS. The XPS survey spectrum (Figure 30a) shows the presence of C, N and O in the catalyst. The total N content on Fe-NCNT-2 catalyst surface was estimated to be 3.3 at.%. To characterise the elemental surrounding of nitrogen atoms, the N1s peaks of the core-level spectrum (Figure 30b) were deconvoluted to four symmetrical peaks as in previous chapters. In the final catalyst, Fe-NCNT-2, the largest fraction of N (45%) is in pyridinic configuration, which has been proposed as one of the most active centres for oxygen electroreduction on N-doped carbon materials, along with the graphitic nitrogen (17%) [161,226]. The as-prepared catalyst Fe-NCNT-1 also contains mostly pyridinic N (47%), but also high amount of graphitic N (37%). The high-resolution spectra in the C1s region (Figure 30c) reveal the presence of the following carbon species: C=C (284.3 eV), C–C (285.1 eV), C–O (286.6 eV), C=N (285.3 eV) and C–N (283.9 eV), along with small amounts of C=O (287.8 eV), O–C=O (288.7 eV) and carbonates (290 eV) [54–56]. Only small amount of Fe could be detected by XPS, 1.6 at.% in Fe-NCNT-1 and 0.26 at.% in Fe-NCNT-2 catalysts, indicating that Fe is partly dissolved in hot acid. The Fe2p XPS peaks are too low for accurate determination of Fe species; however, the main peak is located at rather high binding energy (BE), >710 eV, suggesting that surface Fe is in cationic form. Most likely, metallic Fe and $Fe_3C$ cannot be detected by XPS, because Fe and $Fe_3C$ particles are encapsulated in carbon. The inelastic mean free path for C1s photoelectrons is 2 nm in graphite (2.7 nm theoretical for carbon). A rough estimate for sampling depth ($\lambda$=3, 95% of the signal) would be from 6 to 8 nm. That said, the contribution of surface atoms to the signal is far greater than from deeper layers. Meaningful quantitative information would originate from up to 3–4 nm depth [227]. As such, the graphitic layers of carbon might mask a lot of the Fe signal.

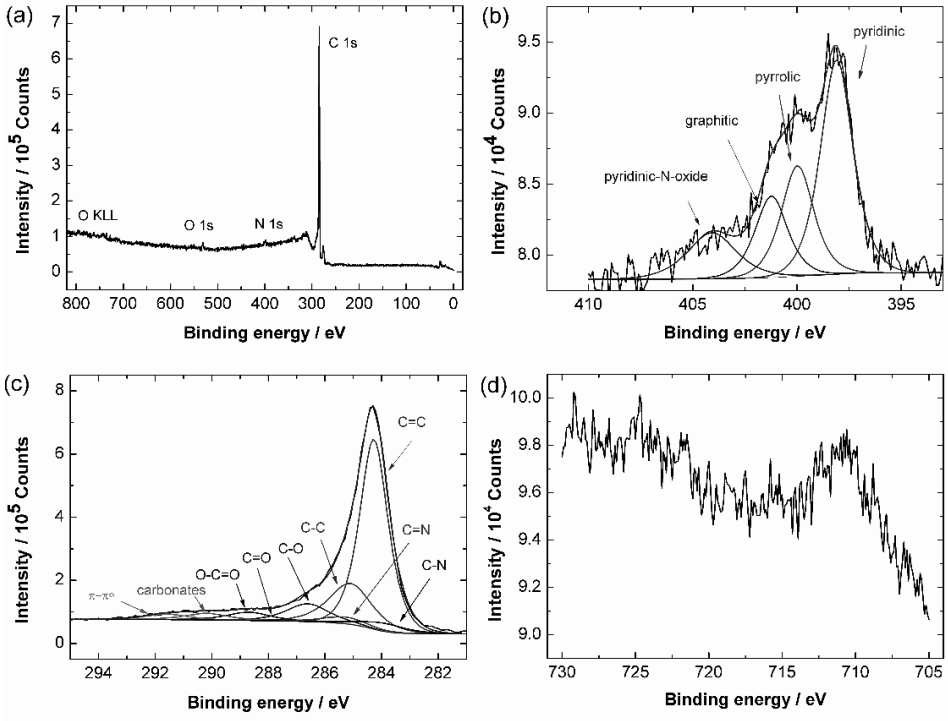


**Figure 30.** XPS survey spectrum (a) and high-resolution XPS spectra in the N1s (b), C1s (c) and Fe2p (d) regions for Fe-NCNT-2 catalyst.

XPS analysis was also conducted with the Co/N/MWCNT catalysts. The XPS spectra are given in Figure 31. The overview spectrum once again shows four characteristic peaks: C1s (284.8 eV), O1s (532.1 eV), N1s (398.2 eV) and Co2p (780 eV). The Co/N/MWCNT-1 catalyst contained 3.3 at.% of nitrogen on the surface, from which the relative concentration of pyridinic-N constitutes 51%, quaternary (graphitic) N 18%, pyrrolic-N 23% and pyridine-N-oxide 8%. For the acid treated Co/N/MWCNT-2 catalyst material, the total nitrogen content was reduced to 2.5 at.%, from which the relative concentration of pyridinic-N constitutes 42%, quaternary (graphitic) N 23%, pyrrolic-N 18% and pyridine-N-oxide 17% showing that acid treatment has no remarkable effect on the distribution of different nitrogen moieties on the surface of the catalyst, but does somewhat decrease the total N content, likely due to oxidation and removal of some of the amorphous carbon. The Co content for Co/N/MWCNT-2 was determined to be 0.8 at.%.

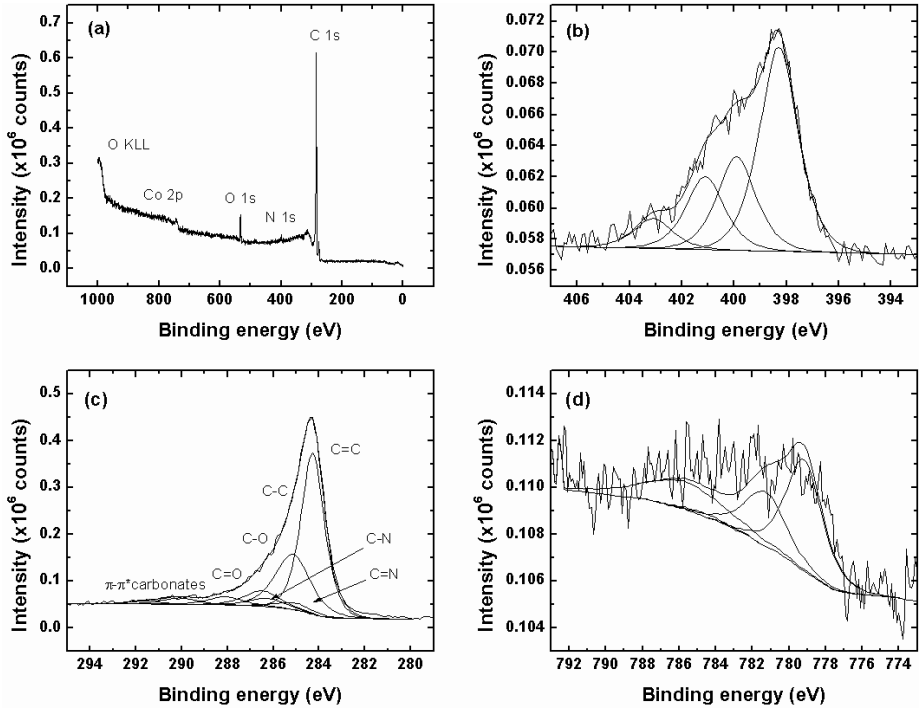


**Figure 31.** XPS survey spectrum (a) and high-resolution XPS spectra in the N1s (b), C1s (c) and Fe2p (d) regions for Co/N/MWCNT-1 catalyst.

Next, the RDE method was used to compare the pristine CNTs, N-doped MWCNTs as well as Fe-NCNT-1 and Fe-NCNT-2 to 60 wt.% Pt/C (the catalyst used as a comparison in the DMFC tests) with the results given in Figure 32 and Table 7. The GC electrodes were coated with 20 µl of a 1 mg ml$^{-1}$ dispersion of the catalyst materials. The dispersion also contained 0.25% of Fumatech FAA3 ionomer (the same ionomer was used in the DMFC). The Fe-NCNT-1 catalyst has rather high ORR activity, the $E_{onset}$ being –135 mV and $E_{1/2}$ –310 mV vs SCE. These values are about 25 mV more positive than those of metal-free N-doped CNTs. After the acid treatment, the ORR activity of the catalyst decreased (data not shown), but following the second pyrolysis, the ORR performance of the catalyst remarkably improved, as the $E_{onset}$ and $E_{1/2}$ shifted positive by 71 mV and 111 mV, respectively. For Fe-NCNT-2, the values of $E_{onset}$ = –63 mV and $E_{1/2}$ = –204 mV vs SCE are only 24 mV and 41 mV more negative, respectively, than those of commercial 60 wt.% Pt/C. The activity decay as a result of the acid treatment has been attributed partly to dissolving the active Fe species and partly to protonation of N centres and subsequent adsorption of anions [71,73]. However, it has also been shown that the latter can be reversed with heat-treatment or immersing in alkaline solution, therefore, it should not affect the ORR results in 0.1 M KOH [71]. Dissolution of surface Fe is also confirmed by XPS, where no Fe was detected in acid-treated material before second pyrolysis. Fe signal, although much lower, appeared again after second heat-treatment, which explains

the higher ORR activity of Fe-NCNT-2. This increase has been proposed to be due to creating some new active sites [53] or formation of Fe clusters near to Fe–$N_x$ sites [220].

The same method was used to study the Co/N/MWCNT materials, however the ionomer in this case was Tokuyama AS-4 (the same as in the AEMFC test), with a concentration of 0.25% in the 1 mg $ml^{-1}$ dispersion used to coat the GC electrodes with the studied catalysts. For both Co/N/MWCNT catalysts, a significant positive shift is seen in comparison with the NCNT (doped using only DCDA, but otherwise the same method) catalyst. The effect of acid treatment and second pyrolysis is also immediately apparent, with both the $E_{onset}$ and $E_{1/2}$ shifting to the positive side. The origins of the high activity of these catalysts are the same as for the Fe-based ones: Co-$N_x$ sites and particulate Co species covered in graphitic N-doped carbon layers are formed during the pyrolysis, which have an increased electrocatalytic activity towards the ORR when compared to NCNT. In addition to the Co covered in carbon overlayers, it has been found that Co nanoparticles containing Co-Co bonds with a length of 4 Å can bind $O_2$ molecules effectively and even split the O=O bond without the presence of any Co-$N_x$ sites [228,229]. This is also witnessed here as the acid treatment has less of an effect on the Co-based catalyst (during the acid treatment, these "bare" cobalt species are obviously leached out and no longer play a role in Co/N/MWCNT-2). In addition to this, morphological changes in the catalyst during doping, acid treatment and re-pyrolysis also take place and change the ORR activity. During the second heat treatment, the size of Co particles grew (as visible from the microscopy) and the carbon overlayer also grew thicker (this was also noticed for the Fe-based material). The number of carbon overlayers has been suggested as an important activity descriptor in such catalysts as it changes the free energy of the intermediates of ORR, thereby also changing the activity of the catalyst [75].

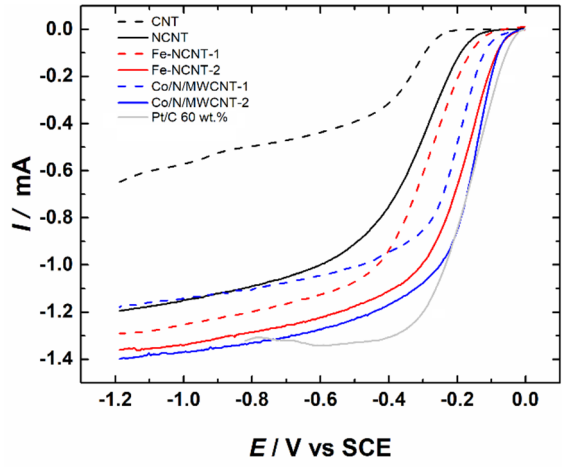


**Figure 32.** ORR polarisation curves for MWCNTs, metal-free N-doped CNTs, Fe/Co-containing N-doped CNTs and a commercial Pt/C catalyst in 0.1 M KOH. $v$ = 10 mV $s^{-1}$, $\omega$ = 1900 rpm.

**Table 7.** ORR parameters of the pristine CNTs, Fe-, Co- and/or nitrogen-doped MWCNTs and Pt/C in 0.1 M KOH.

| Catalyst | $E_{onset}$ (mV vs SCE) | $E_{1/2}$ (mV vs SCE) | $j_k$ at 0.8 V vs RHE (mA cm$^{-2}$) |
|---|---|---|---|
| CNT | –270 | –391 | 0 |
| NCNT | –162 | –341 | 1.0 |
| Fe-NCNT-1 | –135 | –310 | 1.7 |
| Fe-NCNT-2 | –63 | –204 | 7.9 |
| Co/N/MWCNT-1 | –98 | –241 | 5.6 |
| Co/N/MWCNT-2 | –63 | –168 | 12.4 |
| 60 wt.% Pt/C | –39 | –163 | 15.0 |

RDE polarisation curves were recorded at varying rotation rates to study the Fe-NCNT-2 material with the K-L analysis (Figure 33). The slightly inclined current plateaus observed could be due to porosity of the material that causes the potential-dependent $O_2$ penetration depth inside the catalyst layer or by inhomogeneous distribution of active sites on the electrode [230]. Somewhat higher reduction current densities than theoretical ones for a 4-electron reduction of $O_2$ might arise from slightly non-laminar flowing conditions due to the rough electrode surface and catalyst porosity as the RDE theory expects the electrode to have a thickness of 1–10 μm [231]. The RDE data was analysed using the K-L equation (10). The K-L plots derived from the RDE data in Figure 33a are presented in Figure 33b. From the slopes of these plots, the *n* value was calculated (inset of Figure 33b). It is evident that the value of *n* does not depend on the potential and is close to 4, which implies that $O_2$ is fully reduced to water. This is in accordance to previous results of the ORR studies using Fe-containing CNTs in alkaline solutions [22,26,35]. A low peroxide yield is an important prerequisite for the application of the catalyst in fuel cells, as peroxide is known to induce the degradation of the membrane, especially in the presence of Fe [64]. It should be noted that a rather low catalyst loading on the electrode (100 μg cm$^{-2}$) was used. Considering this the Fe-NCNT-2 shows remarkably high electrocatalytic activity as the mass activity (MA – kinetic current per mass of the catalyst on the electrode) of this catalyst at 0.8 V vs RHE is 65 A g$^{-1}$. The MA of commercial 60% Pt/C is only about two times higher (120 A $g^{-1}_{catalyst}$, e.g. 200 A $g^{-1}_{Pt}$). For Fe-NCNT-1 and NCNT the values of MA are lower, 12.6 and 7.0 A g$^{-1}$, respectively.

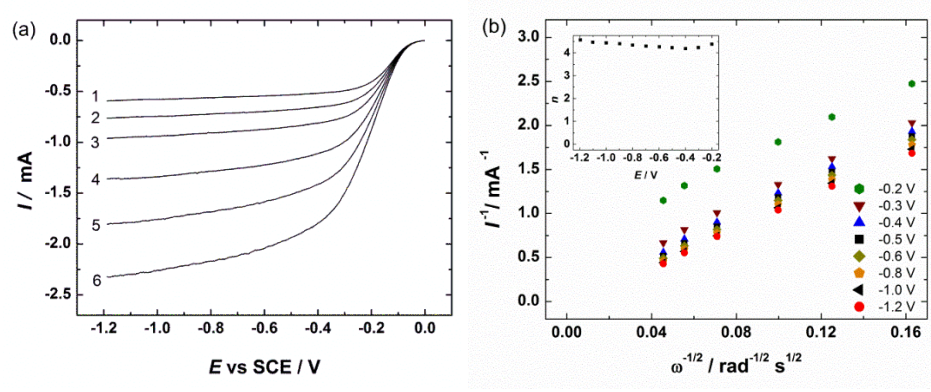


**Figure 33.** (a) ORR polarisation curves for Fe-NCNT-2 catalyst in 0.1 M KOH at various electrode rotation rates: (1) 360, (2) 610, (3) 960, (4) 1900, (5) 3100 and (6) 4600 rpm. $v = 10$ mV s$^{-1}$. (b) Koutecky-Levich plots for $O_2$ electroreduction derived from data presented in (a). Inset displays the dependence of $n$ on electrode potential.

Comparison of the ORR polarisation curves of Fe-containing catalysts with those of metal-free CNTs reveals that the presence of Fe in the pyrolysed material enhances the ORR activity of the catalyst. As the XPS results have indicated that Fe-NCNT-2 material also contains a large amount of pyridinic and graphitic nitrogen, it is expected that part of the ORR activity is due to these centres. However, as the activity of Fe-NCNT-2 surpasses that of metal-free N-doped CNTs (Figure 34), it is also assumed that there must be some other, probably Fe-containing centres available. To confirm this, the ORR on Fe-NCNT-2 was studied in the presence of cyanide anions, which are known to coordinate strongly with iron, thereby poisoning these centres [232–234]. Figure 34 shows that adding $CN^-$ remarkably decreases the ORR activity of the catalyst, as the polarisation curve shifts negative ($\Delta E_{1/2} = 75$ mV) and diffusion-limited current decreases slightly. This suggests that Fe-$N_x$/C centres play an important role in oxygen reduction electrocatalysis on Fe-NCNT-2 catalyst. A similar conclusion has been reached previously in many works, as reviewed by Masa et al. [235]. DFT calculations have indicated that improved catalytic activity of carbon shell could arise from the electron transfer from Fe particles to carbon surface, which leads to a decreased local work function [236]. It can be further decreased by doping N atoms into carbon lattice [236], however, catalysts with very low or zero nitrogen content containing carbon-coated $Fe_3C$ particles have also displayed rather high ORR activity [222]. It has been recently concluded and supported by DFT calculations that Fe/$Fe_3C$ nanoparticles promote the activity of the neighbouring Fe–$N_x$ sites [220]. Therefore, it is likely that the ORR may also occur on encapsulated Fe and/or $Fe_3C$ particles in Fe-NCNT catalysts. This is supported by the fact that the value of MA for Fe-NCNT-2 in the presence of $CN^-$ is about 12.4 A g$^{-1}$, still higher than that of metal-free NCNTs. The XPS results also suggest that the decrease of the activity of Fe-NCNT-1 after acid treatment can be related to

dissolution of $Fe/Fe_3C$ nanoparticles, as proposed in ref. [220]. After the second heat treatment, new active sites are either revealed from under the soluble or oxidised species or created during the pyrolysis process, increasing the activity again.

An important characteristic of the ORR catalysts from the practical point of view is their methanol tolerance, which is essential for application in DMFCs (as in this study), where methanol may pass across the membrane from the anode compartment. The methanol tolerance test showed that even the methanol concentration as high as 3 M did not affect the shape of the ORR polarisation curves of Fe-NCNT-2 catalyst, indicating a remarkable tolerance to the presence of methanol (Figure 34).

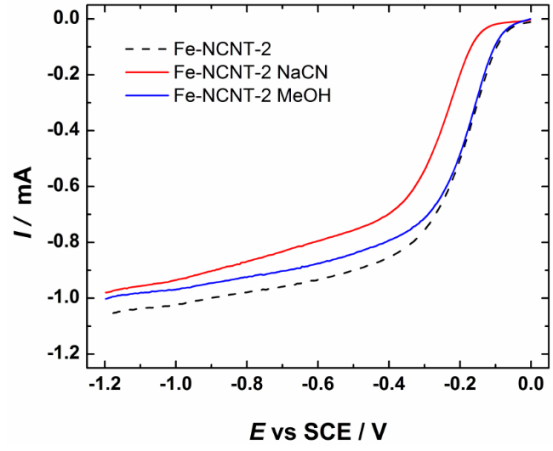


**Figure 34.** ORR polarisation curves for Fe-NCNT-2 catalyst in 0.1 M KOH in the presence of 3 M MeOH (blue curve) and 10 mM NaCN (red curve). $\nu = 10$ mV $s^{-1}$, $\omega = 960$ rpm.

A similar K-L study as for the Fe-based materials was also conducted for the Co-derived catalysts (Figure 35). Similar to the Fe-NCNT materials, the *n* values are near 4 in the whole range of potentials studied for Co/N/MWCNT-2 and the extrapolation of the K-L plot to y-axis gives an intercept near zero, meaning that the process was entirely under diffusion control. The optimal Co surface content in Co-N-C materials has been quoted to be 0.86 at.% [237], 0.98 at.% [238] or 1.0 at.% [239] in the literature thus far, so the optimal range is likely between 0.8–1.0 at.% (Co/N/MWCNT-2 contained 0.8 at.% of Co on the surface as determined by XPS). It is likely that other synthetic methods might be able to increase this value without the agglomeration of surface (and thus atomically disperse) Co to nanoparticles, but it seems that with the current synthesis methods this is the optimal value.

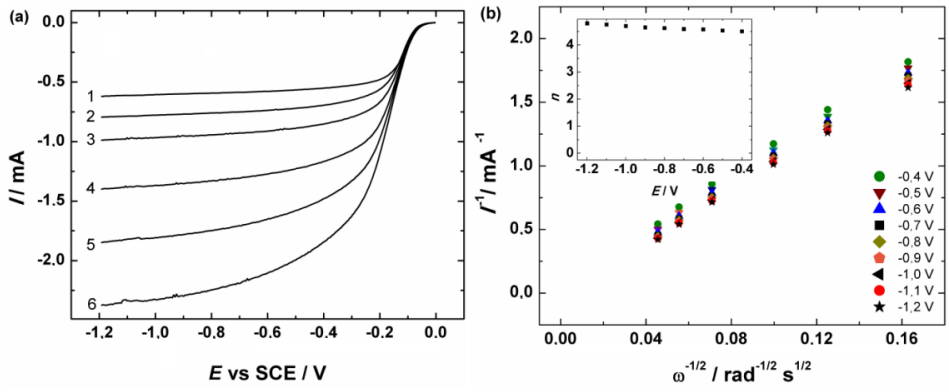


**Figure 35.** (a) ORR polarisation curves for Co/N/MWCNT-2 catalyst in 0.1 M KOH at various electrode rotation rates: (1) 360, (2) 610, (3) 960, (4) 1900, (5) 3100 and (6) 4600 rpm. $\nu$ = 10 mV $s^{-1}$. (b) Koutecky-Levich plots for $O_2$ electroreduction derived from data presented in (a). Inset displays the dependence of $n$ on electrode potential.

The second key issue, durability, was also studied on both the Fe- and Co-containing N-doped catalysts. The Fe-NCNT-2 catalyst was subjected to a short-term durability testing (Figure 36a). The results indicated that this material is highly stable in alkaline solution, as the RDE polarisation curves before and after 1000 potential cycles in $O_2$-saturated 0.1 M KOH solution are almost identical. A small decrease in the limiting current density (about 0.01 mA) can be noticed and the kinetic current at –0.2 V decreases by only 8.6%. In the case of Co/N/MWCNT-2, the results were much the same, as seen on Figure 36b. During the 1000 potential cycles in the same range there was no change in the onset potential and very little change in the limiting current values.

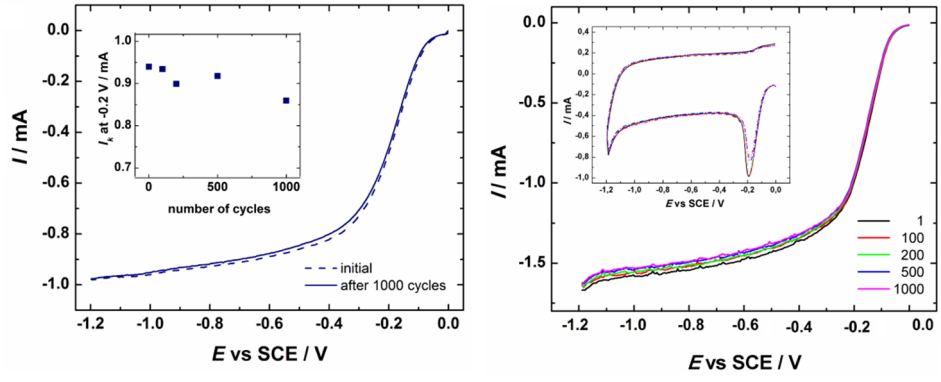


**Figure 36.** (a) ORR polarisation curves for Fe-NCNT-2 catalyst in 0.1 M KOH before and after the stability test. $\nu$ = 10 mV $s^{-1}$, $\omega$ = 960 rpm. Inset shows the change of the kinetic current calculated at –0.2 V vs SCE during potential cycling. (b) RDE polarisation curves for oxygen reduction on Co/N/MWCNT-2 at a scan rate of 10 mV $s^{-1}$ for 1, 100, 200, 500, and 1000 potential cycles in $O_2$-saturated 0.1 M KOH solution. $\nu$ = 10 mV $s^{-1}$, $\omega$ = 1900 rpm with the inset showing CV curves at 100 mV $s^{-1}$.

After success in the preliminary RDE tests, the Fe-NCNT-2 catalyst was used as the cathode in an alkaline DMFC with a Fumatech FAA3 membrane. The polarisation and power density curves are presented in Figure 37, normalised to both the fuel cell area (Figure 37a–b) and cathode catalyst mass (Figure 37c–d).

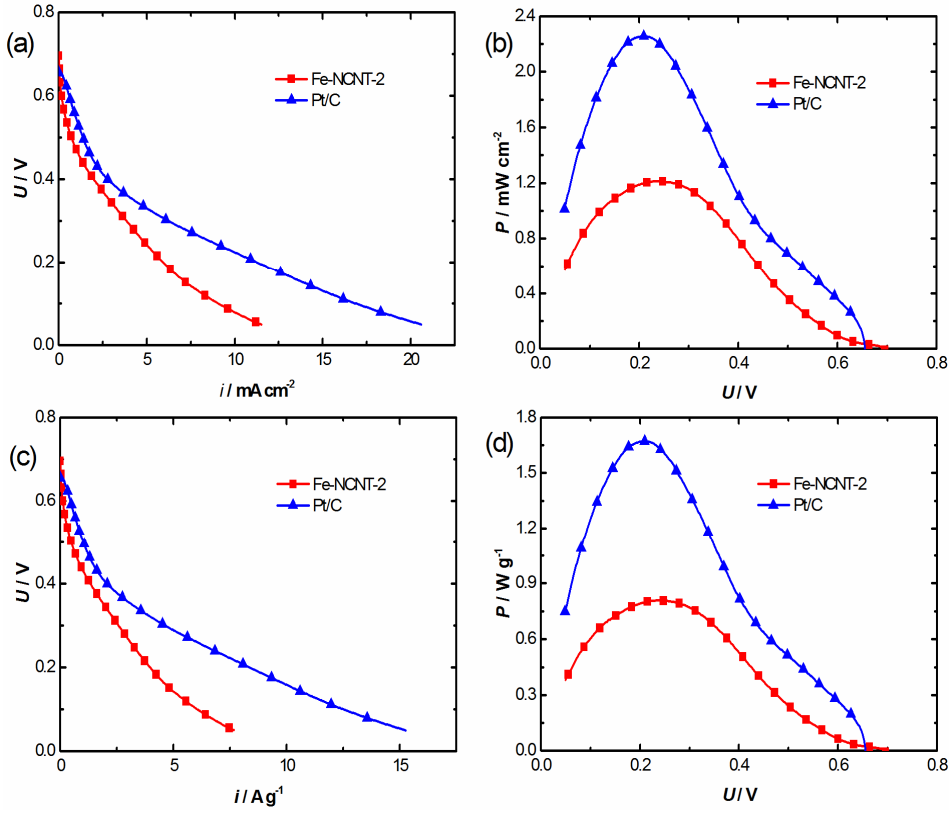


**Figure 37.** Fuel cell performance of Fe-NCNT-2 (1.50 mg $cm^{-2}$) and Pt/C (1.35 $mg_{Pt}$ $cm^{-2}$) catalysts in alkaline DMFC with a Fumatech FAA3 membrane: 1 M methanol at the anode (0.2 ml $min^{-1}$) and pure dry $O_2$ (200 ml $min^{-1}$) at the cathode at 50 °C. (a) Current density and (b) power density normalised to fuel cell area. (c) Current density and (d) power density normalised to the mass of Pt or Fe-NCNT-2 at the cathode.

It is immediately clear that the Fe-NCNT-2 catalyst performs somewhat worse than commercial Pt/C at high cell voltage (>0.4 V). At lower voltages, its performance is reduced, which could be due to the less alkaline environment in the fuel cell compared to the RDE cell as the membrane is carbonated by $CO_2$ produced at the anode [240,241]. Methanol tolerance of Fe-NCNT-2 is apparent from the high open circuit voltage (OCV) of 0.70 V compared to 0.66 V for Pt/C. Furthermore, due to the high OCV also the maximum power density is reached at a higher potential than with Pt/C, which is important for applications requiring a minimum voltage to work. Maximum power densities for Fe-NCNT-2 and Pt/C are 1.21 mW $cm^{-2}$ at 0.24 V and 2.26 mW $cm^{-2}$ at 0.21 V, respectively. These values

show improvement compared to earlier measurements in a similar alkaline fuel cell without aqueous alkaline electrolyte [211,213,242]. With an aqueous alkaline electrolyte added to fuel solution, a ten-fold increase can be expected [243]. However, we avoided using alkaline solution as it negates the advantage of a solid electrolyte membrane by introducing free cations into the system, which can precipitate with carbonate ions produced from the anode reaction [244]. Finally, the power densities are small compared to acidic DMFCs [245,246] meaning that the lower conductivity of $OH^-$ compared to $H^+$ and membrane properties still limit the performance of the fuel cell.

The mass-specific maximum power density normalised to the cathode catalyst are 0.81 and 1.67 W $g^{-1}$ for Fe-NCNT-2 and Pt/C (only Pt mass included), respectively. This means that the mass activity of Fe-NCNT-2 is 48% of that of Pt and considering that it is made from inexpensive and abundant raw materials, this emphasises its role as an excellent replacement for Pt with higher loadings. The relative performance of Fe-NCNT-2 compared to Pt/C is better than in the RDE measurements. This could be due to mass transfer enhancement through large secondary pores that CNTs tend to form in a fuel cell catalyst layer with the FAA3 ionomer as was shown in previous studies [170,II].

Figure 38 shows the results achieved in a $H_2/O_2$ fuel cell with a Tokuyama A201 membrane using either the Co/N/MWCNT-1 catalyst, a 20 wt.% Pt/C catalyst from E-TEK or the Tanaka 46.1 wt.% Pt/C as the cathode (more details in section 6.9). The Co/N/MWCNT showed higher performance (116 mW $cm^{-2}$) than the CoPc/MWCNT (105 mW $cm^{-2}$) and E-TEK 20% Pt/C catalyst (115 mW $cm^{-2}$) and close to the 46.1 wt.% Tanaka catalyst (133 mW $cm^{-2}$).

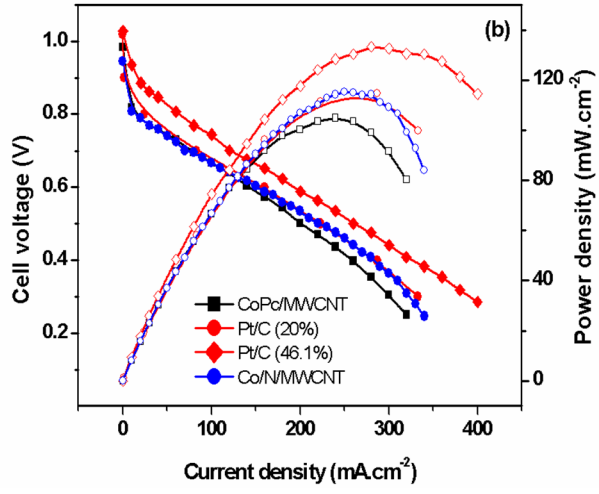


**Figure 38.** AEMFC performance of MEAs with Co/N/MWCNT along with CoPc/MWCNT, E-TEK 20% Pt/C and Tanaka 46% Pt/C catalysts based cathodes using Tokuyama's A201 series anion exchange membrane.

The work on M,N-doped MWCNTs presented here had an important impact in demonstrating the viability of NPMCs as a catalyst in alkaline membrane fuel cells. It showed the effectiveness of transition metal and nitrogen doping to increase the performance of carbon-based catalysts to a level over Pt/C in both alkaline DMFCs and AEMFCs. In addition to that, it laid the groundwork for further progress, as is shown in the next chapters. The synthetic process was optimised and important issues identified (such as the agglomeration of metal into particles).

### 7.2.2 Electroreduction of oxygen on Fe-/Co- and nitrogen-doped MWCNTs in acidic conditions

In addition to tests in 0.1 M KOH and in alkaline fuel cells, the activity of Fe- or Co- and nitrogen-doped MWCNTs was also studied in acidic conditions (i.e. as a replacement for Pt on the cathode of PEMFCs). Catalysts doped with only nitrogen have little activity in acidic media, however, catalysts incorporating transition metals as well are known to be a viable replacement for Pt (as discussed in chapter 4.3.1) [45,73,247–249]. Similar to alkaline media, the RDE method was employed to study the ORR activity of Fe-NCNT and Co/N/MWCNT materials in 0.5 M $H_2SO_4$. Nafion was used as the binder here, with a concentration of 0.05% in the 2 mg $ml^{-1}$ dispersion of catalyst materials. 20 µl of the dispersion was pipetted onto a GC electrode, leading to a loading of 200 µg $cm^{-2}$. A comparison between the NPMCs and 60 wt.% Pt/C is given in Figure 39. The activity of Fe-NCNT-1 and Co/N/MWCNT-1 was rather moderate: the onset potentials were 440 and 430 mV vs SCE, respectively. The treatment in acids significantly lowered the overpotential for ORR on these materials, with the onset potential shifting to 560 mV vs SCE on Fe-NCNT-2 and 520 mV vs SCE for Co/N/MWCNT-2. The reason for the positive shift here is the same as in alkaline media: soluble metal species and amorphous carbon are removed from the surface of the catalyst, leaving more active material by mass and increasing the accessibility of the active sites on the surface of it. The smaller comparative increase in the case of Co is once again due to the disappearance of Co-Co active sites in the Co/N/MWCNT catalyst, which makes the increase relatively lower. Still, as compared to Pt/C catalyst, the ORR activity of M-NCNT catalysts is considerably lower, the $E_{onset}$ being approximately 0.1 V and $E_{1/2}$ ca. 0.15 V more negative for Fe-NCNT2.

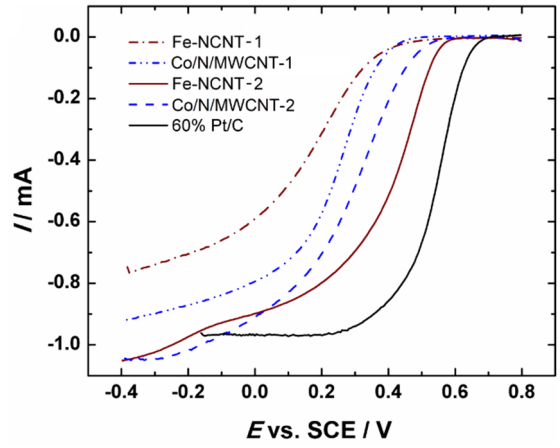


**Figure 39**. RDE polarisation curves for $O_2$ reduction on Fe-NCNT and Co/N/MWCNT catalysts and on a commercial Pt/C catalyst in $O_2$-saturated 0.5 M $H_2SO_4$. $v$ = 10 mV $s^{-1}$, $\omega$ = 1900 rpm.

A K-L study was also conducted on the M-NCNT materials in acidic conditions to further analyse the ORR on these catalysts. Figures 40b and 40d present the K-L plots corresponding to RDE data in Figure 40a and 40c, respectively, and the values of $n$ calculated from the slopes of the K-L plots are shown in the insets. In the case of Fe-NCNT-2 the intercept from extrapolating the K-L plot is over zero, which shows that even at the more negative potential values the ORR process is not diffusion-limited. Both of the catalysts show some nonlinearity in the K-L plots as well, a common occurrence with thick catalyst layers, which somewhat changes the $n$ values calculated [250]. Still, it is evident that these catalysts are different in terms of $n$ values. On Fe-NCNT-2, the reduction of $O_2$ predominantly follows a $4e^-$ pathway at all potentials studied and the main product of the ORR is $H_2O$. However, on Co/N/MWCNT-2 catalyst the value of $n$ is only *ca.* 3.1 at 0.2 V and it increases at more negative potentials up to *ca.* 3.5, indicating that a considerable amount of $H_2O_2$ is produced. This is an undesirable side product, as it can degrade the fuel cell membrane [251] and the production of peroxide decreases the efficiency of the fuel cell. $H_2O_2$ is a neutral molecule in acidic conditions compared to its ionic counterpart $HO_2^-$ ($pK_1$=11.69 at 25 °C [252]) in alkaline conditions and much more likely to desorb from the electrode because the further reduction of $HO_2^-$ in alkaline conditions is much quicker than the reduction of $H_2O_2$ to water in acid [25,45,80,86]. The nanoparticles seen in TEM images in both of the catalysts are known to have a positive effect on the stability of intermediate products on M-$N_x$ active sites (i.e. they are not as quick to desorb and react with parts of the catalyst/fuel cell) [86,233]. Thus the amount of Fe-$N_x$ sites nearby Fe/$Fe_3C$ particles could be higher than Co-$N_x$ near Co-containing particles. A further analysis of this would require a thorough X-ray absorption study, which was outside of the possibilities of the author at the time unfortunately.

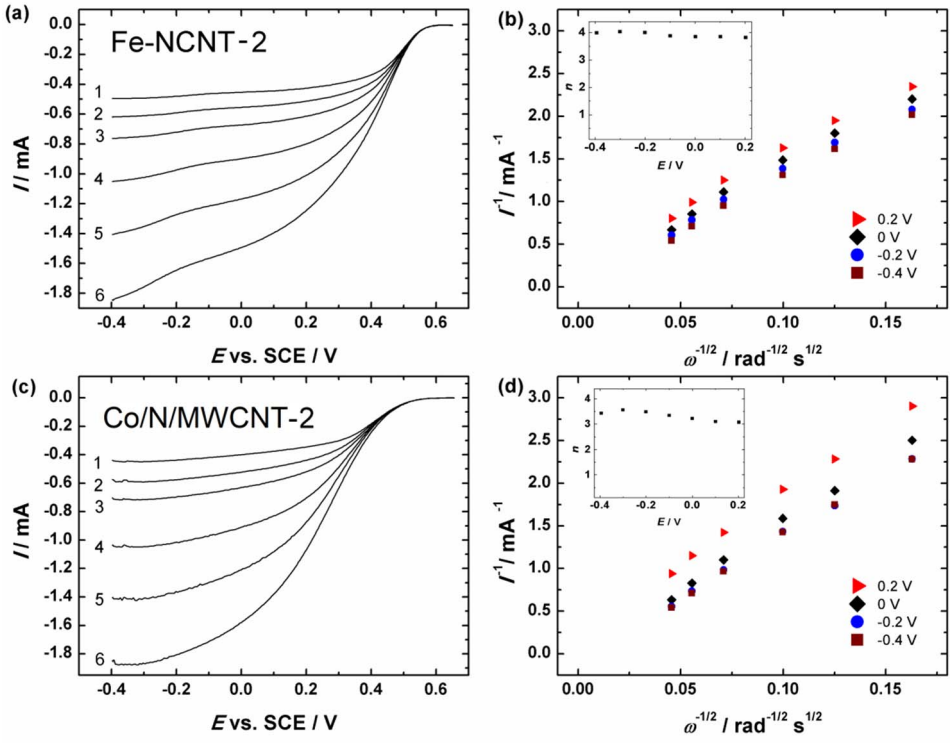


**Figure 40.** RDE polarisation curves for $O_2$ reduction on (a) Fe-NCNT-2 and (c) Co/N/MWCNT-2 catalysts in $O_2$-saturated 0.5 M $H_2SO_4$ at various electrode rotation rates: (1) 360, (2) 610, (3) 960, (4) 1900, (5) 3100 and (6) 4600 rpm. $\nu$ = 10 mV $s^{-1}$. Koutecky-Levich plots for $O_2$ reduction derived from the data presented in (a) and (c) are shown in (b) and (d), respectively. Insets display the dependence of $n$ on electrode potential.

The observation that Fe-containing catalysts are more active for ORR than their Co-containing counterparts is in agreement with several earlier studies [56,65,81]. First, the active centres formed during pyrolysis may differ for Co- and Fe-based materials. For instance, it has been found that while pyrolysing the metal-containing catalysts derived from polyaniline at 900 °C, the Co-N centres decompose and Co-Co bonds form, whereas Fe is suggested to remain as Fe-N structures [221]. The effect of Co-Co bonds on the ORR activity can be seen in numerous works, where cobalt and cobalt oxide nanoparticles catalyse the ORR without Co-$N_x$ centres. It has been found that the $O_2$ molecule binds to the Co-Co centre with length around 4 Å in a *cis* configuration, rendering the O-O bond much more easily broken and favouring the 4-electron pathway. A shorter or longer Co-Co bond means that the $O_2$ molecule binds in a *trans* configuration, which favours the 2-electron pathway [228]. However, it has recently been shown that Co-$N_x$ sites can also catalyse the ORR even without any Co-Co bonds [81]. It has also been found that Co-containing catalysts have more pyridinic-N, but Fe increases the quantity of graphitic and pyrrolic nitrogen [253], which can have its own

implications on the pathway ORR takes [53]. In addition, it has been shown that both metals can catalyse the growth of CNTs by graphitisation of dicyandiamide, Fe precursor yielding the largest carbon nanotubes with highest ORR activity and lowest peroxide production as in this case [254]. The mass activity of 60% Pt/C at 0.5 V *vs.* SCE was 110 A $g^{-1}_{catalyst}$ (183 A $g^{-1}_{Pt}$), a value still far higher than those of Fe-NCNT-2 and Co/N/MWCNT-2, which had mass activities of 5.5 and 1.1 A $g^{-1}$, respectively.

Short-term stability tests were carried out on Fe-NCNT-2 and Co/N/MWCNT-2 catalysts to test their suitability in a real fuel cell. A comparison of the RDE polarisation curves recorded before and after 1000 potential cycles in $O_2$-saturated 0.5 M $H_2SO_4$ solution (Figure 41) shows a rather significant decrease of the activity for Fe-NCNT2, as the value of $I_k$ calculated at 0.5 V decreases from 0.28 mA to 0.10 mA. Co-NCNT2 appears to be more stable, since the change of $I_k$ is negligible during potential cycling. On the other hand, a gradual decrease of the current at negative potentials was observed for Co/N/MWCNT-2, but not for Fe-NCNT-2. Low stability of Fe-containing N-doped catalysts in acidic conditions is a major drawback of NPMCs and this can be due to several reasons, such as leaching of the active metal site, oxidation by $H_2O_2$ and protonation of N centres followed by anion adsorption [255]. The first option is not very likely in this work, as Fe-NCNT-2 was pre-treated in acids that should remove the acid-sensitive metal species, however it must be noted that repetitive $Fe^{2+}/Fe^{3+}$ switching such as in this potential range is known to induce iron dissolution even from Fe-$N_x$ sites stable in acid [90,256]. Oxidation by $H_2O_2$ is possible, however, the K-L analysis (Figure 40) indicates that more $H_2O_2$ is produced by Co/N/MWCNT-2 that appears to be more stable. This may be explained by indirect mechanism involving $^{\bullet}OH$ radicals that are produced from $H_2O_2$ by $Fe^{2+}$ ions in Fenton's reaction [89,255,256]. Another viable explanation to activity decrease is anion binding to protonated N centres [71]. This is also in accordance to our results, as protonation affects the pyridinic N centres and not graphitic N and former is more abundant in Fe-NCNT-2, as suggested by XPS results. As for all carbon-based catalysts, carbon corrosion is a major cause of the deactivation also for metal-containing N-doped materials [90,256], however, it is expected to occur at more positive potentials than here (the range here is up to ca. 0.85 V vs RHE).

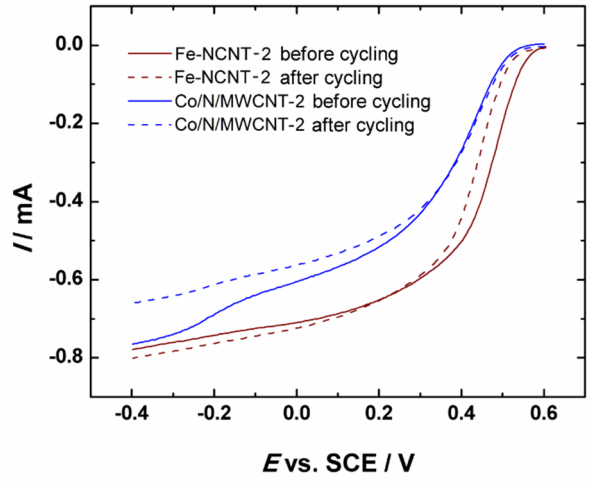


**Figure 41.** RDE polarisation curves for $O_2$ reduction on Fe-NCNT2 and Co-NCNT2 catalysts in $O_2$-saturated 0.5 M $H_2SO_4$ before and after repetitive potential cycling. $\nu = 10$ mV $s^{-1}$, $\omega = 960$ rpm.

## 7.3 Electrocatalysis of oxygen reduction on metal- (Fe or Co) and nitrogen-doped CDCs and MWCNT/CDC composites

The third part of the thesis deals with the electrocatalysis of ORR on Fe-/Co- and nitrogen-doped CDCs and MWCNT/CDC composites in alkaline conditions [VIII–X, XIV] for either the alkaline DMFC [VIII] or $H_2/O_2$ AEMFC [IX,X] and in acidic conditions for the PEMFC [XI–XIII]. The main subject here was the development of a method for doping and reducing the particle size of CDC materials using ball-milling and sonication. For this purpose, multiple variations of ball-milling (dry, wet milling and the usage of different sizes of balls) and ultrasound were used.

### 7.3.1 Fe-/Co- and nitrogen-doped CDCs as catalysts for alkaline membrane fuel cells

Iron/cobalt and nitrogen doping of the CDC materials was done with the same procedure developed in this work previously for MWCNTs [IV,V,VI], which was combined with the nitrogen doping work done on CDCs [VII]. Shortly, TiC (the same one as used in [VII]) was chlorinated by Skeleton Technologies OÜ (Estonia), which was then mixed with DCDA and either $CoCl_2$ or $FeCl_3$ and pyrolysed to create M-N-C active sites (more details are available in section 6.6). These catalysts were tested for ORR catalytic activity and then as the cathode in a DMFC and an AEMFC.

The morphological properties and microstructure of the nitrogen- and Fe-/Co-doped CDC catalysts were studied with SEM (Figure 42a,b). A characteristic area of the Fe-N-CDC sample is shown in Figure 42a, with CDC particles with a crumpled morphology of varying sizes visible. In addition to the doped CDC there are some tubular formations, which can be ascribed to the MWCNTs created from DCDA during the pyrolysis, as seen previously [IV,V,VI]. The carbon nanotubes improve the stability of the otherwise highly amorphous CDC material and also change the mass-transfer properties in the catalyst layer. The channels between larger M-N-CDC grains improve the mass transport in the catalyst layer, which is very important in fuel cell applications and the microporous structure insures efficient ORR electrocatalysis. Figure 42b shows the surface morphology of the Co-N-CDC counterpart, with the crumpled morphology more clearly visible, but overall similar morphology to Fe-N-CDC.

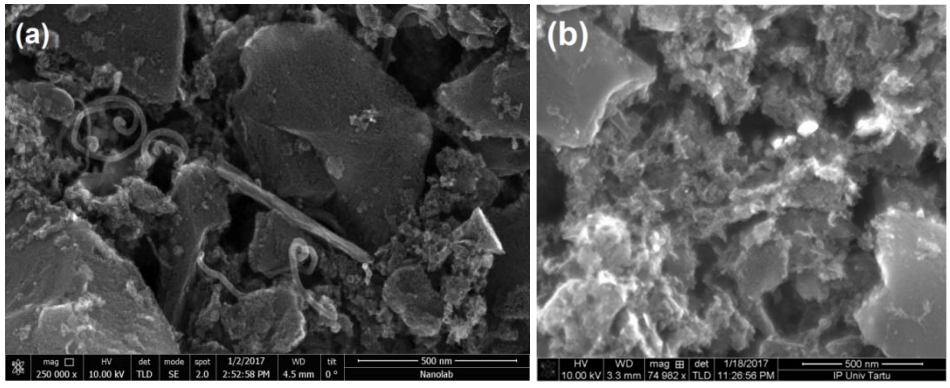


**Figure 42.** SEM images of (a) Fe-N-CDC and (b) Co-N-CDC catalysts.

$N_2$ physisorption was used to study the specific surface area and porosity of the transition metal-containing nitrogen-doped CDC catalysts. The porosity characteristics for the two catalysts are fairly similar, with the Fe-N-CDC catalyst having higher microporosity than the Co-N-CDC catalyst and a somewhat smaller total pore volume and average pore size (Table 8).

**Table 8.** Textural properties of M-N-CDC materials: BET surface area ($S_{BET}$), pore volume ($V_{tot}$), micropore volume ($V_{\mu}$) and average pore size ($d_p$).

| Catalyst | $S_{BET}$, $m^2\ g^{-1}$ | $V_{\mu}$, $cm^3\ g^{-1}$ | $V_{tot}$, $cm^3\ g^{-1}$ | $d_p$, nm |
|---|---|---|---|---|
| Co-N-CDC | 1908 | 0.834 | 1.165 | 1.22 |
| Fe-N-CDC | 1966 | 0.908 | 1.153 | 1.17 |

$N_2$ adsorption-desorption isotherms, presented in Figure 43a, have a typical shape of combined Type I and II adsorption branches, which is often found for micro-mesoporous carbon materials [257]. The N-CDC material from [VII] is also included for comparison. All three isotherms contain the hysteresis loop of Type H4 with the sharp step-down of the desorption branch at $P/P_0$ ~0.4–0.45. Comparison to N-CDC isotherm confirms that the doping with metal has no effect on the mesoporous part of the parent carbon, however, reduces the volume of micropores. Interestingly, the total pore volume is almost equal in N-CDC and M-N-CDC catalysts. With highly porous catalysts it is also very interesting to compare the pore size distributions, which are given on Figure 43b. The pore size distribution for the M-N-CDC catalysts is nearly the same, with Fe-N-CDC having somewhat more pores with a width under 1 nm and also in the 3–4 nm range. When compared to N-CDC, however, it is immediately apparent that many of the pores sized between 1 and 1.5 nm have been filled in the case of M-N-CDC catalysts. The reason is likely M-$N_x$ centres filling the pores in this size range, which could be useful for further choice of CDCs; a maximum number of pores of this size should give a larger number of M-$N_x$ sites in the resulting catalyst when using DCDA and metal salts as the doping materials. This finding is in accordance with previous studies [47] which found the optimal pore size for active sites to be between 0.5 and 2 nm, but further narrows down the range.

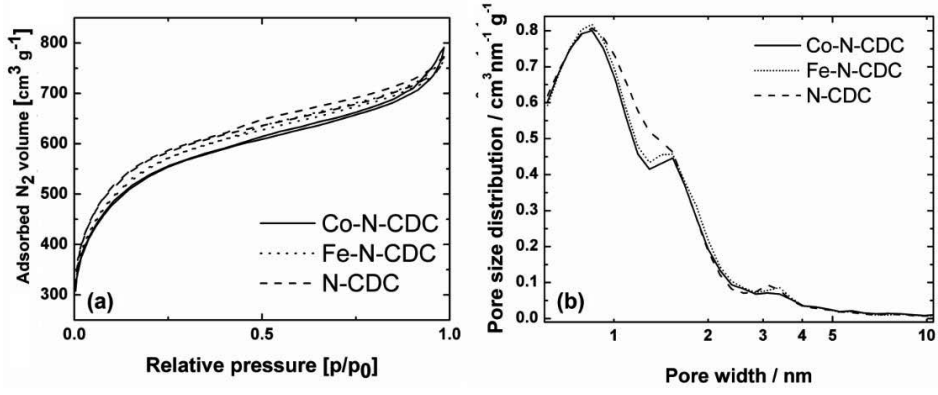


**Figure 43.** Comparison of $N_2$ adsorption-desorption isotherms (a) and pore size distributions (b) for Co-N-CDC, Fe-N-CDC and N-CDC.

SEM-EDX analysis of the Fe-N-CDC catalyst revealed that the N content in the bulk of the material was 4.1 at.% and the Fe content was 1.4 at.%. In the Co-N-CDC material, the nitrogen content was 5.3 at.% and the cobalt content was only 0.65 at.% in the resulting catalyst, however, noting a lower stability of the cobalt phases towards acid leaching. This is likely because of the smaller amount of carbon nanotubes formed during the pyrolysis step (as visible from SEM). Metal nanoparticles inside CNTs are known to be very stable towards acid treatment.

To assess the elemental composition near the surface of the M-N-CDC catalysts, polished Si plates were covered with the catalyst materials and the XPS measurements were undertaken. Figures 44a–c show the results of Co-N-CDC XPS testing and Figures 44d–f the results of the XPS analysis of Fe-N-CDC catalyst. Figure 44a presents the XPS survey spectra for Co-N-CDC, which revealed four recognisable peaks according to the BE values for C1s, N1s, O1s and Co2p. The overall content of oxygen in the surface layer of the catalyst was 1.81 at.%, while the nitrogen content was 4.19 at.% and the cobalt content 0.42 at.%. The relative content of graphitic nitrogen, which corresponds to a nitrogen atom linked to three carbons in a six-member cycle and is considered one of the nitrogen moieties most active towards the ORR was 23.2% in this catalyst. The relative content of the other active type, pyridinic nitrogen, was 50.2%, but this also includes the contribution from Co-$N_x$ sites [258]. The relative contents of two of the other types, pyrrolic-N and pyridinic-N-oxide, were 16.5% and 10.1%, respectively. The XPS survey spectrum for Fe-N-CDC material, which also consisted of four distinct peaks, is presented in Figure 44d. In this case the Fe2p peak is not very well visible as the iron content in the surface layer was only 0.14 at.%. The oxygen content was 2.23 at.% and the nitrogen content 2.51 at.% in this sample. The deconvoluted N1s XPS peak for Fe-N-CDC is shown in Figure 44e. The relative content of pyridinic-N in this catalyst was determined to be 37.6% and the graphitic-N content 23.1%, while the relative contents of pyridinic-N-oxide and pyrrolic-N were 12.1% and 27%, respectively. The high-resolution Co2p and Fe2p XPS spectra are presented in Figures 44c and 44f, but due to the serious difficulties in the deconvolution of these spectra and the low signal-to-noise ratio it was not possible to determine the exact configurations for Co and Fe. It is interesting to note that the catalyst material containing cobalt had a much larger relative content of pyridinic nitrogen than its iron-containing counterpart and both metals changed the relative contents for different types of nitrogen when compared to a similar CDC material doped with only nitrogen [VII]. However, both metals induced the nitrogen content to be much higher in the surface layer of the material, which may increase the overall ORR activity of the catalysts.

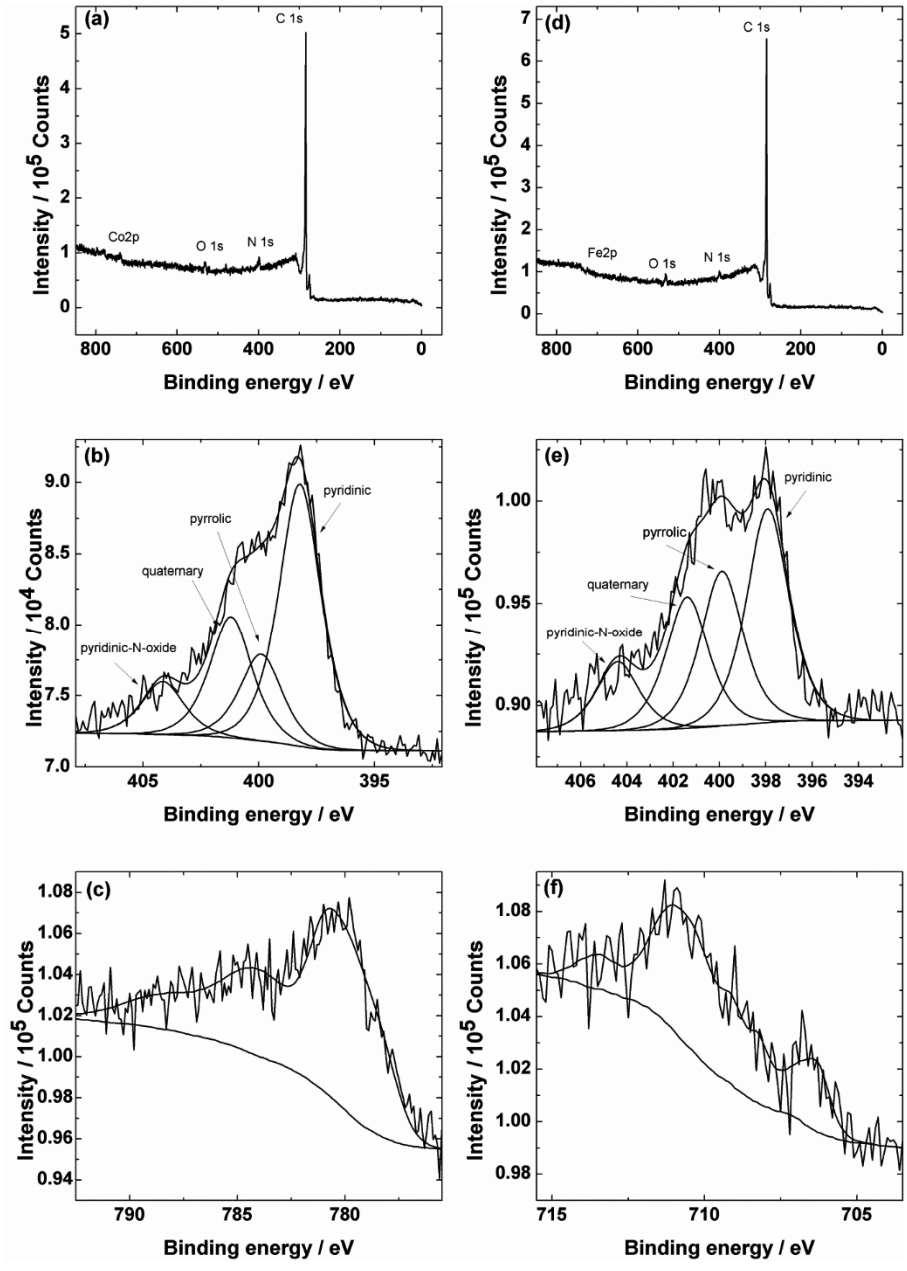


**Figure 44.** XPS wide scan spectra (a,d) and core-level spectra in the N1s (b,e), Co2p (c) and Fe2p (f) regions, for Co-N-CDC and Fe-N-CDC catalysts, respectively.

The RDE method was employed to investigate the electrocatalytic activity of transition metal-containing nitrogen-doped CDC catalysts towards the ORR in 0.1 M KOH solution. Figure 45a shows the $O_2$ reduction polarisation curves for a GC electrode modified with Fe-N-CDC catalyst. The $E_{onset}$ value for this catalyst is 79 mV vs SCE, which is 31 mV more positive than with our previously studied N-doped CDC material. This shows the effect of added transition metal on the catalyst: the Fe-$N_x$ sites and iron particles covered with nitrogen-doped graphitic layers facilitate oxygen reduction and shift the $O_2$ reduction wave somewhat more positive as compared to metal-free nitrogen-doped CDC materials. The reduction current values are also rather high for such a low catalyst loading. Figure 45b demonstrates the K-L plots derived from the ORR polarisation curves with the values of *n* shown in the inset. The *n* values were close to 4 in the whole potential range studied for both of the M-N-CDC catalysts. The values of *n* above 4 can be explained by the structure of the catalyst layer on a GC electrode being somewhat uneven and the catalyst itself being highly porous. This could lead to slightly non-laminar electrolyte solution flows in RDE mode. The electrochemical oxygen reduction behaviour of the Co-N-CDC catalyst presented in Figure 45c is very similar to that of Fe-N-CDC, with the $E_{onset}$ value being somewhat more negative on this catalyst. It is interesting that even though these catalysts have very different nitrogen and metal content on the surface, as identified by the XPS analysis, their overall electrocatalytic ORR activity is nearly the same. The surface-to-bulk ratio of cobalt content in Co-N-CDC material is much higher than surface-to-bulk ratio of iron in Fe-N-CDC, which is due to a larger amount of nitrogen doped carbon-coated iron particles and nanotubes formed during the pyrolysis in Fe-N-CDC visible from the SEM images. As the iron particles covered in carbon do not give an iron signal in XPS, the bulk content as determined by EDX and the surface content as determined by XPS differ much more in this case than in Co-N-CDC. These phases are also more stable in acid, which causes the metal content in the final Fe-N-CDC catalyst to be higher than in Co-N-CDC even though the starting metal concentration was higher in the case of Co. Co-N-CDC also demonstrates high $O_2$ reduction currents and a value of *n* close to 4 (Figure 45d), meaning that $O_2$ is reduced to water via 4-electron pathway on this catalyst. Interestingly, the relative contents of the two nitrogen surface species known to be active (graphitic and pyridinic nitrogen) are rather different in both catalysts but result in a similar ORR electrocatalytic activity. As can be seen, the fact that the transition metal and nitrogen are much more homogeneously distributed in Fe-N-CDC plays little role in the RDE testing of electrocatalyst materials, but in fuel cells the effect is much more prominent.

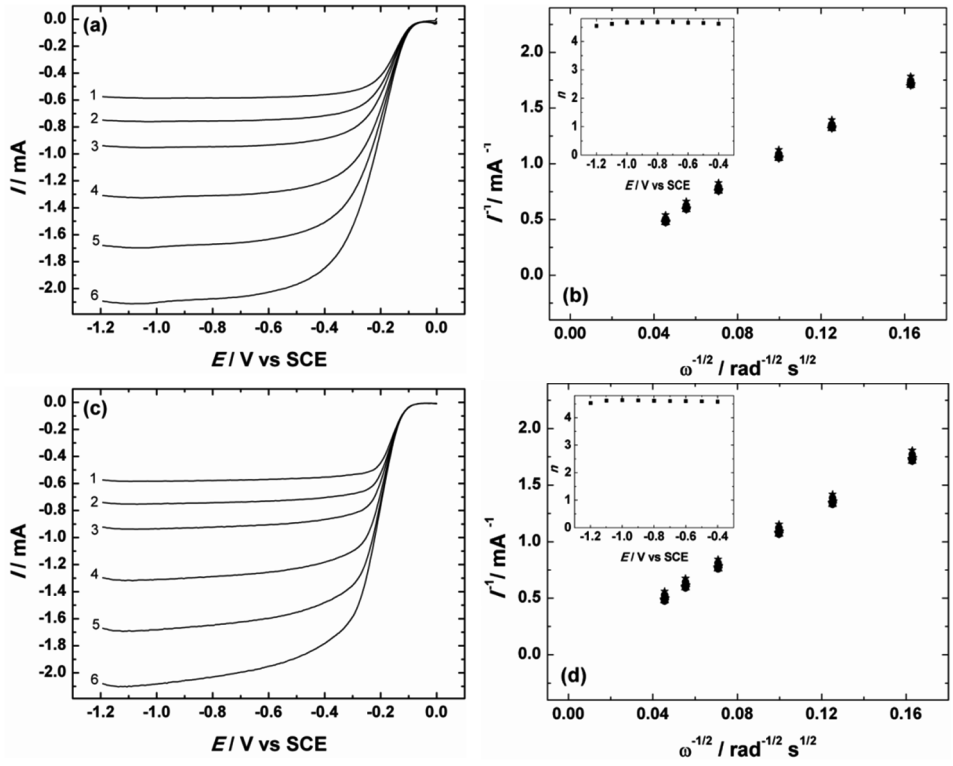


**Figure 45.** RDE polarisation curves for ORR on (a) Fe-N-CDC and (c) Co-N-CDC modified GC electrodes in $O_2$-saturated 0.1 M KOH. $\nu = 10$ mV $s^{-1}$, $\omega$ = (1) 360, (2) 610, (3) 960, (4) 1900, (5) 3100 and (6) 4600 rpm. K-L plots for $O_2$ reduction on (b) Fe-N-CDC and (d) Co-N-CDC catalysts in 0.1 M KOH. Insets show the potential dependence of *n*.

Figure 46 and Table 9 display a comparison of the ORR activity of transition metal-containing nitrogen-doped CDC catalysts and a commercial 60% Pt/C catalyst in $O_2$-saturated 0.1 M KOH solution. Both of the M-N-CDC catalysts behave very similarly, with the $E_{onset}$ value 39 mV (Fe-N-CDC) or 62 mV (Co-N-CDC) more negative than that of the commercial 60 wt.% Pt catalyst (which was used in the DMFC study) and $E_{1/2}$ ~30 mV more negative. The kinetic current densities at 0.8 V vs RHE (converted to the RHE scale by calibrating the SCE electrode vs a Pt wire) were 9.1 and 8.2 mA $cm^{-2}$ for Fe-N-CDC and Co-N-CDC, respectively, exceeding those of the N-doped CDC, but still somewhat below Co/N/MWCNT-2.

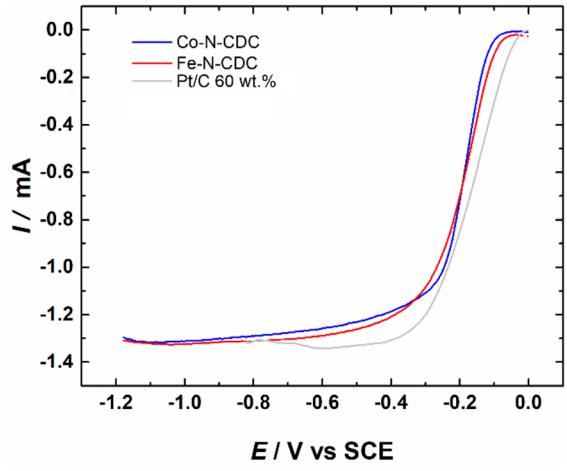


**Figure 46.** A comparison of the RDE results of $O_2$ reduction on Fe-N-CDC, Co-N-CDC and commercial 60% Pt/C modified GC electrodes in $O_2$-saturated 0.1 M KOH solution. $\nu$=10 mV $s^{-1}$, $\omega$ = 1900 rpm.

**Table 9.** ORR parameters of the iron-/cobalt- and nitrogen-doped carbide derived catalyst materials and Pt/C in 0.1 M KOH.

| Catalyst | $E_{onset}$ (mV vs SCE) | $E_{1/2}$ (mV vs SCE) | $j_k$ at 0.8 V vs RHE (mA $cm^{-2}$) |
|---|---|---|---|
| 1094 (base CDC) | –213 | –270 | 0.2 |
| Fe-N-CDC | –79 | –191 | 9.1 |
| Co-N-CDC | –102 | –191 | 8.2 |
| 60 wt.% Pt/C | –40 | –161 | 12.8 |

The stability of the M-N-CDC catalysts was also tested with a modified glassy carbon RDE in $O_2$-saturated 0.1 M KOH. The catalysts were tested during 1000 cycles from 0 to –1.2 V vs. SCE (Figure 47). The $E_{onset}$ and $E_{1/2}$ values remained the same during the whole testing period, with a rather minimal change in the limiting current values, proving the stability of both of these materials in alkaline conditions. In fuel cell the conditions can however be somewhat different, as the mass transfer process is much more affected by the porosity of the catalyst in fuel cells. A large amount of micropores might be favourable to achieve high starting activity [259], but also contributes to a rapid loss in activity of the catalysts due to mass-transfer losses, which are especially apparent in fuel cell conditions as the catalyst layer is thick [33]. The carbon nanotubes between N-doped CDC grains in the M-N-CDC catalysts presented in this work, however, prevent this by creating channels, which facilitate mass transport without a loss in activity as the in-situ formed carbon nanotubes themselves are also highly active towards the ORR [260]. This means the M-N-CDC materials have excellent potential to replace Pt as a cathode catalyst in low-temperature fuel cells, such as alkaline

direct methanol fuel cells. To prove the suitability of these materials in real alkaline DMFCs, Fe-N-CDC was tested as the cathode catalyst and compared to the performance of the commercial 60% Pt/C material as the Fe-N-CDC catalyst had more microporosity, which should lead to a higher activity in fuel cells.

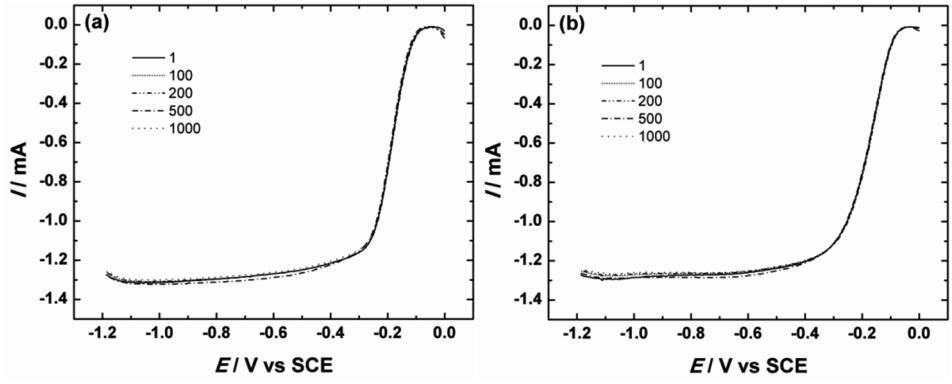


**Figure 47.** The stability of Co-N-CDC (a) and Fe-N-CDC (b) modified GC electrodes in $O_2$-saturated 0.1 M KOH solution during 1000 potential cycles. $\nu = 10$ mV s$^{-1}$, $\omega = 1900$ rpm.

In a DMFC, one of the key problems with platinum-based catalysts is the cross-over of methanol through the anion exchange membrane from the anode side of the cell onto the cathode, which results in a fuel loss in the cathode area and a mixed electrode potential [21]. To eliminate this possibility in our fuel cell testing, we first tested the methanol tolerance of the Co-N-CDC and Fe-N-CDC catalysts in a 0.1 M KOH solution, which also contained 3 M methanol. As seen from Figure 48, the methanol addition has very little effect on the ORR activity of the catalyst and as such the effect of methanol crossover should be negligible.

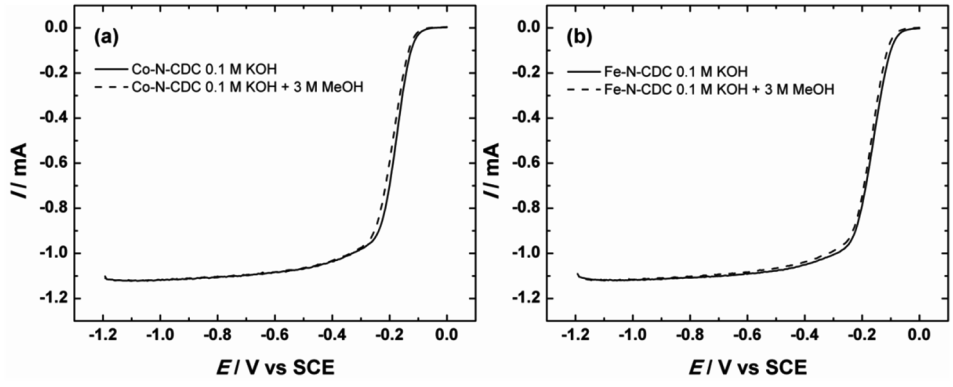


**Figure 48.** ORR polarisation curves on Co-N-CDC (a) and Fe-N-CDC (b) modified GC electrodes in $O_2$-saturated 0.1 M KOH solution with and without 3 M MeOH added. $\nu = 10$ mV s$^{-1}$, $\omega = 1900$ rpm.

Alkaline DMFC testing was performed with Fe-NCDC, Co-NCDC and commercial Pt/C catalysts. The measured polarisation and power density curves are presented in Figure 49, normalised to both the fuel cell area (Figure 49a–b) and cathode catalyst mass (Figure 49c–d). The fuel was 1 M methanol solution in both deionised water and 0.1 M KOH.

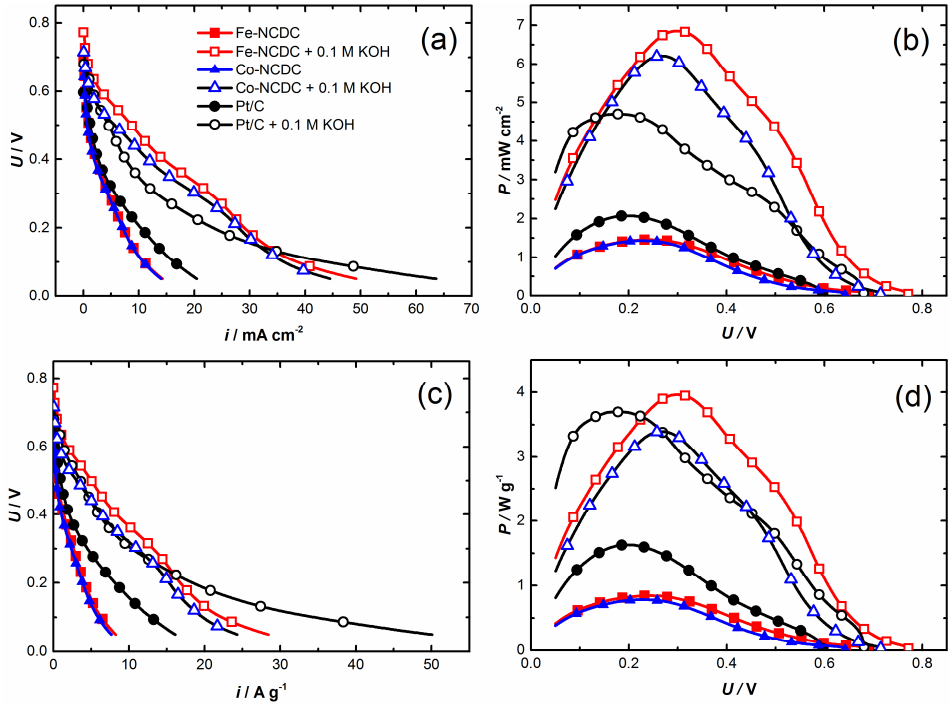


**Figure 49.** DMFC performances of Fe-NCDC (red squares, 1.73 mg $_{\text{Fe-NCDC}}$ cm$^{-2}$), Co-NCDC (blue triangles, 1.83 mg$_{\text{Co-NCDC}}$ cm$^{-2}$) and Pt/C (black circles, 1.27 mg$_{\text{Pt}}$ cm$^{-2}$) catalysts in alkaline DMFC with a Fumatech FAA3 membrane (50°C). At the anode (0.2 ml min$^{-1}$): 1 M methanol (filled symbols) and 1 M methanol with 0.1 M KOH (empty symbols). At the cathode: pure dry $O_2$ (200 ml min$^{-1}$). (a) Current density and (b) power density normalised to fuel cell area. (c) Current density and (d) power density normalised to the mass of Pt or Fe-NCDC at the cathode.

Without 0.1 M KOH, the performance of the DMFC is poor and Pt/C performs better than Co- and Fe-NCDC cathode catalysts. The maximum power densities are 2.07 mW cm$^{-2}$ or 1.63 W $g_{Pt}^{-1}$ at 0.20 V for Pt/C; 1.46 mW cm$^{-2}$ or 0.84 W $g_{\text{Fe-NCDC}}^{-1}$ at 0.24 V for Fe-NCDC and 1.43 mW cm$^{-2}$ or 0.78 W $g_{\text{Co-NCDC}}^{-1}$ at 0.23 V for Co-NCDC. The poor performance can be attributed to the fact that $CO_2$ is produced from methanol at the anode and it will convert to negatively charged $HCO_3^-$ in water [240]. This will then neutralise the MEA by replacing $OH^-$ in the membrane and ionomer affecting also the cathode environment. Furthermore, the conductivity of the system is lowered by the replacement of $OH^-$

with $HCO_3^-$. Pt/C is generally a good ORR catalyst in all environments and can function better than the synthesised catalysts in these challenging neutral conditions. However, the methanol tolerance of Fe- and Co-NCDC can be observed from the high OCV compared to Pt/C (0.69 and 0.64 V versus 0.60 V). This allows the maximum power density to be reached at a higher potential, which is important for applications requiring a minimum voltage to work. The addition of 0.1 M KOH to the fuel solution dramatically improves the DMFC performance as the membrane and the ionomer remain in $OH^-$ form during operation. Fe-NCDC now performs even better than Pt/C: the $P_{max}$ values are 4.70 mW $cm^{-2}$ or 3.70 W $g_{Pt}^{-1}$ at 0.17 V for Pt/C; 6.85 mW $cm^{-2}$ or 3.96 W $g_{Fe\text{-}NCDC}^{-1}$ at 0.30 V for Fe-NCDC and 6.21 mW $cm^{-2}$ or 3.40 W $g_{Co\text{-}NCDC}^{-1}$ at 0.27 V for Co-NCDC. In the case of Fe-NCDC, this indicates a remarkable 7% increase compared to Pt/C in mass specific performance with a catalyst made from cheap and abundant raw materials. The current and power densities for Fe-NCDC are especially high in the whole voltage region from OCV to 0.2 V indicating low activation overpotential and the benefit from methanol tolerance. This can also be seen from the OCVs, which are almost 0.1 V higher than without KOH (0.68 and 0.77 V for Pt/C and Fe-NCDC, respectively). At very high current density region, Pt/C performs better possibly due to mass transfer losses in the unoptimised catalyst layer with Fe-NCDC. Co-NCDC behaves similarly but the overall performance is lower than with Fe-NCDC as is expected from the RDE measurements. The absolute performances are not as impressive as in recent alkaline DMFC studies [240,243,261], however, this is due to the low KOH concentration (0.1 M) we used to have better correspondence to RDE conditions, relatively low catalyst loading (1.73 mg $cm^{-2}$) and the restricted operating temperature (50 °C) due to FAA3 membrane.

Next, the Fe-N-CDC and Co-N-CDC catalysts were tested as the cathode in an AEMFC using the Tokuyama A201 membrane and AS-4 ionomer. The catalysts were synthesised with the same method, albeit from a different TiCDC which led to a somewhat more mesoporous material with less surface area, but a higher surface nitrogen content and very similar ORR activity [IX] (small differences in the ORR activity in RDE mode can arise from the different ionomer used in the studies). Figure 50 compares the single cell AEMFC performance of Tokuyama A201 AEM based MEAs with Co-N-CDC and Fe-N-CDC cathode catalysts, using humidified $H_2$ and $O_2$ gases at 50 ºC. Co-N-CDC and Fe-N-CDC materials performed almost similar, having peak power densities of 78 and 80 mW $cm^{-2}$, respectively. In order to compare the performance of these two CDC supported non-Pt catalysts, commercial 46.1 wt.% Pt/C catalyst was also evaluated and the AEMFC performance was compared at identical operating conditions to other non-platinum catalysts. Tanaka 46.1 wt.% Pt/C catalyst showed the highest performance with the peak power density of 90 mW $cm^{-2}$. At the same time the OCVs of the non-Pt catalysts were only 40 mV lower than the OCV of Pt/C (1.06 V) which shows the great potential of the Co-N-CDC and Fe-N-CDC catalysts to be suitable replacements for Pt-based catalysts in AEMFCs.

However, additional work needs to be done to optimise the operating conditions in order to improve the fuel cell performance at elevated temperature and reach the highest power densities reported in the literature. A power density with Tokuyama's AEM reported by Li et al. was about 180 mW $cm^{-2}$ using Co-Fe/C catalysts [262]. The comparatively similar fuel cell testing results also show the good mass transfer properties of Co-N-CDC and Fe-N-CDC catalysts as the commercial Pt/C catalyst (TKK) is considered to be one of the best catalysts for its optimal specific surface area, porosity and particle size. These optimised catalyst parameters help to efficiently distribute the gases throughout the whole catalyst layer and at the same time a higher number of micropores allow for access to a higher number of active sites. Due to water not being formed on the cathode in AEMFCs the problem of micropore flooding common in PEMFCs is avoided here, allowing for the use of highly microporous catalysts [87,263]. However, at higher current densities there is likely a problem with water removal from the anode. The MEA and fuel cell system needs further optimisation and good choice of GDL depending on the catalyst morphology to reach the highest current densities reported in the literature [262,264–266]. The best AEMFC results often use in-house components such as membranes, GDLs, flow fields or novel MEA fabrication procedures. As a conclusion, it can be summarised that the excellent performance of the Co-N-CDC and Fe-N-CDC catalysts compared to the commercial 46.5 wt.% Pt/C is the combined result of high catalytic activity for ORR and a favourable porous catalyst layer structure providing necessary mass transportation properties.

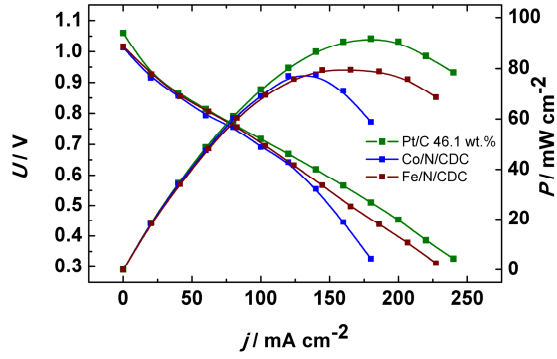


**Figure 50.** $H_2/O_2$ fuel cell performance of MEAs with M/N/CDC catalysts and commercial 46.1 wt.% Pt/C cathodes using a Tokuyama A201 anion exchange membrane. $T$ = 50 ºC, anode: 46.1 wt.% Pt/C.

As seen in [VII–XIII], ball-milling of the CDC material along with the doping agents (especially in the case of Phen) notably decreases the specific surface area. In [XIII] it was displayed that ball-milling alone is not at fault for this effect and that it is a combination of pore closure by Phen and crushing of pores during the ball-milling process. To further increase the performance of Fe-N-CDC in the

mass-transport region, a strategy to decrease the particle size of the catalyst from the micrometre-sized grains to ~100 nm with minimal loss of porosity due to ball-milling was developed using experience and data from ball-milling different CDCs [VII–XIII]. Shortly, the material was ball-milled with zirconia beads either 5 or 0.5 mm in size and in either solid or liquid phase. As a surfactant to further enhance the ball-milling, PVP was added to one sample.

Figure 51 illustrates with SEM the effect of ball-milling on the particle size of the catalysts, after pyrolysis. Figure 51a shows a SEM image of the catalyst obtained by pyrolysis (same conditions as the other samples) of the FeN-SiCDC-wet precursor material. The latter was obtained by mixing SiCDC, Phen and iron(II) acetate in ethanol using simply sonication and followed by drying. A variety of particle sizes is shown with large catalyst particles (diameter higher than 1 μm) dominating and some particles with a diameter over 10 μm also visible. For the same composition of the catalyst precursor (same ratios of SiCDC, Phen and iron(II) acetate) but after ball-milling with 5 mm $ZrO_2$ beads followed by pyrolysis (FeN-SiCDC-5-400, Figure 51b), one can see that the average grain size has decreased somewhat, with a higher fraction of particles in the range of 1 μm vs. those in the range of 5–10 μm in Figure 51a. The particles in FeN-SiCDC-5-400 are also rounder than those in the SiCDC pristine material and in the FeNC catalyst obtained without milling the precursors. Increasing further the ball-milling rotation rate in dry conditions and with 5 mm $ZrO_2$ beads only slightly decreased the particle size of the final catalyst (not shown). In contrast, a significant effect from using smaller $ZrO_2$ beads and in wet conditions (ethanol) can be seen in Figure 51c for the catalyst FeN-SiCDC-0.5-400-wet. It must be noted, in addition, that milling in dry conditions with 0.5 mm beads has, however, negligible effect on the particle sizes because the balls tend to get stuck in the soft precursor mixture and not grind efficiently. This is the reason why, in a following attempt, ethanol was added to allow for movement of the beads. In those conditions, the ball-milling becomes very effective, as the particle sizes seen in Figure 51c and in the close-up in Figure 51d are much smaller than those achieved with 5 mm beads without added ethanol. In Figure 51d, the smooth surface morphology of the particles can also be seen. However, the particle sizes are still quite varied and a significant fraction of particles have a size >1 μm, not ideal for ink preparation and for cathode layer structure. Figures 51e,f show SEM images of the FeNC catalyst prepared in similar conditions (i.e. with added ethanol) but also in addition using PVP, labelled FeN-SiCDC-0.5-400-wet-PVP. Using a surfactant such as PVP further helps to separate smaller particles formed during the ball-milling and to enhance the milling itself, thereby giving a more uniform particle size of <1 μm. This represents a significant breakthrough since decreasing the grain size of CDC-based catalysts to such extent has hitherto been a challenge [77,267,268]. The rough surface structure of the FeN-SiCDC-0.5-400-wet-PVP catalyst is shown with SEM at higher magnification in Figure 51f, suggesting these particles are also highly porous.

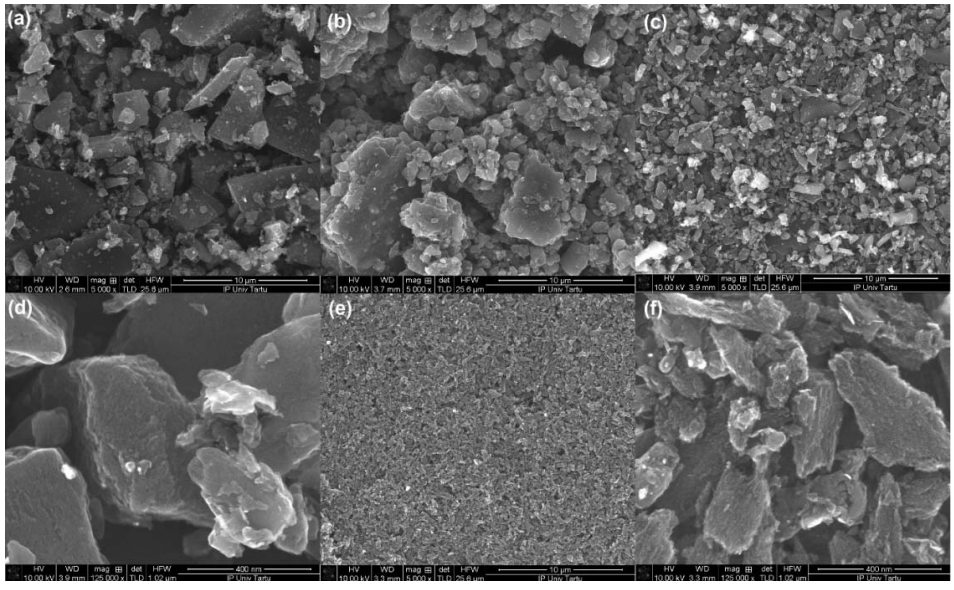


**Figure 51.** SEM micrographs of the FeNC catalysts obtained after same pyrolysis conditions but different milling conditions (a) FeN-SiCDC-400-wet, (b) FeN-SiCDC-5-400, (c,d) FeN-SiCDC-0.5-400-wet and (e,f) FeN-SiCDC-0.5-400-wet-PVP.

The structure of FeN-SiCDC-0.5-400-wet-PVP was further investigated by TEM and HAADF-STEM (Figure 52). In Figure 52a, particles with sizes ranging from tens of nanometres to hundreds of nanometres can be seen along with some denser particles. Figure 52b shows the surface of the catalyst, with amorphous carbon as well as bright nanometric clusters and bright single dots of atoms with higher atomic mass than carbon also visible. The nanosize clusters in this image are identified by EDX mapping to be rich in Zr and O (Figure 52e–f). We assign them therefore to $ZrO_2$ particles coming from the beads and/or the walls of the grinding jar used for the milling. In contrast, the bright dots uniformly distributed over the whole mapped area can be assigned to Fe atoms in Fe-$N_x$ sites as suggested also by the uniform distribution of N atoms (Figure 52c–d).

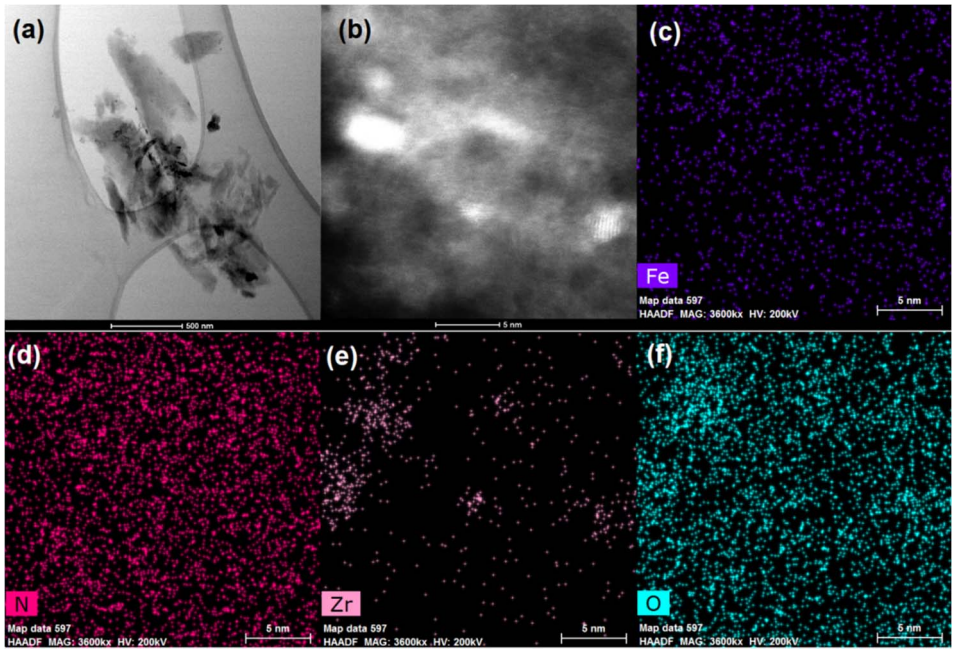


**Figure 52.** (a) TEM and (b) HAADF-STEM images of the FeN-SiCDC-0.5-400-wet-PVP catalyst with (c–f) EDX elemental mapping images from the area shown in (b).

Figure 53a compares the X-ray absorption near-edge structure (XANES) spectra of the four FeNC catalysts of the present study with that of a reference FeNC material comprising only Fe-$N_x$ sites (labelled $Fe_{0.5}$), whose active-site structure was identified in our previous study [44]. The comparison reveals a similar XANES fingerprint for FeN-SiCDC-5-400, FeN-SiCDC-0.5-400, FeN-SiCDC-0.5-400-wet and $Fe_{0.5}$, while FeN-SiCDC-0.5-400-wet-PVP has a slightly different spectrum that can be a result of a minor presence of Fe-based nanoparticles along with Fe-$N_x$ sites (see Figure S4 of ref. [44]). The fully atomically dispersed nature of Fe in FeN-SiCDC-5-400, FeN-SiCDC-0.5-400 and FeN-SiCDC-0.5-400-wet was confirmed by extended X-ray absorption fine structure (EXAFS) spectroscopy. The Fourier transform of the EXAFS spectra (Figure 53b) of the four catalysts of this study reveals a main peak around 1.4 Å (not corrected for the phase shift) assigned to the Fe-N first coordination shell, while a reduction of the intensity of the first-shell peak and the appearance of Fe-Fe contributions for FeN-SiCDC-0.5-400-wet-PVP vs. all other catalysts of the present study indicates the coexistence of $FeN_x$ moieties with metal-based nanoparticles. A linear combination fitting of the FeN-SiCDC-0.5-400-wet-PVP XANES spectrum was carried out using the XANES spectra of FeN-SiCDC-0.5-400-wet (the catalyst prepared identically except for the absence of PVP during milling) and metallic Fe foil as references. As shown in Figure 53c the spectrum of FeN-SiCDC-0.5-400-wet-PVP

is well reproduced by linear addition of the two reference components, with a relative Fe proportion of 92% of Fe-$N_x$ sites and 8% of metallic iron.

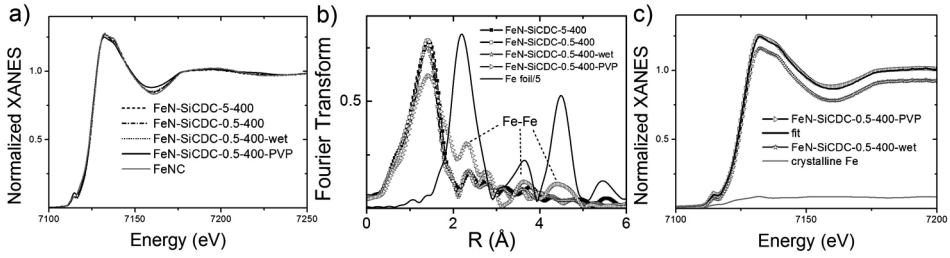


**Figure 53.** XAS characterization of FeNC catalysts. (a) Comparison between the Fe K-edge XANES experimental spectra of FeN-SiCDC-5-400 (dashed line), FeN-SiCDC-0.5-400 (dash-dotted line), FeN-SiCDC-0.5-400-wet (dotted line), FeN-SiCDC-0.5-400-wet-PVP (black line) and FeNC (grey line) from ref. [44]. Note that all the spectra, except for the spectrum of FeN-SiCDC-0.5-400-wet-PVP, are nearly identical. (b) Phase-uncorrected Fourier transform of the experimental EXAFS spectra of the FeN-SiCDC catalysts and the crystalline metallic Fe foil (for the latter, the signal is divided by a factor 5 for easier comparison). (c) Linear combination fitting of the Fe K-edge XANES spectra of FeN-SiCDC-0.5-400-wet-PVP using the XANES spectra of FeN-SiCDC-0.5-400-wet and of a metallic Fe foil as fitting spectral components.

The porosity in the FeNC catalysts of the present study were then investigated with $N_2$ physisorption and compared to those of the SiCDC pristine material. The pore size distributions calculated from the $N_2$ adsorption-desorption isotherms via the QSDFT model are shown in Figure 54 and the calculated textural properties are given in Table 10.

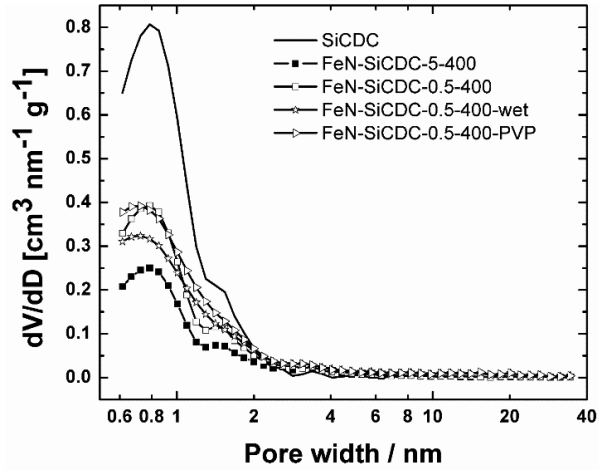


**Figure 54**. Pore size distributions for the pristine SiCDC and for the four FeN-SiCDC catalysts.

Using 5 mm zirconia balls and dry milling, the SSA of the final catalyst decreased more than 3 times when compared to the starting CDC material (458 and 1363 $m^2 g^{-1}$, respectively, Table 10). This is similar in magnitude to the effect we previously observed with 5 mm balls at the same rotation rate, which serves as a starting point [269]. Changing the diameter of the zirconia balls from 5 to 0.5 mm reduced the losses in $S_{BET}$ by a third, resulting in a catalyst with a BET area of 709 $m^2 g^{-1}$ for FeN-SiCDC-0.5-400 compared to 458 $m^2 g^{-1}$ for FeN-SiCDC-5-400. This effect of the size of the zirconia balls on the SSA of the final FeNC catalyst is similar if the milling is performed in ethanol (FeN-SiCDC-0.5-400-wet has a BET area of 735 $m^2 g^{-1}$). However, the PSD of FeN-SiCDC-0.5-400 and FeN-SiCDC-0.5-400-wet are somewhat different (Figure 54), with less volume of pores having a diameter under 1 nm when using wet milling. This probably implies that more micropores of the pristine SiCDC were closed in wet vs. dry milling conditions. Thus, with the different milling conditions investigated here, we identify that resorting to small zirconia beads and combined with wet milling is beneficial for reducing catalyst particle sizes.

Surfactants are known to decrease agglomeration of milled particles and their sticking to the milling jar and milling media, meaning that the final particle size achieved can be smaller [270]. When adding PVP during the milling with small zirconia beads and in wet conditions, the BET surface area of the resulting FeNC is maximum, reaching 865 $m^2 g^{-1}$ (FeN-SiCDC-0.5-400-wet-PVP, Table 10). The loss of BET area compared to SiCDC is thus minimised to *ca* 40%. In our previous study, we determined that when iron(II) acetate and Phen are dispersed on SiCDC without ball-milling, the $S_{BET}$ loss is also around 40%, due to the blocking or filling of some micropores of SiCDC with the new carbon phase derived from Phen during pyrolysis [269]. This means that wet milling with 0.5 mm $ZrO_2$ balls and added PVP in ethanol can completely avoid the negative effect of ball-milling on the BET area.

**Table 10.** Textural properties of FeN-SiCDC catalysts as determined by BET analysis.

| Catalyst | $S_{BET}$, $m^2 g^{-1}$ | $S_{DFT}$, $m^2 g^{-1}$ | $V_{tot}$, $cm^3 g^{-1}$ | $V_{\mu(t\text{-}plot)}$, $cm^3 g^{-1}$ | $V_{\mu(DFT)}$, $cm^3 g^{-1}$ |
|---|---|---|---|---|---|
| SiCDC | 1363 | 1346 | 0.688 | 0.60 | 0.57 |
| FeN-SiCDC-5-400 | 458 | 455 | 0.296 | 0.2 | 0.18 |
| FeN-SiCDC-0.5-400 | 709 | 701 | 0.43 | 0.31 | 0.28 |
| FeN-SiCDC-0.5-400-wet | 735 | 710 | 0.55 | 0.24 | 0.28 |
| FeN-SiCDC-0.5-400-wet-PVP | 865 | 835 | 0.62 | 0.28 | 0.33 |

The bulk elemental content of the FeN-SiCDC catalysts was measured via ICP-MS (Table 11). The iron content is near 0.5 wt.% for all the catalysts, while significant amounts of Zr is also present. The source of Zr is $ZrO_2$ from the grinding jar and the balls used for ball-milling. SiC cores are also seen in the center of some SiCDC particles (Figure 52a), implying that the chlorination pyrolysis used to prepare SiCDC from SiC was incomplete. It is suggested that the residual SiC renders the SiCDC material harder than carbon, or that SiC cores are separated from SiCDC grains during the milling, eroding the ball-milling apparatus since SiC is an extremely hard material and thereby explaining the presence of significant amount of Zr in the catalysts. $ZrO_2$ is present as nanoparticles on the catalyst surface as can be seen from the TEM images (Figure 52). However, in our previous studies, we could exclude the $ZrO_2$ nanoparticles from having a large effect on the high ORR activity observed for the present CDC-based FeNC catalysts [77,267,269].

**Table 11.** Fe and Zr content in FeN-SiCDC catalyst materials as determined by ICP-MS.

| Catalyst | Fe | | Zr | |
|---|---|---|---|---|
| | wt.% | +/– wt.% | wt.% | +/– wt.% |
| FeN-SiCDC-5-400 | 0.506 | 0.015 | 2.703 | 0.027 |
| FeN-SiCDC-0.5-400 | 0.424 | 0.010 | 0.260 | 0.008 |
| FeN-SiCDC-0.5-400-wet | 0.430 | 0.008 | 4.735 | 0.123 |
| FeN-SiCDC-0.5-400-wet-PVP | 0.503 | 0.008 | 3.791 | 0.099 |

The surface elemental composition of the FeN-SiCDC catalysts was analysed by XPS, with the most important results shown in Figure 55 (N1s core-level spectra deconvoluted according to [72]) and in Table 12. An essential factor for the ORR activity is the nitrogen content and speciation. It can be seen that decreasing the zirconia ball size while keeping other ball-milling conditions the same increased the overall N content by about 0.5 at.% (compare FeN-SiCDC-0.5-400 vs FeN-SiCDC-5-400 in Table 12). More importantly, the increased N content is assigned to the ORR-active Fe-$N_x$ and pyridinic-N components. Introducing ethanol during the ball-milling significantly lowered the total N content from ca 4 to 2 at.% (FeN-SiCDC-0.5-400 vs. FeN-SiCDC-0.5-400-wet in Table 12), but also had an important impact on the nitrogen speciation: the overall N content was divided by two, however the Fe-$N_x$ content was kept at a reasonably high level (0.72 at.%). The negative effect when ball-milling in wet conditions on the total N content however was avoided when wet milling was done in the presence of PVP. FeN-SiCDC-0.5-400-wet-PVP has 4.5 at.% N, comparable or even higher than the N content of FeNC catalysts prepared via dry milling. Simultaneously, FeN-SiCDC-0.5-400-wet-PVP shows a higher nitrogen content engaged in Fe-$N_x$ sites, 1.47 at.%.

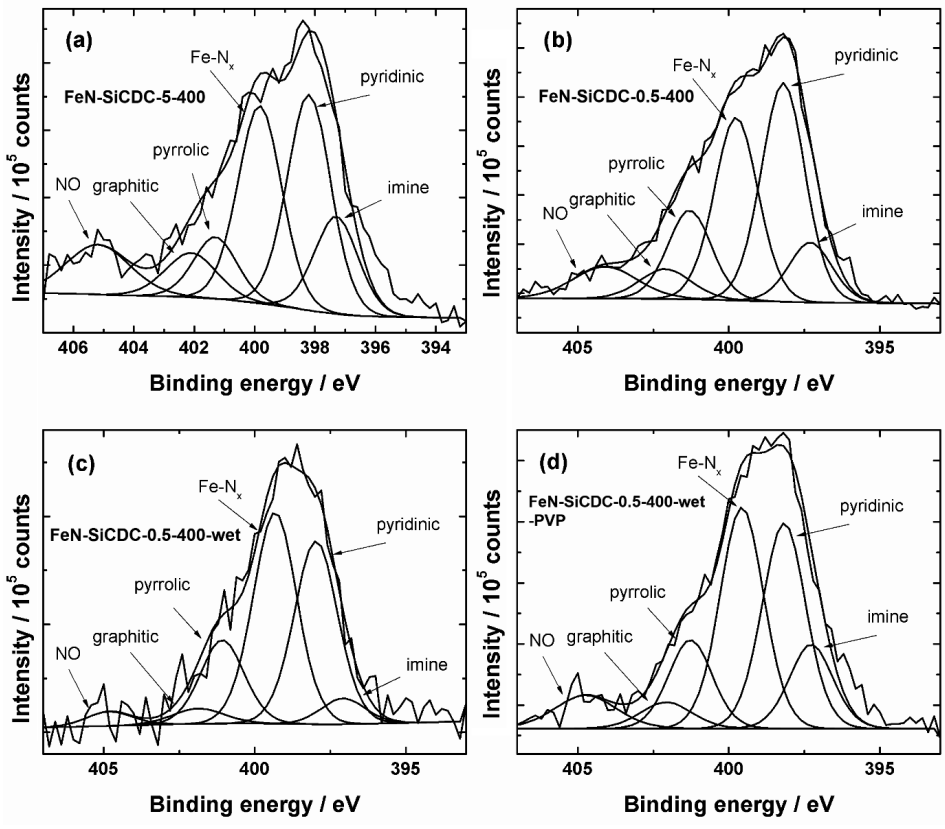


**Figure 55.** XPS N1s core-level spectra for (a) FeN-SiCDC-5-400, (b) FeN-SiCDC-0.5-400, (c) FeN-SiCDC-0.5-400-wet and (d) FeN-SiCDC-0.5-400-wet-PVP.

**Table 12.** Surface elemental composition and N speciation of the FeN-SiCDC catalysts.

| Atomic concentration per element, or per N species | FeN-SiCDC-5-400 | FeN-SiCDC-0.5-400 | FeN-SiCDC-0.5-400-wet | FeN-SiCDC-0.5-400-wet-PVP |
|---|---|---|---|---|
| C at.% | 90.22 | 89.14 | 89.32 | 86.62 |
| O at.% | 6.27 | 6.9 | 8.68 | 8.63 |
| N at.% | 3.5 | 3.94 | 2.01 | 4.5 |
| Pyridinic N at.% | 1.08 | 1.36 | 0.68 | 1.36 |
| Imine at.% | 0.49 | 0.37 | 0.1 | 0.56 |
| Fe-$N_x$ at.% | 0.99 | 1.14 | 0.79 | 1.47 |
| Pyrrolic N at.% | 0.31 | 0.56 | 0.31 | 0.59 |
| Graphitic N at.% | 0.26 | 0.22 | 0.07 | 0.21 |
| NO at.% | 0.37 | 0.29 | 0.06 | 0.31 |

For evaluating the ORR activity of the prepared FeN-SiCDC catalysts, the first method used was RDE. Figure 56 shows a comparison of the electrocatalytic activity of catalysts made by ball-milling a mixture of SiCDC, Phen and iron(II) acetate using $ZrO_2$ beads of different sizes and conditions in $O_2$-saturated 0.1 M KOH solution. Because increasing the rotation rate of the ball-mill during synthesis over 400 rpm only decreased the particle size of the final FeN-SiCDC catalysts somewhat, while bringing with itself more negative effects such as the large decrease in SSA and destruction of the surface structure, which decreased the ORR activity, smaller beads were used as an alternative. Decreasing the ball size in a ball-mill is a known way to decrease the particle size of the final product. Because a smaller particle size also increases the external surface area of a catalyst, this can lead to an increase in the ORR electrocatalytic activity, especially in a fuel cell where mass-transfer is complicated in highly microporous materials such as the SiCDC-based catalysts presented here. Figure 56 shows the ORR activity of catalysts prepared by ball-milling and pyrolysis at 400 rpm with both 5 and 0.5 mm balls employing dry and wet milling. Using simply dry milling with 0.5 mm beads was not very effective, because the catalyst precursor mixture tended to stick to the walls of the $ZrO_2$ grinding jar and not mix very well, likely due to the small force of impact of the smaller beads. The $j_k$ achieved at 0.9 V using this method was 1.2 mA $cm^{-2}$, over two times lower than when using 5 mm balls. However, when ethanol was added to the precursors to create a motor-oil like viscous mixture into the grinding jar, the effects were much more beneficial. The precursors are much better mixed as a result and as can be seen from the SEM images, the particle size is much decreased. This carries on to the ORR activity: the $j_k$ value at 0.9 V vs RHE for FeN-SiCDC-0.5-400-wet catalyst is 2.8 mA $cm^{-2}$. Finally, because adding surfactants during ball-milling is known to enhance ball-milling down particles to the nanometre size, we used PVP for this purpose. Adding surfactants helps to avoid agglomeration of particles during the milling and to further separate them and break them down to smaller ones. The wet milling with smaller balls and PVP also managed to eliminate the negative effect on the $S_{BET}$ of the catalyst from ball-milling. This addition has a large effect on the ORR activity as can be seen from Figure 56. The $j_k$ for FeN-SiCDC-0.5-400-wet-PVP is 3.8 mA $cm^{-2}$, which is the highest in this work and even surpassed that of a commercial Pt/C ($j_k$ = 2.3 mA $cm^{-2}$ at 0.9 V). To elucidate whether or not simply using ethanol and PVP to disperse the precursors without any ball-milling also has the same effect, a FeN-SiCDC-wet catalyst was synthesised by simply sonicating the SiCDC, iron(II) acetate, PVP and Phen in a beaker containing ethanol, which was then dried and pyrolysed at the same conditions as the other catalysts. As seen in Figure 56, the ball-milling has a significant effect, so this is a crucial step in creating an active electrocatalyst for ORR.

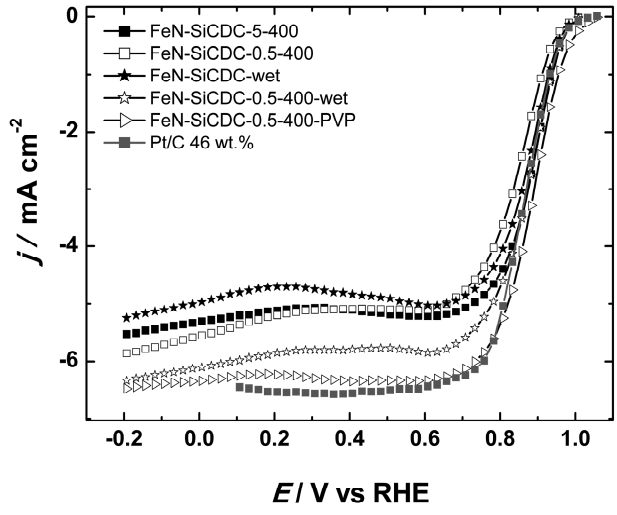


**Figure 56.** Steady-state ORR polarisation curves for the FeN-SiCDC catalysts using different ball-milling conditions and a commercial Pt/C catalyst recorded in $O_2$-saturated 0.1 M KOH. $\omega$ = 1900 rpm. The catalyst loading is 0.2 mg cm$^{-2}$ for the NPMCs and 46 $\mu g_{Pt}$ cm$^{-2}$ for Pt/C.

Figure 57 shows a comparison of the ORR electrocatalytic activity of catalysts made by ball-milling a mixture of SiCDC, Phen and iron(II) acetate using different rotation rates of the ball-mill in $O_2$-saturated 0.1 M KOH solution. For the 100 rpm ball-milled catalyst, the kinetic current density at 0.9 V was 0.7 mA cm$^{-2}$ (Table 13). Raising the rotation rate of the ball-mill to 400 rpm increased the $j_k$ value to 2.9 mA cm$^{-2}$. At 800 rpm, however, $j_k$ at 0.9 V decreased to 0.6 mA cm$^{-2}$, likely due to the CDC surface structure being destroyed by the high impact ball-milling. Using no ball-milling at all and instead sonicating the reactants in ethanol to disperse them followed by drying prior to the pyrolysis step resulted in the $j_k$ value of 2.2 mA cm$^{-2}$. The porosity of the final catalyst decreases as well at higher rotation rates [269], which in turn also counteracts the positive effects of the milling. Pyrolysis of carbon materials in the presence of a nitrogen source (1,10-phenanthroline) and an iron source (iron(II) acetate) is known to create active sites for the ORR [55,77,267,271]. In this case the iron(II) acetate and Phen form the $Fe(Phen)_3$ complex [85]. The Phen ligands protect the Fe atoms from agglomerating during the pyrolysis step, thereby leading to more Fe-$N_x$ sites than iron/iron carbide nanoparticles. As the rotation rate of the ball-mill increases, the dopants are better dispersed onto the carbon material, which itself is also ground into smaller particles with increasing rotation rate. A better dispersion of the precursors also leads to more separation between the Fe atoms. Thus, 400 rpm is selected as the optimum rotation rate for the ball-mill.

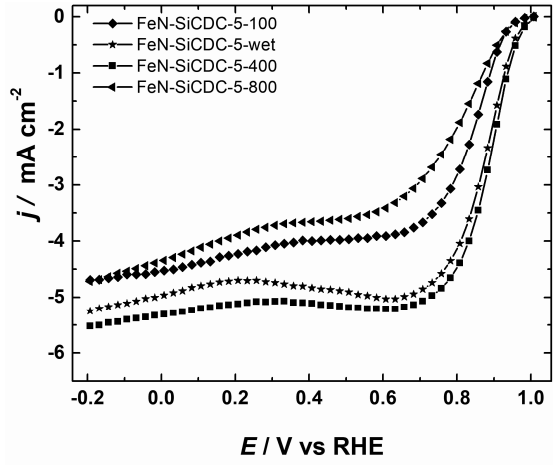


**Figure 57.** Steady-state ORR polarisation curves for the FeN-SiCDC catalysts synthesized using 5 mm $ZrO_2$ balls and different rotation rates for the dry ball-milling and one sample where the reactants were dispersed in ethanol. Polarisation curves were recorded in $O_2$-saturated 0.1 M KOH solution. $\omega$ = 1900 rpm.

For testing the *in situ* activity of the FeN-SiCDC, catalyst-based MEAs with different cathodes and a PtRu/C anode with a HMT-PMBI membrane were sandwiched in a fuel cell as described in the Experimental section. Figure 58 and Table 13 show the results of the AEMFC testing. FeN-SiCDC-5-400, which had the largest particle size, performs the worst at both higher voltages and at higher current densities, with the current density at 0.9 V being 10.3 mA $cm^{-2}$ and the $P_{max}$ achieved 282 mW $cm^{-2}$. Using 0.5 mm $ZrO_2$ beads for wet ball-milling increased the fuel cell performance significantly, with the $j$ at 0.9 V being 36.2 mA $cm^{-2}$ and the $P_{max}$ of 333 mW $cm^{-2}$ for the FeN-SiCDC-0.5-400-wet catalyst. This is likely due to the smaller particle size and better dispersion of the catalyst precursors as well as retaining more surface area than FeN-SiCDC-5-400. A smaller particle size is also beneficial for $O_2$ transport and ionomer access to the active sites, which increases the performance at both high potentials and high current densities. Adding PVP to the precursor mixture enhanced the activity even more, with FeN-SiCDC-0.5-400-wet-PVP showing 52 mA $cm^{-2}$ at 0.9 V and $P_{max}$ of 356 mW $cm^{-2}$. The XPS results showed that the catalyst with added PVP also had the highest elemental contents of nitrogen, especially that of the ORR-active moieties in the near-surface layers, which is an important contributor to the high ORR electrocatalytic activity of this catalyst. This is especially impressive when compared to the respective values obtained with the commercial 46 wt.% Pt/C cathode catalyst (36.5 mA $cm^{-2}$ and 352 mW $cm^{-2}$). This comparison shows that the FeN-SiCDC-0.5-400-wet-PVP catalyst has the second highest ORR activity at 0.9 V and 60 °C in fuel cell, only surpassed by a catalyst labelled as $NH_3$-activated Fe-N-C (80–90 mA $cm^{-2}$ at 0.9 V) [167]. Even considering the peak power density (which depend on many other factors than the sole cathode catalyst ORR activity), the results obtained in this work are surpassed by only five other

reports on Fe-N-C cathodes, obtained with more advanced commercial or developmental ionomers and/or AEMs [167,272–275]. It is well known in the field that the ionomer morphology and AEM properties (thickness, conductivity, water management) affect to an enormous extent the performance of AEMFCs at high current densities [166,167,276], while the accuracy of the humidity control by different fuel cell test stations plays an additional role. Therefore, based on the ORR activity at 0.9 V and the internal comparison to a Pt/C cathode with same AEM and AEI and in a same fuel cell test station in the present work, it is clear that the FeN-SiCDC-0.5-400-wet-PVP catalyst is a promising alternative to the commercial Pt/C catalyst in AEMFC.

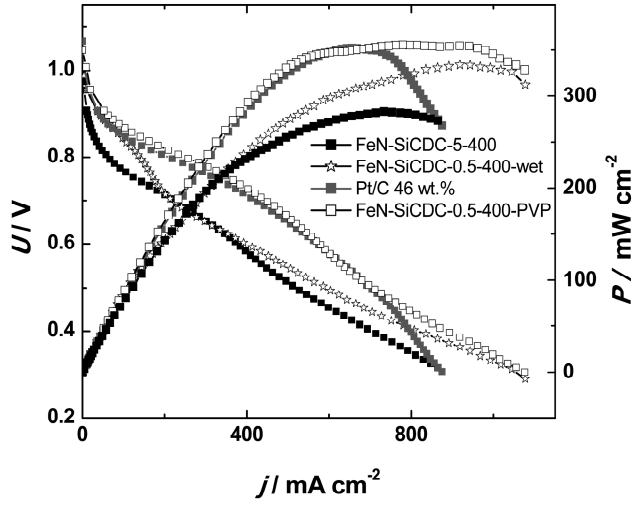


**Figure 58.** Single cell AEMFC polarisation curves using FeN-SiCDC or a commercial Pt/C cathode catalyst (0.4 $mg_{Pt}$ $cm^{-2}$). The anode was a commercial PtRu/C catalyst with 0.8 $mg_{PtRu}$ $cm^{-2}$ loading. T = 60 °C, cathode RH = 100%, anode RH = 82%, backpressure = 200 kPa.

**Table 13.** Kinetic current densities at 0.9 V vs RHE in the RDE setup and current densities at 0.9 V in AEMFC using the FeN-SiCDC catalysts.

| Catalyst | $j_{k,\ 0.9\ V,\ RDE}$ (mA $cm^{-2}$) | $j_{0.9\ V,\ MEA}$ (mA $cm^{-2}$) |
|---|---|---|
| FeN-SiCDC-5-100 | 0.7 | – |
| FeN-SiCDC-5-wet | 2.2 | – |
| FeN-SiCDC-5-400 | 2.9 | 10.3 |
| FeN-SiCDC-5-800 | 0.6 | – |
| FeN-SiCDC-0.5-400 | 1.2 | – |
| FeN-SiCDC-0.5-400-wet | 2.8 | 36.2 |
| FeN-SiCDC-0.5-400-wet-PVP | 3.8 | 52.0 |
| Pt/C 46 wt.% | 2.3 | 36.5 |

### 7.3.2 Fe- and nitrogen-doped MWCNT/CDC composites as catalysts for alkaline membrane fuel cells

The microporous structure of the doped CDCs was thus both a blessing and a curse, as seen in the previous chapter: although it leads to a large amount of very efficient active sites, a lot of them might be buried in the micropores and not available to $O_2$. To alleviate this, the first strategy comprised was to create a composite structure to the one used in the first chapter. The doped CDC particles served as the core of the composite, while a doped MWCNT shell was deposited on top of the CDC particles to improve the mass-transfer properties in fuel cell conditions [X].

The CDC selected for the core was a TiCDC, which was treated with argon and water vapour to further increase its porosity and create an etched surface morphology which was easier to dope with Fe and N. The doping was done with a lower rotation rate of the ball-mill (to avoid loss of surface area in the CDC), Phen as the nitrogen source and iron(II) acetate as the iron source. Phen also acts as a spacer between the iron ions during the pyrolysis as it creates a complex with them. This avoids the agglomeration of iron into particles and increases the utilisation factor of Fe. It also means that there is no need for the acid leaching afterwards. After the first pyrolysis at 800 °C for 1h in $N_2$ atmosphere, MWCNTs, DCDA and more iron(II) acetate was mixed with the catalyst and another pyrolysis was undertaken. The synthesis is described in more detail in chapter 6.7.

Figure 59 presents SEM micrographs of the iron and nitrogen-doped CDC-MWCNT composite materials (Fe-N-comp-1 with a CDC to MWCNT ratio of 1, Fe-N-comp-2 with a CDC to MWCNT ratio of 2 and Fe-N-comp-0.5 with a CDC to MWCNT ratio of 0.5). Figures 59a–c demonstrate the structure of the Fe-N-comp composites on a larger scale, with MWCNT shells seen on top of the CDC particles. The surface of the CDC, which is not covered with MWCNTs shows an etched morphology from the argon/water vapour treatment [188]. The MWCNTs were homogeneously distributed over the CDC particles, forming a network of mesopores in between the microporous Fe-N/CDC, which is beneficial for mass transport in the catalyst layer. Figures 59d–f illustrate the MWCNT bundles with some of the etched CDC surface also visible in Figure 59d. The average size of the CDC particles after nitrogen and iron doping is around 1 µm, with some larger grains and smaller particles also present, although it can be presumed that the smaller particles are largely buried inside the nanotube bundles. All of the composite catalysts appeared quite similar under SEM magnification.

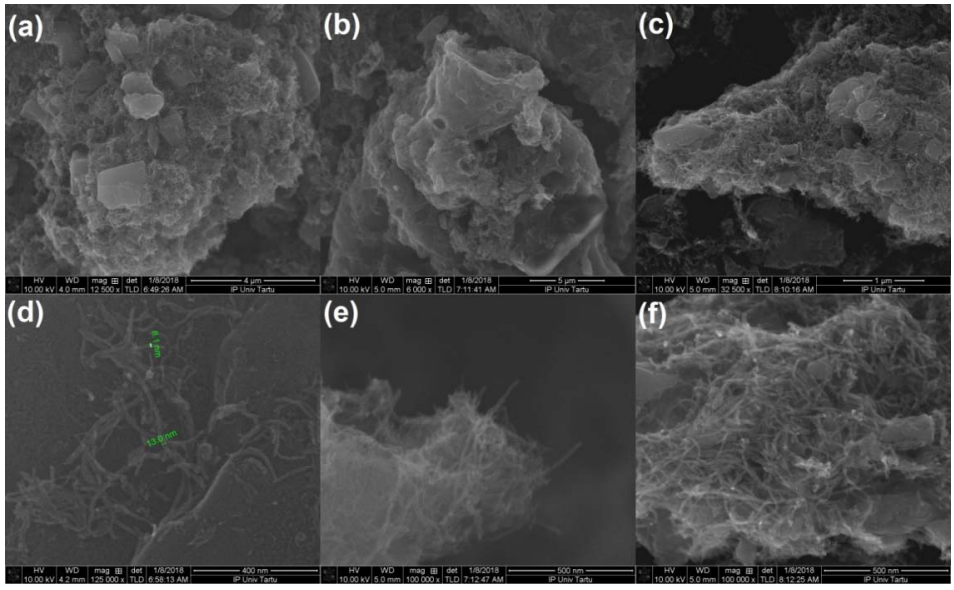


**Figure 59.** Lower magnification (a,b,c) and higher magnification SEM images (d, e, f) of Fe-N-comp-1, Fe-N-comp-2 and Fe-N-comp-0.5, respectively.

The textural properties of the Fe-N-C catalysts are given in Table 14. The BET surface areas of CDC based composite catalysts are in the range of 350–470 $m^2\ g^{-1}$, which is approximately 5 times less compared to the parent CDC material (1997 $m^2\ g^{-1}$). The decrease of surface area during modification is probably caused by blocking of micropores with catalytic additives. During the ball-milling and pyrolysis procedure, the iron and Phen complexes fill the pores and create Fe-$N_x$ active sites into them, which is the likely cause of SSA loss. It is also known that iron can catalyse the graphitisation of microporous materials at high temperatures [277], which also decreases the surface area. It is observed that the micropore volume of composite materials depends slightly on the relative quantity of CNT, while changing from 0.19 $cm^3\ g^{-1}$ to 0.10 $cm^3\ g^{-1}$ in Fe-N-CDC-1 without CNT and Fe-N-comp-0.5 with ~60% of CNT, respectively. CNT additive also affects the total pore volume of composite catalysts from 0.30 to 0.56 $cm^3\ g^{-1}$ in Fe-N-CDC-1 and Fe-N-comp-0.5, respectively. The MWCNTs used in this work have a SSA of about 250–300 $m^2\ g^{-1}$ according to the producer.

**Table 14.** Textural properties of CDC, Fe-N/CDC and Fe-N-comp materials: BET surface area ($S_{BET}$), total pore volume ($V_{tot}$), average pore size ($d_p$), surface area ($S_{DFT}$) and micropore volume ($V_\mu$) calculated from the QSDFT model.

| Catalyst | $S_{BET}$, $m^2\ g^{-1}$ | $V_{tot}$, $cm^3\ g^{-1}$ | $d_p$, nm | $S_{DFT}$, $m^2\ g^{-1}$ | $V_\mu$, $cm^3\ g^{-1}$ |
|---|---|---|---|---|---|
| Fe-N-CDC-1 | 471 | 0.30 | 1.4 | 446 | 0.19 |
| Fe-N-comp-1 | 401 | 0.51 | 2.5 | 407 | 0.13 |
| Fe-N-comp-2 | 440 | 0.49 | 2.4 | 415 | 0.14 |
| Fe-N-comp-0.5 | 349 | 0.56 | 3.1 | 365 | 0.10 |

Figure 60 illustrates the PSD of composite catalysts that shows two main maxima, the peak at ~0.85 nm in a microporous region, and a flat peak at ~3.4 nm in the mesoporous region. The latter peak is more pronounced in materials with CNT additive and can be caused by the voids between amorphous carbon and CNT. Composite catalysts with carbon nanotube additive also have larger mesopores sized 15–20 nm.

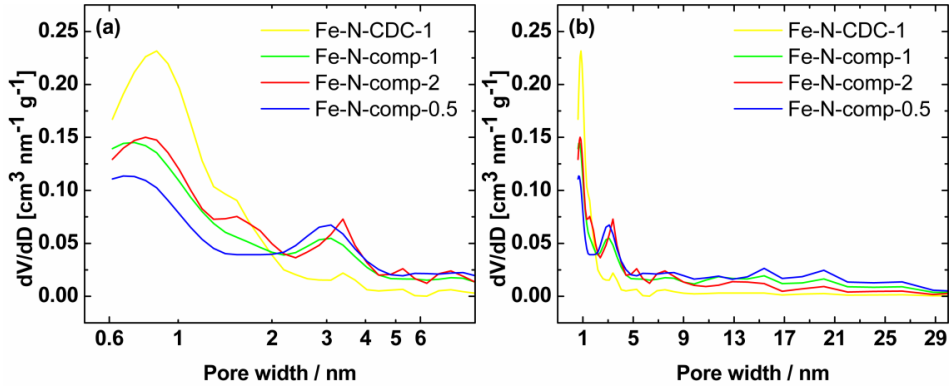


**Figure 60.** Pore size distributions for the Fe-N-C catalysts.

The surface N content and relative contents of nitrogen moieties are given in Table 15. Figure 61 shows the XPS wide scan spectra and N1s and C1s XPS spectra of Fe-N-comp-1, Fe-N-comp-2 and Fe-N-comp-0.5 in the first, second and third column, respectively. The insets in the C1s XPS spectra show a deconvolution of the lower intensity peaks. All of the catalysts contained nearly the same amount of N, with some minor differences in the relative contents of nitrogen moieties. The overall nitrogen content was similar in all catalysts, with the materials with a larger mass fraction of CDC also having somewhat higher N contents. This is likely due to the highly amorphous nature of the CDC, which is more easily doped than the graphitic carbon nanotubes and due to the fact that the CDC was already nitrogen doped prior to the second pyrolysis. All the catalysts had a high concentration of oxygen in the topmost layer (3.9, 6.0 and 2.1 at.%, for Fe-N-comp-1, Fe-N-comp-2 and Fe-N-comp-0.5, respectively), which is due to residual $H_2O$ in the micropores and higher concentration of oxygen-containing groups on the surface of the CDC. This is also confirmed by the catalyst with the highest CDC content having the largest oxygen content.

The surface Fe content was too low to be determined *via* XPS as in the previous chapters, but the bulk Fe content was determined by ICP-MS. The Fe contents in the catalysts were 1.44 wt.% (Fe-N-comp-1), 1.22 wt.% (Fe-N-comp-2) and 1.70 wt.% (Fe-N-comp-0.5), while the concentration of iron in the commercial MWCNTs was determined to be 0.4 wt.%. It is to be noted that the Fe contents determined by ICP-MS may be undervalued due to the lack of a suitable reference material. As the trend for nitrogen concentration on the surface of the catalysts

was in the opposite order, it is likely that the excess iron is present in the form of iron particles instead of Fe-$N_x$ active sites. ICP-MS also detected small amounts ~0.5 wt.% of Zr present from the ball-milling of the catalysts.

**Table 15.** Overall nitrogen content and the relative concentration of nitrogen moieties in the catalyst surface layers as determined by XPS.

| Sample | Total N content, at.% | Fe-$N_x$, % | N-O, % | Graphitic-N, % | Pyridinic-N, % | Pyrrolic-N, % |
|---|---|---|---|---|---|---|
| Fe-N-comp-1 | 1.7 | 20 | 10 | 12 | 33 | 25 |
| Fe-N-comp-2 | 1.8 | 18 | 11 | 12 | 39 | 20 |
| Fe-N-comp-0.5 | 1.5 | 20 | 9 | 13 | 41 | 18 |

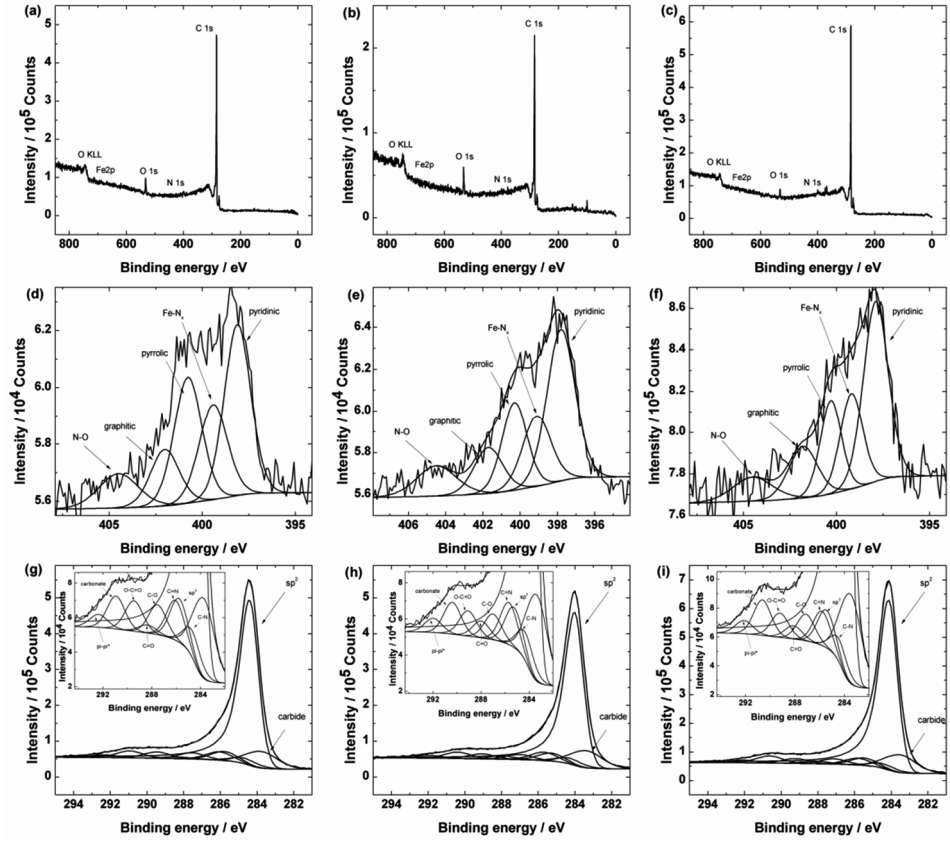


**Figure 61.** XPS survey spectra and core-level spectra in the N1s and C1s regions for (a,d,g) Fe-N-comp-1, (b,e,h) Fe-N-comp-2 and (c,f,i) Fe-N-comp-0.5 samples.

The RDE method was used for studying the oxygen reduction activity of the Fe-N-comp materials in 0.1 M KOH. The ionomer used was Tokuyama AS-4 with a concentration of 12.5 µl in 1 ml of ethanol, into which 1 mg of the catalyst was added and sonicated, after which 20 µl of this dispersion was deposited onto a GC electrode, giving a loading of 100 µg $cm^{-2}$. Figure 62 shows a comparison of the oxygen reduction polarisation curves on GC electrodes modified with the NPMC materials synthesised in this work and a commercial Pt/C catalyst, with Table 16 showing the most important characteristics. The $E_{onset}$ for Fe-N-CNT-1 was –141 mV (defined as the potential where $j$ = –0.25 mA $cm^{-2}$) and the $E_{1/2}$ for this catalyst was –301 mV. The CDC material doped using iron and 1,10-phenantroline had a much more positive $E_{onset}$ of –53 mV and a $E_{1/2}$ of –164 mV, which shows the advantage of the porous CDC material. The ORR activity of the Fe-N-comp-0.5 catalyst, which had 2 times more MWCNTs than Fe-N-comp-1 in the synthesis mixture, yields a catalyst with intermediate activity ($E_{onset}$ = –53 mV and $E_{1/2}$ = –148 mV). Using the step-wise synthesis procedure (with the CDC doped by Phen and iron(II) acetate in the first step and MWCNTs and DCDA added in the second one) with the same amount of MWCNT and CDC yields a catalyst with ORR activity quite similar to that of Fe-N-CDC-1, which is surprising, given that the activity of the Fe,N-co-doped MWCNTs was much lower than that of the catalyst synthesised using CDC. With a ratio of 2:1 (Fe-N-comp-2), the ORR activity of the resulting catalyst exceeds even that of Fe-N-CDC-1 ($E_{onset}$ = –28 mV and $E_{1/2}$ = –121 mV). This is due to an increase in the amount of active sites by using an addition of MWCNT, DCDA and iron(II) acetate. From the XPS data, the overall nitrogen content on the Fe-N-comp-2 catalyst was 0.3 at.% higher than that of Fe-N-comp-0.5, with the relative percentage of the most active moieties nearly the same, which leads to lower overpotential for ORR on this catalyst. The carbon nanotubes form a network on and between the Fe-N-CDC particles as shown on the SEM images, resulting in a more even catalyst layer and better mass transport. The highly conductive MWCNTs can also increase the electron transport and conductivity between the large doped CDC grains. Fe-N-CDC-1, Fe-N-comp-1 and Fe-N-comp-2 also outperformed the commercial Pt/C catalyst ($E_{onset}$ = –53 mV and $E_{1/2}$ = –184 mV).

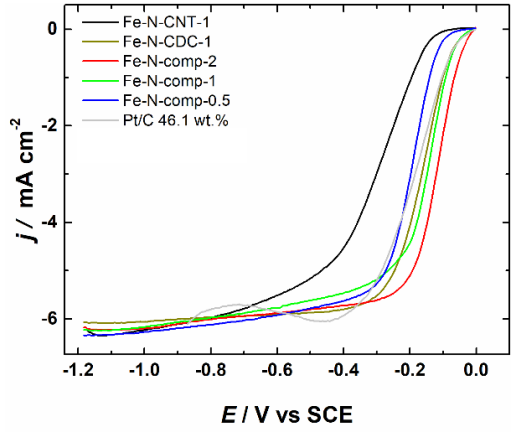


**Figure 62**. Comparison of ORR polarisation curves recorded at 1900 rpm on GC electrodes modified with Fe-N-CNT-1, Fe-N-CDC-1, Fe-N-comp-1, Fe-N-comp-2, Fe-N-comp-0.5 and 46.1 wt.% Pt/C catalysts in $O_2$-saturated 0.1 M KOH solution. $\nu = 10$ mV s$^{-1}$, $\omega = 1900$ rpm.

**Table 16.** ORR parameters of the iron/cobalt and nitrogen-doped carbide-derived carbon catalyst materials and Pt/C in 0.1 M KOH.

| Catalyst | $E_{onset}$ (mV vs SCE) | $E_{1/2}$ (mV vs SCE) | $j_k$ at 0.8 V vs RHE (mA cm$^{-2}$) |
|---|---|---|---|
| Fe-N-CNT-1 | –141 | –301 | 1.9 |
| Fe-N-CDC-1 | –53 | –164 | 14.9 |
| Fe-N-comp-1 | –53 | –148 | 16.9 |
| Fe-N-comp-2 | –28 | –121 | 33 |
| Fe-N-comp-0.5 | –100 | –198 | 7.5 |
| 46.1 wt.% Pt/C | –53 | –184 | 8.7 |

Finally, the performance of the Fe-N-comp materials was compared to Pt/C in a single-cell $H_2/O_2$ AEMFC. Figure 63 shows the results of the AEMFC tests using a commercial 46.1 wt.% Pt/C catalyst as the anode and either the same catalyst or Fe-N-comp catalysts as the cathode. The OCV for the Pt/C catalyst was 1.08 V and 0.98 V for Fe-N-comp-2. The OCVs for Fe-N-comp-1 and Fe-N-comp-0.5 were 0.88 and 0.89 V, respectively. At low current densities the Fe-N-comp-2 catalyst was thus the most efficient out of the NPMCs in the AEMFC, which makes sense as it had the most positive $E_{onset}$ and $E_{1/2}$ in the RDE test. At higher current densities up to 200 mA cm$^{-2}$, however, the Fe-N-comp catalysts showed much increased performance over the Pt/C catalyst, with Fe-N-comp-2 reaching 120 mW cm$^{-2}$ at 0.62 V. This is likely due to the efficient morphological properties of the catalyst layer, where carbon nanotubes form a network between the

CDC particles and better utilisation of the iron present in the catalyst, as although the iron concentration in the catalyst was the lowest as determined by ICP-MS, the nitrogen content and Fe-$N_x$ content on the surface was the highest (data from XPS measurements). At even lower voltages, however, the catalysts with higher CNT content prevail as the mass transport inhibition appears at a much lower current density value for the catalyst containing more CDC than CNT. The $P_{max}$ for Fe-N-comp-1 and Fe-N-comp-2 were 155 and 160 mW $cm^{-2}$, respectively. In the RDE tests, mass transport was less of a problem as the rotation of the electrode supplied ample oxygen to the much thinner catalyst layer, but in the AEMFC testing the mass transport is obviously more complex and the catalysts with higher CNT content and mesoporosity perform much better at high current densities than the largely microporous Fe-N-comp-2. This shows the urgent need for AEMFC testing in addition to RDE as the most active catalyst is not always the most efficient in a real fuel cell. The high catalytic activity of Fe-N-comp-2 in RDE compared to the other composites and Fe-N-CDC-1 can be attributed to two main factors: a slightly higher nitrogen content and thus higher concentration of active sites and a beneficial morphology with mesoporous MWCNT networks around the microporous CDC particles, which create highways between the CDC particles for oxygen diffusion. In high current density operation in an AEMFC, however, $O_2$ diffusion is more inhibited due to a higher ionomer content and thus the catalysts with more carbon nanotube content perform better.

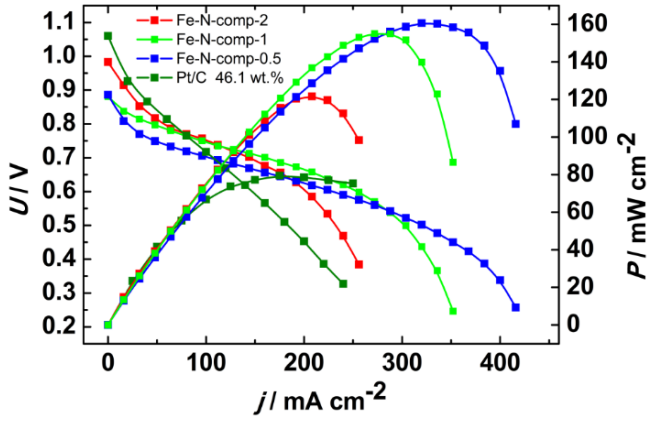


**Figure 63**. Polarisation and power density curves for $H_2/O_2$ AEMFCs using the Tokuyama A201 anion exchange membrane. The anode catalyst was Pt/C and the cathode catalysts are given in the legend. $T$ = 50 ºC.

Table 17 shows a comparison of AEMFC results from this PhD thesis and from the literature with the same AEMs and AEIs. Clearly, all of the catalysts synthesised here are competitive when compared to the best materials in the literature, with Fe-N-comp-0.5 reaching one of the highest power densities published with a Tokuyama A201 AEM and AS-4 ionomer. This owes to its optimised structure

and doping methods developed throughout the work done during this PhD project. Comparing the results achieved with HMT-PMBI AEM and AEI, FeN-SiCDC-0.5-400-wet-PVP also stands out as one of the best performing materials. The efficient reduction of particle size and retention of the porous structure of its parent CDC material are clearly important advancements, which can also help to increase the $P_{max}$ of future catalysts.

**Table 17.** AEMFC performance with M-N-C cathode catalysts.

| Catalyst | Cathode loading (mg cm$^{-2}$) | Anode loading (mg$_{Pt}$ cm$^{-2}$) | T (°C) | Membrane | Ionomer | $P_{max}$ (mW cm$^{-2}$) | Ref. |
|---|---|---|---|---|---|---|---|
| Co/N/MWCNT-1 | 0.6 | 0.2 | 50 | Tokuyama A201 | Tokuyama AS-4 | 116 | IV |
| Fe/N/CDC | 1.5 | 0.46 | 50 | Tokuyama A201 | Tokuyama AS-4 | 80 | IX |
| Co/N/CDC | 1.5 | 0.46 | 50 | Tokuyama A201 | Tokuyama AS-4 | 78 | IX |
| Fe-N-comp-0.5 | 2.6 | 0.46 | 50 | Tokuyama A201 | Tokuyama AS-4 | 160 | X |
| FeN-SiCDC-0.5-400-wet-PVP | 2.0 | 0.8 (PtRu) | 60 | HMT-PMBI | HMT-PMBI | 356 | XIV |
| FePc/C | 1 | 0.4 | 55 | Tokuyama A201 | Tokuyama AS-4 | 120 | [278] |
| Fe-M-LA/C-700 | 4 | 0.4 | 60 | Tokuyama A201 | Tokuyama AS-4 | 137 | [279] |
| FePc/MWCNT | 0.6 | 0.4 | 45 | Tokuyama A201 | Tokuyama AS-4 | 60 | [280] |
| CoPc/MWCNT | 0.6 | 0.2 | 45 | Tokuyama A201 | Tokuyama AS-4 | 100 | [280] |
| Fe-HNCS | 4 | 0.5 | 60 | Tokuyama A201 | Tokuyama AS-4 | 68 | [281] |
| Fe-N-CC | 0.2 | 0.4 | 50 | Tokuyama A201 | Tokuyama AS-4 | 120 | [282] |
| BIDC3 | 4 | 0.3 | 60 | Tokuyama A201 | Tokuyama AS-4 | 47 | [68] |
| Fe-NMG | 3.5 | 0.2 | 70 | Tokuyama A201 | Tokuyama AS-4 | 218 | [283] |
| TiCDC/CNT(1:3) /FePc | 2.0 | 0.37 (PtRu) | 60 | HMT-PMBI | HMT-PMBI | 182 | [284] |
| Fe−N−Gra | 2.0 | 0.8 (PtRu) | 60 | HMT-PMBI | HMT-PMBI | 243 | [285] |
| Fe/IL-PAN-A1000 | 2.0 | 0.6 (PtRu) | 60 | HMT-PMBI | HMT-PMBI | 289 | [286] |
| FeCoNC-at | 2.0 | 0.6 (PtRu) | 60 | HMT-PMBI | HMT-PMBI | 415 | [287] |

### 7.3.3 Fe- and nitrogen-doped CDCs as catalysts for PEMFCs

As outlined in the literature overview, most of the work done on NPMCs and ORR catalysts overall so far has been in acidic conditions due to the availability of a commercial proton exchange membrane (Nafion™). Encouraged by the results achieved with M-N-CDCs in alkaline membrane fuel cells [VIII–X] the ORR activity of these materials was also studied in acidic conditions and in PEMFCs. The first part focuses on the creation of Fe-N-CDC materials from $B_4C$ and TiC and optimisation of iron content, the second part on SiC-derived catalysts and the reduction of particle size and the third part on composite catalysts from MWCNTs and CDCs derived either from $B_4C$, $Mo_2C$ or TiC and increasing stability.

Two CDCs with very different porosity were selected as the first starting materials for Fe-N-CDC catalysts for PEMFC. $B_4C$-derived carbon (CDC-1) is a micro/mesoporous material while TiC-derived carbon (CDC-2) is nearly fully microporous, as can be seen from Figure 64. The textural properties of both the starting materials and the Fe-N-C catalysts are given in Table 18. The main difference between the two starting CDC materials was in the pore size distribution, which is also demonstrated in Figure 64a. The CDC-1 material has a trimodal micro-mesoporous structure with a large amount of mesopores and micropores, while CDC-2 has a unimodal PSD centred at 0.5 nm. The average pore diameter was also accordingly higher for CDC-1 (1.65 nm) compared to CDC-2 (1.05 nm). As there have been various studies claiming that either micropores, mesopores or a combination of both are needed for efficient Fe-N-C catalysts [59,91,258,271,288,289], these CDCs might present an interesting opportunity to study the effect of PSD on Fe-N-C catalyst activity. However, the PSD of two Fe-N-C catalysts with 1 wt.% Fe and prepared identically except for the carbon support (CDC-1 and CDC-2) are quite similar (see Figures 64b–c), in spite of drastically different PSD of the starting CDCs. It is apparent from Table 18 that after ball-milling and pyrolysis in Ar, the specific surface area decreased by about 750–1200 $m^2 g^{-1}$. This may be explained either as a filling of the pores with Phen and Fe acetate or as partial graphitisation of the disordered carbon in CDC during the high-temperature pyrolysis. Iron nanoparticles are known to graphitise disordered carbon materials at high temperatures [214,277], thus closing off some of the pores and decreasing the BET surface area. The effect of Fe content on catalyst morphology and PSD was investigated only for CDC-2 (Table 18) since a much higher ORR activity was observed with CDC-2 derived Fe-N-C catalysts (see later). The effect of Fe content on decreased BET area is however unlikely the major effect at work here since even $Fe_{0.5}$-N/CDC-2, which has a minimum amount of particulate iron according to Mössbauer spectroscopy (see later), has a SSA of 945 $m^2 g^{-1}$, much lower than the starting SSA of 1997 $m^2 g^{-1}$ for CDC-2. Also, increasing the iron content from 0.5 to 2 wt.% in the pre-pyrolysis mixture results in a decrease of SSA of only about 250 $m^2 g^{-1}$, with all three Fe-N-C catalysts derived from CDC-2 having a BET area much lower than that of CDC-2 (Table 18).

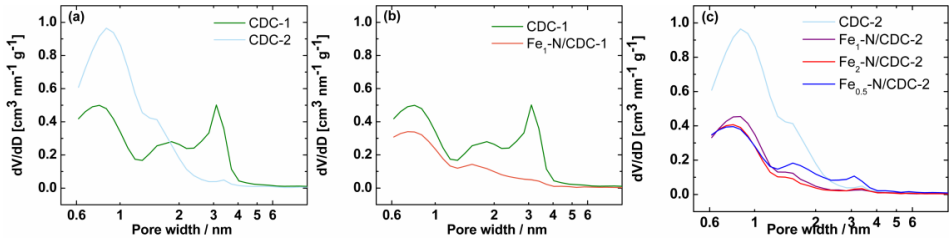


**Figure 64.** Comparison of pore size distributions for the undoped CDC (a), $B_4C$-derived (b) and TiC-derived (c) samples.

**Table 18**. Textural properties of CDC and Fe-N/CDC materials: BET surface area ($S_{BET}$), total pore volume ($V_{tot}$), average pore size ($d_p$), surface area ($S_{DFT}$ ) and micropore volume ($V_\mu$) calculated from the QSDFT model.

| Sample | $S_{BET}$, $m^2\ g^{-1}$ | $V_{tot}$, $cm^3\ g^{-1}$ | $d_p$, nm | $S_{DFT,}$ $m^2\ g^{-1}$ | $V_\mu$, $cm^3\ g^{-1}$ |
|---|---|---|---|---|---|
| CDC-1 | 1493 | 1.236 | 1.65 | 1351 | 0.470 |
| $Fe_1$-N/CDC-1 | 754 | 0.471 | 1.24 | 716 | 0.292 |
| CDC-2 | 1997 | 1.057 | 1.05 | 1759 | 0.811 |
| $Fe_1$-N/CDC-2 | 798 | 0.466 | 1.17 | 770 | 0.321 |
| $Fe_2$-N/CDC-2 | 706 | 0.427 | 1.21 | 709 | 0.280 |
| $Fe_{0.5}$-N/CDC-2 | 945 | 0.704 | 1.48 | 1009 | 0.397 |

In the previous chapters, DCDA, Fe and Co salts were used to dope microporous CDC materials, where the micropore volume of M-N-C catalysts relative to the starting CDC even increased by ca 0.2 $cm^3\ g^{-1}$ during the doping procedure [VIII]. The decrease in surface area observed here is thus much larger than that in our previous work. It can be proposed that Phen either fills the pores more effectively than DCDA, or that it transforms into residual carbon to a higher extent than DCDA. It is also possible that, contrary to DCDA, Phen blocks the pore entrances and in the end, most of the inner porosity is not accessible for electrocatalysis. Looking more closely at the changes in PSD from CDC to $Fe_1$-N/CDC, it can be seen that, with CDC-1, mesopores are nearly completely filled along with a small amount (ca 30%) of micropores while for CDC-2 ca 55–60% of the micropore volume is lost. This is likely due to the preferential filling of mesopores by Phen in CDC-1, while with CDC-2 only micropores are present and therefore all the Phen added during the synthesis fills those pores.

The $^{57}Fe$ Mössbauer spectra of the Fe-N-C catalysts derived from CDC-1 and CDC-2 were collected for a Fe content of 0.5 wt.% in the catalyst precursor. The low Fe content allows a better observation of quadrupole doublets that are assigned to $FeN_xC_y$ moieties. The effect of Fe content on the Fe speciation in CDC-2 derived materials (selected due to their higher ORR activity, see later) was then

investigated by measuring the spectra of the materials $Fe_1$-N/CDC-2 and $Fe_2$-N/CDC-2 as well. The Mössbauer spectra are shown in Figure 65. Compared to commonly reported spectra for Fe-N-C catalysts, the spectrum of $Fe_{0.5}$N/CDC-1 (Figure 65a) is unusual, especially for a catalyst with such a low Fe content and was fitted with a doublet and a sextet with unusual parameters. While the doublet has Mössbauer parameters similar to D1 commonly observed in ORR-active Fe-N-C catalysts, the sextet has, to the best of our knowledge, never been reported before in such catalysts. The average value of the sextet parameters were very similar to those reported for iron boride FeB with a hyperfine field of 9.5 Tesla [290,291].

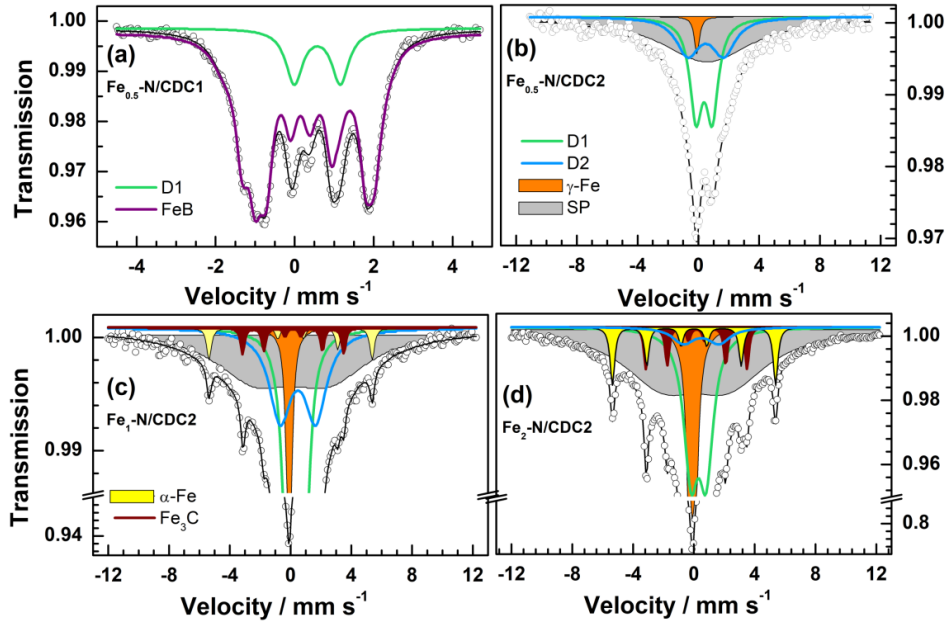


**Figure 65.** Room temperature $^{57}$Fe Mössbauer spectra of (a) $Fe_{0.5}$-N/CDC-1, (b) $Fe_{0.5}$-N/CDC-2, (c) $Fe_1$-N/CDC-2, (d) $Fe_2$-N/CDC-2. For (c) and (d), note that the Y-axis scale is broken in order to improve the visibility of the low intensity components of magnetic Fe (sextets) and of the doublets.

The formation of FeB is in agreement with the presence of boron in CDC-1 derived catalyst (see discussion on presence of boron later in the ICP-MS results section). Concerning the CDC-2 derived catalysts (Figure 65b–d), we observe a broad doublet assigned to superparamagnetic Fe-based (sub-)nanoparticle (labelled SP). The assignment of the broad SP doublet to Fe nanoparticles is supported by EXAFS measurements on $Fe_{0.5}$N/CDC-2 (Figure 66). Apart from this, the Mössbauer spectra of CDC-2 derived samples can be fitted with components usually observed in pyrolysed Fe-N-C catalysts, namely D1, D2, α-Fe, γ-Fe and $Fe_3C$. It can be seen from Figure 65 and Table 19 that the total absorption (%) of α-Fe, γ-Fe, $Fe_3C$ increases with increasing amount of iron precursor on CDC-2.

In summary, the striking difference between CDC-1 and CDC-2 derived catalysts (at 0.5% Fe level) is the low % area (13%) assigned to D1 in $Fe_{0.5}$-N/CDC-1 and the major presence of FeB, while $Fe_{0.5}$-N/CDC-2 comprised a large amount of doublets D1 and D2 (48%).

**Table 19.** Room-temperature Mössbauer parameters of the singlet and sextet components. IS, QS and LW are the isomer shift (relative to α-Fe at room temperature), quadrupole splitting and line width, given in mm $s^{-1}$, respectively. The hyperfine fields are 9.5, 33.3 and 20.6 Tesla for FeB, α-Fe and $Fe_3C$ respectively. IS, QS and LW values are given in mm $s^{-1}$.

| Sample | IS | QS | LW | % area | Label |
|---|---|---|---|---|---|
| (a) $Fe_{0.5}$-N/CDC-1 | 0.26 | 0.23 | 0.39 | 87 | FeB |
| (b) $Fe_{0.5}$-N/CDC-2 | –0.10 | 0.00 | 0.40 | 2 | γ-Fe |
| (c) $Fe_1$-N/CDC-2 | –0.09 | 0.00 | 0.34 | 8 | γ-Fe |
| | 0.17 | 0.00 | 0.30 | 2 | $Fe_3C$ |
| | 0.01 | 0.00 | 0.36 | 3 | α-Fe |
| (d) $Fe_2$-N/CDC-2 | –0.10 | 0.00 | 0.40 | 18 | γ-Fe |
| | 0.17 | 0.00 | 0.30 | 4 | $Fe_3C$ |
| | 0.01 | 0.00 | 0.36 | 6 | α-Fe |

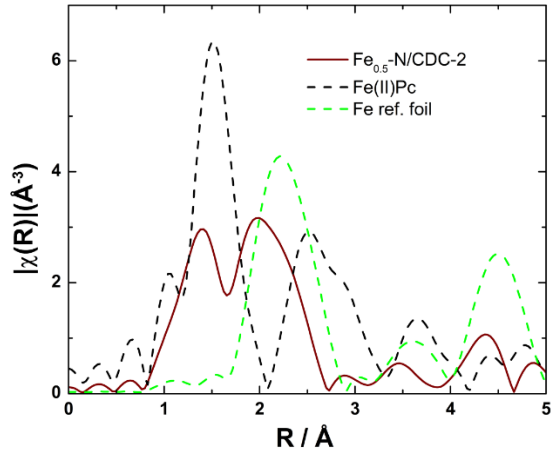


**Figure 66.** The FT-EXAFS of the sample $Fe_{0.5}$N/CDC-2, Fe(II)Pc, and iron foil (intensity reduced by a factor of 6 for the Fe foil, for comparison purpose).

The co-presence of the $FeN_xC_y$ and inorganic Fe species with relatively high content is verified by ex situ X-ray absorption spectroscopy (XAS). As seen in Figure 66, the FT-EXAFS of the $Fe_{0.5}$N/CDC-2 contains a scattering peak around

1.5 Å (without phase correction), overlapping the peak of Fe(II)Pc arisen from the first shell Fe-N scattering; as well as a scattering peak around 2 Å overlapping the first shell Fe-Fe scattering peak in metallic Fe. The high intensity of the Fe-Fe scattering peak supports the presence of high amount inorganic Fe species in the catalyst, which can be linked to the broad SP contribution.

The contents of Fe, B, Ti and Zr in the catalyst materials with 1% Fe at synthesis stage (baseline Fe content) were determined via ICP-MS (Table 20). Obviously, $Fe_1$-N/CDC-1 has a large content of $ZrO_2$ compared to smaller amounts present in the samples synthesised using CDC-2. This is likely due to the fact that there is a rather large amount of $B_4C$ still present in CDC-1 when compared to TiC content in CDC-2, as supported by the high content of B in CDC-1-derived material but low Ti content in CDC-2-derived materials. During the chlorination process, some of the carbide precursor ($B_4C$ or TiC in this case) can get trapped inside the carbon. As $B_4C$ and TiC are very hard (Mohs hardness of approximately 9–10 and 9–9.5, respectively) even compared to $ZrO_2$ (Mohs hardness of ~8), it is probable that, during the ball-milling process, the $ZrO_2$ balls and grinding jar are eroded by the sample, resulting in Zr contamination. The erosion effect also means that a small amount of boron is milled into the jar and balls themselves and can be transferred to other samples. Since $Fe_1$-N/CDC-1 has a larger amount of carbide particles still present, the resulting Zr content is also consequently higher. Regarding the iron contents, $Fe_1$-N/CDC-2 contained surprisingly nearly twice more iron than $Fe_1$-N/CDC-1, while both had the same amount of iron in the catalyst precursor mixture. For CDC-2 materials, the Fe content in catalysts increased linearly with Fe content in the precursors. It is to be noted that the iron concentrations are likely somewhat underestimated here due to the lack of a suitable reference material to confirm the total dissolution of the determined elements from the sample.

**Table 20.** Content of Fe, B, Ti and Zr in the Fe-N/CDC catalysts determined by ICP-MS.

| Sample | Fe wt.% | B wt.% | Ti wt.% | Zr wt.% |
|---|---|---|---|---|
| $Fe_1$-N/CDC-1 | 0.638 | 1.462 | 0.079 | 7.782 |
| $Fe_1$-N/CDC-2 | 1.242 | n.a | 0.148 | 0.192 |
| $Fe_2$-N/CDC-2 | 1.449 | n.a | 0.120 | 0.059 |
| $Fe_{0.5}$-N/CDC-2 | 0.490 | 0.120 | 0.06 | 1.640 |

The Fe-N/CDC materials were first investigated using the RDE setup for assessing the catalytic activity toward the ORR in acid. Figure 67 shows the ORR activity of the CDC-derived Fe-N/CDC materials along with the starting CDC, measured in $O_2$-saturated 0.5 M $H_2SO_4$ solution. The electrolyte was 0.5 M $H_2SO_4$ for Fe-N/CDC catalysts, but for comparison, 0.1 M $HClO_4$ was used for the Pt/C material to avoid activity loss caused by bisulphate adsorption on Pt [292]. Modifying the CDC materials with iron and nitrogen shifts positively the $E_{onset,}$ nearly 300 mV, showing a massive increase in the ORR electrocatalytic activity.

Also, the $E_{1/2}$ for $O_2$ reduction shifted from ca 0.4 to ca 0.8 V vs RHE. The rise in activity is due to a large concentration of Fe-$N_x$ centres formed in the pores of the CDC materials during the pyrolysis procedure, while both starting CDCs have very low ORR activity themselves. Next, the RDE results show that $Fe_1$-N/CDC-2 has a higher ORR activity than $Fe_1$-N/CDC-1. Remarkably, both the values of $E_{onset}$ and $E_{1/2}$ were almost identical for all three CDC-2 based catalysts, showing no significant dependence of overall ORR activity on the iron content in the range of 0.5–2% Fe in the precursor (0.49 to 1.45 wt.% Fe in catalysts, see Table 20) Although the iron content rose by 0.95 wt.% when going from 0.5 wt.% to 2 wt.% of iron in the CDC-2 catalyst precursors, the relative % of iron in the form of D1 and D2 species (the ORR-active species) decreased from 48% to 26% (see Table 20). Thus, the iron added above 0.5% level in the catalyst precursor is present mainly in the form of inorganic iron species rather than $FeN_xC_y$ sites in the final CDC-2-derived catalysts. Comparing the two CDCs, the higher activity of $Fe_1$-N/CDC-2 than $Fe_1$-N/CDC-1 likely arises in part from the larger absolute amount of microporous surface area in CDC-2 vs CDC-1 and the nearly twice higher amount of micropore volume (see Figure 64a). For comparison with similar Fe content in the catalysts, the samples $Fe_{0.5}$-N/CDC-2 and $Fe_1$-N/CDC-1 should be compared (see Table 20). This comparison also reveals a much higher activity for the CDC-2 derived material. Other factors, such as the structural differences and Fe speciation differences coming from the increased content of iron or larger nitrogen content of the catalyst containing less Fe, could also be contributing factors to the increase in kinetic current density. The apparent correlation between activity and micropore surface area may also be a consequence of the different Fe speciation during pyrolysis, metallic Fe particles (present in highly loaded samples) leading to partial graphitization and thus to decreased microporous surface area. For ORR in acid medium, Fe particles encapsulated in carbon are generally accepted to be less active (on a metal-atom basis) than surface Fe-$N_x$ sites.

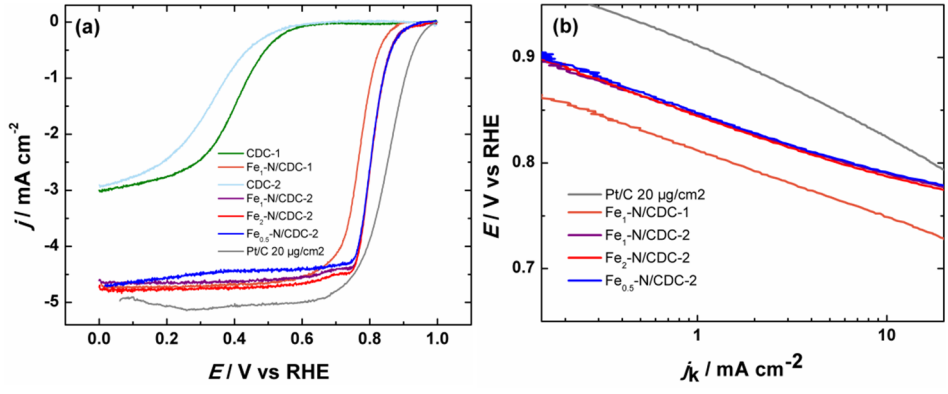


**Figure 67.** (a) ORR polarisation curves (not corrected for iR) measured with RDE method for undoped CDCs, $B_4C$-derived and TiC-derived catalysts in $O_2$-saturated 0.5 M $H_2SO_4$. $\nu$ = 10 mV $s^{-1}$, $\omega$ = 1600 rpm. (b) Tafel plots calculated from the RDE data shown in (a). Catalyst loading = 803 µg $cm^{-2}$, except Pt/C (20 $\mu g_{Pt}$ $cm^{-2}$).

Also of note is the introduction of $ZrO_2$ into $Fe_1$-N/CDC-1, which was not present in high concentration in the catalysts derived from CDC-2. The introduction of $ZrO_2$ seems to result from the combination of milling process and residual presence of hard $B_4C$ in CDC-1. The presence of $B_4C$ in CDC-1 probably also explains the different Fe speciation seen in the CDC-1 derived Fe-N-C catalyst, with a major content of FeB (Figure 65a).

Figure 68 shows the results of stability testing on $Fe_{0.5}$-N/CDC-2. As seen, 10,000 cycles between 0.925 and 0.6 V vs RHE have no effect on the onset potential, while the shape of the polarisation curve and $E_{1/2}$ are minimally influenced. The small loss in activity is likely due to the dissolution of very small amounts of Fe species with a lower durability in acid media, which were noted from the Mössbauer spectra.

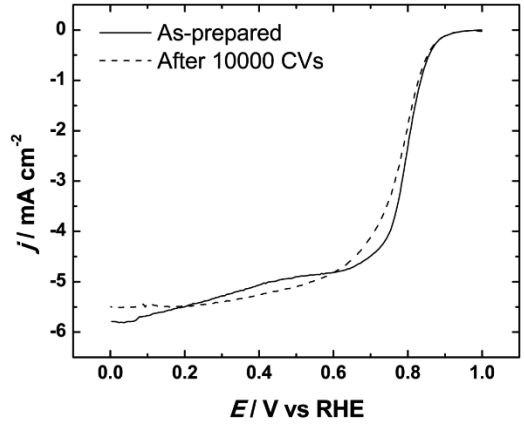


**Figure 68.** ORR polarisation curves of $Fe_{0.5}$-N/CDC-2-modified GC electrodes in $O_2$-saturated 0.5 M $H_2SO_4$ before and after 10,000 CVs. $v$ = 10 mV $s^{-1}$, $\omega$ = 1600 rpm.

The electrocatalytic activity of the three CDC-2 based catalysts toward the ORR in acid media is comparable to some of the best Fe-N-C catalysts found in the literature [43,44,271,293,294]. Within the series of 3 catalysts derived from CDC-2, there is some correlation between i) ORR activity and SSA, and ii) between activity and micropore volume, as shown in Figure 69a.

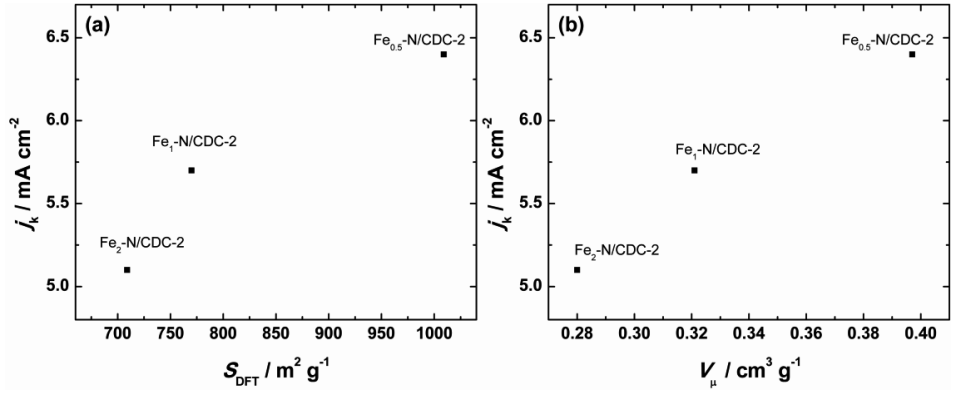


**Figure 69.** The dependence of kinetic current densities on the specific surface area (a) and micropore volume (b) for the three CDC-2 derived Fe-N-C catalysts.

As the Mössbauer spectra also showed for CDC-2 derived catalysts, increasing the iron content did not introduce a much larger amount of Fe-$N_x$ sites, but rather increased the amount of γ-iron, iron carbides and α-iron. Since the increase of these crystallographic iron species did not positively affect the electrocatalytic activity of the catalysts toward oxygen reduction, it can be derived that the ORR activity of the Fe-N/CDC materials originates mainly from $FeN_xC_y$ moieties (doublet component D1 or D2, or some of these two doublet components). Because iron particles, especially those not perfectly covered by carbon layers, can create problems in PEFCs by releasing iron ions and promoting the Fenton's reaction [255], it is therefore preferable to select the catalyst with lower iron loading, i.e. $Fe_{0.5}$-N/CDC-2, and showing the highest electrocatalytic activity (Figure 69).

The same trend of higher activity for CDC-2 derived materials *vs* CDC-1 derived materials was observed in fuel cell measurements, as shown in Figure 70. The catalysts derived from CDC-2 resulted in *ca* 3–4 times higher current density at 0.8 V cell voltage (5–6 *vs* 20 mA $cm^{-2}$), whereas the current density in RDE was nearly 5 times higher at 0.8 V. Most of the active sites in these materials are also likely located deep inside the catalyst grains as the Fe content determined by ICP-MS is much higher than on the surface, since iron was not even detected by XPS (data not shown). It is obviously not optimal to have most of the active sites located deep inside a microporous particle, where the access by $O_2$ is difficult [87,263]. The power performance at 0.6 V could possibly be improved by decreasing the grain size of the catalyst, either by starting off with a finer carbide or ball-milling the CDC using a high rotation rate, liquid ball-milling or even surfactants in the milling mixture, all of which are known to be useful for obtaining smaller particle sizes [295] or optimising the PEMFC cathode catalyst layer (these strategies were later used in [XIV]). Assuming the most active sites for ORR in acid medium are represented by the two doublets in Mössbauer spectroscopy (assigned to $FeN_x$ sites), and assessing the bulk density of $FeN_x$ sites by multiplying the fraction of (D1+D2) from Mössbauer table by the bulk Fe

contents measured by ICP-MS, one gets the following values: 0.24 wt.% ($Fe_{0.5}$-N/CDC-2), 0.54 wt.% ($Fe_1$-N/CDC-2) and 0.38 wt.% ($Fe_2$-N/CDC-2) of Fe-$N_x$. Considering the significant differences in elemental composition, iron species, porosity and structure, the ORR activity for the $Fe_x$-N/CDC-2 catalysts is remarkably similar. Elucidating this further would, however, require a thorough study on the kinetics of the ORR on these catalysts and quantification of available active sites, which is outside the scope of the present work.

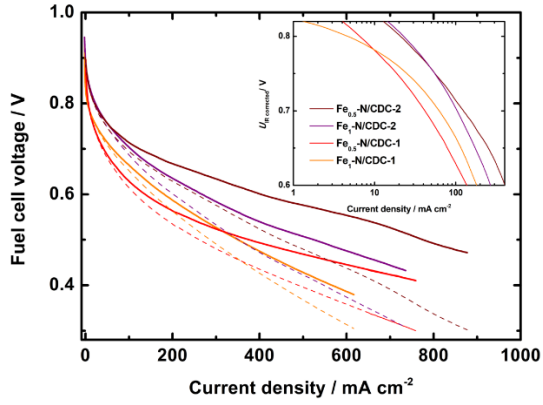


**Figure 70.** PEMFC polarisation curves with cathodes comprising 4 mg $cm^{-2}$ of Fe–N–C catalysts, as-measured (dashed curves) and after iR-correction (solid curves). The fuel cell temperature was 80 °C, pure $O_2$ and $H_2$ gases were humidified at 100% RH at cell temperature, the gas pressure was 1 bar. Inset: Tafel plots at high potential of iR-free polarisation curves.

Thus it was shown that high-performance ORR catalysts can be synthesised by ball-milling a mixture of a CDC, Phen and iron(II) acetate [XI]. However, it was also evident that the ball-milling and/or the addition of Phen as a pore filler decreased the CDC surface area, by more than a half in some cases. This effect has also been reflected in studies by others on catalysts derived from CDCs [296–298]. To shed light to this, the effect of both the pore filler and ball-milling conditions to the SSA, the porosity, and the ORR activity was studied. Some strategies are also presented to alleviate the loss of porosity in the pristine CDC during those synthetic steps, while still retaining the positive effects from the ball-milling and doping procedure. More details on the synthesis methods is available in section 6.6.

Figure 71 displays the $N_2$ adsorption/desorption isotherms for the pristine SiCDC and catalyst materials synthesised from it. Figure 71a shows a comparison of the isotherms for catalysts made from precursor mixtures ball-milled at different rotation rates. It is evident that as the rotation rate increases, the porosity of the resulting catalyst is gradually decreasing. The ball-milling obviously has an effect on the textural properties of catalyst materials as some of the pores are crushed due to the shock, but the Fe and N doping also has a large effect as $Fe_{0.5}$-$Phen_{20}$-SiCDC-wet has almost the same porosity as the catalyst ball-milled

at 200 rpm. Since Phen acts as pore filler here, it also closes some pores during milling process and pyrolysis. In the 100 rpm ball-milled catalyst, the precursors are likely not as well distributed on the CDC surface (Phen molecules did not fill the CDC micropores) and thus close less micropores. The bulk structure of the carbon is less disrupted as well, as seen from the XRD patterns, where the graphitic peak gradually increases as the rotation rate of the ball-mill decreases. The SSA also followed the same trend (Table 21): ball-milling at 800 rpm decreases the SSA by over two thirds with respect to pristine CDC, while decreasing the rotation rate to 100 rpm gives an SSA decrease of only around 15%.

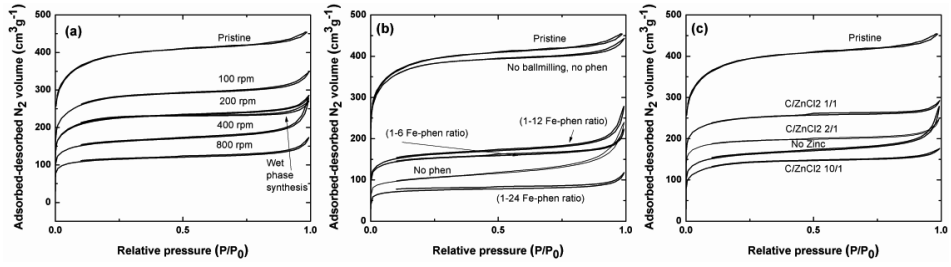


**Figure 71.** $N_2$ adsorption/desorption isotherms for (a) catalyst precursors milled at different rotation rates, (b) different amounts of 1,10-phenantroline in the catalyst precursor mixture and (c) different amounts of $ZnCl_2$ in the catalyst precursor mixture.

**Table 21.** Specific surface areas of the CDC material and the synthesised catalysts.

| Catalyst | SSA ($m^2\ g^{-1}$) |
|---|---|
| SiCDC | 1361 |
| $Fe_{0.5}$-$Phen_{20}$-SiCDC-wet | 829 |
| $Fe_{0.5}$-$Phen_{20}$-SiCDC 100 rpm | 1019 |
| $Fe_{0.5}$-$Phen_{20}$-SiCDC 200 rpm | 817 |
| $Fe_{0.5}$-$Phen_{20}$-SiCDC 400 rpm | 579 |
| $Fe_{0.5}$-$Phen_{20}$-SiCDC 800 rpm | 419 |
| $Fe_{0.5}$-$Phen_{11}$-SiCDC 400 rpm | 548 |
| $Fe_{0.5}$-$Phen_{33}$-SiCDC 400 rpm | 271 |
| $Fe_{0.5}$-$Phen_{20}$-SiCDC-Zn0.1 400 rpm | 511 |
| $Fe_{0.5}$-$Phen_{20}$-SiCDC-Zn0.5 400 rpm | 691 |
| $Fe_{0.5}$-$Phen_{20}$-SiCDC-Zn1.0 400 rpm | 912 |

To elucidate the different effects of the pyrolysis, Phen and ball-milling on the porosity, we optimised the amount of Phen in the precursor mixture and studied its effect on the $N_2$ adsorption isotherms. The amount of Phen in the baseline catalyst precursor formulation (20 wt.%, i.e. 12 Phen molecules per each iron atom) is higher than what is theoretically needed for full complexation of Fe by 6 N atoms (3/1 molar ratio of Phen/Fe). As can be seen from Figure 71b both a smaller and a larger amount of Phen relative to the baseline formulation lead to decreased porosity in the final catalysts. For the increased Phen amount, the effect can be explained simply: more pore filler means that more of the pores are closed off and the amount of $N_2$ adsorbed/desorbed decreases. Interestingly, decreasing the Phen amount in the precursor mixture also decreases the SSA and porosity, which can likely be due to the Phen acting as softening the ball-mill effect: by partially filling the micropores, the Phen molecules mechanically support the pores during the milling, avoiding their complete collapse. During the subsequent pyrolysis, Phen is transformed in a porous carbon domain within micropores, thereby reopening (at least partially) the micropores initially present in CDC. This was also confirmed by ball-milling the CDC alone, without any added Phen, which gave lower porosity than that of both the 12/1 and 6/1 Phen/Fe ratio. Phen also has a profound effect on the catalyst activity toward the ORR, as will be shown later. The effect of pyrolysis on the porosity was confirmed to be rather minor compared to the ball-milling, with very little porosity loss from simply pyrolyzing the CDC (Figure 71b).

To retain the porosity of the catalysts, and thus secure access of $O_2$ to the active sites, while still using the ball-milling method for homogenising the CDC, Phen and Fe precursors, we added $ZnCl_2$ to the precursor mixture. $ZnCl_2$ is a known pore forming agent used to increase the porosity of carbon materials [299]. As can be seen from Figure 71c, using a small amount of $ZnCl_2$ in the precursor mixture slightly decreases the porosity, but as the zinc-to-carbon ratio is increased, the effect on the porosity becomes positive, with the material with a 1/1 $ZnCl_2$/C mass ratio having a SSA of 912 $m^2\ g^{-1}$, much higher compared to the material similarly prepared except for the lack of $ZnCl_2$, 579 $m^2\ g^{-1}$. Adding $ZnCl_2$ decreases the $ZrO_2$ contamination somewhat as well, since it acts as an additional buffer. It is also evident that there are no crystalline Zn-containing compounds in the material left over from the $ZnCl_2$ (Figure 71c).

The Fe and Zr contents in the catalyst materials are given in Table 22. The iron content was around 0.5 wt.% in all of the materials, with the ones having more Zn in the starting mixture seeing an increase in the Fe content, since Zn etches some of the carbon during pyrolysis, while creating porosity and thus the overall Fe content is increased. All of the materials also contained Zr, with the Zr content rising with the ball-mill rotation rate up to point. Adding Zn into the precursor mixture decreased the Zr content since there was more material in the jar, which buffered the milling somewhat as also seen from the BET results.

**Table 22.** Fe and Zr contents in the catalyst materials determined by ICP-MS.

| Catalyst | Fe wt.% | Zr wt.% |
|---|---|---|
| $Fe_{0.5}$-$Phen_{20}$-SiCDC 100 rpm | 0.45 | 0.67 |
| $Fe_{0.5}$-$Phen_{20}$-SiCDC 200 rpm | 0.53 | 0.72 |
| $Fe_{0.5}$-$Phen_{20}$-SiCDC 400 rpm | 0.66 | 3.59 |
| $Fe_{0.5}$-$Phen_{20}$-SiCDC 800 rpm | 0.51 | 2.61 |
| $Fe_{0.5}$-$Phen_{20}$-SiCDC-Zn0.1 400 rpm | 0.49 | 0.21 |
| $Fe_{0.5}$-$Phen_{20}$-SiCDC-Zn0.5 400 rpm | 0.66 | 0.96 |
| $Fe_{0.5}$-$Phen_{20}$-SiCDC-Zn1 400 rpm | 0.74 | 0.99 |

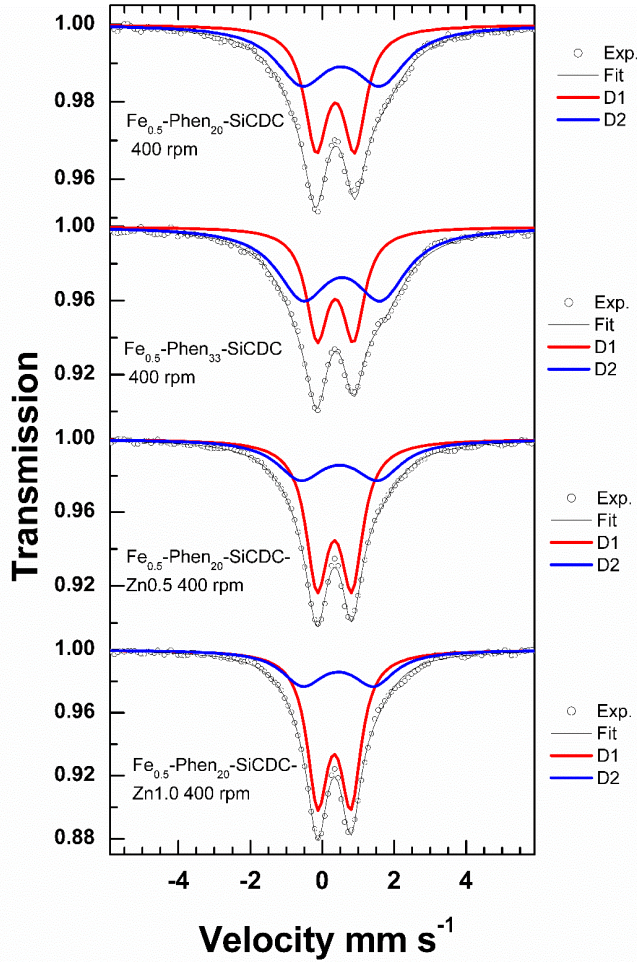


**Figure 72.** $^{57}$Fe Mössbauer spectra of the synthesised catalysts.

The results of the $^{57}$Fe Mössbauer spectroscopy on selected catalysts are given in Figure 72 and Table 23. The first catalyst selected was $Fe_{0.5}$-$Phen_{20}$-SiCDC 400 rpm, which gave the highest activity in RDE mode. $Fe_{0.5}$-$Phen_{33}$-SiCDC 400 rpm was also analysed by Mössbauer spectroscopy, to see if including more Phen into the starting mixture increases or decreases the concentration of some iron species. Finally, two samples synthesised in the presence of $ZnCl_2$ were included to determine whether the notable improvement on activity in PEMFC (discussed later) was due to only increased porosity or also different iron speciation. The selected samples that were characterised by Mössbauer spectroscopy contain only atomically dispersed $FeN_x$ moieties, as shown by the sole presence of quadrupole doublets D1 and D2 in their spectra. No particulate iron phases were detected. Interestingly, the D1/D2 ratio varied a lot among the three selected samples, ranging from 0.68 to 2.14. The D1 doublet is known to correspond to Fe-$N_x$ moieties on the surface, while D2 corresponds either to sites buried deeper in the carbon structure and/or to surface sites also. Increasing the Phen content in the starting catalyst mixture has a clear effect on the distribution of active sites: increasing the Fe to Phen ratio decreases the D1/D2 ratio, which might be interpreted as decreased relative amount of active sites on the surface. Because the Phen is taken in excess, some of it will cover or surround the created Fe-Phen complexes. During the pyrolysis procedure, this Phen will be converted into carbon, which will then stay on top of some of the active sites and will also close some of the porosity (as seen from the BET results). In contrast to the Phen addition effect, adding $ZnCl_2$ in the mixture increased the D1/D2 ratio (Figure 72). This can be interpreted as the Zn addition leading to exposing more $FeN_x$ sites on the surface, all other parameters of the synthesis being otherwise similar.

**Table 23.** Room-temperature Mössbauer parameters of the doublet components. IS, QS and LW are the isomer shift (relative to α-Fe at room temperature), quadrupole splitting and line width, respectively.

| Sample | IS (mm/s) | QS (mm/s) | LW (mm/s) | Abs (%) | D1/D2 | Assign. |
|---|---|---|---|---|---|---|
| $Fe_{0.5}$-$Phen_{20}$-SiCDC 400 rpm | 0.36 | 1.07 | 0.77 | 48.5 | 0.94 | D1 |
| | 0.53 | 2.19 | 1.74 | 51.5 | | D2 |
| $Fe_{0.5}$-$Phen_{33}$-SiCDC 400 rpm | 0.36 | 1.01 | 0.74 | 40.4 | 0.68 | D1 |
| | 0.55 | 2.17 | 1.73 | 59.6 | | D2 |
| $Fe_{0.5}$-$Phen_{20}$-SiCDC-Zn0.5 400 rpm | 0.34 | 0.97 | 0.75 | 63.4 | 1.74 | D1 |
| | 0.47 | 2.15 | 1.58 | 36.6 | | D2 |
| $Fe_{0.5}$-$Phen_{20}$-SiCDC-Zn1.0 400 rpm | 0.33 | 0.92 | 0.70 | 68.1 | 2.14 | D1 |
| | 0.45 | 1.98 | 1.41 | 31.9 | | D2 |

Figure 73 shows the ORR polarisation curves of catalysts synthesised by ball-milling at different rotation rates of the ball-mill. It can be seen that as the rotation rate increases, the diffusion-limited current density values increase (up to 400 rpm), which can be due to two factors: either the reactants for creating active sites are better dispersed on the CDC particles or the particles themselves are decreased in size, in both cases leading to an increase in active surface on the electrode. At 800 rpm, the rotation rate is likely so high that the carbon structure on the surface of the CDCs is disrupted too much, decreasing the activity again. As is seen from the ICP-MS results, the amount of $ZrO_2$ is increased as well with increasing the rotation rate.

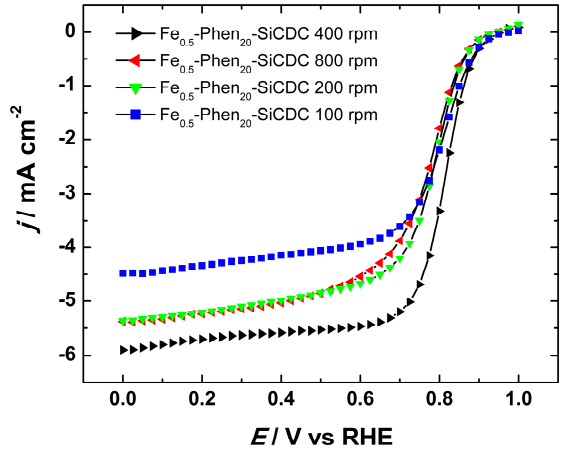


**Figure 73.** Steady-state ORR polarisation curves of the catalysts synthesised using different rotation rates for the ball-mill recorded in $O_2$-saturated 0.5 M $H_2SO_4$ solution. $\omega$ = 1600 rpm.

Since $ZrO_2$ is known to be somewhat active toward the ORR and could thus be the reason for the higher diffusion-limited currents in the case of catalysts milled at a higher rpm of the ball-mill, we decided to conduct RRDE experiments to examine the effect of $ZrO_2$ in the Fe-N-CDC catalysts. Figure 74 shows the RRDE results for three catalysts: One synthesised without any ball-milling, thus containing no $ZrO_2$, one ball-milled at 100 rpm with a very small $ZrO_2$ content and the most active Fe-N-CDC, which was ball-milled at 400 rpm. $ZrO_2$ is known to create high amounts of $H_2O_2$ as a side product [300,301]. As can be seen from the results, both of the ball-milled catalysts had a very small amount of peroxide produced (1–2%) while the catalyst synthesised via wet-phase synthesis produced around 3 times as much $H_2O_2$. This means that either $ZrO_2$ has no contribution to the ORR activity or that the amount of $ZrO_2$ is not enough to create significant peroxide. It also gives proof that ball-milling is needed for a highly selective Fe-N-CDC catalyst.

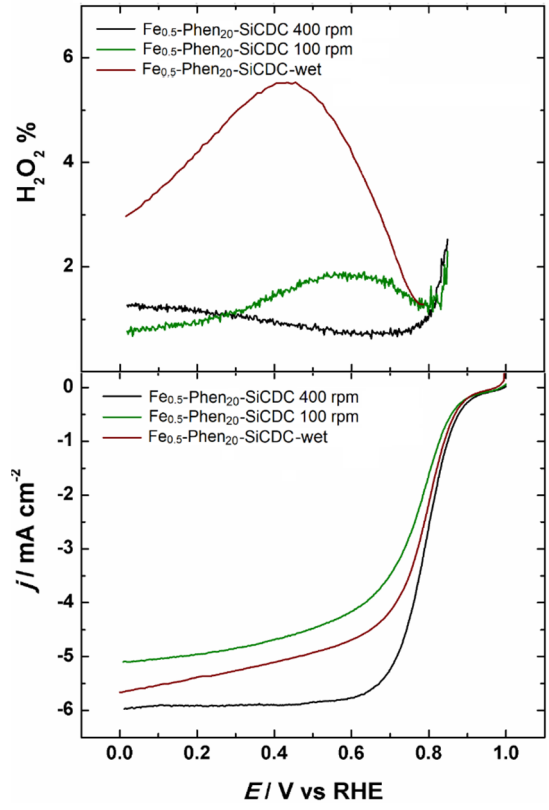


**Figure 74.** Steady-state ORR polarisation curves and $H_2O_2$ yields of the catalysts synthesised using different rotation rates for the ball-mill or via wet-phase synthesis recorded in $O_2$-saturated 0.5 M $H_2SO_4$ solution. $\omega$ = 1600 rpm.

Figure 75 shows the effect of changing the amount of Phen in the catalyst precursor mixture. A Phen-to-iron molar ratio of 12-1 was found to be optimal, while either decreasing or increasing the Phen-to-Fe ratio decreased both the $E_{1/2}$ value and diffusion-limited current density for $O_2$ reduction on the resulting catalysts noticeably. This is likely related to the porosity results, as discussed: more Phen than optimal closes off too much of the porosity, while a very small Phen-to-Fe ratio means that more of the porosity of the CDC is crushed during the ball-milling process. By using more Phen, the ratio of surface Fe-$N_x$ sites to those deeper in the carbon matrix also lowered, which also decreased the activity somewhat.

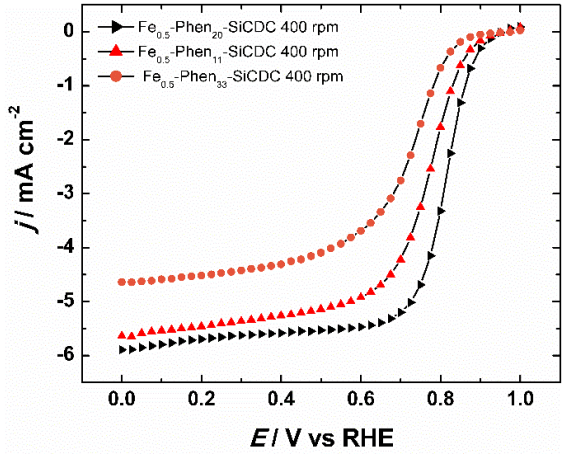


**Figure 75.** Steady-state ORR polarisation curves of the catalysts synthesised using different amounts of Phen recorded in $O_2$-saturated 0.5 M $H_2SO_4$ solution. $\omega$ = 1600 rpm.

Figure 76 shows the effect of $ZnCl_2$ addition to the catalyst precursor mixture in various amounts. The RDE results show little variation as the $ZnCl_2$-to-CDC ratio is increased from 0.1 to 1, with the $E_{1/2}$ value being nearly the same and the diffusion-limited current densities almost unchanged as well, which is surprising considering the effect on the porosity and the difference in the D1/D2 ratios.

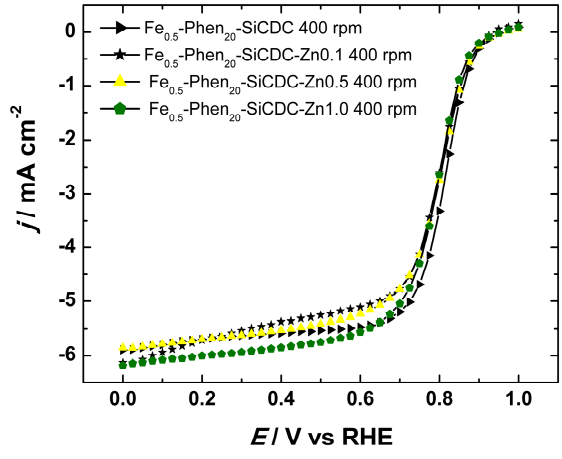


**Figure 76.** Steady-state ORR polarisation curves of the catalysts synthesised using different amounts of $ZnCl_2$ in the catalyst precursor mixture recorded in $O_2$-saturated 0.5 M $H_2SO_4$ solution. $\omega$ = 1600 rpm.

The single-cell $H_2/O_2$ PEMFC polarisation results are shown in Figure 77 and Table 24. The trend of activity follows more or less the trend of porosity: the catalysts with higher porosity, such as the ones synthesized with $ZnCl_2$ addition are much more active than the ones with lower porosities such as the catalyst synthesised with a rotation rate of 800 rpm. The positive correlation between fuel cell activity and the D1/D2 ratio also suggest either that a higher fraction of the $FeN_x$ sites in the Zn-added catalysts are surface sites, or that D1 corresponds to $FeN_x$ sites with a higher TOF than the D2 sites. $Fe_{0.5}$-$Phen_{20}$-SiCDC 100 rpm and especially $Fe_{0.5}$-$Phen_{20}$-SiCDC-wet perform very well in the kinetic region, with the catalyst synthesised in an ethanol suspension without ball milling showing even higher activity at 0.8 V than the ball-milled ones, but fall off very quickly with decreasing potential, likely due to the catalyst particle size being very large because it was not ball-milled or ball-milled at a too low rotation rate. $Fe_{0.5}$-Phen-SiCDC 800 rpm, in turn, has a low performance at high potential, but performs comparatively better at high current densities. $Fe_{0.5}$-$Phen_{20}$-SiCDC 400 rpm showed the highest current at 0.8 V in PEMFC, as it did in RDE testing from the non-$ZnCl_2$ ball-milled materials. $Fe_{0.5}$-$Phen_{20}$-SiCDC-Zn1.0 400 rpm had more than 4 times the current density at 0.8 V when compared to $Fe_{0.5}$-$Phen_{20}$-SiCDC 400 as well as much increased performance at lower potentials, confirming $ZnCl_2$ addition as a successful strategy to increase the ORR performance of this type of materials. Still, the performance is well below that of the commercial Pt/C, which can be ascribed to the very large particle size of CDCs.

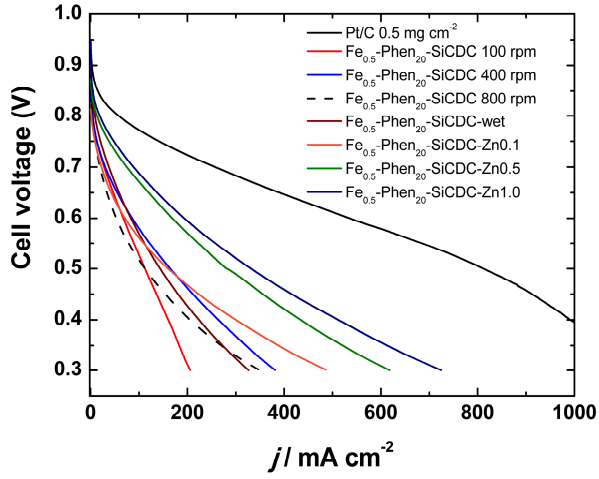


**Figure 77.** Nafion 211 PEMFC $H_2/O_2$ single cell test results with different Fe-N-SiCDC or a Pt/C commercial cathode. The anode was a commercial Pt/C catalyst with 0.5 mg $cm^{-2}$ loading. $T$ = 80 °C, 100% RH, pressure 1.5 bar.

**Table 24.** Kinetic current densities at 0.8 V in the RDE experiment and current densities at 0.8 V in PEM fuel cells using the Fe-N-CDC catalysts.

| Catalyst | $j_{k,\ 0.8\ V,\ RDE}$ (mA cm$^{-2}$) | $j_{0.8\ V,\ MEA}$ (mA cm$^{-2}$) |
|---|---|---|
| $Fe_{0.5}$-Phen-SiCDC 100 rpm | 4.3 | 4.3 |
| $Fe_{0.5}$-Phen-SiCDC 400 rpm | 7.6 | 4.5 |
| $Fe_{0.5}$-Phen-SiCDC 800 rpm | 2.7 | 4.4 |
| $Fe_{0.5}$-Phen-SiCDC-wet | 3.9 | 8.4 |
| $Fe_{0.5}$-Phen-SiCDC 800-Zn0.1 | 4.5 | 1.1 |
| $Fe_{0.5}$-Phen-SiCDC 800-Zn0.5 | 5.2 | 13.0 |
| $Fe_{0.5}$-Phen-SiCDC 800-Zn1.0 | 4.6 | 18.5 |

Learning from the deficiencies shown by the catalysts in PEMFC tests in [XI, XII] we adapted the strategy of creating composites which worked rather well in AEMFC [X] to three new CDCs for ORR electrocatalysis in acid media. The synthesis method is similar to the one presented in [X], with more details available in section 6.6.

For understanding the changes in the catalyst morphology during the synthesis process, all of the starting CDC materials and the synthesised catalysts were studied using SEM. Figure 78a shows a close-up of the surface of the CDC-1 material, while Figure 79a shows the larger CDC particles. The boron-carbide derived material has a heterogeneous particle size distribution, with most particles having a diameter under 1 μm. Figure 78b and 79b show the morphology of the $Mo_2C$-derived CDC-2. This CDC has an uneven disordered surface and a networked structure of larger grains with smaller particles in between, with large channels also visible in Figure 79b. The TiC-derived CDC-3, which is shown in Figures 78c and 79c, had the largest particle size, with most particles larger than 1 μm. The CDC materials doped using Phen and $Fe(OAc)_2$ are shown in Figures 78d–f and 79d–f. All of the catalysts have a rather similar morphology after ball-milling and pyrolysis, with the particle size drastically decreased, while the surface of the catalysts remains similar to the undoped CDC. Figures 78g–i and 79g–i show the morphology and surface of the composite materials. After addition of CNTs and further doping using DCDA and $Fe(OAc)_2$, the iron and nitrogen doped CDC grains, most of which are smaller than 100 nm by that point, are placed between a network of Fe,N-doped carbon nanotubes. The creation of larger channels between the CNTs, (also reflected in the BET results, where the average pore diameter increases nearly 3 times for Fe-Phen-Comp-1 and Fe-Phen-Comp-2 or even over 4 times for Fe-Phen-Comp-3) leading up to micro/mesoporous CDC particles, creates very good conditions for oxygen transport in the catalyst layer.

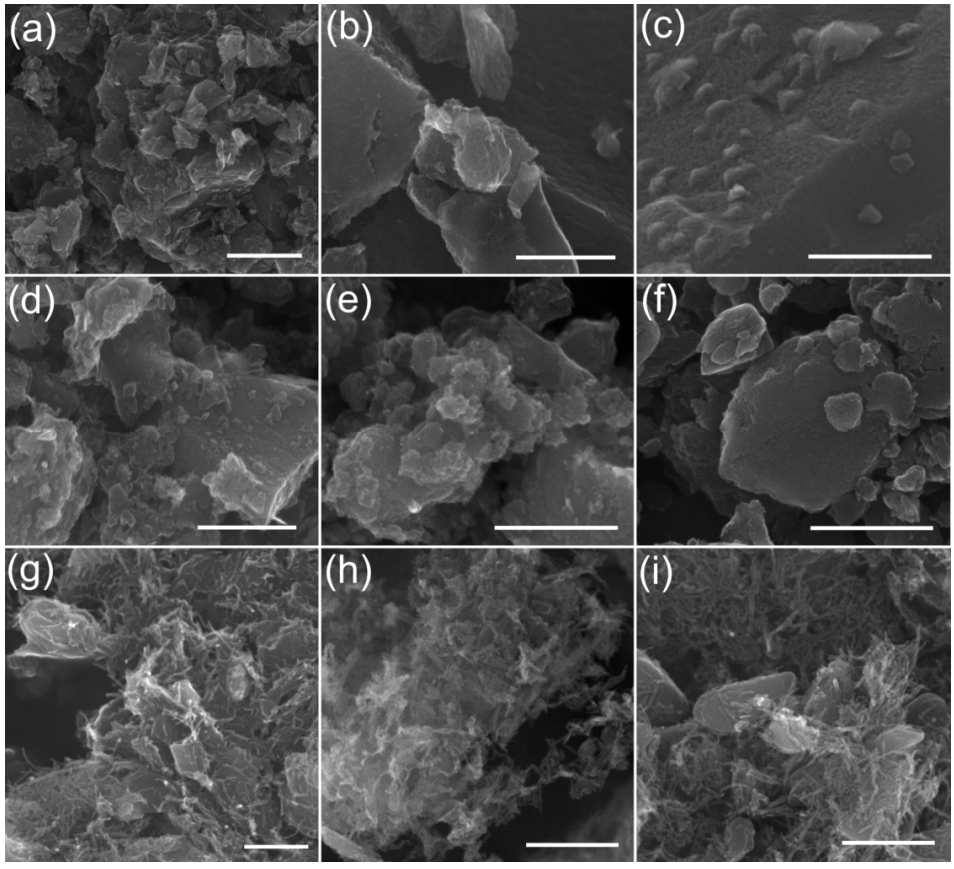


**Figure 78.** SEM micrographs of (a) CDC-1, (b) CDC-2, (c) CDC-3, (d) Fe-Phen-CDC-1, (e) Fe-Phen-CDC-2, (f) Fe-Phen-CDC-3, (g) Fe-Phen-Comp-1, (h) Fe-Phen-Comp-2 and (i) Fe-Phen-Comp-3. Scale bar is 400 nm for all the Figures.

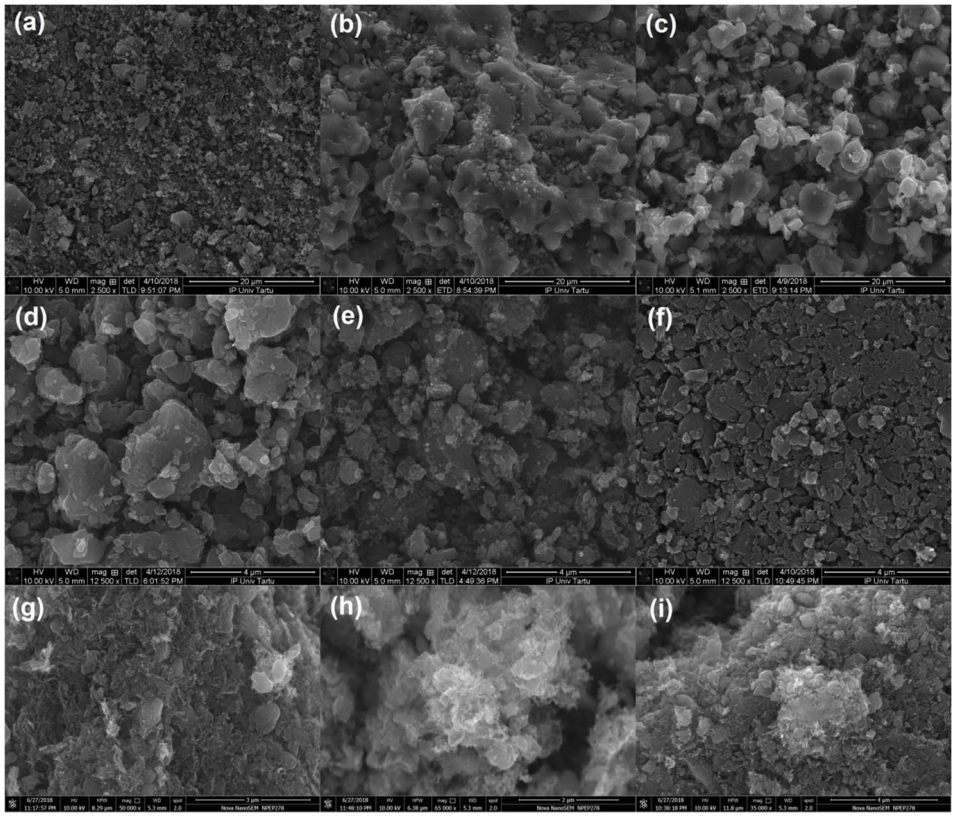


**Figure 79.** SEM micrographs of (a) CDC-1, (b) CDC-2, (c) CDC-3, (d) Fe-Phen-CDC-1, (e) Fe-Phen-CDC-2, (f) Fe-Phen-CDC-3, (g) Fe-Phen-Comp-1, (h) Fe-Phen-Comp-2 and (i) Fe-Phen-Comp-3.

The textural properties of the undoped CDCs, CDCs after doping with Phen and iron(II) acetate and the composite materials are given in Table 25, while the PSDs are shown in Figure 80. All of the starting CDCs purposefully had a similar SSA, while the pore size distribution (PSD) is very different: the boron carbide-derived CDC-1 is the most mesoporous with a trimodal PSD and an average pore diameter of 1.4 nm, the molybdenum carbide-derived CDC-2 is mesoporous as well, but also has significant microporosity with an average pore diameter of 1.6 nm. The titanium carbide-derived CDC-3 is highly microporous with the smallest total pore volume and a $d_p$ of 1.3 nm.

**Table 25.** Porosity characteristics of the carbide-derived carbon and Fe-Phen-C materials: surface area ($S_{DFT}$) and volume of micropores ($V_{\mu}$) calculated according to the QSDFT model, total pore volume ($V_{tot}$), BET surface area ($S_{BET}$) and average pore diameter ($d_p$).

| Catalyst | $S_{DFT}$, $m^2\ g^{-1}$ | $V_{tot}$, $cm^3\ g^{-1}$ | $V_{\mu}$, $cm^3\ g^{-1}$ | $S_{BET}$, $m^2\ g^{-1}$ | $d_p$, nm |
|---|---|---|---|---|---|
| CDC-1 | 1568 | 1.25 | 0.64 | 1802 | 1.6 |
| CDC-2 | 1501 | 0.98 | 0.65 | 1735 | 1.3 |
| CDC-3 | 1572 | 0.75 | 0.63 | 1512 | 1.0 |
| Fe-Phen-CDC-1 | 461 | 0.34 | 0.19 | 501 | 1.5 |
| Fe-Phen-CDC-2 | 446 | 0.32 | 0.18 | 454 | 1.4 |
| Fe-Phen-CDC-3 | 936 | 0.50 | 0.37 | 907 | 1.1 |
| Fe-Phen-comp-1 | 408 | 0.73 | 0.11 | 404 | 3.6 |
| Fe-Phen-comp-2 | 239 | 0.43 | 0.06 | 267 | 3.6 |
| Fe-Phen-comp-3 | 354 | 0.66 | 0.09 | 287 | 3.7 |

The iron and nitrogen doping using $Fe(OAc)_2$ and Phen with ball-milling and pyrolysis obviously has a profound effect on the PSD as seen in Figure 80 – both the microporosity and mesoporosity (where applicable) as well as the SSA (Table 25) decrease by a large amount. For Fe-Phen-CDC-1 and Fe-Phen-CDC-2, the decrease in SSA was over threefold, however Fe-Phen-CDC-3 managed to retain nearly 2 times more surface area. This is likely due to the larger particle size of CDC-3, meaning that more porosity is retained inside of the grains. After the addition of CNTs and pyrolysis in the presence of DCDA and more $Fe(OAc)_2$, the SSA further decreased for all of the catalysts, while the average pore size obviously increases with the creation of additional mesoporosity by the N-doped CNTs on top of the CDC cores (also visible in Figure 80 as the peaks around 3 and 15 nm).

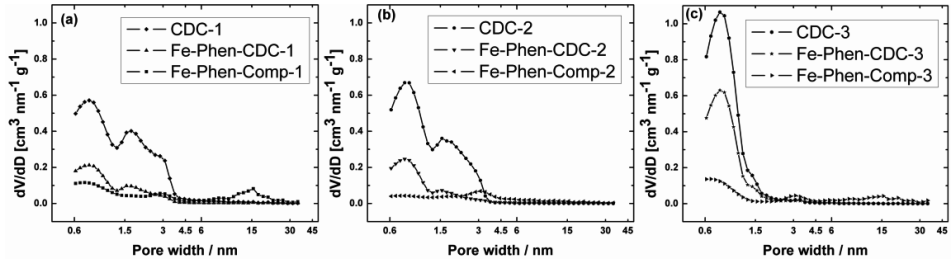


**Figure 80.** Pore size distribution for pristine carbide-derived carbons and catalysts based on CDC-1 (a), CDC-2 (b) and CDC-3 (c).

Figure 81 shows the results of the XPS analysis on the Fe-Phen-CDC materials. Figures 81a–c show the collected XPS survey spectra, while Figures 81d–f show the N1s and Figures 81g–i the C1s high-resolution XPS spectra, respectively. The

XPS wide scans reveal that all of the catalysts had a substantial N1s and O1s signal in addition to the C1s XPS peak, obviously. The high-resolution XPS spectra were deconvoluted to determine the speciation of N and C. For the C1s XPS spectra, only the main components ($sp^3$ and $sp^2$) are shown. There are also minor components visible at lower binding energies from $ZrO_2$. Due to the very low iron contents Fe could not be detected via XPS. The N1s peak was assumed to have 5 components. The pyridinic N peak position was constrained from 398.1 to 397.7 eV with an average peak position at 397.9 eV. The Fe-$N_x$ peak position was constrained from 399.7 to 399.1 eV with an average peak position at 399.3 eV. The pyrrolic peak position was constrained from 401.7 to 400.5 eV with an average peak position at 400.5 eV. The graphitic N peak was constrained from 403 to 402.6 eV with an average peak position at 402.6 eV. All components except for pyridinic N-oxide were assumed the same FWHM constrained from 1 to 2 eV. The pyridinic N-oxide position was constrained from 403.8 to 405.8 eV with an average peak position at 405 eV and a FWHM constraint from 1 to 2.5 eV with an average FWHM of 2.5 eV.

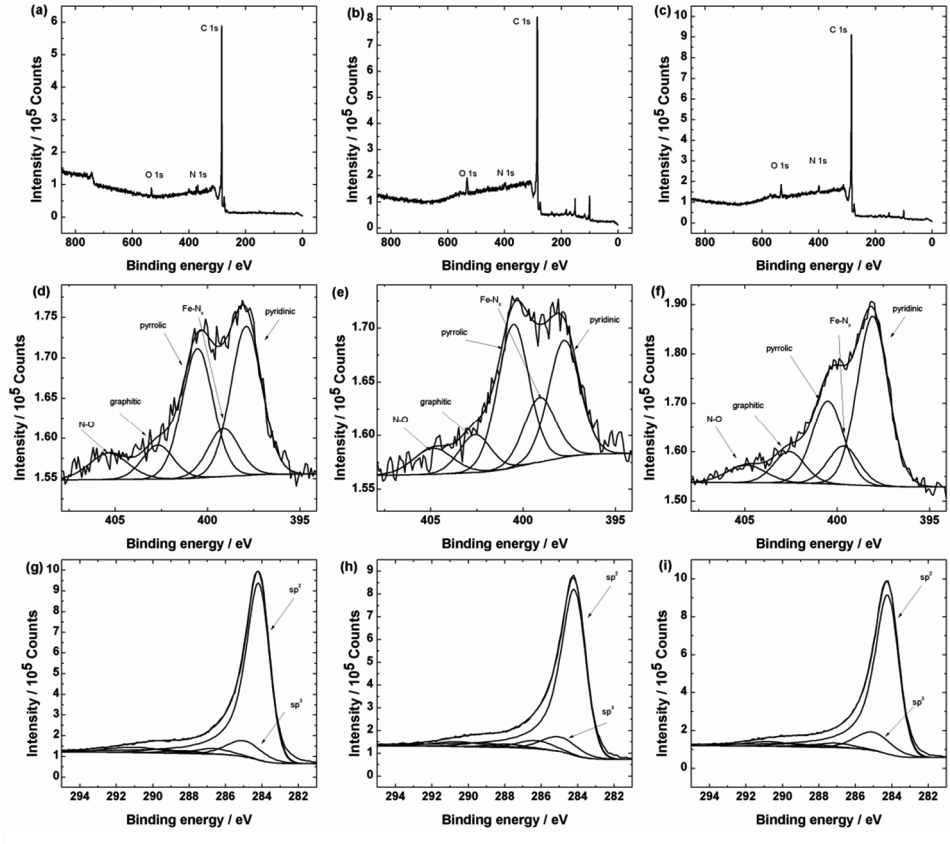


**Figure 81.** XPS survey spectra and N1s and C1s core-level spectra for (a,d,g) Fe-Phen-CDC-1, (b,e,h) Fe-Phen-CDC-2, (c,f,i) Fe-Phen-CDC-3.

Table 26 shows the surface nitrogen content and relative contents of different nitrogen moieties in the Fe-Phen-CDC catalysts. Fe-Phen-CDC-3 had the highest overall N content along with the highest relative content of pyridinic N, which is a N atom connected to two carbon atoms in a six-member ring known to enhance the second step of the ORR in acidic media [72]. Fe-Phen-CDC-1 had the highest relative content of Fe-$N_x$ but due to the overall lower nitrogen content, Fe-Phen-CDC-3 still had the highest total amount of Fe-$N_x$ on the surface with Fe-Phen-CDC-2 following behind. The overall amount of pyrrolic N in each catalyst was rather similar by taking into account the total N content, but Fe-Phen-CDC-3 also had the highest concentration of graphitic N. The higher contents of active components, along with a higher overall N content is beneficial for ORR activity, as can also be seen from the results of electrochemical studies.

**Table 26.** Surface nitrogen content and speciation as-determined by XPS.

| Sample | Total N content | Fe-$N_x$ % | N-O % | Graphitic % | Pyridinic % | Pyrrolic % |
|---|---|---|---|---|---|---|
| Fe-Phen-CDC-1 | 2.6 at.% | 18 | 7 | 9 | 30 | 36 |
| Fe-Phen-CDC-2 | 3.0 at.% | 12 | 8 | 8 | 38 | 33 |
| Fe-Phen-CDC-3 | 4.4 at.% | 11 | 6 | 9 | 50 | 24 |

To study the effect of creating the Fe,N-doped CNT shell on the CDC cores on the crystallographic structure of the catalysts, Fe-Phen-CDC-3 was chosen as the test subject since this material showed the best results in the RDE testing. Figure 82 shows the XRD diffraction pattern of this material and Fe-Phen-Comp-3, the composite created from it. The Fe,N-doped CDC shows a very wide graphitic carbon peak (002) at around 20–26°(2$\theta$) due to the high level of disorder in this carbon material. It is obvious that CNT addition creates more graphitic domains in the catalyst and thus the intensity of the peak at 26°(2$\theta$) assigned to the (002) reflection of graphite increases and narrows down. The broad XRD peak at 40–46°(2$\theta$) is assigned to (100)/(101) reflections of graphite and also intensifies in Fe-Phen-Comp-3. The XRD diffraction patterns of Fe-Phen-Comp-1 and Fe-Phen-Comp-2, which are very similar to that of Fe-Phen-Comp-3, are also presented in Figure 82. The Fe-Phen-Comp-2 material has small amounts of WC in it from pre-milling of the carbide precursor in addition to $ZrO_2$ from milling during synthesis. Other peaks assigned to $ZrO_2$ impurities can also be seen in the diffraction patterns.

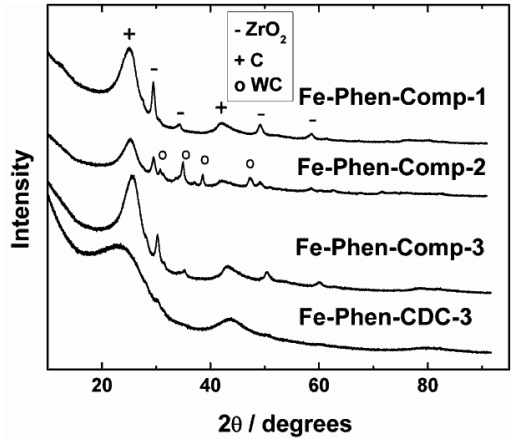


**Figure 82.** XRD patterns of Fe-Phen-CDC-3 and Fe-Phen-Comp catalysts.

The composition of the bulk of the catalysts was determined by ICP-MS and the results are given in Table 27. The carbide derived carbon materials still contain some of the starting carbide, as can be seen from the B, Mo and Ti contents. CDC-3 is the purest, with only a very minor contamination from Ti. Since the parent carbides are extremely hard even when compared to $ZrO_2$, there is also some Zr content in the ball-milled samples.

**Table 27.** Catalyst elemental composition determined by ICP-MS (wt.%)

| Catalyst | B | Ti | Mo | Fe | Zr |
|---|---|---|---|---|---|
| CDC-1 | 0.45 | – | – | – | – |
| CDC-2 | – | – | 4.1 | – | – |
| CDC-3 | – | 0.08 | – | – | – |
| Fe-Phen-CDC-1 | 0.22 | – | – | 0.58 | 2.0 |
| Fe-Phen-CDC-2 | – | – | 1.49 | 0.29 | 3.2 |
| Fe-Phen-CDC-3 | – | 0.22 | – | 0.47 | – |
| Fe-Phen-comp-1 | 0.12 | – | – | 0.25 | 1.6 |
| Fe-Phen-comp-2 | – | – | 2.6 | 1.8 | 2.3 |
| Fe-Phen-comp-3 | – | – | – | 0.54 | 1.3 |

The electrocatalytic activity of all the Fe-Phen-CDC as well as the Fe-Phen-Comp materials in $O_2$-saturated 0.5 M sulphuric acid was studied using the RDE method. A comparison of the ORR polarisation curves is given in Figure 83a, showing all of the Fe-Phen-CDC materials as well as the Fe-Phen-Comp materials and a commercial Pt/C catalyst. The most positive onset potential of

Fe-Phen-CDC-3 is better visible here, as well as the effect of creating a CNT shell on top of the Fe-Phen-CDCs. The half-wave potential for Fe-Phen-CDC-3 is 0.8 V vs RHE. With the creation of the Fe-N-CNT shell around the doped CDC particles, the $E_{1/2}$ is shifted to 40 mV more negative for Fe-Phen-CDC-3 and Fe-Phen-CDC-1, while for Fe-Phen-CDC-2 the shift is around 30 mV. Compared to the commercial Pt/C, the $E_{1/2}$ of Fe-Phen-CDC-3 is only 60 mV more negative. This is especially remarkable considering the very low content of iron in these catalyst materials.

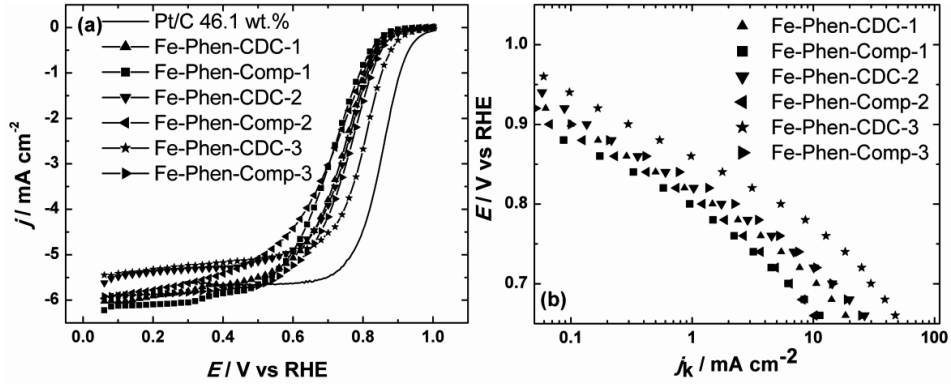


**Figure 83**. (a) Comparison of ORR polarisation curves in $O_2$-saturated 0.5 M $H_2SO_4$ recorded at 1900 rpm for Fe-Phen-C catalysts and a commercial Pt/C catalyst. The loadings are 0.8 mg cm$^{-2}$ for the Fe-Phen-C materials and 46.1 $\mu g_{Pt}$ cm$^{-2}$ for Pt/C. (b) Tafel plots derived from (a).

The kinetic current densities, which are shown in Figure 83b and Table 28, are comparable to those of some state-of-the-art catalysts, especially for the highly active materials derived from TiC. The results also follow the same trend as in a previous study by us, where a different TiC-derived catalyst was much more active than a $B_4C$-derived one due to iron boride formation, which can also be in effect here [267]. Iron boride is less active towards the ORR than the Fe-$N_x$ sites and as such, lowers the activity of the catalyst. For $Mo_2C$-CDC, preferential formation of other types of iron moieties is not known and is likely not in effect. $ZrO_2$, which was also present in the catalysts due to ball-milling, is known to have low activity towards the ORR and does not influence the catalytic activity much [300,302]. Titanium dioxide or carbide, which might also be present in Fe-Phen-CDC-3 at least according to the ICP-MS data, can be disregarded since its ORR activity by itself is rather poor in acid media [303]. The higher electrocatalytic activity for $O_2$ reduction on the CDC-3 derived materials can be explained by the higher amount of micropores and Fe-$N_x$ component as well as pyridinic-N, evident from the XPS data. As the Fe-N-CNT shell is created, the microporosity decreases and there is some loss in the kinetic current density, but this enhances mass-transport, which is vital for fuel cell operation. In RDE mode, the diffusion of $O_2$

to active sites is forced by electrode rotation, but in MEAs with a thick catalyst layer needed to reach platinum-like activities, microporous catalysts are easily flooded [87]. Creating a mesoporous shell using Fe-N-CNTs allows for better mass-transport and could enhance the PEMFC performance.

**Table 28.** Comparison of $E_{1/2}$ and $j_k$ at 0.8 V vs RHE for all the synthesised catalysts.

| Catalyst | Catalyst loading (mg cm$^{-2}$) | $E_{1/2}$ (V vs RHE) | $j_{k,(0.8\ V\ vs\ RHE)}$ (mA cm$^{-2}$) |
|---|---|---|---|
| Fe-Phen-CDC-1 | 0.8 | 0.74 | 1.5 |
| Fe-Phen-Comp-1 | 0.8 | 0.70 | 1 |
| Fe-Phen-CDC-2 | 0.8 | 0.74 | 1.7 |
| Fe-Phen-Comp-2 | 0.8 | 0.71 | 1.2 |
| Fe-Phen-CDC-3 | 0.8 | 0.8 | 5.4 |
| Fe-Phen-Comp-3 | 0.8 | 0.76 | 2.2 |
| $Fe_{0.5}$-N/CDC-2 | 0.8 | 0.81 | 6.4 |

The stability of the Fe-Phen-CDC-3 and the composite created from it was also studied at room temperature and at 70 ºC in 0.5 M $H_2SO_4$ solution. The ORR activity was recorded as steady-state polarisation curves using a step of 20 mV and a hold of 10 s, as for the previous RDE data, and the cycling was done at a sweep rate of 150 mV s$^{-1}$ between 0.925 and 0.6 V. It can be seen that at room temperature, the stability of the catalysts is good in the case of both Fe-Phen-CDC-3 and Fe-Phen-Comp-3, with a $E_{1/2}$ shift of only 10 mV during 5000 potential cycles. It is also to be noted that in both cases, this $E_{1/2}$ shift took place during the first 2000 potential cycles, after which there was nearly no more effect of potential cycling. This is in accordance with other Fe-N-C catalyst stability studies, which have shown that there is a fast current decay at the beginning of cycling followed by a second much slower activity loss [88]. At 70 ºC, the $E_{1/2}$ shift is more intense, with a negative shift of 36 mV for Fe-Phen-CDC-3 (Figure 84c) and 15 mV for Fe-Phen-Comp-3 (Figure 84d) and there was a slight decrease in the limiting current density as well. The main reasons for catalytic activity loss in Fe-N-C catalysts reported in the literature are demetalation of active sites situated in micropores [88] and carbon support oxidation, leading to a loss of TOF on Fe-$N_x$ moieties with no leaching of the iron [90,304]. The core-shell morphology of Fe-Phen-Comp-3 negates both of these effects, as the catalyst is more graphitic and therefore more resistant to carbon oxidation (confirmed by the XRD study) as well as much less microporous (the micropore volume is lowered 4 times and the average pore diameter is increased from 1.1 to 3.7 nm, as shown in Table 25), with only minor loss in the ORR activity when compared to the pure Fe-Phen-CDCs. Chenitz et al. found in their recent study [88] that active sites situated in mesopores are much more resistant to demetalation effects and thus more stable

during the PEMFC operation, so the core-shell composites derived from CDCs and carbon nanotubes are likely to be very stable in PEMFCs. The very low Fe content also reduces the effect of demetalation.

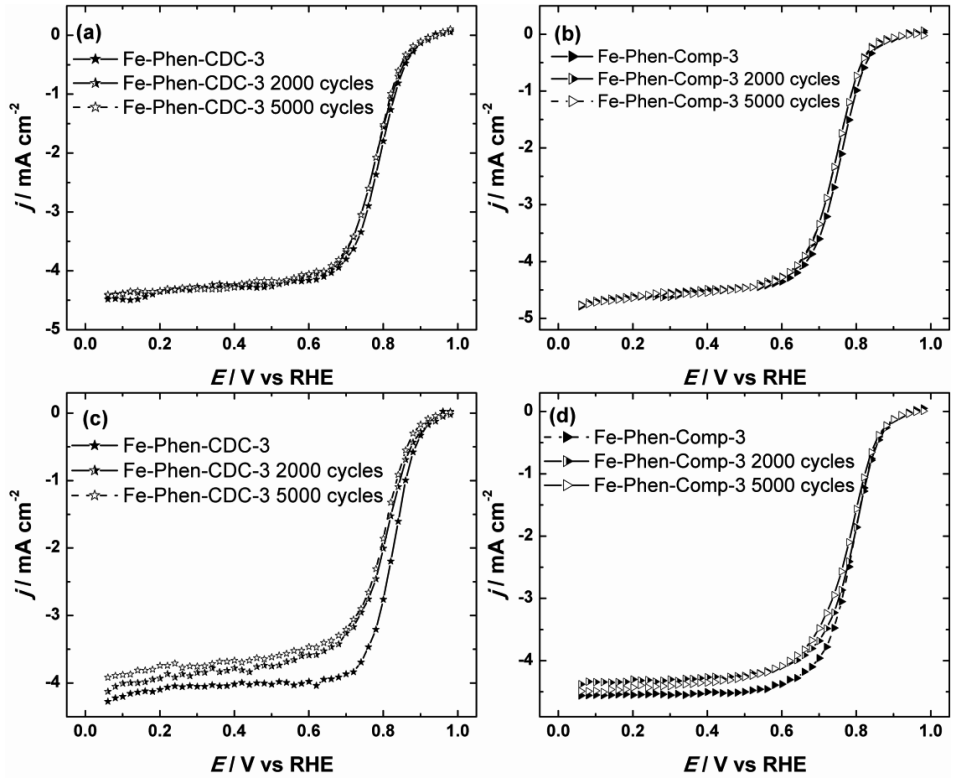


**Figure 84**. Stability of (a,c) Fe-Phen-CDC-3 and (b,d) Fe-Phen-Comp-3 in 0.5 M $H_2SO_4$ solution during 5000 potential cycles at (a,b) 20 ºC and (c,d) 70 ºC. $\omega$ = 960 rpm.

Table 29 shows a comparison of the PEMFC performance of some of the best M-N-C catalysts taken from the literature with the materials presented here. Obviously, the CDC-based catalysts lag somewhat behind the performance of the best NPMCs, with the main reasons presented in the previous chapter (large particle size leading to inefficient mass transport, pore closure due to doping and ball-milling). However, with further improvement of the methods for alleviating these problems developed as part of this PhD thesis and other solutions (such as improving the electrode fabrication), we expect that the CDC-based materials can become competitive in PEMFC as well. The performance at higher potentitals (>0.8 V) is already comparable to some of the best catalysts, as seen from Table 29.

**Table 29.** PEMFC performance with M-N-C cathode catalysts.

| Catalyst | Cathode loading (mg $cm^{-2}$) | Pressure ($kPa_{abs}$) | $j_{0.8\ V}$ (mA $cm^{-2}$) | $j_{0.6\ V}$ (mA $cm^{-2}$) | $P_{max}$ (mW $cm^{-2}$) | Ref. |
|---|---|---|---|---|---|---|
| $Fe_{0.5}$-N/CDC-2 | 4 | 200 | 20 | 250 | 243 | XI |
| $Fe_{0.5}$-Phen-SiCDC 800-Zn1.0 | 4 | 200 | 18.2 | 115 | 217 | XII |
| Fe-N-C Gen-3 | 2.5 | 150 | 50* | 500* | 507* | [305] |
| 1/20/80-Z8-1050 °C-15 min | 3.9 | 200 | 273 | 1250* | 920 | [58] |
| Fe-Ph-MOF fibers | 3 | 200 | 81* | 650* | 496* | [306] |
| $Zn(mIm)_2TPI$ | 3.8 | 150 | 222 | 1100* | 603 | [307] |
| FePhen@MOF-$ArNH_3$ | 3 | 150 | 123* | 480* | 380 | [45] |
| Fe2-Z8-C | 2.8 | 200 | 310* | 1750* | 1156 | [308] |
| Fe–N–C–Phen–PANI | 3.8 | 200 | 35* | 1000* | 531 | [309] |
| LANL Fe1.5-N-C catalyst | 4 | 100 | 75* | 700* | | [310] |
| ZIF-NC-0.5Fe-700 | 3.5 | 150 | 145 | 900* | 732 | [311] |
| Fe-pBDA@C-SCN | 6 | 100 | 111 | 1100* | 597 | [312] |

*Estimated from Figure

# 8. SUMMARY

The aim of this doctoral thesis was to study potential replacements for Pt/C cathode catalysts in PEFCs. To this end, in the first part of the thesis, nitrogen-doped MWCNT/graphene composites were prepared by first oxidising graphite to synthesise graphene oxide, and purifying MWCNTs, which were then doped with semicarbazide, carbohydrazide, biuret, urea and dicyandiamide using flash pyrolysis at 800 °C [I–III]. DCDA was identified as the best nitrogen source, with the $j_k$ at 0.8 V vs RHE of the material doped with DCDA reaching 2.6 mA cm$^{-2}$ in alkaline solution. In an alkaline DMFC, this material had the same $P_{max}$ as a commercial 60 wt.% Pt/C catalyst (0.72 mW cm$^{-2}$). Switching the carbon support from MWCNT/graphene composite to a titanium carbide-derived carbon, the $j_k$ at 0.8 V increased to 7.2 mA cm$^{-2}$, owing to its very high SSA of 2024 m$^2$ g$^{-1}$ [VII]. None of the catalysts in the first part of the thesis showed significant loss in the ORR activity during 1000 potential cycles from 0 to –1.2 V vs SCE. In the second part of the thesis, iron and cobalt were added to the catalyst preparation process to create M-N-C materials from MWCNTs [IV–VI]. Adding $FeCl_3$ to the catalyst precursor mixture in addition to purified MWCNTs and DCDA, the best catalyst showed a $j_k$ value of 7.9 mA cm$^{-2}$ at 0.8 V vs RHE [V] and adding $CoCl_2$ instead managed to increase the performance to 12.4 mA cm$^{-2}$ in alkaline conditions [IV]. M-$N_x$ sites and metal/metal carbide particles covered with nitrogen-doped carbon were identified as the source of the increased activity when compared to simply nitrogen-doped MWCNTs. Using RDE testing, no significant activity loss was seen during 1000 potential cycles from 0 to –1.2 V vs SCE. In an alkaline DMFC, the Fe and N doped catalyst performed comparably to Pt/C, with a $P_{max}$ of 1.21 mW cm$^{-2}$ [V]. The Co- and N-doped material was compared to Pt/C in an $H_2/O_2$ AMEFC, where it showed a $P_{max}$ of 116 mW cm$^{-2}$, exceeding a 20 wt.% Pt/C catalyst [IV]. In acidic conditions, the Fe-NCNT catalyst outperformed the Co-NCNT catalyst, but had lower stability [VI]. Agglomeration of the metal into particles rather than being dispersed in M-$N_x$ catalytic centres was identified as the main problem with this synthesis strategy. In the third part of the thesis, the MWCNT support was again switched to CDCs to improve the ORR activity of the catalyst materials [VIII–XIV]. An Fe-N-CDC material based on TiCDC had a $j_k$ at 0.8 V vs RHE of 9.1 mA cm$^{-2}$, while a Co-N-CDC synthesised with the same method managed 8.2 mA cm$^{-2}$ in 0.1 M KOH [VIII]. In a DMFC, the M-N-CDCs outperformed 60 wt.% Pt/C, with $P_{max}$ of 1.46 and 1.43 mW cm$^{-2}$ for Fe-N-CDC and Co-N-CDC, respectively [VIII]. In an AEMFC, the results were also close to that of a 46 wt.% Pt/C, with $P_{max}$ of 80 and 78 mW cm$^{-2}$ for Fe-N-CDC and Co-N-CDC, respectively, compared to 90 mW cm$^{-2}$ for Pt/C [IX]. The increase in activity compared to M-NCNTs can be ascribed to a higher SSA (allowing for better dispersion of the metal), larger porosity and a higher nitrogen content on the surface of the material. A large particle size of the CDC-based catalysts (1–10 μm) was identified as the main challenge. Making a composite from the Fe-N-CDC with MWCNTs using a multi-step doping process with

1,10-phenanthroline as the additional N source managed to rise the $P_{max}$ to 160 mW $cm^{-2}$ due to an enhanced catalyst layer [X]. These results were improved upon by optimising the ball-milling conditions of the CDC via usage of smaller $ZrO_2$ beads of 0.5 mm in diameter, wet phase milling and the use of PVP as a surfactant to enhance the ball-milling process. These advancements managed to reduce the particle size down to <1 µm while retaining all the porosity lost due to milling and a near atomic dispersion of the metal. As a result, the Fe-N-CDC material outperformed Pt/C in an AEMFC with a $P_{max}$ of 356 mW $cm^{-2}$ and a $j_{0.9\ V}$ of 52 mA $cm^{-2}$ in an MEA, among the best results achieved with the same membrane and ionomer [XIV]. In a PEMFC, a TiCDC catalyst with atomically dispersed Fe-$N_x$ sites managed a $j_{0.8\ V}$ of 20 mA $cm^{-2}$ and a $j_{0.6\ V}$ of 400 mA $cm^{-2}$ [XI]. $ZnCl_2$ addition was identified as another strategy to mitigate surface area losses related to ball-milling and pore closure by Phen during the doping process, leading to a $j_{0.8\ V,\ MEA}$ increase of over four times compared to a Zn-free synthesis [XIII]. A composite material made from TiCDC and MWCNTs showed a significant increase in stability compared to pure CDC-derived catalysts, with the $E_{1/2}$ shift decreased from 38 mV to 15 mV during 5000 cycles from 1 to 0.05 V vs RHE in 0.5 M $H_2SO_4$ at 70 °C [XII]. The research done in this doctoral thesis demonstrated, for the first time, CDC-based fuel cell catalysts capable of performing near to or even better than commercial Pt/C materials. Strategies to prepare composite materials from MWCNT/graphene or CDCs and for retaining porosity during ball-milling were also shown here for the first time, which can and in some cases already have furthered the field of NPMCs as tools for other researchers. The results of the thesis thus present a significant contribution to the field of electrocatalysis of oxygen reduction on non-precious metal catalysts.

# 9. REFERENCES


[1] International Energy Agency, World Energy Balances, 2019. https://www.iea.org/data-and-statistics?country=WORLD&fuel=Energy consumption&indicator=Total final consumption (TFC) by sector.

[2] I. Staffell, D. Scamman, A. Velazquez Abad, P. Balcombe, P.E. Dodds, P. Ekins, N. Shah, K.R. Ward, The role of hydrogen and fuel cells in the global energy system, Energy Environ. Sci. 12 (2019) 463–491. https://doi.org/10.1039/c8ee01157e.

[3] H. Nazir, N. Muthuswamy, C. Louis, S. Jose, J. Prakash, M.E.M. Buan, C. Flox, S. Chavan, X. Shi, P. Kauranen, T. Kallio, G. Maia, K. Tammeveski, N. Lymperopoulos, E. Carcadea, E. Veziroglu, A. Iranzo, A.M. Kannan, Is the H2 economy realizable in the foreseeable future? Part III: H2 usage technologies, applications, and challenges and opportunities, Int. J. Hydrogen Energy 45 (2020) 28217–28239. https://doi.org/10.1016/j.ijhydene.2020.07.256.

[4] F.T. Wagner, B. Lakshmanan, M.F. Mathias, Electrochemistry and the future of the automobile, J. Phys. Chem. Lett. 1 (2010) 2204–2219. https://doi.org/10.1021/jz100553m.

[5] P.C.K. Vesborg, T.F. Jaramillo, Addressing the terawatt challenge: scalability in the supply of chemical elements for renewable energy, RSC Adv. 2 (2012) 7933. https://doi.org/10.1039/c2ra20839c.

[6] D. Papageorgopoulos, Fuel Cells Program Overview, 2019.

[7] S.T. Thompson, D. Papageorgopoulos, Platinum group metal-free catalysts boost cost competitiveness of fuel cell vehicles, Nat. Catal. 2 (2019) 558–561. https://doi.org/10.1038/s41929-019-0291-x.

[8] R. Jasinski, A New Fuel Cell Cathode Catalyst, Nature 201 (1964) 1212–1213. https://doi.org/10.1038/2011212a0.

[9] S. Iijima, Helical microtubules of graphitic carbon, Nature 354 (1991) 56–58. https://doi.org/10.1038/354056a0.

[10] K.S. Novoselov, A.K. Geim, S. V. Morozov, D. Jiang, Y. Zhang, S.V. Dubonos, I. V. Grigorieva, A.A. Firsov, Electric field in atomically thin carbon films, Science 306 (2004) 666–669. https://doi.org/10.1126/science.1102896.

[11] S. Pasupathi, J.C.C. Gomez, H. Su, H. Reddy, P. Bujlo, C. Sita, Recent Advances in High-Temperature PEM Fuel Cells, 2016. https://doi.org/10.1016/c2015-0-06917-9.

[12] T. Stein, Y. Ein-Eli, Challenges and Perspectives of Metal-Based Proton Exchange Membrane's Bipolar Plates: Exploring Durability and Longevity, Energy Technol. 8 (2020) 2000007. https://doi.org/10.1002/ente.202000007.

[13] N. Bizon, Improving the PEMFC energy efficiency by optimizing the fueling rates based on extremum seeking algorithm, Int. J. Hydrogen Energy 39 (2014) 10641–10654. https://doi.org/10.1016/j.ijhydene.2014.04.194.

[14] https://www.fuelcellstore.com/nafion-211, (n.d.).

[15] Z. Chen, J.P. Dodelet, J. Zhang, Non-Noble Metal Fuel Cell Catalysts, Wiley-VCH, Weinheim, Germany, 2014. https://doi.org/10.1002/9783527664900.

[16] D.R. Dekel, Review of cell performance in anion exchange membrane fuel cells, J. Power Sources 375 (2018) 158–169. https://doi.org/10.1016/j.jpowsour.2017.07.117.

[17] L. Osmieri, C. Zafferoni, L. Wang, A.H.A. Monteverde Videla, A. Lavacchi, S. Specchia, Polypyrrole-Derived Fe−Co−N−C Catalyst for the Oxygen Reduction

Reaction: Performance in Alkaline Hydrogen and Ethanol Fuel Cells, ChemElectroChem 5 (2018) 1954–1965. https://doi.org/10.1002/celc.201800420.
[18] Z. Wen, J. Liu, J. Li, Core/shell Pt/C nanoparticles embedded in mesoporous carbon as a methanol-tolerant cathode catalyst in direct methanol fuel cells, Adv. Mater. 20 (2008) 743–747. https://doi.org/10.1002/adma.200701578.
[19] Y. Paik, S.-S. Kim, O.H. Han, Methanol Behavior in Direct Methanol Fuel Cells, Angew. Chem. Int. Ed. 47 (2008) 94–96. https://doi.org/10.1002/anie.200703190.
[20] R.W. Reeve, P.A. Christensen, A.J. Dickinson, A. Hamnett, K. Scott, Methanol-tolerant oxygen reduction catalysts based on transition metal sulfides and their application to the study of methanol permeation, Electrochim. Acta 45 (2000) 4237–4250. https://doi.org/10.1016/S0013-4686(00)00556-9.
[21] M. Ahmed, I. Dincer, A review on methanol crossover in direct methanol fuel cells: Challenges and achievements, Int. J. Energy Res. 35 (2011) 1213–1228. https://doi.org/10.1002/er.1889.
[22] N.A. Anastasijević, V. Vesović, R.R. Adžić, Determination of the kinetic parameters of the oxygen reduction reaction using the rotating ring-disk electrode. Part I. Theory, J. Electroanal. Chem. 229 (1987) 305–316. https://doi.org/10.1016/0022-0728(87)85148-3.
[23] R.R. Adžić, Recent advances in the kinetics of oxygen reduction, in: P.N. Ross, J. Lipkowski (Eds.), Electrocatalysis, Wiley-VCH, New York, 1998, pp. 197–242.
[24] H.A. Gasteiger, S.S. Kocha, B. Sompalli, F.T. Wagner, Activity benchmarks and requirements for Pt, Pt-alloy, and non-Pt oxygen reduction catalysts for PEMFCs, Appl. Catal. B Environ. 56 (2005) 9–35. https://doi.org/10.1016/j.apcatb.2004.06.021.
[25] N. Ramaswamy, S. Mukerjee, Fundamental mechanistic understanding of electrocatalysis of oxygen reduction on Pt and non-Pt surfaces: Acid versus alkaline media, Adv. Phys. Chem. 2012 (2012) 1–17. https://doi.org/10.1155/2012/491604.
[26] T. Mineva, I. Matanovic, P. Atanassov, M.-T. Sougrati, L. Stievano, M. Clémancey, A. Kochem, J.-M. Latour, F. Jaouen, Understanding Active Sites in Pyrolyzed Fe–N–C Catalysts for Fuel Cell Cathodes by Bridging Density Functional Theory Calculations and 57 Fe Mössbauer Spectroscopy, ACS Catal. 9 (2019) 9359–9371. https://doi.org/10.1021/acscatal.9b02586.
[27] T. Asset, P. Atanassov, Iron-Nitrogen-Carbon Catalysts for Proton Exchange Membrane Fuel Cells, Joule 4 (2020) 33–44. https://doi.org/10.1016/j.joule.2019.12.002.
[28] J.M. Nail, G. Anderson, G. Cesar, C.J. Hansen, The Evolution of the PEM Stationary Fuel Cell in the U.S. Innovation System, 2003.
[29] https://www.ir.plugpower.com/Financial-Information/Financial-Summary/default.aspx, (n.d.).
[30] Johnson Matthey, Pgm Market Report, 2019. http://www.platinum.matthey.com/documents/new-item/pgm market reports/pgm_market_report_may_19.pdf.
[31] Platinum facts | Natural Resources Canada, (n.d.). https://www.nrcan.gc.ca/our-natural-resources/minerals-mining/platinum-facts/20520 (accessed October 7, 2020).
[32] D. Sperling, D. Gordon, Two billion cars: driving toward sustainability, 2009.

[33] M. Shao, Q. Chang, J.-P. Dodelet, R. Chenitz, Recent Advances in Electrocatalysts for Oxygen Reduction Reaction, Chem. Rev. 116 (2016) 3594–3657. https://doi.org/10.1021/acs.chemrev.5b00462.
[34] B.G. Pollet, S.S. Kocha, I. Staffell, Current status of automotive fuel cells for sustainable transport, Curr. Opin. Electrochem. 16 (2019) 90–95. https://doi.org/10.1016/j.coelec.2019.04.021.
[35] S. Hussain, H. Erikson, N. Kongi, A. Sarapuu, J. Solla-Gullón, G. Maia, A.M. Kannan, N. Alonso-Vante, K. Tammeveski, Oxygen reduction reaction on nanostructured Pt-based electrocatalysts: A review, Int. J. Hydrogen Energy 45 (2020) 31775–31797. https://doi.org/10.1016/j.ijhydene.2020.08.215.
[36] A. Ly, T. Asset, P. Atanassov, Integrating nanostructured Pt-based electrocatalysts in proton exchange membrane fuel cells, J. Power Sources 478 (2020) 228516. https://doi.org/10.1016/j.jpowsour.2020.228516.
[37] R. Jasinski, Cobalt Phthalocyanine as a Fuel Cell Cathode, J. Electrochem. Soc. 112 (1965) 526. https://doi.org/10.1149/1.2423590.
[38] D. Banham, S. Ye, Current status and future development of catalyst materials and catalyst layers for proton exchange membrane fuel cells: An industrial perspective, ACS Energy Lett. 2 (2017) 629–638. https://doi.org/10.1021/acsenergylett.6b00644.
[39] L. Osmieri, J. Park, D.A. Cullen, P. Zelenay, D.J. Myers, K.C. Neyerlin, Status and challenges for the application of platinum group metal-free catalysts in proton-exchange membrane fuel cells, Curr. Opin. Electrochem. 25 (2021) 100627. https://doi.org/10.1016/j.coelec.2020.08.009.
[40] H. Jahnke, M. Schönborn, G. Zimmermann, Organic dyestuffs as catalysts for fuel cells, in: Phys. Chem. Appl. Dyest., Springer-Verlag, Berlin/Heidelberg, 1976: pp. 133–181. https://doi.org/10.1007/BFb0046059.
[41] S. Gupta, D. Tryk, I. Bae, W. Aldred, E. Yeager, Heat-treated polyacrylonitrile-based catalysts for oxygen electroreduction, J. Appl. Electrochem. 19 (1989) 19–27. https://doi.org/10.1007/BF01039385.
[42] I. Matanovic, K. Artyushkova, P. Atanassov, Understanding PGM-free catalysts by linking density functional theory calculations and structural analysis: Perspectives and challenges, Curr. Opin. Electrochem. 9 (2018) 137–144. https://doi.org/10.1016/j.coelec.2018.03.009.
[43] Q. Jia, N. Ramaswamy, U. Tylus, K. Strickland, J. Li, A. Serov, K. Artyushkova, P. Atanassov, J. Anibal, C. Gumeci, S.C. Barton, M.T. Sougrati, F. Jaouen, B. Halevi, S. Mukerjee, Spectroscopic insights into the nature of active sites in iron–nitrogen–carbon electrocatalysts for oxygen reduction in acid, Nano Energy 29 (2016) 65–82. https://doi.org/10.1016/j.nanoen.2016.03.025.
[44] A. Zitolo, V. Goellner, V. Armel, M.T. Sougrati, T. Mineva, L. Stievano, E. Fonda, F. Jaouen, Identification of catalytic sites for oxygen reduction in iron- and nitrogen-doped graphene materials, Nat. Mater. 14 (2015) 937–942. https://doi.org/10.1038/nmat4367.
[45] K. Strickland, E. Miner, Q. Jia, U. Tylus, N. Ramaswamy, W. Liang, M.T. Sougrati, F. Jaouen, S. Mukerjee, Highly active oxygen reduction non-platinum group metal electrocatalyst without direct metal-nitrogen coordination, Nat. Commun. 6 (2015) 7343. https://doi.org/10.1038/ncomms8343.
[46] E. Yeager, Electrocatalysts for O2 reduction, Electrochim. Acta 29 (1984) 1527–1537. https://doi.org/10.1016/0013-4686(84)85006-9.

[47] F. Jaouen, J. Herranz, M. Lefévre, J.P. Dodelet, U.I. Kramm, I. Herrmann, P. Bogdanoff, J. Maruyama, T. Nagaoka, A. Garsuch, J.R. Dahn, T. Olson, S. Pylypenko, P. Atanassov, E.A. Ustinov, M. Lefèvre, J.P. Dodelet, U.I. Kramm, I. Herrmann, P. Bogdanoff, J. Maruyama, T. Nagaoka, A. Garsuch, J.R. Dahn, T. Olson, S. Pylypenko, P. Atanassov, E.A. Ustinov, Cross-laboratory experimental study of non-noble-metal electrocatalysts for the oxygen reduction reaction, ACS Appl. Mater. Interfaces 1 (2009) 1623–1639. https://doi.org/10.1021/am900219g.

[48] H.M. Barkholtz, D.-J. Liu, Advancements in rationally designed PGM-free fuel cell catalysts derived from metal–organic frameworks, Mater. Horizons. 4 (2017) 20–37. https://doi.org/10.1039/C6MH00344C.

[49] N. Daems, X. Sheng, I.F.J. Vankelecom, P.P. Pescarmona, Metal-free doped carbon materials as electrocatalysts for the oxygen reduction reaction, J. Mater. Chem. A 2 (2014) 4085–4110. https://doi.org/10.1039/C3TA14043A.

[50] J.H. Zagal, F. Bedioui, Electrochemistry of $N_4$ macrocyclic metal complexes: Volume 1: Energy, 2nd ed., Springer International Publishing, Cham, 2016. https://doi.org/10.1007/978-3-319-31172-2.

[51] K. Tammeveski, J.H. Zagal, Electrocatalytic oxygen reduction on transition metal macrocyclic complexes for anion exchange membrane fuel cell application, Curr. Opin. Electrochem. 9 (2018) 207–213. https://doi.org/10.1016/j.coelec.2018.04.001.

[52] J.H. Zagal, M.T.M. Koper, Reactivity Descriptors for the Activity of Molecular $MN_4$ Catalysts for the Oxygen Reduction Reaction, Angew. Chem. Int. Ed. 55 (2016) 14510–14521. https://doi.org/10.1002/anie.201604311.

[53] M. Ferrandon, A.J. Kropf, D.J. Myers, K. Artyushkova, U. Kramm, P. Bogdanoff, G. Wu, C.M. Johnston, P. Zelenay, Multitechnique characterization of a polyaniline-iron-carbon oxygen reduction catalyst, J. Phys. Chem. C 116 (2012) 16001–16013. https://doi.org/10.1021/jp302396g.

[54] M. Vikkisk, I. Kruusenberg, U. Joost, E. Shulga, K. Tammeveski, Electrocatalysis of oxygen reduction on nitrogen-containing multi-walled carbon nanotube modified glassy carbon electrodes, Electrochim. Acta 87 (2013) 709–716. https://doi.org/10.1016/j.electacta.2012.09.071.

[55] M. Lefèvre, E. Proietti, F. Jaouen, J.P. Dodelet, Iron-Based catalysts with improved oxygen reduction activity in polymer electrolyte fuel cells, Science 324 (2009) 71–74. https://doi.org/10.1126/science.1170051.

[56] G. Wu, K.L. More, C.M. Johnston, P. Zelenay, High-performance electrocatalysts for oxygen reduction derived from polyaniline, iron, and cobalt, Science 332 (2011) 443–447. https://doi.org/10.1126/science.1200832.

[57] R. Bashyam, P. Zelenay, A class of non-precious metal composite catalysts for fuel cells, Nature 443 (2006) 63–66. https://doi.org/10.1038/nature05118.

[58] E. Proietti, F. Jaouen, M. Lefèvre, N. Larouche, J. Tian, J. Herranz, J.-P. Dodelet, Iron-based cathode catalyst with enhanced power density in polymer electrolyte membrane fuel cells, Nat. Commun. 2 (2011) 416. https://doi.org/10.1038/ncomms1427.

[59] J. Shui, C. Chen, L. Grabstanowicz, D. Zhao, D.-J. Liu, Highly efficient non-precious metal catalyst prepared with metal–organic framework in a continuous carbon nanofibrous network, Proc. Natl. Acad. Sci. U.S.A. 112 (2015) 10629–10634. https://doi.org/10.1073/pnas.1507159112.

[60] H. Zhang, S. Hwang, M. Wang, Z. Feng, S. Karakalos, L. Luo, Z. Qiao, X. Xie, C. Wang, D. Su, Y. Shao, G. Wu, Single Atomic Iron Catalysts for Oxygen Reduction in Acidic Media: Particle Size Control and Thermal Activation, J. Am. Chem. Soc. 139 (2017) 14143–14149. https://doi.org/10.1021/jacs.7b06514.

[61] Q. Jia, N. Ramaswamy, H. Hafiz, U. Tylus, K. Strickland, G. Wu, B. Barbiellini, A. Bansil, E.F. Holby, P. Zelenay, S. Mukerjee, Experimental Observation of Redox-Induced Fe-N Switching Behavior as a Determinant Role for Oxygen Reduction Activity, ACS Nano 9 (2015) 12496–12505. https://doi.org/10.1021/acsnano.5b05984.

[62] U.I. Kramm, A. Zana, T. Vosch, S. Fiechter, M. Arenz, D. Schmeißer, On the structural composition and stability of Fe–N–C catalysts prepared by an intermediate acid leaching, J. Solid State Electrochem. 20 (2016) 969–981. https://doi.org/10.1007/s10008-015-3060-z.

[63] J.H. Zagal, F. Bedioui, J.P. Dodelet, $N_4$-Macrocyclic Metal Complexes, Springer New York, 2006. https://doi.org/10.1007/978-0-387-28430-9.

[64] N. Zion, D.A. Cullen, P. Zelenay, L. Elbaz, Heat-Treated Aerogel as a Catalyst for the Oxygen Reduction Reaction, Angew. Chemie. 132 (2020) 2504–2510. https://doi.org/10.1002/ange.201913521.

[65] Z. Jiang, J. Yu, T. Huang, M. Sun, Recent advance on polyaniline or polypyrrole-derived electrocatalysts for oxygen reduction reaction, Polymers (Basel). 10 (2018) 1397. https://doi.org/10.3390/polym10121397.

[66] X. Wang, L. Zou, H. Fu, Y. Xiong, Z. Tao, J. Zheng, X. Li, Noble Metal-Free Oxygen Reduction Reaction Catalysts Derived from Prussian Blue Nanocrystals Dispersed in Polyaniline, ACS Appl. Mater. Interfaces 8 (2016) 8436–8444. https://doi.org/10.1021/acsami.5b12102.

[67] A. Serov, K. Artyushkova, E. Niangar, C. Wang, N. Dale, F. Jaouen, M.T. Sougrati, Q. Jia, S. Mukerjee, P. Atanassov, Nano-structured non-platinum catalysts for automotive fuel cell application, Nano Energy 16 (2015) 293–300. https://doi.org/10.1016/j.nanoen.2015.07.002.

[68] R. Gokhale, Y. Chen, A. Serov, K. Artyushkova, P. Atanassov, Novel dual templating approach for preparation of highly active Fe-N-C electrocatalyst for oxygen reduction, Electrochim. Acta 224 (2017) 49–55. https://doi.org/10.1016/j.electacta.2016.12.052.

[69] A.H.A. Monteverde Videla, D. Sebastián, N.S. Vasile, L. Osmieri, A.S. Aricò, V. Baglio, S. Specchia, Performance analysis of Fe–N–C catalyst for DMFC cathodes: Effect of water saturation in the cathodic catalyst layer, Int. J. Hydrogen Energy 41 (2016) 22605–22618. https://doi.org/10.1016/J.IJHYDENE.2016.06.060.

[70] J. Li, M. Chen, D.A. Cullen, S. Hwang, M. Wang, B. Li, K. Liu, S. Karakalos, M. Lucero, H. Zhang, C. Lei, H. Xu, G.E. Sterbinsky, Z. Feng, D. Su, K.L. More, G. Wang, Z. Wang, G. Wu, Atomically dispersed manganese catalysts for oxygen reduction in proton-exchange membrane fuel cells, Nat. Catal. 1 (2018) 935–945. https://doi.org/10.1038/s41929-018-0164-8.

[71] J. Herranz, F. Jaouen, M. Lefèvre, U.I. Kramm, E. Proietti, J.P. Dodelet, P. Bogdanoff, S. Fiechter, I. Abs-Wurmbach, P. Bertrand, T.M. Arruda, S. Mukerjee, Unveiling N-protonation and anion-binding effects on Fe/N/C catalysts for $O_2$ reduction in proton-exchange-membrane fuel cells, J. Phys. Chem. C 115 (2011) 16087–16097. https://doi.org/10.1021/jp2042526.

[72] K. Artyushkova, A. Serov, S. Rojas-Carbonell, P. Atanassov, Chemistry of Multitudinous Active Sites for Oxygen Reduction Reaction in Transition Metal-Nitrogen-Carbon Electrocatalysts, J. Phys. Chem. C 119 (2015) 25917–25928. https://doi.org/10.1021/acs.jpcc.5b07653.

[73] U.I. Kramm, J. Herranz, N. Larouche, T.M. Arruda, M. Lefèvre, F. Jaouen, P. Bogdanoff, S. Fiechter, I. Abs-Wurmbach, S. Mukerjee, J.-P. Dodelet, Structure of the catalytic sites in Fe/N/C-catalysts for $O_2$-reduction in PEM fuel cells, Phys. Chem. Chem. Phys. 14 (2012) 11673. https://doi.org/10.1039/c2cp41957b.

[74] H.T. Chung, D.A. Cullen, D. Higgins, B.T. Sneed, E.F. Holby, K.L. More, P. Zelenay, Direct atomic-level insight into the active sites of a high-performance PGM-free ORR catalyst, Science 357 (2017) 479–484. https://doi.org/10.1126/science.aan2255.

[75] M. Reda, H.A. Hansen, T. Vegge, DFT Study of the Oxygen Reduction Reaction on Carbon-Coated Iron and Iron Carbide, ACS Catal. 8 (2018) 10521–10529. https://doi.org/10.1021/acscatal.8b02167.

[76] S. Ratso, I. Kruusenberg, A. Sarapuu, M. Kook, P. Rauwel, R. Saar, J. Aruväli, K. Tammeveski, Electrocatalysis of oxygen reduction on iron- and cobalt-containing nitrogen-doped carbon nanotubes in acid media, Electrochim. Acta 218 (2016) 303–310. https://doi.org/10.1016/j.electacta.2016.09.119.

[77] S. Ratso, M. Käärik, M. Kook, P. Paiste, V. Kisand, S. Vlassov, J. Leis, K. Tammeveski, Iron and Nitrogen Co-doped Carbide-Derived Carbon and Carbon Nanotube Composite Catalysts for Oxygen Reduction Reaction, ChemElectroChem 5 (2018) 1827–1836. https://doi.org/10.1002/celc.201800132.

[78] R. Sibul, E. Kibena-Põldsepp, S. Ratso, M. Kook, M. Käärik, M. Merisalu, P. Paiste, J. Leis, V. Sammelselg, K. Tammeveski, Nitrogen-doped carbon-based electrocatalysts synthesised by ball-milling, Electrochem. Commun. 93 (2018) 39–43. https://doi.org/10.1016/j.elecom.2018.05.027.

[79] K. Ping, A. Braschinsky, M. Alam, R. Bhadoria, V. Mikli, A. Mere, J. Aruväli, P. Paiste, S. Vlassov, M. Kook, M. Rähn, V. Sammelselg, K. Tammeveski, N. Kongi, P. Starkov, Fused Hybrid Linkers for Metal–Organic Framework-Derived Bifunctional Oxygen Electrocatalysts, ACS Appl. Energy Mater. 3 (2020) 152–157. https://doi.org/10.1021/acsaem.9b02039.

[80] N. Ramaswamy, S. Mukerjee, Influence of inner- and outer-sphere electron transfer mechanisms during electrocatalysis of oxygen reduction in alkaline media, J. Phys. Chem. C 115 (2011) 18015–18026. https://doi.org/10.1021/jp204680p.

[81] A. Zitolo, N. Ranjbar-Sahraie, T. Mineva, J. Li, Q. Jia, S. Stamatin, G.F. Harrington, S.M. Lyth, P. Krtil, S. Mukerjee, E. Fonda, F. Jaouen, Identification of catalytic sites in cobalt-nitrogen-carbon materials for the oxygen reduction reaction, Nat. Commun. 8 (2017) 957. https://doi.org/10.1038/s41467-017-01100-7.

[82] P. Zelenay, D.J. Myers, ElectroCat (Electrocatalysis Consortium), U. S. Department of Energy Annual Merit Review, 2017.

[83] M. Primbs, Y. Sun, A. Roy, D. Malko, A. Mehmood, M.-T. Sougrati, P.-Y. Blanchard, G. Granozzi, T. Kosmala, G. Daniel, P. Atanassov, J. Sharman, C. Durante, A. Kucernak, D. Jones, F. Jaouen, P. Strasser, Establishing reactivity descriptors for platinum group metal (PGM)-free Fe–N–C catalysts for PEM fuel cells, Energy Environ. Sci. 13 (2020) 2480–2500. https://doi.org/10.1039/d0ee01013h.

[84] Y. Zhou, X. Tao, G. Chen, R. Lu, D. Wang, M.X. Chen, E. Jin, J. Yang, H.W. Liang, Y. Zhao, X. Feng, A. Narita, K. Müllen, Multilayer stabilization for fabricating high-loading single-atom catalysts, Nat. Commun. 11 (2020). https://doi.org/10.1038/s41467-020-19599-8.

[85] J. Tian, A. Morozan, M.T. Sougrati, M. Lefèvre, R. Chenitz, J.-P. Dodelet, D. Jones, F. Jaouen, Optimized Synthesis of Fe/N/C Cathode Catalysts for PEM Fuel Cells: A Matter of Iron-Ligand Coordination Strength, Angew. Chem. Int. Ed. 52 (2013) 6867–6870. https://doi.org/10.1002/anie.201303025.

[86] N. Ramaswamy, U. Tylus, Q. Jia, S. Mukerjee, Activity descriptor identification for oxygen reduction on nonprecious electrocatalysts: Linking surface science to coordination chemistry, J. Am. Chem. Soc. 135 (2013) 15443–15449. https://doi.org/10.1021/ja405149m.

[87] G. Zhang, R. Chenitz, M. Lefèvre, S. Sun, J.P. Dodelet, Is iron involved in the lack of stability of Fe/N/C electrocatalysts used to reduce oxygen at the cathode of PEM fuel cells?, Nano Energy 29 (2016) 111–125. https://doi.org/10.1016/j.nanoen.2016.02.038.

[88] R. Chenitz, U.I. Kramm, M. Lefevre, V. Glibin, G. Zhang, S. Sun, J.-P. Dodelet, A specific demetalation of Fe-$N_4$ catalytic sites in the micropores of NC_Ar+NH3 is at the origin of the initial activity loss of this highly active Fe/N/C catalyst used for the reduction of oxygen in PEM fuel cell, Energy Environ. Sci. 11 (2018) 365–382. https://doi.org/10.1039/C7EE02302B.

[89] V. Goellner, V. Armel, A. Zitolo, E. Fonda, F. Jaouen, Degradation by Hydrogen Peroxide of Metal-Nitrogen-Carbon Catalysts for Oxygen Reduction, J. Electrochem. Soc. 162 (2015) H403–H414. https://doi.org/10.1149/2.1091506jes.

[90] C.H. Choi, H.K. Lim, M.W. Chung, G. Chon, N. Ranjbar Sahraie, A. Altin, M.T. Sougrati, L. Stievano, H.S. Oh, E.S. Park, F. Luo, P. Strasser, G. Dražić, K.J.J. Mayrhofer, H. Kim, F. Jaouen, The Achilles' heel of iron-based catalysts during oxygen reduction in an acidic medium, Energy Environ. Sci. 11 (2018) 3176–3182. https://doi.org/10.1039/c8ee01855c.

[91] F. Jaouen, M. Lefèvre, J.P. Dodelet, M. Cai, Heat-treated Fe/N/C catalysts for $O_2$ electroreduction: Are active sites hosted in micropores?, J. Phys. Chem. B 110 (2006) 5553–5558. https://doi.org/10.1021/jp057135h.

[92] A. Mufundirwa, G.F. Harrington, B. Smid, B.V. Cunning, K. Sasaki, S.M. Lyth, Durability of template-free Fe-N-C foams for electrochemical oxygen reduction in alkaline solution, J. Power Sources 375 (2018) 244–254. https://doi.org/10.1016/j.jpowsour.2017.07.025.

[93] K. Kumar, P. Gairola, M. Lions, N. Ranjbar-Sahraie, M. Mermoux, L. Dubau, A. Zitolo, F. Jaouen, F. Maillard, Physical and Chemical Considerations for Improving Catalytic Activity and Stability of Non-Precious-Metal Oxygen Reduction Reaction Catalysts, ACS Catal. 8 (2018) 11264–11276. https://doi.org/10.1021/acscatal.8b02934.

[94] L. Yang, J. Shui, L. Du, Y. Shao, J. Liu, L. Dai, Z. Hu, Carbon-Based Metal-Free ORR Electrocatalysts for Fuel Cells: Past, Present, and Future, Adv. Mater. 31 (2019) 1804799. https://doi.org/10.1002/adma.201804799.

[95] I. Kruusenberg, D. Ramani, S. Ratso, U. Joost, R. Saar, P. Rauwel, A.M. Kannan, K. Tammeveski, Cobalt–Nitrogen Co-doped Carbon Nanotube Cathode Catalyst for Alkaline Membrane Fuel Cells, ChemElectroChem 3 (2016) 1455–1465. https://doi.org/10.1002/celc.201600241.

[96] F.D. Speck, P.G. Santori, F. Jaouen, S. Cherevko, Mechanisms of Manganese Oxide Electrocatalysts Degradation during Oxygen Reduction and Oxygen Evolution Reactions, J. Phys. Chem. C 123 (2019) 25267–25277. https://doi.org/10.1021/acs.jpcc.9b07751.
[97] N.R. Sahraie, U.I. Kramm, J. Steinberg, Y. Zhang, A. Thomas, T. Reier, J.P. Paraknowitsch, P. Strasser, Quantifying the density and utilization of active sites in non-precious metal oxygen electroreduction catalysts, Nat. Commun. 6 (2015) 8618. https://doi.org/10.1038/ncomms9618.
[98] Y. Zhao, L. Yang, S. Chen, X. Wang, Y. Ma, Q. Wu, Y. Jiang, W. Qian, Z. Hu, Can boron and nitrogen co-doping improve oxygen reduction reaction activity of carbon nanotubes?, J. Am. Chem. Soc. 135 (2013) 1201–1204. https://doi.org/10.1021/ja310566z.
[99] C. Domínguez, F.J. Pérez-Alonso, M. Abdel Salam, S.A. Al-Thabaiti, A.Y. Obaid, A.A. Alshehri, J.L. Gómez de la Fuente, J.L.G. Fierro, S. Rojas, On the relationship between N content, textural properties and catalytic performance for the oxygen reduction reaction of N/CNT, Appl. Catal. B Environ. 162 (2015) 420–429. https://doi.org/10.1016/j.apcatb.2014.07.002.
[100] Q. Liu, H. Zhang, H. Zhong, S. Zhang, S. Chen, N-doped graphene/carbon composite as non-precious metal electrocatalyst for oxygen reduction reaction, Electrochim. Acta 81 (2012) 313–320. https://doi.org/10.1016/j.electacta.2012.07.022.
[101] G. Wu, P. Zelenay, Nanostructured nonprecious metal catalysts for oxygen reduction reaction, Acc. Chem. Res. 46 (2013) 1878–1889. https://doi.org/10.1021/ar400011z.
[102] D. Guo, R. Shibuya, C. Akiba, S. Saji, T. Kondo, J. Nakamura, Active sites of nitrogen-doped carbon materials for oxygen reduction reaction clarified using model catalysts, Science 351 (2016) 361–365. https://doi.org/10.1126/science.aad0832.
[103] K. Mamtani, D. Jain, D. Zemlyanov, G. Celik, J. Luthman, G. Renkes, A.C. Co, U.S. Ozkan, Probing the Oxygen Reduction Reaction Active Sites over Nitrogen-Doped Carbon Nanostructures (CNx) in Acidic Media Using Phosphate Anion, ACS Catal. 6 (2016) 7249–7259. https://doi.org/10.1021/acscatal.6b01786.
[104] S. Kabir, K. Artyushkova, A. Serov, P. Atanassov, Role of Nitrogen Moieties in N-Doped 3D-Graphene Nanosheets for Oxygen Electroreduction in Acidic and Alkaline Media, ACS Appl. Mater. Interfaces 10 (2018) 11623–11632. https://doi.org/10.1021/acsami.7b18651.
[105] S. Ratso, I. Kruusenberg, M. Vikkisk, U. Joost, E. Shulga, I. Kink, T. Kallio, K. Tammeveski, Highly active nitrogen-doped few-layer graphene/carbon nanotube composite electrocatalyst for oxygen reduction reaction in alkaline media, Carbon 73 (2014) 361–370. https://doi.org/10.1016/j.carbon.2014.02.076.
[106] S. Ratso, I. Kruusenberg, U. Joost, R. Saar, K. Tammeveski, Enhanced oxygen reduction reaction activity of nitrogen-doped graphene/multi-walled carbon nanotube catalysts in alkaline media, Int. J. Hydrogen Energy 41 (2016) 22510–22519. https://doi.org/10.1016/j.ijhydene.2016.02.021.
[107] A. Ferre-Vilaplana, E. Herrero, Why nitrogen favors oxygen reduction on graphitic materials, Sustain. Energy Fuels 3 (2019) 2391–2398. https://doi.org/10.1039/c9se00262f.

[108] H. Niwa, K. Horiba, Y. Harada, M. Oshima, T. Ikeda, K. Terakura, J. ichi Ozaki, S. Miyata, X-ray absorption analysis of nitrogen contribution to oxygen reduction reaction in carbon alloy cathode catalysts for polymer electrolyte fuel cells, J. Power Sources 187 (2009) 93–97. https://doi.org/10.1016/j.jpowsour.2008.10.064.
[109] C. Tang, Q. Zhang, Nanocarbon for Oxygen Reduction Electrocatalysis: Dopants, Edges, and Defects, Adv. Mater. 29 (2017) 1604103 . https://doi.org/10.1002/adma.201604103.
[110] C.V. Rao, C.R. Cabrera, Y. Ishikawa, In search of the active site in nitrogen-doped carbon nanotube electrodes for the oxygen reduction reaction, J. Phys. Chem. Lett. 1 (2010) 2622–2627. https://doi.org/10.1021/jz100971v.
[111] Z.Z. Chen, D. Higgins, H. Tao, R.S. Hsu, Z.Z. Chen, Highly Active Nitrogen-Doped Carbon Nanotubes for Oxygen Reduction Reaction in Fuel Cell Applications, J. Phys. Chem. C 113 (2009) 21008–21013. https://doi.org/10.1021/jp908067v.
[112] J.D. Wiggins-Camacho, K.J. Stevenson, Mechanistic discussion of the oxygen reduction reaction at nitrogen-doped carbon nanotubes, J. Phys. Chem. C 115 (2011) 20002–20010. https://doi.org/10.1021/jp205336w.
[113] A.C.M. Carvalho, M.C. Dos Santos, Nitrogen-substituted nanotubes and nano-junctions: Conformation and electronic properties, J. Appl. Phys. 100 (2006) 084305. https://doi.org/10.1063/1.2357646.
[114] R. Czerw, M. Terrones, J.C. Charlier, X. Blase, B. Foley, R. Kamalakaran, N. Grobert, H. Terrones, D. Tekleab, P.M. Ajayan, W. Blau, M. Rühle, D.L. Carroll, Identification of Electron Donor States in N-Doped Carbon Nanotubes, Nano Lett. 1 (2001) 457–460. https://doi.org/10.1021/nl015549q.
[115] R. Liu, D. Wu, X. Feng, K. Müllen, Nitrogen-doped ordered mesoporous graphitic arrays with high electrocatalytic activity for oxygen reduction, Angew. Chem. Int. Ed. 49 (2010) 2565–2569. https://doi.org/10.1002/anie.200907289.
[116] R. Wang, T. Zhou, H. Li, H. Wang, H. Feng, J. Goh, S. Ji, Nitrogen-rich meso-porous carbon derived from melamine with high electrocatalytic performance for oxygen reduction reaction, J. Power Sources 261 (2014) 238–244. https://doi.org/10.1016/j.jpowsour.2014.03.057.
[117] W. Wei, H. Liang, K. Parvez, X. Zhuang, X. Feng, K. Müllen, Nitrogen-doped carbon nanosheets with size-defined mesopores as highly efficient metal-free catalyst for the oxygen reduction reaction, Angew. Chem. Int. Ed. 53 (2014) 1570–1574. https://doi.org/10.1002/anie.201307319.
[118] A. Sarapuu, L. Samolberg, K. Kreek, M. Koel, L. Matisen, K. Tammeveski, Cobalt- and iron-containing nitrogen-doped carbon aerogels as non-precious metal catalysts for electrochemical reduction of oxygen, J. Electroanal. Chem. 746 (2015) 9–17. https://doi.org/10.1016/j.jelechem.2015.03.021.
[119] S.-A. Wohlgemuth, R.J. White, M.-G. Willinger, M.-M. Titirici, M. Antonietti, A one-pot hydrothermal synthesis of sulfur and nitrogen doped carbon aerogels with enhanced electrocatalytic activity in the oxygen reduction reaction, Green Chem. 14 (2012) 1515-1523. https://doi.org/10.1039/c2gc35309a.
[120] X. Fu, J. Jin, Y. Liu, Q. Liu, K. Niu, J. Zhang, X. Cao, Graphene-xerogel-based non-precious metal catalyst for oxygen reduction reaction, Electrochem. Commun. 28 (2013) 5–8. https://doi.org/10.1016/j.elecom.2012.11.017.

[121] M. Vikkisk, I. Kruusenberg, S. Ratso, U. Joost, E. Shulga, I. Kink, P. Rauwel, K. Tammeveski, E. Shulg, I. Kink, P. Rauwel, K. Tammeveski, Enhanced electrocatalytic activity of nitrogen-doped multi-walled carbon nanotubes towards the oxygen reduction reaction in alkaline media, RSC Adv. 5 (2015) 59495–59505. https://doi.org/10.1039/C5RA08818F.
[122] M. Glerup, J. Steinmetz, D. Samaille, O. Stéphan, S. Enouz, A. Loiseau, S. Roth, P. Bernier, Synthesis of N-doped SWNT using the arc-discharge procedure, Chem. Phys. Lett. 387 (2004) 193–197. https://doi.org/10.1016/j.cplett.2004.02.005.
[123] R.M. Yadav, J. Wu, R. Kochandra, L. Ma, C.S. Tiwary, L. Ge, G. Ye, R. Vajtai, J. Lou, P.M. Ajayan, Carbon Nitrogen Nanotubes as Efficient Bifunctional Electrocatalysts for Oxygen Reduction and Evolution Reactions, ACS Appl. Mater. Interfaces 7 (2015) 11991–12000. https://doi.org/10.1021/acsami.5b02032.
[124] K. Parvez, S. Yang, Y. Hernandez, A. Winter, A. Turchanin, X. Feng, K. Müllen, Nitrogen-doped graphene and its iron-based composite as efficient electrocatalysts for oxygen reduction reaction, ACS Nano. 6 (2012) 9541–9550. https://doi.org/10.1021/nn302674k.
[125] M. Li, L. Zhang, Q. Xu, J. Niu, Z. Xia, N-doped graphene as catalysts for oxygen reduction and oxygen evolution reactions: Theoretical considerations, J. Catal. 314 (2014) 66–72. https://doi.org/10.1016/j.jcat.2014.03.011.
[126] M. Vikkisk, I. Kruusenberg, U. Joost, E. Shulga, I. Kink, K. Tammeveski, Electrocatalytic oxygen reduction on nitrogen-doped graphene in alkaline media, Appl. Catal. B Environ. 147 (2014) 369–376. https://doi.org/10.1016/j.apcatb.2013.09.011.
[127] Z. Lin, M. Song, Y. Ding, Y. Liu, M. Liu, C. Wong, Facile preparation of nitrogen-doped graphene as a metal-free catalyst for oxygen reduction reaction, Phys. Chem. Chem. Phys. 14 (2012) 3381. https://doi.org/10.1039/c2cp00032f.
[128] K.K. Türk, I. Kruusenberg, J. Mondal, P. Rauwel, J. Kozlova, L. Matisen, V. Sammelselg, K. Tammeveski, Oxygen electroreduction on MN4-macrocycle modified graphene/multi-walled carbon nanotube composites, J. Electroanal. Chem. 756 (2015) 69–76. https://doi.org/10.1016/j.jelechem.2015.08.014.
[129] I. Kruusenberg, S. Ratso, M. Vikkisk, P. Kanninen, T. Kallio, A.M. Kannan, K. Tammeveski, Highly active nitrogen-doped nanocarbon electrocatalysts for alkaline direct methanol fuel cell, J. Power Sources 281 (2015) 94–102. https://doi.org/10.1016/j.jpowsour.2015.01.167.
[130] C.H. Choi, M.W. Chung, H.C. Kwon, J.H. Chung, S.I. Woo, Nitrogen-doped graphene/carbon nanotube self-assembly for efficient oxygen reduction reaction in acid media, Appl. Catal. B Environ. 144 (2014) 760–766. https://doi.org/10.1016/j.apcatb.2013.08.021.
[131] Y. Zhang, W.-J. Jiang, X. Zhang, L. Guo, J.-S. Hu, Z. Wei, L.-J. Wan, Engineering self-assembled N-doped graphene–carbon nanotube composites towards efficient oxygen reduction electrocatalysts, Phys. Chem. Chem. Phys. 16 (2014) 13605–13609. https://doi.org/10.1039/C4CP00757C.
[132] D.C. Higgins, M.A. Hoque, F. Hassan, J.Y. Choi, B. Kim, Z. Chen, Oxygen reduction on graphene-carbon nanotube composites doped sequentially with nitrogen and sulfur, ACS Catal. 4 (2014) 2734–2740. https://doi.org/10.1021/cs5003806.

[133] Y. Ma, L. Sun, W. Huang, L. Zhang, J. Zhao, Q. Fan, W. Huang, Three-dimensional nitrogen-doped carbon nanotubes/graphene structure used as a metal-free electrocatalyst for the oxygen reduction reaction, J. Phys. Chem. C 115 (2011) 24592–24597. https://doi.org/10.1021/jp207736h.
[134] Y. Gogotsi, Nanomaterials Handbook, 2006. https://doi.org/10.1201/9781420004014.
[135] P. Trogadas, T.F. Fuller, P. Strasser, Carbon as catalyst and support for electrochemical energy conversion, Carbon 75 (2014) 5–42. https://doi.org/10.1016/j.carbon.2014.04.005.
[136] Y. Shao, S. Zhang, M.H. Engelhard, G. Li, G. Shao, Y. Wang, J. Liu, I.A. Aksay, Y. Lin, Nitrogen-doped graphene and its electrochemical applications, J. Mater. Chem. 20 (2010) 7491. https://doi.org/10.1039/c0jm00782j.
[137] H. Tao, Q. Fan, T. Ma, S. Liu, H. Gysling, J. Texter, F. Guo, Z. Sun, Two-dimensional materials for energy conversion and storage, Prog. Mater. Sci. 111 (2020) 100637. https://doi.org/10.1016/j.pmatsci.2020.100637.
[138] S. Chandra, S. Sahu, P. Pramanik, A novel synthesis of graphene by dichromate oxidation, Mater. Sci. Eng. B Solid-State Mater. Adv. Technol. 167 (2010) 133–136. https://doi.org/10.1016/j.mseb.2010.01.029.
[139] H. Wang, T. Maiyalagan, X. Wang, Review on recent progress in nitrogen-doped graphene: Synthesis, characterization, and its potential applications, ACS Catal. 2 (2012) 781–794. https://doi.org/10.1021/cs200652y.
[140] L. Peng, Z. Xu, Z. Liu, Y. Wei, H. Sun, Z. Li, X. Zhao, C. Gao, An iron-based green approach to 1-h production of single-layer graphene oxide, Nat. Commun. 6 (2015) 1–9. https://doi.org/10.1038/ncomms6716.
[141] X. Liu, X. Wang, G. Licht, S. Licht, Transformation of the greenhouse gas carbon dioxide to graphene, J. $CO_2$ Util. 36 (2020) 288–294. https://doi.org/10.1016/j.jcou.2019.11.019.
[142] S. Niyogi, M.A. Hamon, H. Hu, B. Zhao, P. Bhowmik, R. Sen, M.E. Itkis, R.C. Haddon, Chemistry of single-walled carbon nanotubes, Acc. Chem. Res. 35 (2002) 1105–1113. https://doi.org/10.1021/ar010155r.
[143] I. Kruusenberg, N. Alexeyeva, K. Tammeveski, J. Kozlova, L. Matisen, V. Sammelselg, J. Solla-Gullón, J.M. Feliu, Effect of purification of carbon nanotubes on their electrocatalytic properties for oxygen reduction in acid solution, Carbon 49 (2011) 4031–4039. https://doi.org/10.1016/j.carbon.2011.05.048.
[144] V. Datsyuk, M. Kalyva, K. Papagelis, J. Parthenios, D. Tasis, A. Siokou, I. Kallitsis, C. Galiotis, Chemical oxidation of multiwalled carbon nanotubes, Carbon 46 (2008) 833–840. https://doi.org/10.1016/j.carbon.2008.02.012.
[145] M. Pumera, B. Šmíd, K. Veltruská, Influence of Nitric Acid Treatment of Carbon Nanotubes on Their Physico-Chemical Properties, J. Nanosci. Nanotechnol. 9 (2009) 2671–2676. https://doi.org/10.1166/jnn.2009.031.
[146] N. Alexeyeva, K. Tammeveski, Electrochemical Reduction of Oxygen on Multiwalled Carbon Nanotube Modified Glassy Carbon Electrodes in Acid Media, Electrochem. Solid-State Lett. 10 (2007) F18. https://doi.org/10.1149/1.2713657.
[147] A.H. Brozena, J. Moskowitz, B. Shao, S. Deng, H. Liao, K.J. Gaskell, Y. Wang, Outer wall selectively oxidized, water-soluble double-walled carbon nanotubes, J. Am. Chem. Soc. 132 (2010) 3932–3938. https://doi.org/10.1021/ja910626u.
[148] Q. Shen, X. Liu, W. Jin, Solubility increase of multi-walled carbon nanotubes in water, Carbon 60 (2013) 562–563. https://doi.org/10.1016/j.carbon.2013.04.022.

[149] Y. Zhai, Y. Dou, D. Zhao, P.F. Fulvio, R.T. Mayes, S. Dai, Carbon materials for chemical capacitive energy storage, Adv. Mater. 23 (2011) 4828–4850. https://doi.org/10.1002/adma.201100984.
[150] R.K. Dash, G. Yushin, Y. Gogotsi, Synthesis, structure and porosity analysis of microporous and mesoporous carbon derived from zirconium carbide, Microporous Mesoporous Mater. 86 (2005) 50–57. https://doi.org/10.1016/j.micromeso.2005.05.047.
[151] A. Jänes, T. Thomberg, H. Kurig, E. Lust, Nanoscale fine-tuning of porosity of carbide-derived carbon prepared from molybdenum carbide, Carbon 47 (2009) 23–29. https://doi.org/10.1016/j.carbon.2008.07.010.
[152] A. Jänes, L. Permann, M. Arulepp, E. Lust, Electrochemical characteristics of nanoporous carbide-derived carbon materials in non-aqueous electrolyte solutions, Electrochem. Commun. 6 (2004) 313–318. https://doi.org/10.1016/j.elecom.2004.01.009.
[153] M. Schmirler, T. Knorr, T. Fey, A. Lynen, P. Greil, B.J.M. Etzold, Fast production of monolithic carbide-derived carbons with secondary porosity produced by chlorination of carbides containing a free metal phase, Carbon 49 (2011) 4359–4367. https://doi.org/10.1016/j.carbon.2011.06.013.
[154] J. Leis, A. Perkson, M. Arulepp, M. Käärik, G. Svensson, Carbon nanostructures produced by chlorinating aluminium carbide, Carbon 39 (2001) 2043–2048. https://doi.org/10.1016/S0008-6223(01)00020-3.
[155] J. Leis, M. Arulepp, M. Käärik, A. Perkson, The effect of $Mo_2C$ derived carbon pore size on the electrical double-layer characteristics in propylene carbonate-based electrolyte, Carbon 48 (2010) 4001–4008. https://doi.org/10.1016/j.carbon.2010.07.003.
[156] H. Meng, N. Larouche, M. Lefvre, F. Jaouen, B. Stansfield, J.P. Dodelet, Iron porphyrin-based cathode catalysts for polymer electrolyte membrane fuel cells: Effect of NH3and Ar mixtures as pyrolysis gases on catalytic activity and stability, Electrochim. Acta 55 (2010) 6450–6461. https://doi.org/10.1016/j.electacta.2010.06.039.
[157] X.X. Wang, D.A. Cullen, Y.-T. Pan, S. Hwang, M. Wang, Z. Feng, J. Wang, M.H. Engelhard, H. Zhang, Y. He, Y. Shao, D. Su, K.L. More, J.S. Spendelow, G. Wu, Nitrogen-Coordinated Single Cobalt Atom Catalysts for Oxygen Reduction in Proton Exchange Membrane Fuel Cells, Adv. Mater. 30 (2018) 1706758. https://doi.org/10.1002/adma.201706758.
[158] A. Uddin, L. Dunsmore, H. Zhang, L. Hu, G. Wu, S. Litster, High Power Density Platinum Group Metal-free Cathodes for Polymer Electrolyte Fuel Cells, ACS Appl. Mater. Interfaces 12 (2020) 2216–2224. https://doi.org/10.1021/acsami.9b13945.
[159] Y. Shao, J.P. Dodelet, G. Wu, P. Zelenay, PGM-Free Cathode Catalysts for PEM Fuel Cells: A Mini-Review on Stability Challenges, Adv. Mater. 31 (2019) 1807615. https://doi.org/10.1002/adma.201807615.
[160] Z. Yang, H. Nie, X. Chen, X. Chen, S. Huang, Recent progress in doped carbon nanomaterials as effective cathode catalysts for fuel cell oxygen reduction reaction, J. Power Sources. 236 (2013) 238–249. https://doi.org/10.1016/j.jpowsour.2013.02.057.
[161] H.R. Byon, J. Suntivich, E.J. Crumlin, Y. Shao-Horn, Fe-N-modified multi-walled carbon nanotubes for oxygen reduction reaction in acid, Phys. Chem. Chem. Phys. 13 (2011) 21437–21445. https://doi.org/Doi 10.1039/C1cp23029h.

[162] A. Sarapuu, K. Kreek, K. Kisand, M. Kook, M. Uibu, M. Koel, K. Tammeveski, Electrocatalysis of oxygen reduction by iron-containing nitrogen-doped carbon aerogels in alkaline solution, Electrochim. Acta 230 (2017) 81–88. https://doi.org/10.1016/j.electacta.2017.01.157.
[163] D. Banham, J. Choi, T. Kishimoto, S. Ye, Integrating PGM-Free Catalysts into Catalyst Layers and Proton Exchange Membrane Fuel Cell Devices, Adv. Mater. 31 (2019) 1804846. https://doi.org/10.1002/adma.201804846.
[164] D. Banham, T. Kishimoto, Y. Zhou, T. Sato, K. Bai, J.I. Ozaki, Y. Imashiro, S. Ye, Critical advancements in achieving high power and stable nonprecious metal catalyst-based MEAs for real-world proton exchange membrane fuel cell applications, Sci. Adv. 4 (2018) eaar7180. https://doi.org/10.1126/sciadv.aar7180.
[165] J.R. Varcoe, P. Atanassov, D.R. Dekel, A.M. Herring, M.A. Hickner, P.A. Kohl, A.R. Kucernak, W.E. Mustain, K. Nijmeijer, K. Scott, T. Xu, L. Zhuang, Anion-exchange membranes in electrochemical energy systems, Energy Environ. Sci. 7 (2014) 3135–3191. https://doi.org/10.1039/c4ee01303d.
[166] W.E. Mustain, Understanding how high-performance anion exchange membrane fuel cells were achieved: Component, interfacial, and cell-level factors, Curr. Opin. Electrochem. 12 (2018) 233–239. https://doi.org/10.1016/J.COELEC.2018.11.010.
[167] H.A. Firouzjaie, W.E. Mustain, Catalytic Advantages, Challenges, and Priorities in Alkaline Membrane Fuel Cells, ACS Catal. 10 (2020) 225–234. https://doi.org/10.1021/acscatal.9b03892.
[168] S. Gottesfeld, D.R. Dekel, M. Page, C. Bae, Y. Yan, P. Zelenay, Y.S. Kim, Anion exchange membrane fuel cells: Current status and remaining challenges, J. Power Sources 375 (2018) 170–184. https://doi.org/10.1016/j.jpowsour.2017.08.010.
[169] Z.F. Pan, L. An, T.S. Zhao, Z.K. Tang, Advances and challenges in alkaline anion exchange membrane fuel cells, Prog. Energy Combust. Sci. 66 (2018) 141–175. https://doi.org/10.1016/j.pecs.2018.01.001.
[170] N. Ramaswamy, S. Mukerjee, Alkaline Anion-Exchange Membrane Fuel Cells: Challenges in Electrocatalysis and Interfacial Charge Transfer, Chem. Rev. 119 (2019) 11945–11979. https://doi.org/10.1021/acs.chemrev.9b00157.
[171] Q. He, E.J. Cairns, Review—Recent Progress in Electrocatalysts for Oxygen Reduction Suitable for Alkaline Anion Exchange Membrane Fuel Cells, J. Electrochem. Soc. 162 (2015) F1504–F1539. https://doi.org/10.1149/2.0551514jes.
[172] L. Osmieri, L. Pezzolato, S. Specchia, Recent trends on the application of PGM-free catalysts at the cathode of anion exchange membrane fuel cells, Curr. Opin. Electrochem. 9 (2018) 240–256. https://doi.org/10.1016/j.coelec.2018.05.011.
[173] A. Sarapuu, E. Kibena-Põldsepp, M. Borghei, K. Tammeveski, Electrocatalysis of oxygen reduction on heteroatom-doped nanocarbons and transition metal-nitrogen-carbon catalysts for alkaline membrane fuel cells, J. Mater. Chem. A 6 (2018) 776–804. https://doi.org/10.1039/C7TA08690C.
[174] Y. Meng, W. Song, H. Huang, Z. Ren, S.Y. Chen, S.L. Suib, Structure-property relationship of bifunctional $MnO_2$ nanostructures: Highly efficient, ultra-stable electrochemical water oxidation and oxygen reduction reaction catalysts identified in alkaline media, J. Am. Chem. Soc. 136 (2014) 11452–11464. https://doi.org/10.1021/ja505186m.
[175] Y. Liang, Y. Li, H. Wang, J. Zhou, J. Wang, T. Regier, H. Dai, Co3O4 nanocrystals on graphene as a synergistic catalyst for oxygen reduction reaction, Nat. Mater. 10 (2011) 780–786. https://doi.org/10.1038/nmat3087.

[176] P.G. Santori, F.D. Speck, J. Li, A. Zitolo, Q. Jia, S. Mukerjee, S. Cherevko, F. Jaouen, Effect of Pyrolysis Atmosphere and Electrolyte pH on the Oxygen Reduction Activity, Stability and Spectroscopic Signature of $FeN_x$ Moieties in Fe-N-C Catalysts, J. Electrochem. Soc. 166 (2019) F3311–F3320. https://doi.org/10.1149/2.0371907jes.
[177] Y. Wang, Y. Yang, S. Jia, X. Wang, K. Lyu, Y. Peng, H. Zheng, X. Wei, H. Ren, L. Xiao, J. Wang, D.A. Muller, H.D. Abruña, B.J. Hwang, J. Lu, L. Zhuang, Synergistic Mn-Co catalyst outperforms Pt on high-rate oxygen reduction for alkaline polymer electrolyte fuel cells, Nat. Commun. 10 (2019) 1506. https://doi.org/10.1038/s41467-019-09503-4.
[178] X. Peng, V. Kashyap, B. Ng, S. Kurungot, L. Wang, J. Varcoe, W. Mustain, High-Performing PGM-Free AEMFC Cathodes from Carbon-Supported Cobalt Ferrite Nanoparticles, Catalysts 9 (2019) 264. https://doi.org/10.3390/catal9030264.
[179] J. Guo, A. Hsu, D. Chu, R. Chen, Improving oxygen reduction reaction activities on carbon-supported Ag nanoparticles in alkaline solutions, J. Phys. Chem. C 114 (2010) 4324–4330. https://doi.org/10.1021/jp910790u.
[180] A.L. Ong, K.K. Inglis, D.K. Whelligan, S. Murphy, J.R. Varcoe, Effect of cationic molecules on the oxygen reduction reaction on fuel cell grade Pt/C (20 wt%) catalyst in potassium hydroxide (aq, 1 mol dm-3), Phys. Chem. Chem. Phys. 17 (2015) 12135–12145. https://doi.org/10.1039/c4cp04973j.
[181] Q. He, X. Yang, R. He, A. Bueno-López, H. Miller, X. Ren, W. Yang, B.E. Koel, Electrochemical and spectroscopic study of novel Cu and Fe-based catalysts for oxygen reduction in alkaline media, J. Power Sources 213 (2012) 169–179. https://doi.org/10.1016/j.jpowsour.2012.04.029.
[182] P.G. Santori, F.D. Speck, S. Cherevko, H.A. Firouzjaie, X. Peng, W.E. Mustain, F. Jaouen, High Performance FeNC and Mn-oxide/FeNC Layers for AEMFC Cathodes, J. Electrochem. Soc. 167 (2020) 134505. https://doi.org/10.1149/1945-7111/abb7e0.
[183] P.G. Santori, A.N. Mondal, D.R. Dekel, F. Jaouen, The critical importance of ionomers on the electrochemical activity of platinum and platinum-free catalysts for anion-exchange membrane fuel cells, Sustain. Energy Fuels 4 (2020) 3300–3307. https://doi.org/10.1039/d0se00483a.
[184] L. Dai, Y. Xue, L. Qu, H.-J. Choi, J.-B. Baek, Metal-Free Catalysts for Oxygen Reduction Reaction, Chem. Rev. 115 (2015) 4823–4892. https://doi.org/10.1021/cr5003563.
[185] W.S. Hummers, R.E. Offeman, Preparation of Graphitic Oxide, J. Am. Chem. Soc. 80 (1958) 1339. https://doi.org/10.1021/ja01539a017.
[186] L. Sun, L. Wang, C. Tian, T. Tan, Y. Xie, K. Shi, M. Li, H. Fu, Nitrogen-doped graphene with high nitrogen level via a one-step hydrothermal reaction of graphene oxide with urea for superior capacitive energy storage, RSC Adv. 2 (2012) 4498. https://doi.org/10.1039/c2ra01367c.
[187] J. Leis, M. Arulepp, A. Perkson, Method to modify pore characteristics of porous carbon and porous carbon amterials produced by the same method, WO2004/094307, 2004.
[188] M. Käärik, M. Arulepp, M. Kook, U. Mäeorg, J. Kozlova, V. Sammelselg, A. Perkson, J. Leis, Characterisation of steam-treated nanoporous carbide-derived carbon of TiC origin: structure and enhanced electrochemical performance, J. Porous Mater. 25 (2018) 1057–1070. https://doi.org/10.1007/s10934-017-0517-8.

[189] M. Carmo, V.A. Paganin, J.M. Rosolen, E.R. Gonzalez, Alternative supports for the preparation of catalysts for low-temperature fuel cells: The use of carbon nanotubes, J. Power Sources 142 (2005) 169–176. https://doi.org/10.1016/j.jpowsour.2004.10.023.
[190] A.G. Wright, J. Fan, B. Britton, T. Weissbach, H.-F. Lee, E.A. Kitching, T.J. Peckham, S. Holdcroft, Hexamethyl-p-terphenyl poly(benzimidazolium): a universal hydroxide-conducting polymer for energy conversion devices, Energy Environ. Sci. 9 (2016) 2130–2142. https://doi.org/10.1039/C6EE00656F.
[191] M.P. Seah, I.S. Gilmore, S.J. Spencer, Quantitative XPS: I. Analysis of X-ray photoelectron intensities from elemental data in a digital photoelectron database, J. Electron Spectros. Relat. Phenomena. 120 (2001) 93–111. https://doi.org/10.1016/S0368-2048(01)00311-5.
[192] A.L. Ankudinov, B. Ravel, J.J. Rehr, S.D. Conradson, Real-space multiple-scattering calculation and interpretation of x-ray-absorption near-edge structure, Phys. Rev. B. 58 (1998) 7565–7576. https://doi.org/10.1103/PhysRevB.58.7565.
[193] B. Ravel, M. Newville, ATHENA, ARTEMIS, HEPHAESTUS: data analysis for X-ray absorption spectroscopy using IFEFFIT, J. Synchrotron Radiat. 12 (2005) 537–541. https://doi.org/10.1107/S0909049505012719.
[194] P.M. Schaber, J. Colson, S. Higgins, D. Thielen, B. Anspach, J. Brauer, Thermal decomposition (pyrolysis) of urea in an open reaction vessel, Thermochim. Acta 424 (2004) 131–142. https://doi.org/10.1016/j.tca.2004.05.018.
[195] P. Gross, H.A. Höppe, Biuret—A Crucial Reaction Intermediate for Understanding Urea Pyrolysis To Form Carbon Nitrides: Crystal-Structure Elucidation and In Situ Diffractometric, Vibrational and Thermal Characterisation, Chem. Eur. J. 26 (2020) 14366–14376. https://doi.org/10.1002/chem.202001396.
[196] J. Lilloja, E. Kibena-Põldsepp, A. Sarapuu, A. Kikas, V. Kisand, M. Käärik, M. Merisalu, A. Treshchalov, J. Leis, V. Sammelselg, Q. Wei, S. Holdcroft, K. Tammeveski, Nitrogen-doped carbide-derived carbon/carbon nanotube composites as cathode catalysts for anion exchange membrane fuel cell application, Appl. Catal. B Environ. 272 (2020) 119012. https://doi.org/10.1016/j.apcatb.2020.119012.
[197] A.M. Bernhard, D. Peitz, M. Elsener, A. Wokaun, O. Kröcher, Hydrolysis and thermolysis of urea and its decomposition byproducts biuret, cyanuric acid and melamine over anatase TiO 2, Appl. Catal. B Environ. 115–116 (2012) 129–137. https://doi.org/10.1016/j.apcatb.2011.12.013.
[198] S. Kundu, W. Xia, W. Busser, M. Becker, D.A. Schmidt, M. Havenith, M. Muhler, The formation of nitrogen-containing functional groups on carbon nanotube surfaces: a quantitative XPS and TPD study, Phys. Chem. Chem. Phys. 12 (2010) 4351–4359. https://doi.org/10.1039/b923651a.
[199] M.S. Dresselhaus, A. Jorio, M. Hofmann, G. Dresselhaus, R. Saito, Perspectives on carbon nanotubes and graphene Raman spectroscopy, Nano Lett. 10 (2010) 751–758. https://doi.org/10.1021/nl904286r.
[200] J.H. Lehman, M. Terrones, E. Mansfield, K.E. Hurst, V. Meunier, Evaluating the characteristics of multiwall carbon nanotubes, Carbon 49 (2011) 2581–2602. https://doi.org/10.1016/j.carbon.2011.03.028.
[201] L. Bokobza, J. Zhang, Raman spectroscopic characterization of multiwall carbon nanotubes and of composites, Express Polym. Lett. 6 (2012) 601–608. https://doi.org/10.3144/expresspolymlett.2012.63.

[202] K. Tammeveski, K. Kontturi, R.J. Nichols, R.J. Potter, D.J. Schiffrin, Surface redox catalysis for $O_2$ reduction on quinone-modified glassy carbon electrodes, J. Electroanal. Chem. 515 (2001) 101–112. https://doi.org/10.1016/S0022-0728(01)00633-7.
[203] A.J. Bard, L.R. Faulkner, Electrochemical Methods, 2nd ed., Wiley, New York, 2001.
[204] R.E. Davis, G.L. Horvath, C.W. Tobias, The solubility and diffusion coefficient of oxygen in potassium hydroxide solutions, Electrochim. Acta. 12 (1967) 287–297. https://doi.org/10.1016/0013-4686(67)80007-0.
[205] D.R. Lide, CRC Handbook of Chemistry and Physics, 82nd ed., CRC Press, Boca Raton, 2001. https://doi.org/10.1021/ja906434c.
[206] S. Yasuda, L. Yu, J. Kim, K. Murakoshi, Selective nitrogen doping in graphene for oxygen reduction reactions, Chem. Commun. 49 (2013) 9627. https://doi.org/10.1039/c3cc45641b.
[207] T. Sharifi, G. Hu, X. Jia, T. Wågberg, Formation of active sites for oxygen reduction reactions by transformation of nitrogen functionalities in nitrogen-doped carbon nanotubes, ACS Nano 6 (2012) 8904–8912. https://doi.org/10.1021/nn302906r.
[208] K. Gong, F. Du, Z. Xia, M. Durstock, L. Dai, Nitrogen-doped carbon nanotube arrays with high electrocatalytic activity for oxygen reduction, Science 323 (2009) 760–764. https://doi.org/10.1126/science.1168049.
[209] H. Li, W. Kang, L. Wang, Q. Yue, S. Xu, H. Wang, J. Liu, Synthesis of three-dimensional flowerlike nitrogen-doped carbons by a copyrolysis route and the effect of nitrogen species on the electrocatalytic activity in oxygen reduction reaction, Carbon 54 (2013) 249–257. https://doi.org/10.1016/j.carbon.2012.11.036.
[210] A. Ferre-Vilaplana, E. Herrero, Understanding the chemisorption-based activation mechanism of the oxygen reduction reaction on nitrogen-doped graphitic materials, Electrochim. Acta 204 (2016) 245–254. https://doi.org/10.1016/J.ELECTACTA.2016.04.039.
[211] P. Kanninen, M. Borghei, O. Sorsa, E. Pohjalainen, E.I. Kauppinen, V. Ruiz, T. Kallio, Highly efficient cathode catalyst layer based on nitrogen-doped carbon nanotubes for the alkaline direct methanol fuel cell, Appl. Catal. B Environ. 156–157 (2014) 341–349. https://doi.org/10.1016/j.apcatb.2014.03.041.
[212] T.N. Danks, R.C.T. Slade, J.R. Varcoe, Alkaline anion-exchange radiation-grafted membranes for possible electrochemical application in fuel cells, J. Mater. Chem. 13 (2003) 712–721. https://doi.org/10.1039/b212164f.
[213] A. Santasalo-Aarnio, S. Hietala, T. Rauhala, T. Kallio, In and ex situ characterization of an anion-exchange membrane for alkaline direct methanol fuel cell (ADMFC), J. Power Sources 196 (2011) 6153–6159. https://doi.org/10.1016/j.jpowsour.2011.03.028.
[214] J. Leis, A. Perkson, M. Arulepp, P. Nigu, G. Svensson, Catalytic effects of metals of the iron subgroup on the chlorination of titanium carbide to form nanostructural carbon, Carbon 40 (2002) 1559–1564. https://doi.org/10.1016/S0008-6223(02)00019-2.
[215] A. Ferrari, J. Robertson, Interpretation of Raman spectra of disordered and amorphous carbon, Phys. Rev. B - Condens. Matter Mater. Phys. 61 (2000) 14095–14107. https://doi.org/10.1103/PhysRevB.61.14095.

[216] Y. Liang, Y. Li, H. Wang, H. Dai, Strongly coupled inorganic/nanocarbon hybrid materials for advanced electrocatalysis, J. Am. Chem. Soc. 135 (2013) 2013–2036. https://doi.org/10.1021/ja3089923.
[217] P.H. Matter, L. Zhang, U.S. Ozkan, The role of nanostructure in nitrogen-containing carbon catalysts for the oxygen reduction reaction, J. Catal. 239 (2006) 83–96. https://doi.org/10.1016/j.jcat.2006.01.022.
[218] G. Yang, W. Choi, X. Pu, C. Yu, Scalable synthesis of bi-functional high-performance carbon nanotube sponge catalysts and electrodes with optimum C–N–Fe coordination for oxygen reduction reaction, Energy Environ. Sci. 8 (2015) 1799–1807. https://doi.org/10.1039/C5EE00682A.
[219] Y. Yao, H. Xiao, P. Wang, P. Su, Z. Shao, Q. Yang, CNTs@Fe–N–C core–shell nanostructures as active electrocatalyst for oxygen reduction, J. Mater. Chem. A 2 (2014) 11768. https://doi.org/10.1039/C4TA01237B.
[220] W.J. Jiang, L. Gu, L. Li, Y. Zhang, X. Zhang, L.J. Zhang, J.Q. Wang, J.S. Hu, Z. Wei, L.J. Wan, Understanding the High Activity of Fe-N-C Electrocatalysts in Oxygen Reduction: Fe/Fe3C Nanoparticles Boost the Activity of Fe-Nx, J. Am. Chem. Soc. 138 (2016) 3570–3578. https://doi.org/10.1021/jacs.6b00757.
[221] G. Wu, K.L. More, P. Xu, H.L. Wang, M. Ferrandon, A.J. Kropf, D.J. Myers, S. Ma, C.M. Johnston, P. Zelenay, A carbon-nanotube-supported graphene-rich non-precious metal oxygen reduction catalyst with enhanced performance durability, Chem. Commun. 49 (2013) 3291–3293. https://doi.org/10.1039/c3cc39121c.
[222] Y. Hu, J.O. Jensen, W. Zhang, L.N. Cleemann, W. Xing, N.J. Bjerrum, Q. Li, Hollow spheres of iron carbide nanoparticles encased in graphitic layers as oxygen reduction catalysts, Angew. Chem. Int. Ed. 53 (2014) 3675–3679. https://doi.org/10.1002/anie.201400358.
[223] J. Liang, R.F. Zhou, X.M. Chen, Y.H. Tang, S.Z. Qiao, Fe-N decorated hybrids of CNTs grown on hierarchically porous carbon for high-performance oxygen reduction, Adv. Mater. 26 (2014) 6074–6079. https://doi.org/10.1002/adma.201401848.
[224] S. Zhang, B. Liu, S. Chen, Synergistic increase of oxygen reduction favourable Fe-N coordination structures in a ternary hybrid of carbon nanospheres/carbon nanotubes/graphene sheets, Phys. Chem. Chem. Phys. 15 (2013) 18482–18490. https://doi.org/10.1039/c3cp53760a.
[225] S. Zhang, H. Zhang, Q. Liu, S. Chen, Fe-N doped carbon nanotube/graphene composite: Facile synthesis and superior electrocatalytic activity, J. Mater. Chem. A 1 (2013) 3302–3308. https://doi.org/10.1039/c2ta01351g.
[226] G. Liu, X. Li, J.W. Lee, B.N. Popov, A review of the development of nitrogen-modified carbon-based catalysts for oxygen reduction at USC, Catal. Sci. Technol. 1 (2011) 207–217. https://doi.org/10.1039/c0cy00053a.
[227] XPS,AES,UPS and ESCA, laSurface.com, (n.d.). http://www.lasurface.com/xps/imfp.php (accessed October 20, 2020).
[228] H.Y. Liu, M.J. Weaver, C.B. Wang, C.K. Chang, Dependence of electrocatalysis for oxygen reduction by adsorbed dicobalt cofacial porphyrins upon catalyst structure, J. Electroanal. Chem. 145 (1983) 439–447. https://doi.org/10.1016/S0022-0728(83)80098-9.
[229] J. Zhang (Ed.), PEM fuel cell electrocatalysts and catalyst layers: Fundamentals and applications, Springer, 2008, pp. 1–1137. https://doi.org/10.1007/978-1-84800-936-3.

[230] S.L. Gojković, S. Gupta, R.F. Savinell, Heat-treated iron(III) tetramethoxyphenyl porphyrin chloride supported on high-area carbon as an electrocatalyst for oxygen reduction: Part III. Detection of hydrogen-peroxide during oxygen reduction, Electrochim. Acta 45 (1999) 889–897. https://doi.org/10.1016/S0013-4686(99)00294-7.
[231] V. Di Noto, E. Negro, A. Nale, G. Pagot, K. Vezzù, P. Atanassov, Hidden in plain sight: unlocking the full potential of cyclic voltammetry with the thin-film rotating (ring) disk electrode studies for the investigation of oxygen reduction reaction electrocatalysts, Curr. Opin. Electrochem. 25 (2021) 100626. https://doi.org/10.1016/j.coelec.2020.08.008.
[232] Y. Li, W. Zhou, H. Wang, L. Xie, Y. Liang, F. Wei, J.-C. Idrobo, S.J. Pennycook, H. Dai, An oxygen reduction electrocatalyst based on carbon nanotube–graphene complexes, Nat. Nanotechnol. 7 (2012) 394–400. https://doi.org/10.1038/nnano.2012.72.
[233] U. Tylus, Q. Jia, K. Strickland, N. Ramaswamy, A. Serov, P. Atanassov, S. Mukerjee, Elucidating oxygen reduction active sites in pyrolyzed metal-nitrogen coordinated non-precious-metal electrocatalyst systems, J. Phys. Chem. C 118 (2014) 8999–9008. https://doi.org/10.1021/jp500781v.
[234] M.S. Thorum, J.M. Hankett, A.A. Gewirth, Poisoning the oxygen reduction reaction on carbon-supported Fe and Cu electrocatalysts: Evidence for metal-centered activity, J. Phys. Chem. Lett. 2 (2011) 295–298. https://doi.org/10.1021/jz1016284.
[235] J. Masa, W. Xia, M. Muhler, W. Schuhmann, On the Role of Metals in Nitrogen-Doped Carbon Electrocatalysts for Oxygen Reduction, Angew. Chem. Int. Ed. 54 (2015) 10102–10120. https://doi.org/10.1002/anie.201500569.
[236] D. Deng, L. Yu, X. Chen, G. Wang, L. Jin, X. Pan, J. Deng, G. Sun, X. Bao, Iron Encapsulated within Pod-like Carbon Nanotubes for Oxygen Reduction Reaction, Angew. Chem. Int. Ed. 52 (2013) 371–375. https://doi.org/10.1002/anie.201204958.
[237] J. Song, C. Zhu, S. Fu, Y. Song, D. Du, Y. Lin, Optimization of cobalt/nitrogen embedded carbon nanotubes as an efficient bifunctional oxygen electrode for rechargeable zinc–air batteries, J. Mater. Chem. A 4 (2016) 4864–4870. https://doi.org/10.1039/C6TA00615A.
[238] L. Li, X. Yuan, Z. Ma, Z.-F. Ma, Properties of Pyrolyzed Carbon-Supported Cobalt-Polypyrrole as Electrocatalyst toward Oxygen Reduction Reaction in Alkaline Media, J. Electrochem. Soc. 162 (2015) F359–F365. https://doi.org/10.1149/2.0081504jes.
[239] X. Yuan, H.D. Sha, X.L. Ding, H.C. Kong, H. Lin, W. Wen, T. Huang, Z. Guo, Z.F. Ma, Y. Yang, Comparative investigation on the properties of carbon-supported cobalt-polypyrrole pyrolyzed at various conditions as electrocatalyst towards oxygen reduction reaction, Int. J. Hydrogen Energy 39 (2014) 15937–15947. https://doi.org/10.1016/j.ijhydene.2014.03.205.
[240] G.K.S. Prakash, F.C. Krause, F.A. Viva, S.R. Narayanan, G.A. Olah, Study of operating conditions and cell design on the performance of alkaline anion exchange membrane based direct methanol fuel cells, J. Power Sources 196 (2011) 7967–7972. https://doi.org/10.1016/j.jpowsour.2011.05.056.
[241] M.C. Figueiredo, R.M. Arán-Ais, V. Climent, T. Kallio, J.M. Feliu, Evidence of Local pH Changes during Ethanol Oxidation at Pt Electrodes in Alkaline Media, ChemElectroChem 2 (2015) 1254–1258. https://doi.org/10.1002/celc.201500151.

[242] J.R. Varcoe, R.C.T. Slade, Prospects for alkaline anion-exchange membranes in low temperature fuel cells, Fuel Cells 5 (2005) 187–200. https://doi.org/10.1002/fuce.200400045.
[243] R. Janarthanan, A. Serov, S.K. Pilli, D.A. Gamarra, P. Atanassov, M.R. Hibbs, A.M. Herring, Direct Methanol Anion Exchange Membrane Fuel Cell with a Non-Platinum Group Metal Cathode based on Iron-Aminoantipyrine Catalyst, Electrochim. Acta 175 (2015) 202–208. https://doi.org/10.1016/j.electacta.2015.03.209.
[244] M.S. Naughton, F.R. Brushett, P.J.A. Kenis, Carbonate resilience of flowing electrolyte-based alkaline fuel cells, J. Power Sources 196 (2011) 1762–1768. https://doi.org/10.1016/j.jpowsour.2010.09.114.
[245] D. Sebastián, A. Serov, I. Matanovic, K. Artyushkova, P. Atanassov, A.S. Aricò, V. Baglio, Insights on the extraordinary tolerance to alcohols of Fe-N-C cathode catalysts in highly performing direct alcohol fuel cells, Nano Energy 34 (2017) 195–204. https://doi.org/10.1016/j.nanoen.2017.02.039.
[246] D. Sebastián, V. Baglio, A.S. Aricò, A. Serov, P. Atanassov, Performance analysis of a non-platinum group metal catalyst based on iron-aminoantipyrine for direct methanol fuel cells, Appl. Catal. B Environ. 182 (2016) 297–305. https://doi.org/10.1016/j.apcatb.2015.09.043.
[247] F. Jaouen, E. Proietti, M. Lefèvre, R. Chenitz, J.-P. Dodelet, G. Wu, H.T. Chung, C.M. Johnston, P. Zelenay, Recent advances in non-precious metal catalysis for oxygen-reduction reaction in polymer electrolyte fuel cells, Energy Environ. Sci. 4 (2011) 114. https://doi.org/10.1039/c0ee00011f.
[248] X. Xie, C. He, B. Li, Y. He, D.A. Cullen, E.C. Wegener, A.J. Kropf, U. Martinez, Y. Cheng, M.H. Engelhard, M.E. Bowden, M. Song, T. Lemmon, X.S. Li, Z. Nie, J. Liu, D.J. Myers, P. Zelenay, G. Wang, G. Wu, V. Ramani, Y. Shao, Performance enhancement and degradation mechanism identification of a single-atom Co–N–C catalyst for proton exchange membrane fuel cells, Nat. Catal. (2020). https://doi.org/10.1038/s41929-020-00546-1.
[249] U. Koslowski, I. Herrmann, P. Bogdanoff, C. Barkschat, S. Fiechter, N. Iwata, H. Takahashi, H. Nishikori, Evaluation and Analysis of PEM-FC Performance using Non-Platinum Cathode Catalysts based on Pyrolysed Fe- and Co-Porphyrins – Influence of a Secondary Heat-treatment, ECS Trans. (2008) 125–141. https://doi.org/10.1149/1.3039771.
[250] R. Zhou, Y. Zheng, M. Jaroniec, S.Z. Qiao, Determination of the Electron Transfer Number for the Oxygen Reduction Reaction: From Theory to Experiment, ACS Catal. 6 (2016) 4720–4728. https://doi.org/10.1021/acscatal.6b01581.
[251] F.D. Coms, The Chemistry of Fuel Cell Membrane Chemical Degradation, ECS Trans. 16 (2019) 235–255. https://doi.org/10.1149/1.2981859.
[252] M.R. Tarasevich, A. Sadkowski, E. Yeager, Oxygen Electrochemistry, in: B.E. Conway, J.O'M. Bockris, E. Yeager, S.U.M. Khan, R.E. White (Eds.), Comprehensive Treatise of Electrochemistry, Plenum Press, New York, vol. 7, 1983, pp. 301–398. https://doi.org/10.1007/978-1-4613-3584-9_6.
[253] H.S. Oh, H. Kim, The role of transition metals in non-precious nitrogen-modified carbon-based electrocatalysts for oxygen reduction reaction, J. Power Sources 212 (2012) 220–225. https://doi.org/10.1016/j.jpowsour.2012.03.098.
[254] X. Wang, Q. Li, H. Pan, Y. Lin, Y. Ke, H. Sheng, M.T. Swihart, G. Wu, Size-controlled large-diameter and few-walled carbon nanotube catalysts for oxygen reduction, Nanoscale 7 (2015) 20290–20298. https://doi.org/10.1039/C5NR05864C.

[255] D. Banham, S. Ye, K. Pei, J.I. Ozaki, T. Kishimoto, Y. Imashiro, A review of the stability and durability of non-precious metal catalysts for the oxygen reduction reaction in proton exchange membrane fuel cells, J. Power Sources 285 (2015) 334–348. https://doi.org/10.1016/j.jpowsour.2015.03.047.
[256] V. Goellner, C. Baldizzone, A. Schuppert, M.T. Sougrati, K. Mayrhofer, F. Jaouen, Degradation of Fe/N/C catalysts upon high polarization in acid medium, Phys. Chem. Chem. Phys. 16 (2014) 18454–18462. https://doi.org/10.1039/c4cp02882a.
[257] M. Thommes, K. Kaneko, A. V. Neimark, J.P. Olivier, F. Rodriguez-Reinoso, J. Rouquerol, K.S.W. Sing, Physisorption of gases, with special reference to the evaluation of surface area and pore size distribution (IUPAC Technical Report), Pure Appl. Chem. 87 (2015) 1051–1069. https://doi.org/10.1515/pac-2014-1117.
[258] H.W. Liang, W. Wei, Z.S. Wu, X. Feng, K. Müllen, Mesoporous metal-nitrogen-doped carbon electrocatalysts for highly efficient oxygen reduction reaction, J. Am. Chem. Soc. 135 (2013) 16002–16005. https://doi.org/10.1021/ja407552k.
[259] Y. Sun, J. Wu, J. Tian, C. Jin, R. Yang, Sulfur-doped carbon spheres as efficient metal-free electrocatalysts for oxygen reduction reaction, Electrochim. Acta 178 (2015) 806–812. https://doi.org/10.1016/j.electacta.2015.08.059.
[260] S. Fu, C. Zhu, H. Li, D. Du, Y. Lin, One-step synthesis of cobalt and nitrogen co-doped carbon nanotubes and their catalytic activity for the oxygen reduction reaction, J. Mater. Chem. A 3 (2015) 12718–12722. https://doi.org/10.1039/C5TA01293G.
[261] M. Lei, J. Wang, J.R. Li, Y.G. Wang, H.L. Tang, W.J. Wang, Emerging methanol-tolerant AlN nanowire oxygen reduction electrocatalyst for alkaline direct methanol fuel cell, Sci. Rep. 4 (2014) 6013. https://doi.org/10.1038/srep06013.
[262] X. Li, B.N. Popov, T. Kawahara, H. Yanagi, Non-precious metal catalysts synthesized from precursors of carbon, nitrogen, and transition metal for oxygen reduction in alkaline fuel cells, J. Power Sources 196 (2011) 1717–1722. https://doi.org/10.1016/j.jpowsour.2010.10.018.
[263] L. Yang, N. Larouche, R. Chenitz, G. Zhang, M. Lefèvre, J.-P.P. Dodelet, Activity, Performance, and Durability for the Reduction of Oxygen in PEM Fuel Cells, of Fe/N/C Electrocatalysts Obtained from the Pyrolysis of Metal-Organic-Framework and Iron Porphyrin Precursors, Electrochim. Acta 159 (2015) 184–197. https://doi.org/10.1016/j.electacta.2015.01.201.
[264] Q. He, Q. Li, S. Khene, X. Ren, F.E. López-Suárez, D. Lozano-Castelló, A. Bueno-López, G. Wu, High-loading cobalt oxide coupled with nitrogen-doped graphene for oxygen reduction in anion-exchange-membrane alkaline fuel cells, J. Phys. Chem. C 117 (2013) 8697–8707. https://doi.org/10.1021/jp401814f.
[265] Y. Leng, L. Wang, M.A. Hickner, C.Y. Wang, Alkaline membrane fuel cells with in-situ cross-linked ionomers, Electrochim. Acta 152 (2015) 93–100. https://doi.org/10.1016/j.electacta.2014.11.055.
[266] S. Lee, M. Choun, Y. Ye, J. Lee, Y. Mun, E. Kang, J. Hwang, Y.H. Lee, C.H. Shin, S.H. Moon, S.K. Kim, E. Lee, J. Lee, Designing a Highly Active Metal-Free Oxygen Reduction Catalyst in Membrane Electrode Assemblies for Alkaline Fuel Cells: Effects of Pore Size and Doping-Site Position, Angew. Chem. Int. Ed. 54 (2015) 9230–9234. https://doi.org/10.1002/anie.201501590.

[267] S. Ratso, N. Ranjbar Sahraie, M.T. Sougrati, M. Käärik, M. Kook, R. Saar, P. Paiste, Q. Jia, J. Leis, S. Mukerjee, F. Jaouen, K. Tammeveski, Synthesis of highly-active Fe-N-C catalysts for PEMFC with carbide-derived carbons, J. Mater. Chem. A 6 (2018) 14663–14674. https://doi.org/10.1039/c8ta02325e.

[268] S. Ratso, I. Kruusenberg, M. Käärik, M. Kook, R. Saar, P. Kanninen, T. Kallio, J. Leis, K. Tammeveski, Transition metal-nitrogen co-doped carbide-derived carbon catalysts for oxygen reduction reaction in alkaline direct methanol fuel cell, Appl. Catal. B Environ. 219 (2017) 276–286. https://doi.org/10.1016/j.apcatb.2017.07.036.

[269] S. Ratso, M.T. Sougrati, M. Käärik, M. Merisalu, M. Rähn, V. Kisand, A. Kikas, P. Paiste, J. Leis, V. Sammelselg, F. Jaouen, K. Tammeveski, Effect of Ball-Milling on the Oxygen Reduction Reaction Activity of Iron and Nitrogen Co-doped Carbide-Derived Carbon Catalysts in Acid Media, ACS Appl. Energy Mater. 2 (2019) 7952–7962. https://doi.org/10.1021/acsaem.9b01430.

[270] A. Nouri, C. Wen, Surfactants in Mechanical Alloying/Milling: A Catch-22 Situation, Crit. Rev. Solid State Mater. Sci. 39 (2014) 81–108. https://doi.org/10.1080/10408436.2013.808985.

[271] J. Li, S. Ghoshal, W. Liang, M.-T. Sougrati, F. Jaouen, B. Halevi, S. McKinney, G. McCool, C. Ma, X. Yuan, Z.-F. Ma, S. Mukerjee, Q. Jia, Structural and mechanistic basis for the high activity of Fe–N–C catalysts toward oxygen reduction, Energy Environ. Sci. 9 (2016) 2418–2432. https://doi.org/10.1039/C6EE01160H.

[272] Y.J. Sa, D.J. Seo, J. Woo, J.T. Lim, J.Y. Cheon, S.Y. Yang, J.M. Lee, D. Kang, T.J. Shin, H.S. Shin, H.Y. Jeong, C.S. Kim, M.G. Kim, T.Y. Kim, S.H. Joo, A General Approach to Preferential Formation of Active Fe-Nx Sites in Fe-N/C Electrocatalysts for Efficient Oxygen Reduction Reaction, J. Am. Chem. Soc. 138 (2016) 15046–15056. https://doi.org/10.1021/jacs.6b09470.

[273] S.H. Lee, J. Kim, D.Y. Chung, J.M. Yoo, H.S. Lee, M.J. Kim, B.S. Mun, S.G. Kwon, Y.-E. Sung, T. Hyeon, Design Principle of Fe–N–C Electrocatalysts: How to Optimize Multimodal Porous Structures?, J. Am. Chem. Soc. 141 (2019) 2035–2045. https://doi.org/10.1021/jacs.8b11129.

[274] J. Woo, S.Y. Yang, Y.J. Sa, W.Y. Choi, M.H. Lee, H.W. Lee, T.J. Shin, T.Y. Kim, S.H. Joo, Promoting Oxygen Reduction Reaction Activity of Fe-N/C Electrocatalysts by Silica-Coating-Mediated Synthesis for Anion-Exchange Membrane Fuel Cells, Chem. Mater. 30 (2018) 6684–6701. https://doi.org/10.1021/acs.chemmater.8b02117.

[275] H. Zhang, S. Zhang, Y. Wang, J. Si, Y. Chen, L. Zhuang, S. Chen, Boosting the Performance of Iron-Phthalocyanine as Cathode Electrocatalyst for Alkaline Polymer Fuel Cells Through Edge-Closed Conjugation, ACS Appl. Mater. Interfaces 10 (2018) 28664–28671. https://doi.org/10.1021/acsami.8b09074.

[276] S.T. Thompson, D. Peterson, D. Ho, D. Papageorgopoulos, Perspective—The Next Decade of AEMFCs: Near-Term Targets to Accelerate Applied R&D, J. Electrochem. Soc. 167 (2020) 084514. https://doi.org/10.1149/1945-7111/ab8c88.

[277] M. Käärik, M. Arulepp, M. Karelson, J. Leis, The effect of graphitization catalyst on the structure and porosity of SiC derived carbons, Carbon 46 (2008) 1579–1587. https://doi.org/10.1016/j.carbon.2008.07.003.

[278] H.A. Miller, M. Bellini, W. Oberhauser, X. Deng, H. Chen, Q. He, M. Passaponti, M. Innocenti, R. Yang, F. Sun, Z. Jiang, F. Vizza, Heat treated carbon supported iron( <scp>ii</scp> )phthalocyanine oxygen reduction catalysts: elucidation of the structure–activity relationship using X-ray absorption spectroscopy, Phys. Chem. Chem. Phys. 18 (2016) 33142–33151. https://doi.org/10.1039/C6CP06798K.

[279] H.C. Huang, Y.C. Lin, S.T. Chang, C.C. Liu, K.C. Wang, H.P. Jhong, J.F. Lee, C.H. Wang, Effect of a sulfur and nitrogen dual-doped Fe-N-S electrocatalyst for the oxygen reduction reaction, J. Mater. Chem. A 5 (2017) 19790–19799. https://doi.org/10.1039/c7ta05030e.

[280] I. Kruusenberg, L. Matisen, Q. Shah, A.M. Kannan, K. Tammeveski, Non-platinum cathode catalysts for alkaline membrane fuel cells, Int. J. Hydrogen Energy 37 (2012) 4406–4412. https://doi.org/10.1016/j.ijhydene.2011.11.143.

[281] J. Sanetuntikul, C. Chuaicham, Y.-W. Choi, S. Shanmugam, Investigation of hollow nitrogen-doped carbon spheres as non-precious Fe–$N_4$ based oxygen reduction catalysts, J. Mater. Chem. A 3 (2015) 15473–15481. https://doi.org/10.1039/C5TA02677F.

[282] G.A. Ferrero, K. Preuss, A. Marinovic, A.B. Jorge, N. Mansor, D.J.L. Brett, A.B. Fuertes, M. Sevilla, M.M. Titirici, Fe-N-Doped Carbon Capsules with Outstanding Electrochemical Performance and Stability for the Oxygen Reduction Reaction in Both Acid and Alkaline Conditions, ACS Nano 10 (2016) 5922–5932. https://doi.org/10.1021/acsnano.6b01247.

[283] M.M. Hossen, K. Artyushkova, P. Atanassov, A. Serov, Synthesis and characterization of high performing Fe-N-C catalyst for oxygen reduction reaction (ORR) in Alkaline Exchange Membrane Fuel Cells, J. Power Sources 375 (2018) 214–221. https://doi.org/10.1016/j.jpowsour.2017.08.036.

[284] R. Praats, M. Käärik, A. Kikas, V. Kisand, J. Aruväli, P. Paiste, M. Merisalu, J. Leis, V. Sammelselg, J.H. Zagal, S. Holdcroft, N. Nakashima, K. Tammeveski, Electrocatalytic oxygen reduction reaction on iron phthalocyanine-modified carbide-derived carbon/carbon nanotube composite electrocatalysts, Electrochim. Acta 334 (2020) 135575. https://doi.org/10.1016/j.electacta.2019.135575.

[285] R. Sibul, E. Kibena-Põldsepp, S. Ratso, M. Kook, M.T. Sougrati, M. Käärik, M. Merisalu, J. Aruväli, P. Paiste, A. Treshchalov, J. Leis, V. Kisand, V. Sammelselg, S. Holdcroft, F. Jaouen, K. Tammeveski, Iron- and Nitrogen-Doped Graphene-Based Catalysts for Fuel Cell Applications, ChemElectroChem 7 (2020) 1739–1747. https://doi.org/10.1002/celc.202000011.

[286] M. Mooste, E. Kibena-Põldsepp, V. Vassiljeva, A. Kikas, M. Käärik, J. Kozlova, V. Kisand, M. Külaviir, S. Cavaliere, J. Leis, A. Krumme, V. Sammelselg, S. Holdcroft, K. Tammeveski, Electrospun Polyacrylonitrile-Derived Co or Fe Containing Nanofibre Catalysts for Oxygen Reduction Reaction at the Alkaline Membrane Fuel Cell Cathode, ChemCatChem 12 (2020) 4568–4581. https://doi.org/10.1002/cctc.202000658.

[287] K. Kisand, A. Sarapuu, D. Danilian, A. Kikas, V. Kisand, M. Rähn, A. Treshchalov, M. Käärik, M. Merisalu, P. Paiste, J. Aruväli, J. Leis, V. Sammelselg, S. Holdcroft, K. Tammeveski, Transition metal-containing nitrogen-doped nanocarbon catalysts derived from 5-methylresorcinol for anion exchange membrane fuel cell application, J. Colloid Interface Sci. 584 (2021) 263–274. https://doi.org/10.1016/j.jcis.2020.09.114.

[288] T. Sun, L. Xu, S. Li, W. Chai, Y. Huang, Y. Yan, J. Chen, Cobalt-nitrogen-doped ordered macro-/mesoporous carbon for highly efficient oxygen reduction reaction, Appl. Catal. B Environ. 193 (2016) 1–8. https://doi.org/10.1016/j.apcatb.2016.04.006.
[289] J.Y. Cheon, T. Kim, Y. Choi, H.Y. Jeong, M.G. Kim, Y.J. Sa, J. Kim, Z. Lee, T.H. Yang, K. Kwon, O. Terasaki, G.G. Park, R.R. Adzic, S.H. Joo, Ordered mesoporous porphyrinic carbons with very high electrocatalytic activity for the oxygen reduction reaction, Sci. Rep. 3 (2013) 2715. https://doi.org/10.1038/srep02715.
[290] J.D. Cooper, T.C. Gibb, N.N. Greenwood, R. V. Parish, Chemical applications of the mössbauer effect. Part 1.—The bonding in iron borides, Trans. Faraday Soc. 60 (1964) 2097–2104. https://doi.org/10.1039/TF9646002097.
[291] T. Kanaizuka, Interpretation of Mössbauer Spectra of β-FeB and Its Low Temperature Modification, α-FeB, Phys. Status Solidi. 69 (1982) 739–744. https://doi.org/10.1002/pssa.2210690237.
[292] N. Markovic, Kinetics of Oxygen Reduction on Pt(hkl) Electrodes: Implications for the Crystallite Size Effect with Supported Pt Electrocatalysts, J. Electrochem. Soc. 144 (1997) 1591-1597. https://doi.org/10.1149/1.1837646.
[293] Y. Chen, R. Gokhale, A. Serov, K. Artyushkova, P. Atanassov, Novel highly active and selective Fe-N-C oxygen reduction electrocatalysts derived from in-situ polymerization pyrolysis, Nano Energy 38 (2017) 201–209. https://doi.org/10.1016/j.nanoen.2017.05.059.
[294] X. Fu, P. Zamani, J.Y. Choi, F.M. Hassan, G. Jiang, D.C. Higgins, Y. Zhang, M.A. Hoque, Z. Chen, In Situ Polymer Graphenization Ingrained with Nanoporosity in a Nitrogenous Electrocatalyst Boosting the Performance of Polymer-Electrolyte-Membrane Fuel Cells, Adv. Mater. 29 (2017) 1604456. https://doi.org/10.1002/adma.201604456.
[295] C. Suryanarayana, Mechanical alloying and milling, Prog. Mater. Sci. 46 (2001) 1–184. https://doi.org/10.1016/S0079-6425(99)00010-9.
[296] R. Jäger, P.E. Kasatkin, E. Härk, P. Teppor, T. Romann, R. Härmas, I. Tallo, U.Mäeorg, U. Joost, P. Paiste, K. Kirsimäe, E. Lust, The effect of N precursors in Fe-N/C type catalysts based on activated silicon carbide derived carbon for oxygen reduction activity at various pH values, J. Electroanal. Chem. 823 (2018) 593–600. https://doi.org/10.1016/j.jelechem.2018.06.040.
[297] P. Teppor, R. Jäger, E. Härk, U. Joost, I. Tallo, P. Paiste, K. Kirsimäe, E. Lust, Oxygen Reduction Reaction on Nitrogen and Cobalt Modified Silicon Carbide Derived Carbon in Acidic Media, ECS Trans. 85 (2018) 855–863. https://doi.org/10.1149/08513.0855ecst.
[298] P.E. Kasatkin, R. Jäger, E. Härk, P. Teppor, I. Tallo, U. Joost, K. Šmits, R. Kanarbik, E. Lust, Fe-N/C catalysts for oxygen reduction based on silicon carbide derived carbon, Electrochem. Commun. 80 (2017) 33–38. https://doi.org/10.1016/j.elecom.2017.05.001.
[299] M. Härmas, T. Thomberg, H. Kurig, T. Romann, A. Jänes, E. Lust, Microporous–mesoporous carbons for energy storage synthesized by activation of carbonaceous material by zinc chloride, potassium hydroxide or mixture of them, J. Power Sources 326 (2016) 624–634. https://doi.org/10.1016/J.JPOWSOUR.2016.04.038.

[300] P. Madkikar, T. Mittermeier, H.A. Gasteiger, M. Piana, Synergistic Effect on the Activity of ZrO2 -Fe as PGM-Free ORR Catalysts for PEMFCs, J. Electrochem. Soc. 164 (2017) F831–F833. https://doi.org/10.1149/2.1091707jes.
[301] J.F. Carneiro, L.C. Trevelin, A.S. Lima, G.N. Meloni, M. Bertotti, P. Hammer, R. Bertazzoli, M.R.V. Lanza, Synthesis and Characterization of $ZrO_2$/C as Electrocatalyst for Oxygen Reduction to $H_2O_2$, Electrocatalysis 8 (2017) 189–195. https://doi.org/10.1007/s12678-017-0355-0.
[302] Y. Liu, A. Ishihara, S. Mitsushima, K. Ota, Influence of sputtering power on oxygen reduction reaction activity of zirconium oxides prepared by radio frequency reactive sputtering, Electrochim. Acta 55 (2010) 1239–1244. https://doi.org/10.1016/J.ELECTACTA.2009.10.042.
[303] J.-H. Kim, A. Ishihara, S. Mitsushima, N. Kamiya, K.-I. Ota, Catalytic activity of titanium oxide for oxygen reduction reaction as a non-platinum catalyst for PEFC, Electrochim. Acta 52 (2007) 2492–2497. https://doi.org/10.1016/J.ELECTACTA.2006.08.059.
[304] C.H. Choi, C. Baldizzone, J.P. Grote, A.K. Schuppert, F. Jaouen, K.J.J. Mayrhofer, Stability of Fe-N-C catalysts in acidic medium studied by operando spectroscopy, Angew. Chem. Int. Ed. 54 (2015) 12753–12757. https://doi.org/10.1002/anie.201504903.
[305] A. Serov, Active and Durable PGM-free Cathodic Electrocatalysts for Fuel Cell Application, in: n.d. https://www.hydrogen.energy.gov/pdfs/review20/fc305_serov_2020_o.pdf (accessed November 23, 2020).
[306] P.N. Pintauro, Fuel Cell Membrane-Electrode-Assemblies with PGM-free Nanofiber Cathodes, 2019.
[307] H. Barkholtz, L. Chong, Z. Kaiser, T. Xu, D.-J. Liu, Highly Active Non-PGM Catalysts Prepared from Metal Organic Frameworks, Catalysts 5 (2015) 955–965. https://doi.org/10.3390/catal5020955.
[308] Q. Liu, X. Liu, L. Zheng, J. Shui, The Solid-Phase Synthesis of an Fe-N-C Electrocatalyst for High-Power Proton-Exchange Membrane Fuel Cells, Angew. Chem. Int. Ed. 57 (2018) 1204–1208. https://doi.org/10.1002/anie.201709597.
[309] J.Y. Choi, L. Yang, T. Kishimoto, X. Fu, S. Ye, Z. Chen, D. Banham, Is the rapid initial performance loss of Fe/N/C non precious metal catalysts due to micropore flooding?, Energy Environ. Sci. 10 (2017) 296–305. https://doi.org/10.1039/c6ee03005j.
[310] P. Zelenay, D. Myers, 2020 Hydrogen and Fuel Cells Program Annual Merit Review, Electrocatalysis Consortium, n.d. www.hydrogen.energy.gov/pdfs/review19/plenary_fuel_cell_papageorgopoulos_2019.pdf (accessed November 24, 2020).
[311] J. Li, H. Zhang, W. Samarakoon, W. Shan, D.A. Cullen, S. Karakalos, M. Chen, D. Gu, K.L. More, G. Wang, Z. Feng, Z. Wang, G. Wu, Thermally Driven Structure and Performance Evolution of Atomically Dispersed $FeN_4$ Sites for Oxygen Reduction, Angew. Chem. Int. Ed. 58 (2019) 18971–18980. https://doi.org/10.1002/anie.201909312.
[312] C. Shu, Y. Chen, X.D. Yang, Y. Liu, S. Chong, Y. Fang, Y. Liu, W.H. Yang, Enhanced Fe dispersion via “pinning” effect of thiocyanate ion on ferric ion in Fe-N-S-doped catalyst as an excellent oxygen reduction reaction electrode, J. Power Sources 376 (2018) 161–167. https://doi.org/10.1016/j.jpowsour.2017.11.093.

# 10. SUMMARY IN ESTONIAN

## Hapniku elektrokatalüütiline redutseerumine mitteväärismetallkatalüsaatoritel

Käesoleva doktoritöö põhieesmärgiks oli uurida odavaid ja kättesaadavaid asendusmaterjale süsinikmaterjalidele kantud plaatinakatalüsaatoritele (Pt/C) hapniku redutseerumisreaktsiooniks polümeer-elektrolüüt kütuseelementide (PEFC) katoodil. Sellel eesmärgil sünteesiti ja karakteriseeriti töö esimeses osas grafiidist valmistatud grafeenoksiidi ja puhastatud mitmeseinalistest süsiniknanotorudest (MWCNT) valmistatud lämmastikuga dopeeritud komposiitkatalüsaatoreid [I–III]. Lämmastikuga dopeerimiseks kasutati semikarbasiidi, karbohüdrasiidi, biureeti, uureat ja ditsüaandiamiidi (DCDA), millest parima tulemuse andis DCDA. DCDA abil valmistatud katalüsaatori kineetiline voolutihedus ($j_k$) 0,1 M KOH lahuses 0,8 V juures pöörduva vesinikelektroodi (RHE) suhtes oli 2,6 mA $cm^{-2}$. Anioonvahetusmembraaniga otseses metanool-kütuseelemendis (DMFC) saavutati selle materjaliga maksimaalne võimsustihedus ($P_{max}$) 0,72 mW $cm^{-2}$, mis oli ligikaudu sama kui 60% Pt/C katalüsaatoril. Süsinikkandja vahetamisel komposiitmaterjalilt karbiidset päritolu süsiniku (CDC) vastu tõusis $j_k$ väärtus 7,2 mA $cm^{-2}$ peale, mida seostati CDC-põhise katalüsaatori väga suure eripinnaga (2024 $m^2$ $g^{-1}$) [VII]. Mitte ühegi doktoritöö esimeses osas kasutatud katalüsaatori puhul ei täheldatud aktiivsuse kadu tsükleerimisel 0 kuni –1,2 V kalomelelektroodi suhtes 1000 tsükli vältel. Doktoritöö teises osas sünteesiti ja karakteriseeriti raua või koobalti ja lämmastikuga dopeeritud süsiniknanotorusid [IV–VI]. $FeCl_3$ lisamisel sünteesisegusse (lisaks MWCNT-dele ja DCDA-le) saavutati 0,1 M KOH lahuses 0,8 V juures RHE suhtes $j_k$ väärtus 7,9 mA $cm^{-2}$ [V] ning $CoCl_2$ kasutamisel 12,4 mA $cm^{-2}$ [IV]. Elektrokatalüütilise aktiivsuse kasvu põhjuseks oli N-dopeeritud süsinikuga kaetud metalli/metallikarbiidi või -oksiidi osakeste ning M-$N_x$ tsentrite teke katalüsaatormaterjalis, mis käituvad hapniku redutseerumise aktiivtsentritena. Pöörleva ketaselektroodi meetodil (RDE) läbi viidud stabiilsustesti vältel ei täheldatud mingit aktiivsuse langust. Aluselises DMFC-s oli Fe ja N dopeeritud materjali aktiivsus sarnane Pt/C katalüsaatorile ($P_{max}$ = 1,21 mW $cm^{-2}$) [V]. Co ja N dopeeritud materjal oli AEMFC-s isegi aktiivsem kui 20% Pt/C ($P_{max}$ = 116 mW $cm^{-2}$) [IV]. Happelises keskkonnas oli Fe ja N dopeeritud katalüsaator aktiivsem kui Co ja N dopeeritud materjal, kuid kahjuks kehvema stabiilsusega [VI]. Põhiliseks probleemiks selle sünteesimeetodi puhul oli metalli aglomereerumine osakesteks, mille katalüütiline aktiivsus on väiksem kui M-$N_x$ katalüütilistel tsentritel. Doktoritöö kolmandas osas sünteesiti CDC-l põhinevaid Fe või Co ja lämmastikuga dopeeritud süsinikkatalüsaatoreid [VIII–XIV]. TiCDC-l põhineva Fe ja N dopeeritud materjaliga saavutati 0,8 V vs RHE juures 0,1 M KOH lahuses $j_k$ väärtuseks 9,1 mA $cm^{-2}$, samas kui Co-N-CDC materjali puhul oli see 8,2 mA $cm^{-2}$ [VIII]. DMFC-s olid mõlemad katalüsaatorid aktiivsemad kui 60% Pt/C, Fe-N-CDC puhul oli $P_{max}$ 1,46 ja Co-N-CDC puhul 1,43 mW $cm^{-2}$ [VIII]. AEMFC testides saadi Fe-N-

CDC puhul $P_{max}$ väärtuseks 80 ja Co-N-CDC puhul 78 mW cm$^{-2}$ [IX]. Aktiivsuse kasvu põhjuseks võrreldes süsiniknanotorudel põhinevate katalüsaatoritega oli materjali suurem eripind, poorsus ning lämmastiku kontsentratsioon pindkihis. Põhiliseks probleemiks, eriti kütuseelemendis, oli CDC osakeste suurus (1–10 μm). CDC ja MWCNT komposiidi valmistamine 1,10-fenantroliini sekundaarse lämmastikuallikana ja mitmeetapilist sünteesiprotseduuri kasutades andis eelnevatest veelgi paremaid tulemusi: Fe ja N dopeeritud komposiitmaterjali $P_{max}$ väärtus oli 160 mW cm$^{-2}$ [X]. Selle peamiseks põhjuseks on sellest materjalist valmistatud elektroodi optimeeritum struktuur kütuseelemendis, mis muudab massiülekande efektiivsemaks. Viimaks kasutati katalüsaatori valmistamiseks kuulveskis jahvatamise optimeerimist. 5 mm $ZrO_2$ kuulide vahetamine 0,5 mm diameetriga kuulide vastu ning jahvatamine etanooli keskkonnas polüvinüülpürrolidooni juuresolekul vähendas katalüsaatori osakeste diameetrit <1 μm. Sel meetodil välditi ka jahvatamisest tulenevat poorsuse langust ning saavutati metalli parem jaotumine katalüsaatori pinnale M-$N_x$ tsentritesse. Fe ja N dopeeritud katalüsaator andis AEMFC-s $P_{max}$ väärtuseks 356 mW cm$^{-2}$ ning $j_k$ väärtuseks 0,9 V juures 52 mA cm$^{-2}$, mis on üks parimaid sama membraaniga kütuseelemendis saavutatud tulemusi [XIV]. Prootonvahetusmembraaniga kütuseelemendis (PEMFC) saadi TiCDC-l põhineva katalüsaatoriga $j_{0,8\ V}$ väärtuseks 20 mA cm$^{-2}$ ja $j_{0,6\ V}$ väärtuseks 400 mA cm$^{-2}$ [XI]. Siin leiti, et $ZnCl_2$ lisamine sünteesisegusse võimaldab samuti jahvatamise ja 1,10-fenantroliiniga dopeerimisest tulenevaid poorsuse ja eripinna kadusid vältida, mis suurendas $j_{0,8\ V}$ väärtust neljakordselt [XIII]. TiCDC ja MWCNT valmistatud komposiitmaterjali puhul täheldati, et 5000 tsükli vältel potentsiaalivahemikus 1 kuni 0,005 V RHE suhtes 0,5 M $H_2SO_4$ lahuses 70 °C juures vähenes poollainepotentsiaali nihe üle 2 korra võrreldes ilma MWCNT lisandita katalüsaatoriga [XII]. Käesolevas doktoritöös sünteesiti ja karakteriseeriti esimest korda CDC-l põhinevaid katalüsaatoreid, mis näitasid kommertsiaalse Pt/C katalüsaatoriga võrreldes sarnast või isegi kõrgemat aktiivsust. Esmakordselt demonstreeriti sünteesistrateegiaid MWCNT/grafeen ja MWCNT/CDC komposiitkatalüsaatorite valmistamiseks ning kuulveskis jahvatamise negatiivsete efektide vähendamiseks, mida on juba kirjanduses kasutatud edasisteks arenguteks mitte-väärismetallkatalüsaatorite vallas. Selles doktoritöös saadud tulemused osutavad märkimisväärsele edasiminekule hapniku redutseerumise elektrokatalüüsi alal.

# 11. ACKNOWLEDGEMENTS

My deepest thanks go to my supervisors, Dr. Ivar Kruusenberg and Associate Professor Kaido Tammeveski for their hard work and contributions not only to the results presented in this thesis, but also towards teaching me how to be a scientist. No written words can rightfully represent all their efforts. Two other major influences and contributors were Dr. Ave Sarapuu, who was a co-supervisor of my MSc thesis and Dr. Frédéric Jaouen, who supervised my visiting research at ICGM in Montpellier.

I would like to thank all of the co-authors of the publications that this thesis is based on: Jaan Aruväli, Assoc. Prof. Qingying Jia, Dr. Urmas Joost, Dr. Maike Käärik, Prof. Tanja Kallio, Prof. Arunachala M. Kannan, Dr. Petri Kanninen, Dr. Arvo Kikas, Dr. Ilmar Kink, Dr. Vambola Kisand, Mati Kook, Dr. Jaan Leis, Maido Merisalu, Prof. Sanjeev Mukerjee, Dr. Päärn Paiste, Dr. Martti Pärs, Laurits Puust, Dr. Mihkel Rähn, Dilip Ramani, Dr, Protima Rauwel, Rando Saar, Dr. Nastaran Ranjbar Sahraie, Prof. Väino Sammelselg, Dr. Jevgeni Šulga, Dr. Moulay-Tahar Sougrati, Dr. Andrea Zitolo, Prof. Steven Holdcroft, Merilin Vikkisk and Dr. Sergei Vlassov. In addition, I would like to sincerely thank everyone in our working group who have also contributed to this work either directly, with advice, inspiration, or simply with kind words and encouragement.

This work has been financially supported by the EU through the European Regional Development Fund (TK141 "Advanced materials and high technology devices for energy recuperation systems"), the Smart specialisation scholarship for Sander Ratso, the Dora+ programme and the Graduate School of Functional Materials and Technologies. This work was also financially supported by the Estonian Research Council (IUT20-16, IUT2-25, IUT34-14, PUT1689, PRG4, PRG723, Grant No. 9323, FP7 INCO-2013-3 ERA-NET Action INNO INDIGO under grant agreement No. 609515) and the Estonian Nanotechnology Competence Center. Financial support by the Archimedes Foundation (Project No. 3.2.0501.10-0011 and Project No. 3.2.0501.10-0015) and the Estonian Roadmap Infrastructure project NAMUR is also acknowledged. The Estonian-French PARROT program financed by the Estonian Research Council and Campus France is gratefully acknowledged.

I would also like to give deep thanks my parents, Signe and Allan Ratso, my sister Helen Ratso and my grandmother Aino Ratso for their continuing support to my studies and research.

Finally, I would like to thank Marge Oopkaup from Tallinn French School for lighting the interest in me towards chemistry.

# PUBLICATIONS

# CURRICULUM VITAE


**Name:** Sander Ratso
**Date of birth:** 26.09.1991
**Citizenship**: Estonian
**E-mail:** sander.ratso@ut.ee

**Current occupation:** National Institute of Chemical Physics and Biophysics, Junior Researcher (1,00)


**Education:**

Tallinn French School, 2010, secondary education
University of Tartu, 2015, BSc (Chemistry)
University of Tartu, 2017, MSc (Chemistry)
University of Tartu, 2017–..., PhD Student (Chemistry)

**Professional experience:**

| | |
|---|---|
| 16.06.2014–31.12.2019 | University of Tartu, Insitute of Chemistry, chemist |
| 06.02.2017–28.04.2017 | Université de Montpellier, Institut Charles Gerhardt Montpellier, UMR 5253, electrocatalysis trainee |
| 15.09.2018–17.12.2018 | Université de Montpellier, Institut Charles Gerhardt Montpellier, UMR 5253, visiting PhD student |
| 01.03.2020–... | National Institute of Chemical Physics and Biophysics, Junior Researcher (1,00) |

**Honors and scholarships:**

2015 Sander Ratso, Estonian National Contest for University Students, Estonian Research Council, 1st prize for the work "Electrochemical reduction of oxygen on nitrogen-doped carbon nanomaterials"
2017 Sander Ratso, Estonian National Contest for University Students, Estonian Research Council, 1st prize for the work "Electrochemical reduction of oxygen on Co, Fe-containing nitrogen doped multiwalled carbon nanotubes"
2017 Erasmus+ traineeship programme
2018 Dora+ scholarship for PhD student mobility
2019 Dora+ scholarship for short study visits
2019 Prize for the best poster at the conference "Electrolysis and Fuel Cell Discussions – Towards Catalysts Free of Critical Raw Materials for Fuel Cells and Electrolysers"
2019 Sander Ratso, First Prize, The Dr. Bernard S. Baker Student Award for Fuel Cell Research

**Major scientific publications:**


1. S. Ratso, I. Kruusenberg, M. Vikkisk, U. Joost, E. Shulga, I. Kink, T. Kallio, K. Tammeveski, Highly active nitrogen-doped few-layer graphene/carbon nanotube composite electrocatalyst for oxygen reduction reaction in alkaline media, Carbon 73 (2014) 361–370.
2. I. Kruusenberg, S. Ratso, M. Vikkisk, P. Kanninen, T. Kallio, A.M. Kannan, K. Tammeveski, Highly active nitrogen-doped nanocarbon electrocatalysts for alkaline direct methanol fuel cell, Journal of Power Sources 281 (2015) 94–102.
3. M. Vikkisk, I. Kruusenberg, S. Ratso, U. Joost, E. Shulga, I. Kink, P. Rauwel, K. Tammeveski, Enhanced electrocatalytic activity of nitrogen-doped multi-walled carbon nanotubes towards the oxygen reduction reaction in alkaline media, RSC Advances 5 (2015) 59495–59505.
4. S. Ratso, I. Kruusenberg, U. Joost, R. Saar, K. Tammeveski, Enhanced oxygen reduction reaction activity of nitrogen-doped graphene/multi-walled carbon nanotube catalysts in alkaline media, International Journal of Hydrogen Energy 41 (2016) 22510–22519.
5. I. Kruusenberg, D. Ramani, S. Ratso, U. Joost, R. Saar, P. Rauwel, A.M. Kannan, K. Tammeveski, Cobalt-nitrogen co-doped carbon nanotube cathode catalyst for alkaline membrane fuel cells, ChemElectroChem 3 (2016) 1455–1465.
6. S. Ratso, I. Kruusenberg, A. Sarapuu, P. Rauwel, R. Saar, U. Joost, J. Aruväli, P. Kanninen, T. Kallio, K. Tammeveski, Enhanced oxygen reduction reaction activity of iron-containing nitrogen-doped carbon nanotubes for alkaline direct methanol fuel cell application, Journal of Power Sources 332 (2016) 129–138.
7. S. Ratso, I. Kruusenberg, A. Sarapuu, M. Kook, P. Rauwel, R. Saar, J. Aruväli, K. Tammeveski, Electrocatalysis of oxygen reduction on iron- and cobalt-containing nitrogen-doped carbon nanotubes in acid media, Electrochimica Acta 218 (2016) 303–310.
8. S. Ratso, I. Kruusenberg, M. Käärik, M. Kook, R. Saar, M. Pärs, J. Leis, K. Tammeveski, Highly efficient nitrogen-doped carbide-derived carbon materials for oxygen reduction reaction in alkaline media, Carbon 113 (2017) 159–169.
9. S. Ratso, I. Kruusenberg, M. Käärik, M. Kook, R. Saar, P. Kanninen, T. Kallio, J. Leis, K. Tammeveski, Transition metal-nitrogen co-doped carbide-derived carbon catalysts for oxygen reduction reaction in alkaline direct methanol fuel cell, Applied Catalysis B: Environmental 219 (2017) 276–286.
10. S. Ratso, I. Kruusenberg, M. Käärik, M. Kook, L. Puust, R. Saar, J. Leis, K. Tammeveski, Highly efficient transition metal and nitrogen co-doped carbide-derived carbon electrocatalysts for anion exchange membrane fuel cells, Journal of Power Sources 375 (2018) 233–243.

11. S. Ratso, M. Käärik, M. Kook, P. Paiste, V. Kisand, S. Vlassov, J. Leis, K. Tammeveski, Iron and nitrogen co-doped carbide-derived carbon and carbon nanotube composite catalysts for oxygen reduction reaction, ChemElectroChem 5 (2018) 1827–1836.
12. S. Ratso, N. Ranjbar Sahraie, M.T. Sougrati, M. Käärik, M. Kook, R. Saar, P. Paiste, Q. Jia, J. Leis, S. Mukerjee, F. Jaouen, K. Tammeveski, Synthesis of highly-active Fe-N-C catalysts for PEMFC with carbide-derived carbons, Journal of Materials Chemistry A 6 (2018) 14663–14674.
13. S. Ratso, M. Käärik, M. Kook, P. Paiste, J. Aruväli, S. Vlassov, V. Kisand, J. Leis, A.M. Kannan, K. Tammeveski, High performance catalysts based on Fe/N co-doped carbide-derived carbon and carbon nanotube composites for oxygen reduction reaction in acid media, International Journal of Hydrogen Energy 44 (2019) 12636–12648.
14. S. Ratso, M.T. Sougrati, M. Käärik, M. Merisalu, M. Rähn, V. Kisand, A. Kikas, P. Paiste, J. Leis, V. Sammelselg, F. Jaouen, K. Tammeveski, Effect of ball-milling on the oxygen reduction reaction activity of iron and nitrogen co-doped carbide-derived carbon catalysts in acid media, ACS Applied Energy Material 2 (2019) 7952–7962.
15. R. Sibul, E. Kibena-Põldsepp, S. Ratso, M. Kook, M. Käärik, M. Merisalu, P. Paiste, J. Leis, V. Sammelselg, K. Tammeveski, Nitrogen-doped carbon-based electrocatalysts synthesised by ball-milling, Electrochemistry Communications 93 (2018) 39–43.
16. R. Sibul, E. Kibena-Põldsepp, S. Ratso, M. Kook, M.T. Sougrati, M. Käärik, M. Merisalu, J. Aruväli, P. Paiste, A. Treshchalov, J. Leis, V. Kisand, V. Sammelselg, S. Holdcroft, F. Jaouen, K. Tammeveski, Iron- and nitrogen-doped graphene-based catalysts for fuel cell applications, ChemElectroChem 7 (2020) 1739–1747.
17. S. Ratso, A. Zitolo, M. Käärik, M. Merisalu, M. Rähn, A. Kikas, V. Kisand, P. Paiste, J. Leis, V. Sammelselg, S. Holdcroft, F. Jaouen, K. Tammeveski, Non-precious metal cathodes for anion exchange membrane fuel cells from ball-milled iron and nitrogen doped carbide-derived carbons (Renewable Energy, In press).

# ELULOOKIRJELDUS


**Nimi:** Sander Ratso
**Sünniaeg:** 26.09.1991
**Kodakondsus**: eestlane
**E-post:** sander.ratso@ut.ee

**Töökoht:** Keemilise ja Bioloogilise Füüsika Instituut, nooremteadur (1,00)


**Hariduskäik:**
Tallinna Prantsuse Lütseum, 2010, keskharidus
Tartu Ülikool, 2015, BSc (keemia)
Tartu Ülikool, 2017, MSc (keemia)
Tartu Ülikool, 2017–..., doktorant (keemia)

**Teenistuskäik:**

| | |
|---|---|
| 16.06.2014–31.12.2019 | Tartu Ülikool, Keemia instituut, keemik |
| 06.02.2017–28.04.2017 | Montpellier Ülikool, Charles Gerhardti Montpellier Instituut, UMR 5253, elektrokatalüüsi praktikant |
| 15.09.2018–17.12.2018 | Montpellier Ülikool, Charles Gerhardti Montpellier Instituut, UMR 5253, külalisdoktorant |
| 01.03.2020–... | Keemilise ja Bioloogilise Füüsika instituut, nooremteadur (1,00) |

**Auhinnad ja stipendiumid:**
2015 Sander Ratso, Üliõpilaste teadustööde riiklik konkurss 2015, Eesti Teadusagentuur, I preemia konkursitöö „Hapniku elektrokeemiline redutseerumine lämmastikuga dopeeritud süsiniknanomaterjalidel“ eest.
2017 Sander Ratso, Üliõpilaste teadustööde riiklik konkurss 2017, Eesti Teadusagentuur, I preemia konkursitöö „Hapniku elektrokeemiline redutseerumine lämmastikuga dopeeritud rauda või koobaltit sisaldavatel mitmeseinalistel süsiniknanotorudel“ eest.
2019 Sander Ratso, Dr. Bernard S. Bakeri tudengipreemia 1. auhind kütuseelementide alase teadustöö eest
2019 Sander Ratso, Preemia parima posterettekande eest konverentsil “Electrolysis and Fuel Cell Discussions – Towards Catalysts Free of Critical Raw Materials for Fuel Cells and Electrolysers”.

**Olulisemad publikatsioonid:**

1. S. Ratso, I. Kruusenberg, M. Vikkisk, U. Joost, E. Shulga, I. Kink, T. Kallio, K. Tammeveski, Highly active nitrogen-doped few-layer graphene/carbon nanotube composite electrocatalyst for oxygen reduction reaction in alkaline media, Carbon 73 (2014) 361–370.

2. I. Kruusenberg, S. Ratso, M. Vikkisk, P. Kanninen, T. Kallio, A.M. Kannan, K. Tammeveski, Highly active nitrogen-doped nanocarbon electrocatalysts for alkaline direct methanol fuel cell, Journal of Power Sources 281 (2015) 94–102.
3. M. Vikkisk, I. Kruusenberg, S. Ratso, U. Joost, E. Shulga, I. Kink, P. Rauwel, K. Tammeveski, Enhanced electrocatalytic activity of nitrogen-doped multi-walled carbon nanotubes towards the oxygen reduction reaction in alkaline media, RSC Advances 5 (2015) 59495–59505.
4. S. Ratso, I. Kruusenberg, U. Joost, R. Saar, K. Tammeveski, Enhanced oxygen reduction reaction activity of nitrogen-doped graphene/multi-walled carbon nanotube catalysts in alkaline media, International Journal of Hydrogen Energy 41 (2016) 22510–22519.
5. I. Kruusenberg, D. Ramani, S. Ratso, U. Joost, R. Saar, P. Rauwel, A.M. Kannan, K. Tammeveski, Cobalt-nitrogen co-doped carbon nanotube cathode catalyst for alkaline membrane fuel cells, ChemElectroChem 3 (2016) 1455–1465.
6. S. Ratso, I. Kruusenberg, A. Sarapuu, P. Rauwel, R. Saar, U. Joost, J. Aruväli, P. Kanninen, T. Kallio, K. Tammeveski, Enhanced oxygen reduction reaction activity of iron-containing nitrogen-doped carbon nanotubes for alkaline direct methanol fuel cell application, Journal of Power Sources 332 (2016) 129–138.
7. S. Ratso, I. Kruusenberg, A. Sarapuu, M. Kook, P. Rauwel, R. Saar, J. Aruväli, K. Tammeveski, Electrocatalysis of oxygen reduction on iron- and cobalt-containing nitrogen-doped carbon nanotubes in acid media, Electrochimica Acta 218 (2016) 303–310.
8. S. Ratso, I. Kruusenberg, M. Käärik, M. Kook, R. Saar, M. Pärs, J. Leis, K. Tammeveski, Highly efficient nitrogen-doped carbide-derived carbon materials for oxygen reduction reaction in alkaline media, Carbon 113 (2017) 159–169.
9. S. Ratso, I. Kruusenberg, M. Käärik, M. Kook, R. Saar, P. Kanninen, T. Kallio, J. Leis, K. Tammeveski, Transition metal-nitrogen co-doped carbide-derived carbon catalysts for oxygen reduction reaction in alkaline direct methanol fuel cell, Applied Catalysis B: Environmental 219 (2017) 276–286.
10. S. Ratso, I. Kruusenberg, M. Käärik, M. Kook, L. Puust, R. Saar, J. Leis, K. Tammeveski, Highly efficient transition metal and nitrogen co-doped carbide-derived carbon electrocatalysts for anion exchange membrane fuel cells, Journal of Power Sources 375 (2018) 233–243.
11. S. Ratso, M. Käärik, M. Kook, P. Paiste, V. Kisand, S. Vlassov, J. Leis, K. Tammeveski, Iron and nitrogen co-doped carbide-derived carbon and carbon nanotube composite catalysts for oxygen reduction reaction, ChemElectroChem 5 (2018) 1827–1836.

12. S. Ratso, N. Ranjbar Sahraie, M.T. Sougrati, M. Käärik, M. Kook, R. Saar, P. Paiste, Q. Jia, J. Leis, S. Mukerjee, F. Jaouen, K. Tammeveski, Synthesis of highly-active Fe-N-C catalysts for PEMFC with carbide-derived carbons, Journal of Materials Chemistry A 6 (2018) 14663–14674.
13. S. Ratso, M. Käärik, M. Kook, P. Paiste, J. Aruväli, S. Vlassov, V. Kisand, J. Leis, A.M. Kannan, K. Tammeveski, High performance catalysts based on Fe/N co-doped carbide-derived carbon and carbon nanotube composites for oxygen reduction reaction in acid media, International Journal of Hydrogen Energy 44 (2019) 12636–12648.
14. S. Ratso, M.T. Sougrati, M. Käärik, M. Merisalu, M. Rähn, V. Kisand, A. Kikas, P. Paiste, J. Leis, V. Sammelselg, F. Jaouen, K. Tammeveski, Effect of ball-milling on the oxygen reduction reaction activity of iron and nitrogen co-doped carbide-derived carbon catalysts in acid media, ACS Applied Energy Material 2 (2019) 7952–7962.
15. R. Sibul, E. Kibena-Põldsepp, S. Ratso, M. Kook, M. Käärik, M. Merisalu, P. Paiste, J. Leis, V. Sammelselg, K. Tammeveski, Nitrogen-doped carbon-based electrocatalysts synthesised by ball-milling, Electrochemistry Communications 93 (2018) 39–43.
16. R. Sibul, E. Kibena-Põldsepp, S. Ratso, M. Kook, M.T. Sougrati, M. Käärik, M. Merisalu, J. Aruväli, P. Paiste, A. Treshchalov, J. Leis, V. Kisand, V. Sammelselg, S. Holdcroft, F. Jaouen, K. Tammeveski, Iron- and nitrogen-doped graphene-based catalysts for fuel cell applications, ChemElectroChem 7 (2020) 1739–1747.
17. S. Ratso, A. Zitolo, M. Käärik, M. Merisalu, M. Rähn, A. Kikas, V. Kisand, P. Paiste, J. Leis, V. Sammelselg, S. Holdcroft, F. Jaouen, K. Tammeveski, Non-precious metal cathodes for anion exchange membrane fuel cells from ball-milled iron and nitrogen doped carbide-derived carbons (Renewable Energy, Trükis).

# DISSERTATIONES CHIMICAE UNIVERSITATIS TARTUENSIS

1. **Toomas Tamm.** Quantum-chemical simulation of solvent effects. Tartu, 1993, 110 p.
2. **Peeter Burk.** Theoretical study of gas-phase acid-base equilibria. Tartu, 1994, 96 p.
3. **Victor Lobanov.** Quantitative structure-property relationships in large descriptor spaces. Tartu, 1995, 135 p.
4. **Vahur Mäemets.** The $^{17}O$ and $^{1}H$ nuclear magnetic resonance study of $H_2O$ in individual solvents and its charged clusters in aqueous solutions of electrolytes. Tartu, 1997, 140 p.
5. **Andrus Metsala.** Microcanonical rate constant in nonequilibrium distribution of vibrational energy and in restricted intramolecular vibrational energy redistribution on the basis of slater's theory of unimolecular reactions. Tartu, 1997, 150 p.
6. **Uko Maran.** Quantum-mechanical study of potential energy surfaces in different environments. Tartu, 1997, 137 p.
7. **Alar Jänes.** Adsorption of organic compounds on antimony, bismuth and cadmium electrodes. Tartu, 1998, 219 p.
8. **Kaido Tammeveski.** Oxygen electroreduction on thin platinum films and the electrochemical detection of superoxide anion. Tartu, 1998, 139 p.
9. **Ivo Leito.** Studies of Brønsted acid-base equilibria in water and non-aqueous media. Tartu, 1998, 101 p.
10. **Jaan Leis.** Conformational dynamics and equilibria in amides. Tartu, 1998, 131 p.
11. **Toonika Rinken.** The modelling of amperometric biosensors based on oxidoreductases. Tartu, 2000, 108 p.
12. **Dmitri Panov.** Partially solvated Grignard reagents. Tartu, 2000, 64 p.
13. **Kaja Orupõld.** Treatment and analysis of phenolic wastewater with microorganisms. Tartu, 2000, 123 p.
14. **Jüri Ivask.** Ion Chromatographic determination of major anions and cations in polar ice core. Tartu, 2000, 85 p.
15. **Lauri Vares.** Stereoselective Synthesis of Tetrahydrofuran and Tetrahydropyran Derivatives by Use of Asymmetric Horner-Wadsworth-Emmons and Ring Closure Reactions. Tartu, 2000, 184 p.
16. **Martin Lepiku.** Kinetic aspects of dopamine $D_2$ receptor interactions with specific ligands. Tartu, 2000, 81 p.
17. **Katrin Sak.** Some aspects of ligand specificity of P2Y receptors. Tartu, 2000, 106 p.
18. **Vello Pällin.** The role of solvation in the formation of iotsitch complexes. Tartu, 2001, 95 p.
19. **Katrin Kollist.** Interactions between polycyclic aromatic compounds and humic substances. Tartu, 2001, 93 p.

20. **Ivar Koppel.** Quantum chemical study of acidity of strong and superstrong Brønsted acids. Tartu, 2001, 104 p.
21. **Viljar Pihl.** The study of the substituent and solvent effects on the acidity of OH and CH acids. Tartu, 2001, 132 p.
22. **Natalia Palm.** Specification of the minimum, sufficient and significant set of descriptors for general description of solvent effects. Tartu, 2001, 134 p.
23. **Sulev Sild.** QSPR/QSAR approaches for complex molecular systems. Tartu, 2001, 134 p.
24. **Ruslan Petrukhin.** Industrial applications of the quantitative structure-property relationships. Tartu, 2001, 162 p.
25. **Boris V. Rogovoy.** Synthesis of (benzotriazolyl)carboximidamides and their application in relations with *N*- and *S*-nucleophyles. Tartu, 2002, 84 p.
26. **Koit Herodes.** Solvent effects on UV-vis absorption spectra of some solvatochromic substances in binary solvent mixtures: the preferential solvation model. Tartu, 2002, 102 p.
27. **Anti Perkson.** Synthesis and characterisation of nanostructured carbon. Tartu, 2002, 152 p.
28. **Ivari Kaljurand.** Self-consistent acidity scales of neutral and cationic Brønsted acids in acetonitrile and tetrahydrofuran. Tartu, 2003, 108 p.
29. **Karmen Lust.** Adsorption of anions on bismuth single crystal electrodes. Tartu, 2003, 128 p.
30. **Mare Piirsalu.** Substituent, temperature and solvent effects on the alkaline hydrolysis of substituted phenyl and alkyl esters of benzoic acid. Tartu, 2003, 156 p.
31. **Meeri Sassian.** Reactions of partially solvated Grignard reagents. Tartu, 2003, 78 p.
32. **Tarmo Tamm.** Quantum chemical modelling of polypyrrole. Tartu, 2003. 100 p.
33. **Erik Teinemaa.** The environmental fate of the particulate matter and organic pollutants from an oil shale power plant. Tartu, 2003. 102 p.
34. **Jaana Tammiku-Taul.** Quantum chemical study of the properties of Grignard reagents. Tartu, 2003. 120 p.
35. **Andre Lomaka.** Biomedical applications of predictive computational chemistry. Tartu, 2003. 132 p.
36. **Kostyantyn Kirichenko.** Benzotriazole – Mediated Carbon–Carbon Bond Formation. Tartu, 2003. 132 p.
37. **Gunnar Nurk.** Adsorption kinetics of some organic compounds on bismuth single crystal electrodes. Tartu, 2003, 170 p.
38. **Mati Arulepp.** Electrochemical characteristics of porous carbon materials and electrical double layer capacitors. Tartu, 2003, 196 p.
39. **Dan Cornel Fara.** QSPR modeling of complexation and distribution of organic compounds. Tartu, 2004, 126 p.
40. **Riina Mahlapuu.** Signalling of galanin and amyloid precursor protein through adenylate cyclase. Tartu, 2004, 124 p.

41. **Mihkel Kerikmäe.** Some luminescent materials for dosimetric applications and physical research. Tartu, 2004, 143 p.
42. **Jaanus Kruusma.** Determination of some important trace metal ions in human blood. Tartu, 2004, 115 p.
43. **Urmas Johanson.** Investigations of the electrochemical properties of polypyrrole modified electrodes. Tartu, 2004, 91 p.
44. **Kaido Sillar.** Computational study of the acid sites in zeolite ZSM-5. Tartu, 2004, 80 p.
45. **Aldo Oras.** Kinetic aspects of dATPαS interaction with $P2Y_1$ receptor. Tartu, 2004, 75 p.
46. **Erik Mölder.** Measurement of the oxygen mass transfer through the air-water interface. Tartu, 2005, 73 p.
47. **Thomas Thomberg.** The kinetics of electroreduction of peroxodisulfate anion on cadmium (0001) single crystal electrode. Tartu, 2005, 95 p.
48. **Olavi Loog.** Aspects of condensations of carbonyl compounds and their imine analogues. Tartu, 2005, 83 p.
49. **Siim Salmar.** Effect of ultrasound on ester hydrolysis in aqueous ethanol. Tartu, 2006, 73 p.
50. **Ain Uustare.** Modulation of signal transduction of heptahelical receptors by other receptors and G proteins. Tartu, 2006, 121 p.
51. **Sergei Yurchenko.** Determination of some carcinogenic contaminants in food. Tartu, 2006, 143 p.
52. **Kaido Tämm.** QSPR modeling of some properties of organic compounds. Tartu, 2006, 67 p.
53. **Olga Tšubrik.** New methods in the synthesis of multisubstituted hydrazines. Tartu. 2006, 183 p.
54. **Lilli Sooväli.** Spectrophotometric measurements and their uncertainty in chemical analysis and dissociation constant measurements. Tartu, 2006, 125 p.
55. **Eve Koort.** Uncertainty estimation of potentiometrically measured ph and p$K_a$ values. Tartu, 2006, 139 p.
56. **Sergei Kopanchuk.** Regulation of ligand binding to melanocortin receptor subtypes. Tartu, 2006, 119 p.
57. **Silvar Kallip.** Surface structure of some bismuth and antimony single crystal electrodes. Tartu, 2006, 107 p.
58. **Kristjan Saal.** Surface silanization and its application in biomolecule coupling. Tartu, 2006, 77 p.
59. **Tanel Tätte.** High viscosity $Sn(OBu)_4$ oligomeric concentrates and their applications in technology. Tartu, 2006, 91 p.
60. **Dimitar Atanasov Dobchev**. Robust QSAR methods for the prediction of properties from molecular structure. Tartu, 2006, 118 p.
61. **Hannes Hagu**. Impact of ultrasound on hydrophobic interactions in solutions. Tartu, 2007, 81 p.
62. **Rutha Jäger.** Electroreduction of peroxodisulfate anion on bismuth electrodes. Tartu, 2007, 142 p.

63. **Kaido Viht.** Immobilizable bisubstrate-analogue inhibitors of basophilic protein kinases: development and application in biosensors. Tartu, 2007, 88 p.
64. **Eva-Ingrid Rõõm.** Acid-base equilibria in nonpolar media. Tartu, 2007, 156 p.
65. **Sven Tamp.** DFT study of the cesium cation containing complexes relevant to the cesium cation binding by the humic acids. Tartu, 2007, 102 p.
66. **Jaak Nerut.** Electroreduction of hexacyanoferrate(III) anion on Cadmium (0001) single crystal electrode. Tartu, 2007, 180 p.
67. **Lauri Jalukse.** Measurement uncertainty estimation in amperometric dissolved oxygen concentration measurement. Tartu, 2007, 112 p.
68. **Aime Lust.** Charge state of dopants and ordered clusters formation in $CaF_2$:Mn and $CaF_2$:Eu luminophors. Tartu, 2007, 100 p.
69. **Iiris Kahn**. Quantitative Structure-Activity Relationships of environmentally relevant properties. Tartu, 2007, 98 p.
70. **Mari Reinik.** Nitrates, nitrites, N-nitrosamines and polycyclic aromatic hydrocarbons in food: analytical methods, occurrence and dietary intake. Tartu, 2007, 172 p.
71. **Heili Kasuk.** Thermodynamic parameters and adsorption kinetics of organic compounds forming the compact adsorption layer at Bi single crystal electrodes. Tartu, 2007, 212 p.
72. **Erki Enkvist.** Synthesis of adenosine-peptide conjugates for biological applications. Tartu, 2007, 114 p.
73. **Svetoslav Hristov Slavov**. Biomedical applications of the QSAR approach. Tartu, 2007, 146 p.
74. **Eneli Härk.** Electroreduction of complex cations on electrochemically polished Bi(*hkl*) single crystal electrodes. Tartu, 2008, 158 p.
75. **Priit Möller.** Electrochemical characteristics of some cathodes for medium temperature solid oxide fuel cells, synthesized by solid state reaction technique. Tartu, 2008, 90 p.
76. **Signe Viggor.** Impact of biochemical parameters of genetically different pseudomonads at the degradation of phenolic compounds. Tartu, 2008, 122 p.
77. **Ave Sarapuu.** Electrochemical reduction of oxygen on quinone-modified carbon electrodes and on thin films of platinum and gold. Tartu, 2008, 134 p.
78. **Agnes Kütt.** Studies of acid-base equilibria in non-aqueous media. Tartu, 2008, 198 p.
79. **Rouvim Kadis.** Evaluation of measurement uncertainty in analytical chemistry: related concepts and some points of misinterpretation. Tartu, 2008, 118 p.
80. **Valter Reedo.** Elaboration of IVB group metal oxide structures and their possible applications. Tartu, 2008, 98 p.
81. **Aleksei Kuznetsov.** Allosteric effects in reactions catalyzed by the cAMP-dependent protein kinase catalytic subunit. Tartu, 2009, 133 p.

82. **Aleksei Bredihhin.** Use of mono- and polyanions in the synthesis of multisubstituted hydrazine derivatives. Tartu, 2009, 105 p.
83. **Anu Ploom.** Quantitative structure-reactivity analysis in organosilicon chemistry. Tartu, 2009, 99 p.
84. **Argo Vonk.** Determination of adenosine $A_{2A}$- and dopamine $D_1$ receptor-specific modulation of adenylate cyclase activity in rat striatum. Tartu, 2009, 129 p.
85. **Indrek Kivi.** Synthesis and electrochemical characterization of porous cathode materials for intermediate temperature solid oxide fuel cells. Tartu, 2009, 177 p.
86. **Jaanus Eskusson.** Synthesis and characterisation of diamond-like carbon thin films prepared by pulsed laser deposition method. Tartu, 2009, 117 p.
87. **Marko Lätt.** Carbide derived microporous carbon and electrical double layer capacitors. Tartu, 2009, 107 p.
88. **Vladimir Stepanov.** Slow conformational changes in dopamine transporter interaction with its ligands. Tartu, 2009, 103 p.
89. **Aleksander Trummal.** Computational Study of Structural and Solvent Effects on Acidities of Some Brønsted Acids. Tartu, 2009, 103 p.
90. **Eerold Vellemäe.** Applications of mischmetal in organic synthesis. Tartu, 2009, 93 p.
91. **Sven Parkel.** Ligand binding to 5-$HT_{1A}$ receptors and its regulation by $Mg^{2+}$ and $Mn^{2+}$. Tartu, 2010, 99 p.
92. **Signe Vahur.** Expanding the possibilities of ATR-FT-IR spectroscopy in determination of inorganic pigments. Tartu, 2010, 184 p.
93. **Tavo Romann**. Preparation and surface modification of bismuth thin film, porous, and microelectrodes. Tartu, 2010, 155 p.
94. **Nadežda Aleksejeva.** Electrocatalytic reduction of oxygen on carbon nanotube-based nanocomposite materials. Tartu, 2010, 147 p.
95. **Marko Kullapere.** Electrochemical properties of glassy carbon, nickel and gold electrodes modified with aryl groups. Tartu, 2010, 233 p.
96. **Liis Siinor.** Adsorption kinetics of ions at Bi single crystal planes from aqueous electrolyte solutions and room-temperature ionic liquids. Tartu, 2010, 101 p.
97. **Angela Vaasa.** Development of fluorescence-based kinetic and binding assays for characterization of protein kinases and their inhibitors. Tartu 2010, 101 p.
98. **Indrek Tulp.** Multivariate analysis of chemical and biological properties. Tartu 2010, 105 p.
99. **Aare Selberg.** Evaluation of environmental quality in Northern Estonia by the analysis of leachate. Tartu 2010, 117 p.
100. **Darja Lavõgina.** Development of protein kinase inhibitors based on adenosine analogue-oligoarginine conjugates. Tartu 2010, 248 p.
101. **Laura Herm.** Biochemistry of dopamine $D_2$ receptors and its association with motivated behaviour. Tartu 2010, 156 p.

102. **Terje Raudsepp.** Influence of dopant anions on the electrochemical properties of polypyrrole films. Tartu 2010, 112 p.
103. **Margus Marandi.** Electroformation of Polypyrrole Films: *In-situ* AFM and STM Study. Tartu 2011, 116 p.
104. **Kairi Kivirand.** Diamine oxidase-based biosensors: construction and working principles. Tartu, 2011, 140 p.
105. **Anneli Kruve.** Matrix effects in liquid-chromatography electrospray mass-spectrometry. Tartu, 2011, 156 p.
106. **Gary Urb.** Assessment of environmental impact of oil shale fly ash from PF and CFB combustion. Tartu, 2011, 108 p.
107. **Nikita Oskolkov.** A novel strategy for peptide-mediated cellular delivery and induction of endosomal escape. Tartu, 2011, 106 p.
108. **Dana Martin.** The QSPR/QSAR approach for the prediction of properties of fullerene derivatives. Tartu, 2011, 98 p.
109. **Säde Viirlaid.** Novel glutathione analogues and their antioxidant activity. Tartu, 2011, 106 p.
110. **Ülis Sõukand.** Simultaneous adsorption of $Cd^{2+}$, $Ni^{2+}$, and $Pb^{2+}$ on peat. Tartu, 2011, 124 p.
111. **Lauri Lipping.** The acidity of strong and superstrong Brønsted acids, an outreach for the "limits of growth": a quantum chemical study. Tartu, 2011, 124 p.
112. **Heisi Kurig.** Electrical double-layer capacitors based on ionic liquids as electrolytes. Tartu, 2011, 146 p.
113. **Marje Kasari.** Bisubstrate luminescent probes, optical sensors and affinity adsorbents for measurement of active protein kinases in biological samples. Tartu, 2012, 126 p.
114. **Kalev Takkis.** Virtual screening of chemical databases for bioactive molecules. Tartu, 2012, 122 p.
115. **Ksenija Kisseljova**. Synthesis of aza-$\beta^3$-amino acid containing peptides and kinetic study of their phosphorylation by protein kinase A. Tartu, 2012, 104 p.
116. **Riin Rebane.** Advanced method development strategy for derivatization LC/ESI/MS. Tartu, 2012, 184 p.
117. **Vladislav Ivaništšev.** Double layer structure and adsorption kinetics of ions at metal electrodes in room temperature ionic liquids. Tartu, 2012, 128 p.
118. **Irja Helm.** High accuracy gravimetric Winkler method for determination of dissolved oxygen. Tartu, 2012, 139 p.
119. **Karin Kipper.** Fluoroalcohols as Components of LC-ESI-MS Eluents: Usage and Applications. Tartu, 2012, 164 p.
120. **Arno Ratas.** Energy storage and transfer in dosimetric luminescent materials. Tartu, 2012, 163 p.
121. **Reet Reinart-Okugbeni**. Assay systems for characterisation of subtype-selective binding and functional activity of ligands on dopamine receptors. Tartu, 2012, 159 p.

122. **Lauri Sikk.** Computational study of the Sonogashira cross-coupling reaction. Tartu, 2012, 81 p.
123. **Karita Raudkivi.** Neurochemical studies on inter-individual differences in affect-related behaviour of the laboratory rat. Tartu, 2012, 161 p.
124. **Indrek Saar.** Design of GalR2 subtype specific ligands: their role in depression-like behavior and feeding regulation. Tartu, 2013, 126 p.
125. **Ann Laheäär.** Electrochemical characterization of alkali metal salt based non-aqueous electrolytes for supercapacitors. Tartu, 2013, 127 p.
126. **Kerli Tõnurist.** Influence of electrospun separator materials properties on electrochemical performance of electrical double-layer capacitors. Tartu, 2013, 147 p.
127. **Kaija Põhako-Esko.** Novel organic and inorganic ionogels: preparation and characterization. Tartu, 2013, 124 p.
128. **Ivar Kruusenberg.** Electroreduction of oxygen on carbon nanomaterial-based catalysts. Tartu, 2013, 191 p.
129. **Sander Piiskop.** Kinetic effects of ultrasound in aqueous acetonitrile solutions. Tartu, 2013, 95 p.
130. **Ilona Faustova**. Regulatory role of L-type pyruvate kinase N-terminal domain. Tartu, 2013, 109 p.
131. **Kadi Tamm.** Synthesis and characterization of the micro-mesoporous anode materials and testing of the medium temperature solid oxide fuel cell single cells. Tartu, 2013, 138 p.
132. **Iva Bozhidarova Stoyanova-Slavova.** Validation of QSAR/QSPR for regulatory purposes. Tartu, 2013, 109 p.
133. **Vitali Grozovski**. Adsorption of organic molecules at single crystal electrodes studied by *in situ* STM method. Tartu, 2014, 146 p.
134. **Santa Veikšina**. Development of assay systems for characterisation of ligand binding properties to melanocortin 4 receptors. Tartu, 2014, 151 p.
135. **Jüri Liiv.** PVDF (polyvinylidene difluoride) as material for active element of twisting-ball displays. Tartu, 2014, 111 p.
136. **Kersti Vaarmets.** Electrochemical and physical characterization of pristine and activated molybdenum carbide-derived carbon electrodes for the oxygen electroreduction reaction. Tartu, 2014, 131 p.
137. **Lauri Tõntson**. Regulation of G-protein subtypes by receptors, guanine nucleotides and $Mn^{2+}$. Tartu, 2014, 105 p.
138. **Aiko Adamson.** Properties of amine-boranes and phosphorus analogues in the gas phase. Tartu, 2014, 78 p.
139. **Elo Kibena**. Electrochemical grafting of glassy carbon, gold, highly oriented pyrolytic graphite and chemical vapour deposition-grown graphene electrodes by diazonium reduction method. Tartu, 2014, 184 p.
140. **Teemu Näykki.** Novel Tools for Water Quality Monitoring – From Field to Laboratory. Tartu, 2014, 202 p.
141. **Karl Kaupmees.** Acidity and basicity in non-aqueous media: importance of solvent properties and purity. Tartu, 2014, 128 p.

142. **Oleg Lebedev**. Hydrazine polyanions: different strategies in the synthesis of heterocycles. Tartu, 2015, 118 p.
143. **Geven Piir.** Environmental risk assessment of chemicals using QSAR methods. Tartu, 2015, 123 p.
144. **Olga Mazina.** Development and application of the biosensor assay for measurements of cyclic adenosine monophosphate in studies of G protein-coupled receptor signalinga. Tartu, 2015, 116 p.
145. **Sandip Ashokrao Kadam.** Anion receptors: synthesis and accurate binding measurements. Tartu, 2015, 116 p.
146. **Indrek Tallo.** Synthesis and characterization of new micro-mesoporous carbide derived carbon materials for high energy and power density electrical double layer capacitors. Tartu, 2015, 148 p.
147. **Heiki Erikson.** Electrochemical reduction of oxygen on nanostructured palladium and gold catalysts. Tartu, 2015, 204 p.
148. **Erik Anderson.** *In situ* Scanning Tunnelling Microscopy studies of the interfacial structure between Bi(111) electrode and a room temperature ionic liquid. Tartu, 2015, 118 p.
149. **Girinath G. Pillai.** Computational Modelling of Diverse Chemical, Biochemical and Biomedical Properties. Tartu, 2015, 140 p.
150. **Piret Pikma.** Interfacial structure and adsorption of organic compounds at Cd(0001) and Sb(111) electrodes from ionic liquid and aqueous electrolytes: an *in situ* STM study. Tartu, 2015, 126 p.
151. **Ganesh babu Manoharan.** Combining chemical and genetic approaches for photoluminescence assays of protein kinases. Tartu, 2016, 126 p.
152. **Carolin Siimenson**. Electrochemical characterization of halide ion adsorption from liquid mixtures at Bi(111) and pyrolytic graphite electrode surface. Tartu, 2016, 110 p.
153. **Asko Laaniste.** Comparison and optimisation of novel mass spectrometry ionisation sources. Tartu, 2016, 156 p.
154. **Hanno Evard.** Estimating limit of detection for mass spectrometric analysis methods. Tartu, 2016, 224 p.
155. **Kadri Ligi.** Characterization and application of protein kinase-responsive organic probes with triplet-singlet energy transfer. Tartu, 2016, 122 p.
156. **Margarita Kagan.** Biosensing penicillins' residues in milk flows. Tartu, 2016, 130 p.
157. **Marie Kriisa.** Development of protein kinase-responsive photoluminescent probes and cellular regulators of protein phosphorylation. Tartu, 2016, 106 p.
158. **Mihkel Vestli.** Ultrasonic spray pyrolysis deposited electrolyte layers for intermediate temperature solid oxide fuel cells. Tartu, 2016, 156 p.
159. **Silver Sepp**. Influence of porosity of the carbide-derived carbon on the properties of the composite electrocatalysts and characteristics of polymer electrolyte fuel cells. Tartu, 2016, 137 p.
160. **Kristjan Haav**. Quantitative relative equilibrium constant measurements in supramolecular chemistry. Tartu, 2017, 158 p.

161. **Anu Teearu**. Development of MALDI-FT-ICR-MS methodology for the analysis of resinous materials. Tartu, 2017, 205 p.
162. **Taavi Ivan**. Bifunctional inhibitors and photoluminescent probes for studies on protein complexes. Tartu, 2017, 140 p.
163. **Maarja-Liisa Oldekop**. Characterization of amino acid derivatization reagents for LC-MS analysis. Tartu, 2017, 147 p.
164. **Kristel Jukk**. Electrochemical reduction of oxygen on platinum- and palladium-based nanocatalysts. Tartu, 2017, 250 p.
165. **Siim Kukk**. Kinetic aspects of interaction between dopamine transporter and *N*-substituted nortropane derivatives. Tartu, 2017, 107 p.
166. **Birgit Viira**. Design and modelling in early drug development in targeting HIV-1 reverse transcriptase and Malaria. Tartu, 2017, 172 p.
167. **Rait Kivi**. Allostery in cAMP dependent protein kinase catalytic subunit. Tartu, 2017, 115 p.
168. **Agnes Heering**. Experimental realization and applications of the unified acidity scale. Tartu, 2017, 123 p.
169. **Delia Juronen**. Biosensing system for the rapid multiplex detection of mastitis-causing pathogens in milk. Tartu, 2018, 85 p.
170. **Hedi Rahnel.** ARC-inhibitors: from reliable biochemical assays to regulators of physiology of cells. Tartu, 2018, 176 p.
171. **Anton Ruzanov.** Computational investigation of the electrical double layer at metal–aqueous solution and metal–ionic liquid interfaces. Tartu, 2018, 129 p.
172. **Katrin Kestav.** Crystal Structure-Guided Development of Bisubstrate-Analogue Inhibitors of Mitotic Protein Kinase Haspin. Tartu, 2018, 166 p.
173. **Mihkel Ilisson.** Synthesis of novel heterocyclic hydrazine derivatives and their conjugates. Tartu, 2018, 101 p.
174. **Anni Allikalt.** Development of assay systems for studying ligand binding to dopamine receptors. Tartu, 2018, 160 p.
175. **Ove Oll.** Electrical double layer structure and energy storage characteristics of ionic liquid based capacitors. Tartu, 2018, 187 p.
176. **Rasmus Palm.** Carbon materials for energy storage applications. Tartu, 2018, 114 p.
177. **Jörgen Metsik.** Preparation and stability of poly(3,4-ethylenedioxythiophene) thin films for transparent electrode applications. Tartu, 2018, 111 p.
178. **Sofja Tšepelevitš.** Experimental studies and modeling of solute-solvent interactions. Tartu, 2018, 109 p.
179. **Märt Lõkov.** Basicity of some nitrogen, phosphorus and carbon bases in acetonitrile. Tartu, 2018, 104 p.
180. **Anton Mastitski**. Preparation of α-aza-amino acid precursors and related compounds by novel methods of reductive one-pot alkylation and direct alkylation. Tartu, 2018, 155 p.
181. **Jürgen Vahter**. Development of bisubstrate inhibitors for protein kinase CK2. Tartu, 2019, 186 p.

182. **Piia Liigand.** Expanding and improving methodology and applications of ionization efficiency measurements. Tartu, 2019, 189 p.
183. **Sigrid Selberg.** Synthesis and properties of lipophilic phosphazene-based indicator molecules. Tartu, 2019, 74 p.
184. **Jaanus Liigand.** Standard substance free quantification for LC/ESI/MS analysis based on the predicted ionization efficiencies. Tartu, 2019, 254 p.
185. **Marek Mooste.** Surface and electrochemical characterisation of aryl film and nanocomposite material modified carbon and metal-based electrodes. Tartu, 2019, 304 p.
186. **Mare Oja.** Experimental investigation and modelling of pH profiles for effective membrane permeability of drug substances. Tartu, 2019, 306 p.
187. **Sajid Hussain.** Electrochemical reduction of oxygen on supported Pt catalysts. Tartu, 2019, 220 p.
188. **Ronald Väli.** Glucose-derived hard carbon electrode materials for sodium-ion batteries. Tartu, 2019, 180 p.
189. **Ester Tee.** Analysis and development of selective synthesis methods of hierarchical micro- and mesoporous carbons. Tartu, 2019, 210 p.
190. **Martin Maide.** Influence of the microstructure and chemical composition of the fuel electrode on the electrochemical performance of reversible solid oxide fuel cell. Tartu, 2020, 144 p.
191. **Edith Viirlaid.** Biosensing Pesticides in Water Samples. Tartu, 2020, 102 p.
192. **Maike Käärik.** Nanoporous carbon: the controlled nanostructure, and structure-property relationships. Tartu, 2020, 162 p.
193. **Artur Gornischeff.** Study of ionization efficiencies for derivatized compounds in LC/ESI/MS and their application for targeted analysis. Tartu, 2020, 124 p.
194. **Reet Link.** Ligand binding, allosteric modulation and constitutive activity of melanocortin-4 receptors. Tartu, 2020, 108 p.
195. **Pilleriin Peets.** Development of instrumental methods for the analysis of textile fibres and dyes. Tartu, 2020, 150 p.
196. **Larisa Ivanova.** Design of active compounds against neurodegenerative diseases. Tartu, 2020, 152 p.
197. **Meelis Härmas.** Impact of activated carbon microstructure and porosity on electrochemical performance of electrical double-layer capacitors. Tartu, 2020, 122 p.
198. **Ruta Hecht.** Novel Eluent Additives for LC-MS Based Bioanalytical Methods. Tartu, 2020, 202 p.
199. **Max Hecht.** Advances in the Development of a Point-of-Care Mass Spectrometer Test. Tartu, 2020, 168 p.
200. **Ida Rahu.** Bromine formation in inorganic bromide/nitrate mixtures and its application for oxidative aromatic bromination. Tartu, 2020, 116 p.